A Numerical Study of Micro Synthetic Jet and Its Applications in Thermal Management

A Thesis
Presented to
The Academic Faculty

by

Shuo Li

In Partial Fulfillment
of the Requirements for the Degree
Doctor of Philosophy

The G. W. Woodruff School of Mechanical Engineering
Georgia Institute of Technology
December 2005

A Numerical Study of Micro Synthetic Jet and Its Applications in Thermal Management

Approved by:

Professor Marc K. Smith, Advisor

Mechanical Engineering

Professor Ari Glezer

Mechanical Engineering

Professor Yogendra Joshi

Mechanical Engineering

Professor Sue Ann Bidstrup Allen

Chemical Engineering

Professor Fotis Sotiropoulos

Civil Engineering

Date Approved: November 2005

To my parents and my grandparents!

ACKNOWLEDGEMENTS

First, I want to thank my advisor, Dr. Marc K. Smith, for without his dedicated instruction, I would not have been able to complete this work. I appreciate his patience to allow me to learn a lot from my own mistakes. I would like to thank Dr. Glezer and his research group for generous help on the experimental data and enlightening discussion. I also want to express my thanks to all my committee members for their understanding and patience.

TABLE OF CONTENTS

LIST OF TABLES

LIST OF FIGURES

SUMMARY

A numerical study of axisymmetric synthetic jet flow was conducted. The synthetic jet cavity was modeled as a rigid chamber with a piston-like moving diaphragm at its bottom. The Shear-Stress-Transportation (SST) k-ω turbulence model was employed to simulate turbulence. Based on time-mean analysis, three flow regimes were identified for typical synthetic jet flows. Typical vortex dynamics and flow patterns were analyzed. The effects of changes of working frequency, cavity geometry, and nozzle geometry were investigated. A control-volume model of synthetic jet cavity was proposed based on the numerical study, which consists of two first-order ODEs. With appropriately selected parameters, the model was able to predict the cavity pressure and average velocity through the nozzle within 10% errors compared with full simulations. The cavity model can be used to generate the boundary conditions for synthetic jet simulations and the agreement to the full simulation results was good. The saving of computational cost is significant. It was found that synthetic jet impingement heat transfer outperforms conventional jet impingement heat transfer with equivalent average jet velocity. Normal jet impingement heat transfer using synthetic jet was investigated numerically too. The effects of changes of design and working parameters on local heat transfer on the impingement plate were investigated. Key flow structures and heat transfer characteristics were identified. At last, a parametric study of an active heat sink employing synthetic jet technology was conducted using Large Eddy Simulation (LES). Optimal design parameters were recommended base on the parametric study.

CHAPTER I

INTRODUCTION

Currently, human society relies on electronic systems more than any other time in human history. The importance of the reliability of these electronic systems can never be overestimated. There are a lot of factors that may affect the reliability of electronic systems, such as temperature, humidity, vibration, dust and so on. Thermal overstressing is by far the most common cause of failure in modern electronic systems. The electrical energy consumed by electrical circuits eventually is converted into thermal energy. The accumulation of thermal energy increases the temperature of the electronic component. Because circuits can only operate reliably within a certain temperature range, the heat generated from electronic parts has to be effectively dissipated from the system to maintain a suitable temperature.

In the modern microelectronics industry, there are trends to design and manufacture low power consumption and small-sized systems. Advanced fabrication technologies and the demand of more functionality also push forward system integration to higher levels, like today's ultra large scale integration (USL). All of these result in higher power densities on microchips. Heat generated from newly developed high-speed, high-power, high-density microchips has reached 100W/cm^2. Efficient removal of heat from today's highly integrated ICs remains a major bottleneck (Tummala et al. [60]). Some new means of heat removal are needed to break this bottleneck.

Another thermal problem in integrated circuits is that the temperature distribution can be quite non-uniform: the temperature at some spots is significantly higher than others, which could damage the electronic component itself or cause the failure of the whole system. This situation is common in high performance microchips, where the base material (silicon) is not good in terms of heat conduction and the packaging structure/technique may not provide a sufficiently low thermal resistance in all directions to maintain a uniform temperature field.

In short, thermal issues are crucial in the design of microelectronic systems. A desired cooling solution for modern electronic systems should be able to efficiently remove large amounts of heat and simultaneously control the local temperature distribution.

1.1 Typical thermal management approaches

Generally, thermal management of an electronic system consists of two levels of mechanisms to reject heat from the integrated circuit (die) to the environment. The first level is local or device-level, in which the heat generated from an integrated circuit is rejected to the packaged surface and substrate through appropriate packaging techniques. In the second level, heat is removed from the packaged IC surface to the ambient.

Numerous transistors, resistors, capacitors and other devices are integrated in a silicon die (chip). In a typical wire-bond package, the silicon die is bonded directly to a substrate material, usually with epoxy. This substrate die assembly is then molded to protect it from environmental hazards and has electrical leads around it to provide electrical connections to the circuit board. Heat generated from the chip is conducted into the substrate, through which heat is removed to the circuit board, and at last to the environment. Once the semiconductor design is finished, it's infeasible, if not impossible, to do any management to change the device-level thermal characteristics. Therefore the thermal management techniques discussed in this work mainly involve the second level, in which heat is removed from chip surfaces to the ambient.

Although heat conduction is important within microelectronic components, radiation and convection heat transfer are more important mechanism for heat transfer to the ambient. At temperature less than 100 °C, radiation heat transfer is comparable to natural convection heat transfer, but it is much weaker than forced convection heat transfer. Therefore, in second-level thermal management, convection heat transfer is the key mechanism to improve.

Convection heat transfer can be expressed as:

$$Q = h \cdot A \cdot (T_w - T_f) \tag{1.1}$$

in which, h is the convection heat transfer coefficient, A is the surface area for convection heat transfer, and $(T_w - T_f)$ is the temperature difference between the heat transfer surface and the fluid. To increase the heat transfer rate Q, we could increase h, A, or $(T_w - T_f)$.

Commonly employed thermal management solutions for high heat dissipation applications include high speed fan-driven heat sinks, liquid cooling systems, direct immersion cooling, micro refrigeration systems, heat pipes, thermoelectric coolers, etc. These different solutions gain better heat transfer performance by improving the key parameters of convection heat transfer in equation 1.1.

For high-speed, fan-driven heat sinks, the high-speed air flow increases the convection heat transfer coefficient. Using materials with good thermal conductive properties increases the temperature difference. And, if well designed, the heat transfer surface area of the heat sink can also be increased. However, the fan's relatively high power consumption and noise are two obvious disadvantages.

The heat transfer coefficient for liquid convection heat transfer is much higher than that for air convection heat transfer. A liquid can also provide a larger heat removal capability. In addition, the temperature increase when fluid flows over a heat transfer surface is smaller because of the larger specific heat C_p of the liquid. These, in turn, increase the temperature difference for convection. Difficulties related to liquid cooling techniques are the complex liquid supply system (reservoir, pipes/hoses) and possible liquid leakage.

Direct immersion cooling utilizes two-phase heat transfer. The circuit board is placed in a fluid with a low boiling point (e.g. Fluorinert FC-72) to take the advantage of very high heat transfer coefficient of boiling heat transfer. The latent heat of phase change also helps to enhance the heat transfer. However one characteristic of boiling heat transfer creates a problem: the high superheat before boiling region may result in thermal overshoot: the temperature of the fluid reaches a much higher point than expected and could destroy the electronic system.

A micro-refrigeration system is able to maintain lower temperature than ambient, but it is difficult to fit the whole system into a small space. Coolant leakage is another potential problem.

A heat pipe is an effective technique to provide high heat-flux heat transfer between two surfaces. However, other techniques are still needed to reject the heat to the ambient. Heat pipes are very useful in situations where conventional heat removal devices are hard to fit

in. A typical example is a laptop computer. In this device size limitations prevent a big heat sink from directly being mounted on the microprocessor, like in a desktop computer. The heat pipe is used to transfer the heat from the microprocessor to a heat sink some distance away.

A thermoelectric cooler uses the Peltier effect of some semiconductor materials to create a high temperature pole and a low temperature pole, which can be used to cool the target electronic component. It is compact, with no moving component, and therefore, no noise. And it is solid state, so no coolant is used. The system could be very simple. However, like heat-pipe technology, heat is only transferred from one side of the device to the other, and so other techniques are need to remove the heat to the ambient. Another problem is that its power consumption is significant.

Currently, there is no satisfying technique for thermal management of microsystems, and so researchers and engineers continue to develop new techniques to improve the efficiency and effectiveness of thermal management. As mentioned before, a good thermal management solution should have the capability to remove a large amount of heat, and at same time, it should have a mechanism to control the local temperature distribution. The solution itself should be reliable and robust. Besides these, for microsystems, power consumption, size, and system complexity are also important considerations.

1.2 Synthetic jets

In recent years, micro-electro-mechanical systems (MEMS) have become prevalent, both in commercial applications and scientific inquiry. Among these, the micro synthetic jet has shown promise in the applications of active flow control and thermal environment management for microelectronic devices. It has been used in micro-mixing and boundary layer control. Research on the use of synthetic jets for heat transfer is relatively new, especially for a micro-synthetic jet.

Flow control can improve the efficiency and performance of many fluid-mechanical systems. Through improved flow control, pump impellers could achieve a greater mass flux and aircraft propellers could generate greater thrust for a given power input. Control of

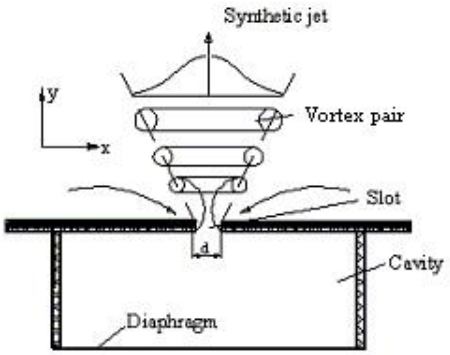

Figure 1.1: Schematic of a synthetic jet in still air

the transition to turbulence over the wing of an aircraft could lower drag forces. Improving the turbulent mixing in engines would result in lower pollutive emissions and increased fuel efficiency.

Synthetic jets have shown potential applications in flow control. The flow direction of a planar jet can be altered substantially by the reattachment of a separated jet to an adjacent solid surface using a synthetic jet (Smith and Glezer [53]). Synthetic jets are also a promising technique in thermal management. Improved fluid mixing and higher heat transfer coefficients have been demonstrated in electronic cooling applications using synthetic jets.

A simple synthetic jet consists of a diaphragm located at the bottom of a small cavity that has an orifice in the face opposite the diaphragm (Figure 1.1). In general, synthetic jets do not necessarily have to be configured like in this example. The orifice/nozzle and the diaphragm could be placed almost anywhere in the cavity that fits design requirements. The diaphragm is forced to oscillate by electrical, mechanical, magnetic, or other means. During one cycle, fluid is expelled through the orifice as the diaphragm moves upwards. This induces a vortex ring at the edge of the orifice due to flow separation. The vortex ring then moves outwards under its own momentum. When the diaphragm moves down, it pulls fluid into the cavity. However, the vortex ring has moved far enough from the orifice so that it is unaffected by the entrainment of fluid into the cavity. As the result of the periodic movements of the diaphragm, a jet flow is established in which the net mass in and

out of the orifice during one cycle is zero. This is a unique property of a synthetic jet. An obvious benefit of a synthetic jet is that it requires no fluid supply, but it is able to supply a momentum flux, alter pressure distributions, and introduce arbitrary scales of flow size into another flow. A synthetic jet can be fabricated over a wide range of scales. The possibility of fabrication by MEMS technology makes it attractive in the application of local thermal management for micro systems.

Synthetic jets have also shown some attractive characteristics for micro system applications compared to conventional jets. It has been observed that for $y/dj \geq 10$ (the non-dimensional distance from the jet exit), a steady turbulent jet flow is established, compared to $y/dj \geq 40$ for a conventional jet. It is important for some microsystem applications that the jet flow is formed in a relatively short distance. In addition, the potentially high velocity jet flow formed by the micro synthetic jet makes it an attractive forced convective flow source in heat transfer applications.

Jet impingement is widely used when high rates of heat transfer are desired. Well-arranged micro jet(s) can also efficiently control the local temperature distribution. There have been numerous experimental and theoretical investigations concerning jet impingement heat transfer from turbine blade cooling to rapid convective heating. Similarly synthetic jet impingement could be used to control the local temperature distribution.

In summary, the synthetic jet technique could provide a full solution for thermal management with both large heat removal capability and local temperature control mechanisms. Compared to other commonly used thermal management approaches, synthetic-jet technology has advantages like low-power consumption and the possibility of on-chip thermal management. However, research on thermal management employing synthetic jets is relatively new. The unknowns of this technology hinder its adoption by the semiconductor industry.

1.3 Summary of investigation

First, the numerical models and methods used in this study, including mesh quality, time step size, and turbulence model, were validated by physical and numerical experiments.

Two dimensional validation was completed through a grid-dependence study, a time-step-size study and by comparison of simulation results with experimental results provided by Vukasinovic et al. [64]. Three dimensional validation was completed through a grid independence study and a time-step-size study.

Appropriate numerical models then were employed to complete the following investigations.

- Numerical study of the flow characteristics of a synthetic jet with a full actuator cavity in the flow domain

  Based on documented research findings, the characteristics of a synthetic jet flow were investigated. We focused on the near-field flow region, because it is not only the most important region in thermal management, but it is also the crucial region affecting the evolution of the synthetic jet. The effects of actuator cavity geometry design (mainly volume and shape), motion of the driving diaphragm, and working frequency on the behavior of the jet were studied numerically.

- Modeling of the synthetic jet actuator cavity

  In most applications in fluidic control and thermal management, the flow details in the actuator cavity are not of interest. The computational cost related to resolving the flow field in the cavity is also relatively high. In most engineering applications, this computational cost could be avoided by modeling the cavity. A reduced-order model of the actual cavity was proposed based on the unsteady Bernolli's equation and mechanical energy conservation analysis. The reduced-order model provides a time-periodic B.C. imposed at the orifice/nozzle boundary.

  Two first order ODEs are solved numerically to give a mathematical relation between the velocity and pressure through the nozzle/orifice, and the volume and volume change (the motion of the membrane/diaphragm) of the cavity. In other words, once the volume and volume change are known, the velocity and pressure through the nozzle can be determined using this model. The comparison between simulations with a full actuator cavity and simulations with a modeled actuator shows this model

works well.

- Numerical study of impingement heat transfer employing micro-synthetic jet/jets

  Jet impingement heat transfer using a synthetic jet is an attractive method to control hot spots in microelectronic systems. A systematic study of the flow and heat transfer characteristics of an impinging synthetic jet was done using the cavity model developed earlier. To obtain the best performance for synthetic jet impingement heat transfer, a parameter optimization was performed. The results suggested an optimal geometry, working frequency, and amplitude of the membrane motion for the synthetic jet.

- Parameter study of active heat sink

  An active heat sink using synthetic jets is a novel device designed to remove large amounts of heat by integrating synthetic jets with a heat sink. The periodically reconstructed boundary layer formed by the synthetic jet flow enhances the heat transfer compared to a fan-driven heat sink. In addition, by changing the orientation of the jet exit (nozzle or slot), jet impingement can enhance the local heat transfer even more. Typical flow patterns corresponding to different designs with different orientations of the jet exit, working frequencies, and size and shape of the nozzle (or slot) were identified. Heat transfer performance of different geometry designs were compared to find the optimal parameters. A large eddy simulation (LES) was employed to simulate the turbulent flow.

1.4 Codes and software

Two commercial CFD packages were used in this research: CFDACE+ and FLUENT. These packages have been used in industry for years and are proven to have the capability to solve engineering problems with complex flows, if a suitable numerical model is used.

CFDACE+ is a general-purpose CFD code with multi-domain solution capabilities. It is based on a strongly conservative finite volume formulation using a non-orthogonal curvilinear coordination system with a structured, co-located grid arrangement. CFDACE+ is one of the few commercial CFD codes offering the capability to simulate the motion of

the oscillating membrane of a synthetic jet by using a moving-wall boundary condition. A fully implicit, patched multi-block solution procedure is used, which accounts for moving grids, sliding grids, and rotating coordinate systems. The solver of CFDACE+ is based on SIMPLEC and PISO, using advanced linear equation solvers including a preconditioned conjugate gradient squared algorithm and a symmetric strongly implicit procedure. The PISO (Pressure Implicit Solution by split Operator) algorithm is used to correct the velocities and to improve the initially assumed pressure fields. This algorithm is particularly suitable for the transient calculations, for which it has been shown to be considerably more efficient than iterative methods. The available turbulence models include the mixing length model, Baldwin-Lomax model, standard $k-\epsilon$ model, RNG $k-\epsilon$ model, Kato-Launder model, low Re $k-\epsilon$, and $k-\omega$ model. A LES model is in development. CFDACE+ is developed by CFDRC, the entire suit includes CFDGEOM, the mesh generating package; CFDACE, the structured mesh solver; CFDACE(U), the unstructured mesh solver; CFDVIEW the post processing and visualization package. CFDACE+ version 6.3 was used to model and investigate the nature of the flow inside the cavity using a standard $k-\epsilon$ turbulence model [1, 12].

Fluent is a commercial CFD code from Fluent Inc. It was first introduced in 1983, gained rapid acceptance in the marketplace and it is the most widely used CFD software in the world. Fluent is based on a finite volume formulation using a non-orthogonal curvilinear coordinate system. Pressure / velocity computing is achieved by the SIMPLEC algorithm, resulting in a set of algebraic equations which are solved using a line-by-line triangle matrix algorithm, accelerated by an additive-correction type of multi-grid method and block-correction. A PISO algorithm with neighbor correction and skewness correction have been available since version 4.52. The available turbulence models are standard $k-\epsilon$ model, RNG $k-\epsilon$ model, RSM (Reynolds Stress Method) model, and LES model. There is a parallel version of FLUENT that only uses multiprocessor machines. Since FLUENT 6.1, a new feature: dynamic mesh was introduced, which provides several powerful techniques to model the mesh/geometry deformation problem. In this study, Fluent 6.1/6.0 was used to study the behavior of the synthetic jet and its applications in electronic cooling and flow

control [2, 12].

Although both Fluent and CFDACE+ packages provide post processing capabilities, FieldView by Intelligent Light was employed as the main post-processing and visualization tool.

1.5 Dissertation outline

After the introduction, a literature review of all the studies related to this dissertation is given in Chapter 2. In Chapter 3, the numerical study of the flow characteristics of a synthetic jet is documented. The synthetic jet actuator cavity models are derived and validated in Chapter 4. Chapter 5 and Chapter 6 document the numerical investigation of axisymmetric synthetic jet impingement heat transfer and the parametric study of an active heat sink. The validations of numerical models are placed into the corresponding chapters where these models are used. In Chapter 7, a summary of the entire work is given, which concludes this dissertation.

CHAPTER II

LITERATURE REVIEW

The phenomenon that an oscillating boundary or transmission of sound (acoustic streaming) induces fluid motion was first observed several decades ago. In 1950s, Ingard and Labate [20] used standing waves in an acoustically driven circular tube to induce an oscillating velocity field in the vicinity of an end plate and observed the formation of zero-net mass flux jets from opposing trains of vortex rings on both sides of the orifice. Mednikov and Novitskii [31] produced an air jet using a low frequency oscillating plane in a resonance cavity and measured average streaming velocities of up to 17 m/s. The streaming was produced by an oscillating solid boundary, the high velocity was attributed to the dissipation of acoustic energy in the resonance cavity [19].

An innovative actuator to achieve streaming, called the synthetic jet actuator, was first proposed by Coe et al. [9]. Allen and Glezer [3] investigated a two-dimensional actuator with an exit orifice 0.5 mm wide by 76.2 mm long driven by a piezoelectric diaphragm. With the working frequency at 1000 Hz, the peak instantaneous velocity at the orifice was 20 m/s. The corresponding Reynolds number was 6000 based on the peak velocity and orifice width.

James et al. [22] experimentally investigated a round turbulent submerged water jet produced by a resonantly driven diaphragm. They conjectured that the jet was synthesized by mutual interactions within a train of vortex rings formed during a cycle of the surface oscillation. There is no net mass injection across the flow boundary and the jet is formed entirely of axisymmetrically entrained fluid. Smith and Glezer [54] showed that a turbulent jet could be synthesized without net mass injection by a train of vortex rings that are formed at the edge of a circular orifice in a sealed cavity bounded by a vibrating membrane.

Because of the relative simplicity of its design and no external piping necessary for jet creation, the synthetic jet is of great interest to the fluids community for its potential applications in flow control and thermal management and has attracted intensive research during the past decade.

A synthetic jet is a promising active flow-control element. Smith and Glezer(1997) [53] used a synthetic jet to effect thrust vectoring and to manipulate small-scale motions in conventional air jets. Millimeter-scale high aspect ratio actuator jets were placed along the

long sides and near the exit plane of a primary rectangular jet scaling one to two orders of magnitude larger. Direct excitation of small scale motions was obtained and turbulent dissipation was enhanced.

Watson et al. (2003) [66] experimentally studied the flow interactions between multiple synthetic jets. They found there exists a minimum spacing between actuators to produce a single coherent synthetic jet from each actuator in an array. The combined effects of the yaw angle and the orifice spacing could either reduce or enhance the amount of coherent vorticity present in the flow.

Wu and Breuer (2003) [68] studied the dynamics of synthetic-jet-actuator arrays for flow control experimentally. Near-wall turbulent boundary layer control by synthetic jet arrays operated at low Reynolds number (15-70), a Strouhal number around 1, and a high Stokes number (40) was studied. It was found that the discrete vortices generated at each cycle of the actuator merge to form a steady jet quickly, i.e., as close as five orifice diameters from the actuator exit.

Synthetic-jet techniques can be used to improve mixing processes [7, 8, 47]. Chen et al.(1999, 2000) [7, 8] applied synthetic jet techniques to improve the mixing process in the combustor of a gas turbine engine. They found that improvement is independent of frequency up to 140 Hz and that the configurations and orientations of the synthetic jets are not important. Also an upper limit in the actuation of synthetic jets exists, beyond which further improvement is negligible.

Ritchie et al.(2000) [48] performed an experimental study on the mixing in coaxial jets using nine circumferentially arranged synthetic jets. They found small-scale mixing effects were strong in the very near field and downstream in the inner mixing layer; on the other hand large-scale structures are more important downstream and have a greater effect on the outside mixing layer.

2.1 Numerical study of synthetic jet flow

Time-dependent flows involving unsteady flow control are difficult not only to compute with CFD, but also to measure experimentally. "Numerical simulation of such a device is

a challenging attempt, both from theoretical point of view and in terms of computational power. Experiment is still very difficult to imagine, CFD is the main analysis tool for the flow control problem using synthetic jet actuators." (Nae 2000) [38] The majority of the research on synthetic jets is experimental because of the difficulties in a numerical study. However, with the advance of computational power, numerical investigations are playing a more important role, especially in those areas where experiments are difficult to perform.

CFD/CHT simulations can provide details of the flow and heat transfer in micro systems with sizes less than 500 μm with reasonable effort. In addition, some important flow or heat transfer parameters, like the local heat transfer coefficient, are difficult to measure experimentally. Numerical simulations can readily provide such detailed information once the flow and temperature fields are computed.

To fully simulate the synthetic jet system, investigators have to model the time dependent motion of the deformed membrane/diaphragm. Two difficulties will be met. First, dynamic meshing or similar techniques have to be employed to allow the mesh to be appropriately modified (either remeshed or deformed) when the geometry of the cavity changes in a time dependent manner. Secondly, the fluid-structure interaction between the membrane and the fluid in the cavity has to be considered. If there is significant deformation of the membrane because of the fluid-structure interaction, some sort of modeling has to be done to precisely represent the profile of the membrane. This is necessary when the membrane material is soft, flexible, or the pressure in the cavity is very high.

Another challenge is the modeling of turbulence. Because of the small length scale of a synthetic jet, the Reynolds number is generally small. A Reynolds number of several hundred is typical for a mini-jet (orifice diameter around several millimeters). For micro-jets, the Reynolds number can be even smaller. Typically, for these values of the Reynolds number, the flow is laminar or even in the creeping-flow regime. However, because of the oscillating nature of the flow, perturbations are introduced very strongly, which cause the flow to develop turbulence in some regions. Therefore, the target domain for simulation probably consists of laminar flow, turbulent flow, and transitional flow at the same time. In addition, the self-similarity of the synthetic jet does not necessarily imply the flow is

turbulent since the dependence of the centerline velocity and the radial spreading on the downstream distance is the same for laminar and turbulent jets (Schilichting 1987 [52]).

For synthetic-jet flow, the maximum Reynolds number occurs in the nozzle/orifice. In general, it is an oscillating flow. In oscillating flows, the transition to turbulent flow occurs at lower Reynolds numbers than steady flow (Ohmi et al. 1982)[39]. In their study, they discussed the four flow types classified by Hino et al. with respect to the Reynolds number, and the phase of the oscillation:

- Region(I): all laminar flow
- Region(II): small amplitude perturbations appear in the early part of the accelerating phase in the central portion of a pipe
- Region (III): small amplitude perturbations exist in the higher velocity phase
- Region (IV): turbulent bursts occur in the decelerating phase

A fifth region exists, in which turbulent bursts occurs in the accelerating phase as well as in the decelerating phase.

The critical Reynolds numbers that separate these regions were found experimentally. Hino et al. defined the Reynolds number for oscillating pipe flow Re_{os}:

$$Re_{os} = 2 \cdot R \cdot |u_{m,os,l}|/\nu \tag{2.1}$$

$u_{m,os,l}$ is the mean velocity of the oscillating flow.

For the critical Reynolds number separating region (IV) from (I), (II), or (III). Several expressions were adopted by researchers, in summary, they are:

$$Re_{os,c} = 780\sqrt{\omega'} \ (2.3 \leq \sqrt{\omega'} \leq 8.8) \tag{2.2}$$

$$Re_{os,c} = 710\sqrt{\omega'} \ (4.0 \leq \sqrt{\omega'} \leq 40) \tag{2.3}$$

$$Re_{os,c} = 400\sqrt{\omega'} \ (42 \leq \sqrt{\omega'} \leq 71) \tag{2.4}$$

where $\omega' = R^2 \cdot \omega/\nu$

Experimental results showed that the flow is laminar when $Re_{os} \leq Re_{os,c}$. When $Re_{os} > Re_{os,c}$, the presentation of turbulence in the flow can be assured.

Numerical simulation of turbulent flow can be roughly divided into the following categories: direct numerical simulation (DNS), large eddy simulation (LES) and calculations based on the Reynolds averaged Navier-Stokes (RANS) equations. All of these approaches have been used in the numerical study of synthetic jets.

In 2004, a CFD validation workshop for synthetic jets and turbulent separation control (CFD-VAL2004) was held in Williamburg, Virginia. Flows of a synthetic jet into quiescent air and a synthetic jet into a turbulent boundary layer crossflow were studied in this workshop. The summary of this workshop indicates that overall for synthetic jets, CFD can only qualitatively predict the flow physics. For the case of synthetic jet into quiescent air, because there existed significant variation between two measurement techniques (PIV and hotwire), it is uncertain regarding how to best model the unsteady boundary conditions in the simulation [50]. The contributed simulations include LES, reduced-order model, laminar simulation (both 2D and 3D) and unsteady RANS (URANS). Most submissions didn't model the actual shape of the cavity (and the diaphragm). It was also found that the time step had very little effect for any of solutions. The effect of grid was relatively small near the wall but it could be larger away from the wall. Turbulence model's effect on the CFD results was found to be fairly significant for this case. And $k-\omega$ SST model is one of the models agreed best with the data among the URANS models. Higher order methods didn't appear to be any obvious benefits from doing so in testing cases.

2.2 Numerical Approach

Any ordinary viscous, Newtonian flow without a body force can be described using the following governing equations, known as the Navier-Stokes equations:

$$\frac{\partial \rho}{\partial t} + \frac{\partial(\rho \cdot U_i)}{\partial x_i} = 0 \tag{2.5}$$

$$\frac{\partial(\rho \cdot U_i)}{\partial t} + \frac{\partial(\rho \cdot U_i U_j)}{\partial x_i} = -\frac{\partial P}{\partial x_i} + \frac{\partial}{\partial x_i}\{\mu_e(\frac{\partial U_i}{\partial x_j} + \frac{\partial U_j}{\partial x_i})\} \tag{2.6}$$

If heat transfer is involved, the governing equations then should include the energy equation and Navier-Stokes equations.

Both laminar flow and turbulent flow were observed in related experiments of synthetic jet flows. It was also observed that both laminar flow and turbulent flow were present at the same time, but in different flow regions. For laminar flows, we could numerically solve the above governing equations with a suitable grid and time step. For turbulent or transitional flow, some turbulence model has to be used to solve the problem. Turbulence strongly affects important global features of the flow. So the accurate and reliable prediction of turbulent flow phenomena is important.

There are many turbulence models available today. The following is a brief review of several commonly used turbulence models. Detailed information on model selection and comparison for each part of this work are described in the corresponding chapters.

The following are some commonly used models in the RANS catalog: mixing length model, standard $k-\epsilon$ model and its modified versions like Low Reynolds number $k-\epsilon$, RNG (Renormalization Group $k-\epsilon$ model), $k-\omega$ model and its modified versions, and Reynolds Stress Model (RSM) [5, 11].

The $k-\epsilon$ model is the most widely used turbulence model. The standard $k-\epsilon$ model is a two-equation model that employs partial differential equations to govern the transport of the turbulent kinetic energy k and its dissipation rate ϵ.

The standard $k-\epsilon$ model for flow without a body force is described by the following equations:

continuity equation:

$$\frac{\partial \rho}{\partial t} + \frac{\partial(\rho \cdot U_i)}{\partial x_i} = 0 \tag{2.7}$$

momentum equation:

$$\frac{\partial(\rho \cdot U_i)}{\partial t} + \frac{\partial(\rho \cdot U_i U_j)}{\partial x_i} = -\frac{\partial P}{\partial x_i} + \frac{\partial}{\partial x_i}\{\mu_e(\frac{\partial U_i}{\partial x_j} + \frac{\partial U_j}{\partial x_i})\} \tag{2.8}$$

transport equation for k:

$$\frac{\partial(\rho \cdot k)}{\partial t} + \frac{\partial(\rho \cdot U_i k)}{\partial x_j} = \frac{\partial}{\partial x_j}(\frac{\mu_e}{\sigma_1}\frac{\partial k}{\partial x_j}) + G - \rho\epsilon \tag{2.9}$$

transport equation for ϵ:

$$\frac{\partial(\rho \cdot \epsilon)}{\partial t} + \frac{\partial(\rho \cdot U_i \epsilon)}{\partial x_j} = \frac{\partial}{\partial x_j}(\frac{\mu_e}{\sigma_2}\frac{\partial \epsilon}{\partial x_j}) + \frac{\epsilon}{k}(C_1 G - C_2 \rho \epsilon) \tag{2.10}$$

where, $\mu_e = \mu + \mu_t$, $\mu_t = C_\mu \rho \frac{k^2}{\epsilon}$, $G = \mu_t(\frac{\partial U_i}{\partial x_j} + \frac{\partial U_j}{\partial x_i})\frac{\partial U_i}{\partial x_j}$

The standard $k - \epsilon$ model coefficients are $\sigma_1 = 1.0$, $\sigma_2 = 1.3$, $C_\mu = 0.009$, $C_1 = 1.44$, and $C_2 = 1.92$.

Generally, the $k - \epsilon$ model is used for high Re turbulent flow. Some improvements and modifications have been attempted to make the $k-\epsilon$ model work better for other turbulent flows. High Reynolds number $k - \epsilon$ models require the use of wall functions. However, the commonly used wall functions may not be accurate in flows with large separation, heat transfer, or relaminarization.

In this study, the Re number is small because of the small geometry of micro synthetic jets. Therefore a modified $k - \epsilon$ model for low Re number was used. The low Reynolds number $k-\epsilon$ model allows integration of the momentum and $k-\epsilon$ equations all the way to the wall. The $k - \epsilon$ equations were modified to include the effect of molecular viscosity in the near-wall regions. So the difficulty associated with wall function could be circumvented. The wall shear stress is computed from finite differences for this model. Therefore the first grid-point should be placed in the laminar sublayer, which means that very fine grids near solid boundaries should be used.

There are many factors, such as grid distribution and inlet turbulence conditions, that may affect the $k - \epsilon$ model in predicting the flow field of a synthetic jet accurately. For the influence of mesh distribution on the simulations of synthetic jets, some investigations have been reported. Kral et al. [23] studied two kinds of mesh distributions, a coarse grid and a fine grid. They demonstrated that the basic flow fields of synthetic jets are captured on both grids, but the fine grid captures the dynamics of the actuator in more detail. As for the effect of inlet turbulence conditions and different $k - \epsilon$ models on the synthetic jet calculations, there is no work present in the literature so far.

While the standard $k-\epsilon$ model is based on the traditional Reynolds-averaging technique, the RNG model is derived by a more rigorous statistical (scale-elimination) technique.

RNG theory provides an analytically derived differential formula for effective viscosity that accounts for low Reynolds number effects. Although the RNG model provides substantial improvements over the standard $k-\epsilon$ model, the RNG model is still based on the isotropic eddy-viscosity concept and a high Reynolds number model. Consequently, there is a limit to what the RNG model can offer when the anisotropy of turbulence has a dominant effect on the mean flow, like in highly swirling flows, flows with strong streamline curvature, stress-driven secondary flows, and the evolution of streamwise vortices.

It is well known that models based on the ϵ-equation lead to an overprediction of the turbulent length scale in flows with adverse pressure gradients, resulting in high wall shear stress and high heat transfer rates. In combination with low-Re number extensions, the ϵ-equation has been proven to be numerically stiff, leading to a significant reduction in numerical robustness. In addition, these models require a very fine near-wall resolution, which is typically one order of magnitude higher than for other one- and two-equation models.

The experience with low-Reynolds number formulations for heat transfer predictions using the ϵ-equation has been a significant overprediction of the local Nusselt number at reattachment points. Considering the numerous deficiencies of the standard ϵ-equation near the wall, alternative formulations, both of the scale-equation and of the near-wall treatment are required.

An alternative to the ϵ-equation is the ω-equation in the form developed by Wilcox (1993) [67]. Instead of the equation for the turbulent dissipation rate, ϵ, an equation for the specific dissipation rate, ω, of the large scales is used. The ω-equation has significant advantages near the surface and accurately predicts the turbulent length scale in adverse pressure gradient flows, leading to improved wall shear stress and heat transfer predictions. Furthermore, the model has a very simple low-Re formulation, which does not require additional non-linear wall damping terms. The correct sublayer behaviour is achieved through a Dirichlet boundary condition for ω. Near the wall, the convective terms in the ω-equation are zero and the equation is dominated by the elliptic diffusion terms, by non-linear source terms, and by the boundary conditions. Another main advantage of the $k-\omega$ model is

its robustness even for complex applications, and the reduced resolution demands for an integration to the wall.

The turbulent kinetic energy, k, and its specific dissipation rate, ω, are described by the following transport equations:

the k-equation:

$$\frac{\partial(\rho k)}{\partial t} + \frac{\partial(\rho U_i k)}{\partial x_j} = P_k - \beta' \rho k \omega + \frac{\partial}{\partial x_j}(\Gamma_k \frac{\partial k}{\partial x_j}), \tag{2.11}$$

the ω-equation:

$$\frac{\partial(\rho \omega)}{\partial t} + \frac{\partial(\rho U_i \omega)}{\partial x_j} = \alpha \frac{\omega}{k} P_k - \beta \rho \omega^2 + \frac{\partial}{\partial x_j}(\Gamma_\omega \frac{\partial \omega}{\partial x_j}) \tag{2.12}$$

where $\Gamma_k = \mu + \frac{\mu_t}{\sigma_k}$, $\Gamma_\omega = \mu + \frac{\mu_t}{\sigma_\omega}$, $\mu_t = \rho \cdot \frac{k}{\omega}$.

The model constants have the following default values: $\beta' = 0.09$, $\alpha = 5/9$, $\beta = 3/40$, $\sigma_k = 2.0$, and $\sigma_\omega = 2.0$ [67].

Unlike statistical simulations based on the Reynolds-averaged equations (RANS), large eddy simulation retains the full three dimensional and time dependent nature of the fluctuating turbulent field. The origin of LES lies in the early weather prediction models, and the method has been practiced now for about 30 years. It has only gradually been applied to engineering-type flows (Peyret 1996) [42].

In LES, the large-scale (grid-scale, GS) part of the turbulent fluctuations is computed explicitly while the small-scale (subgrid-scale, SGS) motions are modeled. These ideas are based on two assumptions, which appear reasonable in both practical experience and theoretical considerations: most global features of turbulent flows, like averaged mixing rates or averaged losses, are governed by the dynamics of the largest scales and depend only little on the small scale turbulence. These global features are of primary interest, so reliable simulation is desired. Small-scale turbulence becomes independent of the strong inhomogeneities which are typical for the energy containing eddies, and thus tends to local isotropy.

In a large-eddy simulation, any dependent variable $f(U, T, etc.)$ of the flow is split into a GS part $\bar{f}$ and a SGS part f' :

$$f(x_1, x_2, x_3, t) = \bar{f}(x_1, x_2, x_3, t) + f'(x_1, x_2, x_3, t) \tag{2.13}$$

The GS turbulence is defined by applying explicitly a spatial filtering operation based on a convolution integral:

$$\bar{f}(x_1, x_2, x_3, t) = \int_D \prod_{i=1}^{3} h_i(x_i - x_i' \cdot \Delta_i) f(x_1', x_2', x_3', t) dx_1' dx_2' dx_3', \tag{2.14}$$

where h_i denotes the filter function in the ith direction and Δ_i is the width of the filter which selects the size of the smallest resolved eddies. A number of filter functions have been suggested for application in LES, the most prominent among them being the Gaussian filter, the cut-off filter in spectral space, and the top hat filter in real space.

Applying the filtering operation to the Navier-Stokes equations yields the equations of motion for the large-scale flow field. For incompressible flow, the filtered convective term of the N-S equation becomes:

$$\frac{\partial}{\partial x_k}(\overline{u_i \cdot u_k}) = \frac{\partial}{\partial x_k}(\overline{u_i} \cdot \overline{u}_k) + \frac{\partial}{\partial x_k}(L_{ik} + C_{ik} + R_{ik}) \tag{2.15}$$

where $L_{ij} = \overline{\overline{u}_i \cdot \overline{u}_j} - \overline{u}_i \cdot \overline{u}_j$, $C_{ij} = \overline{\overline{u}_i \cdot u_j'} + \overline{u_i' \cdot \overline{u}_j}$, and $R_{ij} = \overline{u_i' \cdot u_j'}$

These three terms are denoted as Leonard stresses (L_{ij}), cross stresses (C_{ij}), and SGS Reynolds stresses (R_{ij}), respectively. The cross stresses and the Reynolds stresses reflect directly the decomposition of the velocity fields into a GS and SGS part, and invariably have to be modeled. Leonard stresses are defined by the GS velocities only and can in principle either be modeled or computed.

Subgrid models have to be used to close the resulting equation set. The Smagorinsky model was the first SGS model, and is still widely used for non-homogeneous turbulence. It is an eddy-viscosity type model, where SGS stresses are set proportional to the strain rates of the resolved field. The proportional constant C_s is known as the Smagorinsky constant. Lily derived a relation between the subgrid length scale and the Smagorinsky constant Cs:

$$C_s = \frac{1}{\pi}(\frac{2}{3\alpha})^{\frac{3}{4}}, \tag{2.16}$$

where α is the Kolmogorov constant.

It was found that the optimum value for C_s varies from flow to flow, ranging between 0.07 and 0.24. The governing equation set can then be discretized and solved numerically to complete the simulation.

The other sub-grid scale model available in FLUENT is the RNG-based subgrid-scale eddy viscosity model. This model has improved performance in the low-Reynolds-number region. Thus, it is more suitable for transitional flows and wall-bounded flows.

In LES, only eddies that are large enough to contain information about the geometry and dynamics of the specific problem under investigation are resolved. All structures on a smaller scale are treated as universal following the viewpoint of Kolmogorov. But there is no real separation between the large and small scales; the division is just convention [24]. The scale of flux carrying eddies is limited by the presence of a wall. Near the wall, flow scales should be smaller, so care has to be taken to avoid incorrect results in the near-wall region. Three approaches have been used:

1. use sufficiently refined mesh in the near-wall region,

2. formulate more complicated subgrid scale models in hope of describing the energy-containing near-wall effects, (This approach has not yet been completed successfully.) and

3. decouple LES from the details of the near wall physics by formulating approximate boundary condition.

In DNS of turbulence, the numerical resolution is sufficiently fine so as to resolve all scales of motion that carry significant energy. However, such resolution requirements make DNS prohibitively expensive. A RANS approach like the $k-\epsilon$ model is much cheaper computationally but requires non-universal closure models, which are often difficult to construct especially in problems involving complicated geometry and flow separation. The intermediate approach is LES. Although computationally LES is less costly than DNS, it is much more expensive than a statistical simulation of the same flow. LES always requires fully three-dimensional and time dependent calculations. It also needs to be conducted over long periods of time to obtain stable and significant statistics.

Kral et al.(1998) [5, 23] employed the Reynolds-averaged Navier-Stokes (RANS) equations combined with the Spalart-Allmaras one equation turbulence model to simulate synthetic jet actuators. Both compressible and incompressible cases were studied. The synthetic jet actuator cavity was not simulated or modeled. Instead, a suction/blowing type boundary condition was used. The velocity profile at the orifice exit was assumed to be:

$$\tilde{\nu}_n(\xi, \eta = 0, t) = V_0 f(\xi) \sin \omega t \tag{2.17}$$

in which, $f(\xi)$ is the spatial variation over the orifice. Several different $f(\xi)$s were used:

$$f(\xi) = \begin{cases} 1 \\ \sin(\pi\xi) \\ \sin^2(\pi\xi) \end{cases} \tag{2.18}$$

The issue of using a laminar simulation or a Reynolds averaged turbulence model was discussed also. In their laminar simulation, the synthetic jet didn't form into a typical jet, but retained the character of a train of vortex pairs. Their comparison of the simulation results with experimental data demonstrated that the RANS approach is capable of simulating synthetic jet flow. They found that their modeled boundary condition captured the essential features of the jet. On a Cray C90, less than 30 Cray minutes per period were used with a maximum flow divergence of 1.0x10^{-4} and one Cray hour per period were used with a maximum flow divergence of 1.0x10^{-6}. Results were analyzed after 7 cycles. Results appeared to agree with the experimental observations by Smith and Glezer (1998) [54]: the near field is dominated by the formation of counter-rotating vortex pairs. The vortex cores become smeared by turbulent diffusion downstream. In the experiments, the vortices break down into a planar turbulent jet beyond approximately 8-10 slot widths from the aperture.

Mittal et al. (2001) [34] employed a stationary Cartesian mesh to simulate synthetic jet flow with the configuration of a synthetic jet interacting with a flat-plate boundary layer using the incompressible RANS equations. The diaphragm was modeled as a moving boundary in an effort to accurately compute the flow inside the synthetic jet cavity. The simulation results extracted some interesting flow physics associated with the vortex dynamics of the jet and provided some insight into the scaling of the performance characteristics of the jet with some device parameters.

Utturkar et al.(2002) [62] numerically investigated the sensitivity of synthetic jet flow to the design of the actuator cavity. The effect of changes in the cavity aspect ratio and the placement of the piezoelectric diaphragm on the jet flow were examined. They found that wide-ranging modifications of the cavity design have a relatively limited effect on the synthetic jet flow.

Moran et al.(2000) [36] simulated a 10:1 scale acoustic resonator that was basically an irregular shaped synthetic jet using CFD. Both compressible and incompressible models were studied. Only ten time steps per period were simulated for incompressible cases. For compressible cases, 40 time steps per cycle were used. They claimed the simulation could predict the resonant frequency.

Mallinson et al.(1999) [30] used the RANS equations and a standard $k - \epsilon$ model to numerically simulate an unsteady incompressible two-dimensional synthetic jet and related applications. They demonstrated that the computed mean velocity had broad agreement with experimental results. However, there was a discrepancy in the near-jet exit region. Based on this work, the authors suggested that a large-eddy simulation (LES) may overcome some of the problems seen in their simulations.

Nae(2000) [38, 37] presented a numerical simulation of a synthetic jet using an unsteady compressible RANS CFD code. Turbulence was modeled using the $k - \epsilon$ model with a choice of wall laws or a two-layer approach. The solver was based on a combination of finite-volume and finite-element methods, using general unstructured meshes and a choice of Roe or Osher schemes for the convective part of the system. The results from several types of simulations validated the code and the corresponding boundary conditions. A top speed of Ma=0.105 for the blowing stroke was achieved. He found that a top-hat velocity profile boundary condition was in good agreement with the cavity simulation: 50% in blowing and more than 70% for the suction phase. Since only 5 cycles were simulated, it is likely that the flow never reached a periodic state. The external flow analysis was based on simulations employing a jet-exit velocity profile instead of a full-cavity simulation. Frequencies simulated were 5 and 10 Hz. He simulated the unsteady flow control using synthetic jet actuators. He concluded that flow control using synthetic jet actuators is

possible.

Olsson et al.(1998) [40] conducted large eddy simulations (LES) to study the mean velocity, turbulence statistics, SGS-model effects, and the dynamic behavior of the synthetic jet with a focus on the near-wall region. The difference of turbulence statistics between different simulations was analyzed.

Rizzetta et al.(1999) [49] employed a direct numerical simulation (DNS) to calculate the flow field within a two dimensional actuator cavity, as well as exterior to it. The accuracy of the numerical results was assessed via grid resolution and time-step size studies. Features of the resultant flow fields were elucidated and the comparison of the numerical data with measurement was encouraging.

In numerical studies conducted by Lee et al. [24, 25, 26], DNS of a turbulent boundary layer was coupled with an immersed boundary method to simulate the detailed shape and actuator motion of an array of synthetic jets formed by a MEMS device. Results showed that the inactive low profile MEMS devices had a weak effect on the boundary layer. The formation of the 3D synthetic jets and their interaction with the local structure was shown in detail. In their 2D DNS simulations, fair agreement between the simulation and experimental data (Smith and Glezer 1998 [54]) for a region $x/h < 8$ was observed. A piston-like motion of the actuator membrane was used in the simulation. Besides the Reynolds number and Strouhal number study, the effect of changes in the lip thickness, lip geometry, and the size of the domain were investigated.

Since a synthetic-jet-like flow can also be formed by acoustic waves, acoustic researchers have investigated devices similar to the synthetic jet, such as a Helmholtz resonator. In these studies, an inviscid flow has been assumed. The Euler equations instead of the Navier Stokes equations were solved. Even though the flow was similar to a synthetic jet, the research was conducted from the point view of acoustic characteristics. Dequand et al.(2003) [10] investigated a Helmholtz-like resonator with self-sustained oscillations to find the coupling between vortex shedding and acoustical resonance. Experimental measurements and numerical simulations were conducted. An analytical model was also proposed. This work focused mainly on acoustics and the design parameters associated with the resonator neck

geometry.

All of the three numerical approaches to model turbulence (DNS, LES and RANS) have been used in the numerical investigation of synthetic jets. When turbulence is not strong and/or relaminarization occurs, the accuracy of the RANS approach is doubtable. DNS and LES provide more precise predictions to some extent, although they need much more computational time and storage compared to the RANS approach. As discussed earlier, $k-\epsilon$ and $k-\omega$ models were employed in the present 2D studies, while LES was used to simulate the 3D problems.

2.3 Characteristics of a synthetic jet

A synthetic jet is a time-averaged fluid motion generated by sufficiently strong oscillatory flow. The design and optimization of a micro synthetic jet system is complex. The performance of the system is a function of many parameters, such as Reynolds number (Re), Prandtl Number (Pr), the actuator cavity geometry, nozzle geometry, etc. The working frequency, amplitude, and the physical characteristics of the driving diaphragm also play important roles in the operation of the system. To optimize the design of this micro system, knowledge of how these parameters affect the flow field and heat transfer rate is desired.

As some researchers have found, synthetic-jet flow cannot be formed if some key criteria are not satisfied. In their study of a round turbulent water jet produced by a resonantly driven submerged diaphragm, James et al.(1996) [22] found that the jet was formed only when the oscillation amplitude of the diaphragm exceeded a given threshold. When this occurred, a small cluster of cavitation bubbles formed and disappeared near the center of the diaphragm during each cycle. The streamwise velocity of the jet was about 1m/s. The Reynolds number was only around 2000, although a turbulent jet was observed. They also observed that the mean flow of the jet exhibited a tendency toward self-similarity, like high-Reynolds-number conventional jets.

Smith et al.(1998) [54] investigated the formation, evolution, and interaction of co-flowing pairs of plane synthetic jets array using particle image velocimetry (PIV). The strong entrainment of ambient fluid induced near the flow orifice by the jet formation was

exploited for dynamic vectoring of adjacent jets by varying the amplitude or the relative phase of their driving waveforms. It was observed that in the near-exit-field region, the combined flow transports more fluid, the entrainment of ambient fluid toward the jet orifice is stronger, and the combined jet spreads faster with streamwise distance. In the far field the scaled velocity distributions of the combined jets was similar to single jets, but with a larger flow rate. The effect of the suction cycle on vortex trajectories was different. When the vortex impulse was too small, the vortex was completely sucked back into the orifice and was not advected past the near-exit-field domain during the blowing stroke. Slightly stronger vortices were slowed down and remained essentially motionless during the suction cycle.

Gilarranz et al.(1998) [17] measured the flow field generated by a synthetic water jet using PIV. A synthetic jet actuator was theoretically characterized. CFD simulations (without a cavity) of the flow field were conducted to compare with experimental results. In the frequency ranging from 10 to 1000 Hz, and for relatively large oscillation of the diaphragm, a synthetic jet could be formed. With small oscillations, a net suction flow was produced. This implies that there are some critical conditions for a synthetic jet to be synthesized.

Smith and Swift(2003) [55] argued that a threshold stroke length exists for jet formation. Based on an order-of-magnitude analysis, Utturkar et al. (2003) [61] showed that the jet could be formed only when the ratio of Reynolds number to the square of the Stokes number is greater than a certain value ($Re/S^2 > K$) . Comparing with the experimental data of Ingard and Labate and Smith et al., they found that for two-dimensional synthetic jets, K is around 2 and for an axisymmetric jet, K is around 0.16.

Although the induced flow near the actuator is substantially different than the flow near the orifice of a conventional jet, the far-field mean flows of synthetic and conventional jets are quite similar. It was found (Smith and Glezer 1997) [53] that for self-similar synthetic jets, the entrainment rate dQ/dx is invariant with downstream distance and is proportional to Q_0/D_0, where Q_0 is volume flow rate at the jet orifice, and D_0 is the jet diameter at the jet orifice.

$$\frac{dQ}{dx} = 0.203 Q_0 D_0 \tag{2.19}$$

This is lower than entrainment rates measured in the far field of conventional turbulent jets (James and Glezer 1996) [22].

Once the jet is formed, the time-periodic motion induced by the actuator does not affect the evolution of the mean flow very much. Compared to a conventional jet, there is no potential core in synthetic-jet flow and it becomes fully developed near the actuator. The time-averaged flow of a synthetic jet shows self-similarity like a conventional jet.

Smith and Glezer (1998) [54] showed that a low Reynolds number synthetic jet has many characteristics that resemble continuous higher Reynolds number jets. Important parameters of synthetic jets include: length scales, velocity scales and dimensionless stroke length and the Reynolds number based on the impulse per unit width.

They assumed that the exit velocity profile is invariant, and that synthetic jets created by a sinusoidal flow are completely determined by two independent dimensionless parameters: non-dimensional stroke length and momentum based Reynolds number. These two parameters were calculated using the characteristic velocity which was defined as:

$$U_0 = L_{stroke} f = \frac{1}{T} \int_0^{\frac{T}{2}} u_0(t) dt \tag{2.20}$$

where L_{stroke} is the stroke length (the length of the slug of fluid pushed the slot during the blowing stroke), $T = 1/f$ is the oscillation period. This velocity could be used to calculate the Reynolds number.

The stroke length is another important parameter to characterize a synthetic jet. If we take the nozzle/orifice diameter as the length scale, it then is defined as L_{stroke}/d_j,

$$L_{stroke} = \int_0^{\tau} u_0(t) dt \tag{2.21}$$

where, $u_0(t)$ is the velocity at the exit plane of the orifice and $\tau = \frac{1}{2}T$ is the time of discharge or half the period of the diaphragm motion.

If we take the length scale as d_j, the Reynolds number based on the impulse per unit width is defined as

$$Re_{I_0} = I_0/\mu d_j \tag{2.22}$$

where $I_0 = \rho d_j \int_0^{\frac{T}{2}} {u_0}^2(t) dt$.

Because the Reynolds number of most documented synthetic jets is very small compared to continuous jets, direct comparison between these two jets has been limited. Through experimental measurements and flow visualization, Smith and Swift (2003) [55] compared characteristics of synthetic jets and continuous jets with matched Reynolds number. They found that in the far field the self similar velocity profiles of synthetic jet shows very similar characteristics to continuous jets. In the near field, synthetic jets are dominated by vortex pairs, which entrain more fluid than continuous jets. Therefore, synthetic jets grow more rapidly, both in terms of jet width and volume flux than continuous jets.

As mentioned before, due to the difference in Reynolds number ranges, direct comparison between synthetic jets and continuous jet is not well documented. In this work, some numerical comparison studies were done.

Important parameters that affect the characteristics of synthetic jets include the geometry of the actuator cavity and nozzle, working frequency, and the amplitude of the actuator diaphragm. Some work has been performed to address these parameters.

A detailed parametric study of the interaction of a synthetic jet and a flat plate boundary layer was conducted by Mittal et al.(2001) [34]. They employed a Cartesian grid incompressible flow solver with second-order spatial accuracy. The oscillating diaphragm was modeled on a stationary Cartesian mesh. Their simulations showed that the presence of the crossflow significantly affected jet-flow characteristics, such as the dynamics of the vortex structures and the jet-velocity profiles. They used the moments of the jet velocity profiles to characterize the jet and found that skewness could be another important characteristic of the jet velocity profile. They found that the degree of skewness was greater when the Reynolds number was higher.

Utturkar et al.(2002) [62] examined the sensitivity of synthetic jets to the design of the jet cavity using numerical simulations. Although, they commented that the compressibility effects in the cavity may be significant and that changes in the cavity shape and/or the placement of the diaphragm may change the acoustic characteristics of the cavity, they only simulated incompressible cases. When there is no external flow present, no significant

difference (< 7% deviation) in the velocity profile was observed with cavity shape modification. This conclusion implies that the details of cavity design and diaphragm placement do not play a crucial role in determining the performance of the synthetic jet, at least in the incompressible regime. They also commented that if one's goal was primarily modeling and predicting the external jet flow, then rough models of the cavity might suffice. However, due to the range of parameters they studied, the above comments are not universal.

2.4 Synthetic-jet cavity model

For most engineering applications, it is the jet flow that is of interest. However, the computational cost associated with simulating the flow in the cavity makes up a large percent of the total computational cost. To avoid this portion of the computational cost, analytical/numerical models of the cavity are highly desired. A cavity model should be able to relate the key jet flow characteristics to the key cavity design parameters. For applications where the near field is important, like synthetic-jet impingement, the model should also be able to reproduce the flow field near the jet exit in simulations.

The first model is actually the "slug" model proposed by Smith and Glezer(1998) [54] in which the velocity profile was assumed uniform in space. The two key parameters that characterize the synthetic jet are the stroke length and Strohal number. However, this model assumes that the velocity profile is invariant, and so the velocity field near the jet exit is not reproduced well. Thus even though the slug model is very useful to characterize the far-field synthetic jet, it is not suitable for the present work.

The Helmholtz resonator model is often adopted to investigate the frequency domain characteristics of a synthetic jet. In the Helmholtz resonator, as shown in Figure 2.1, a plug of air of mass m is assumed to exist in the air in the neck of the resonator. This mass is elastically restrained by the air cushion existing inside the chamber. The natural vibrations of this system can be calculated in the same way as for a spring-mass vibratory system.

If the neck of the resonator has length L and cross section area A, then the mass of the air plug in the neck is $m = \rho LA$, where ρ is density. The inertial force is

$$K_t = -mx^2 = -\rho AL\ddot{x} \tag{2.23}$$

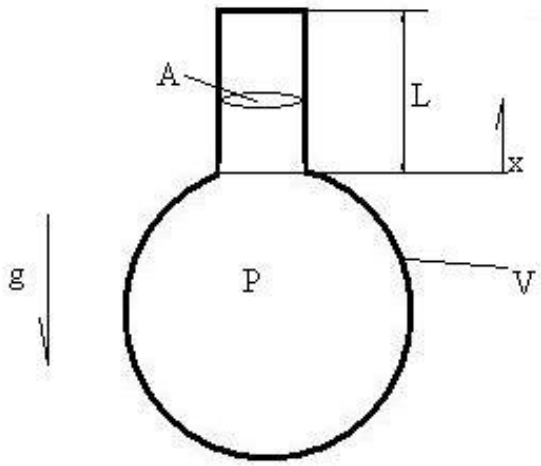

Figure 2.1: Model of Helmholtz resonator

where x is the displacement.

The restoring force is the pressure difference between the air inside and outside of the chamber,

$$K_d = A \cdot \Delta P \tag{2.24}$$

Assuming an adiabatic process inside the chamber, we have

$$P_0 V_0^k = (P_0 + \Delta P)(V_0 + \Delta V)^k \tag{2.25}$$

where k=1.4, andP_0 and V_0 are the chamber pressure and volume.

Assuming small values of ΔP, ΔV

$$\Delta P = \frac{P_0 k \Delta V}{V_0} = \frac{P_0 k A x}{V_0} \tag{2.26}$$

Balancing the restoring force and inertial force, yields the second-order system,

$$\ddot{x} + \omega^2 x = 0, \omega^2 = \frac{P_0 k A}{\rho L V_0} \tag{2.27}$$

Employing this model to calculate synthetic-jet natural frequencies, one finds that the results are significantly higher than the natural frequencies obtained from numerical simulations. This is because the physics of synthetic-jet flow is very different from that of a Helmholtz resonator.

Synthetic jets represent a coupled electromechanical system with frequency-dependent properties determined by device dimensions and material properties. The analysis and design of coupled-domain transducer systems are commonly performed using lumped-element models. The main assumption employed in lumped-element modeling is that the characteristic length scales of the governing physical phenomena are much larger than the largest geometric dimension of the transducer.

Rathnasingham and Breuer (1997) [45] developed a low-order model of a synthetic jet, using a control-volume model for the flow and an empirical model for the structural dynamics of the diaphragm. The synthetic-jet cavity was modeled as a piston moving in a cylinder. An important assumption was that the orifice area is large enough so that viscous effects in the cavity may be ignored. Then, the cavity pressure change drives a flow through the orifice with a uniform velocity. The process was assumed to be isothermal. The structural movement and fluid flow were modeled. Five coupled, non-linear, first-order ODEs that govern the membrane position and velocity, the fluid density and pressure, and the jet velocity were derived. The model could predict trends in behavior of the membrane actuator.

Gilarranz et al.(1998) [17] assumed that only an axial velocity existed in the cavity and formulated and solved a simplified Navier-Stokes equation using the method of separation of variables. The pressure gradient was assumed to vary sinusoidally with time. The solution for the velocity was similar to Rathnasingham's (1997) [45] results, except for one term, which Gilarranz argued was not a solution of the original problem.

Rao et al.(2000) [44] formulated another model for the actuator. The diaphragm was modeled as a piston moving in a sinusoidal manner. The unsteady Bernoulli's equation was used to find the pressure acting on the diaphragm. This was combined with the incompressible continuity equation to relate the diaphragm motion and flow rate. The pressure on the diaphragm was determined to be:

$$p = \rho[\frac{A_m}{A} \cdot l' \cdot \frac{d}{dt}(\frac{dx}{dt}) + \frac{A_m}{A_0}^2 \cdot \frac{1}{2} \cdot (\frac{dx}{dt})^2] \tag{2.28}$$

where, A_m is the cross-sectional area of the membrane, A_0 is the cross-sectional area of the

nozzle, l' is the acceleration length in the unsteady Bernoulli's equation, to be determined by numerical simulation, and x is the displacement of the piston-like moving membrane, which was given as a sinusoidal function.

The model parameter l' was determined by matching results with a CFD simulation (using FIDAP) with a diaphragm velocity of 6 m/s. The predicted results for the case of a diaphragm velocity of 30 m/s compared well with CFD simulation in term of pressure variation with time. However, except the diaphragm displacement, no other design information is included in this model. And this model does not predict any information on the synthetic-jet velocity profile either. The main purpose of this model was to find the power requirement for driving a cavity with a piston-like moving diaphragm.

Gallas et al.(2003) [13] proposed a lumped-element model of a piezoelectric-driven synthetic jet actuator. The individual components of the synthetic jet were modeled as elements of an equivalent circuit using conjugate power variables. They derived the frequency-response function of the circuit to obtain the volume flow rate through the orifice per applied voltage across the piezoceramic.

Pes et al.(2002) [41] modeled the two dimensional synthetic jet using a neural-network-based method. They carried out simulations to characterize the behavior of an isolated jet by varying the working frequency and membrane oscillation amplitude. A commercial CFD package CFD++ was used in their simulations. The detailed flow was studied using momentum coefficient, momentum thickness, displacement thickness, and shape factor. This information was then used to train the deterministic source terms in a neural network. Both quiescent external flow and a jet with an external cross flow were studied. They reported that considerable reduction of computational cost could be achieved by using this method. Neural networks can be used to model complex data relationships. According to the universal approximation theorem, a neural network with one hidden layer is able to approximate any continuous function in any domain with a given accuracy. In this study 25 neurons were used in the hidden layer. In their work, synthetic-jet unsteadiness in calculations of flow fields without the presence of both a cavity and an orifice was achieved. However, the physical meaning of this model is not clear. If the actual situation is not close to the training

cases, the accuracy of the results is also in doubt. This is especially true with regard to the accuracy of the flow field in the near-jet-exit region, where the flow is calculated with no nozzle present.

There are several other techniques for the production of reduced order models for flow simulations of synthetic jet. Proper Orthogonal Decomposition (POD) is a statistically based, order-reduction method that calculates the singular value decomposition of the covariance operator of output measurement. This technique is based on optimality criteria. Wavelets and multi-resolution methods are also promising methods that could be used to build reduced models for flow simulation.

Rediniotis et al.(1999) [47] developed a reduced-order POD model of a synthetic jet. They showed that reasonably accurate representations of synthetic jet flow could be achieved using very low dimensional models, with subsequent formulation of control based on the reduced-order models. They also addressed controllability and optimal control issues. The Strouhal number was varied to produce a range of different flow fields. However, it is not feasible to directly apply these reduced models to simulations using commercial CFD codes.

2.5 Thermal management using synthetic jets

Synthetic jet technology provides a low cost, low-power method of effective, on-demand, localized thermal management. It also could provide global, system-level heat removal through an active heat sink.

Jet impingement is technically preferred in applications requiring high heat transfer rates. Well-arranged micro-jet(s) can efficiently control the local temperature distribution. There have been numerous experimental and theoretical investigations concerning jet impingement heat transfer from turbine blade cooling to rapid convective heating. But little research on impingement heat transfer employing synthetic jets has been reported.

The flow of a single conventional circular jet impinging orthogonally on a plane surface is commonly divided into four zones, as shown in figure 2.2 (Jambunathan, 1992) [21]:

1. Initial mixing region: this is a mixing or shear region surrounding an inviscid core where the fluid velocity at the nozzle centerline (u_m) is almost equal to the nozzle exit

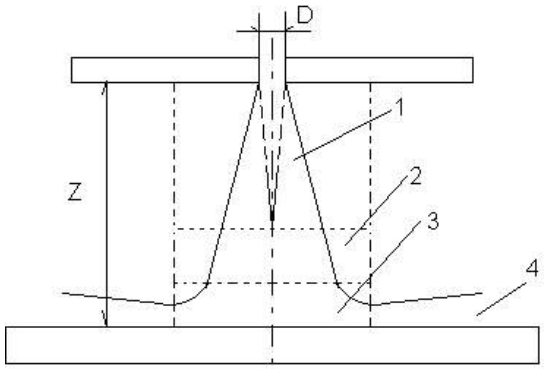

Figure 2.2: Flow zones in a impinging jet, Zone 1, initial mixing region; Zone 2, established jet; Zone 3, deflection zone; Zone 4, wall jet

velocity (u_o). Gautner et al.(1970) [16] suggested a core length of six nozzle diameters;

2. Established jet or fully developed jet zone where the axial velocity decreases with increasing distance from the nozzle exit;

3. Deflection zone: this region is near the impingement plate where the axial velocity rapidly decreases and the static pressure rises. This zone extends approximately two nozzle diameters from the plate surface. The height of the deflection zone was proposed to be 1.2D by Giralt et al.(1977) [18]

4. Wall jet zone: a wall jet exhibits higher levels of heat transfer than a parallel flow, due to turbulence generated by the shear between the wall jet and the ambient air that is transported to the boundary layer at the heat transfer surface.

In their single steady jet impingement study, Gardon and Cobonpue (1962) [15] found that the maximum heat transfer from single jet impingement on a heated plate occurred at a nozzle to plate (z/D) spacing between $6 \sim 7$ nozzle diameters. For $z/D > 6$, the maximum heat transfer coefficient occurred at some distance from the stagnation point (x/D); for $z/D < 6$, the maximum value occurs at x/D=0.5, which is slightly displaced from the stagnation point. When z/D is small, the impingement jet becomes a wall jet immediately, and a second maximum heat transfer coefficient occurs at x/D=2, at which point the flow transitions from laminar to turbulent flow. In their study, the Reynolds number was in the

range of 7,000 to 112,000. Similar observations were documented by Baughn and Shimuzu (1989) [4]. They found the secondary maximum local Nusselt number at x/D=1.8.

Besides impingement heat transfer varing with different geometrical parameters like the nozzle-to-plate distance (z/D) and distance from the stagnation point (x/D), turbulence plays an important role too. In a study conducted by Gardon and Akfirat (1965) [14], it was found that artificially induced turbulence affects the impingement heat transfer at small nozzle-to-plate distances. The stagnation point heat transfer coefficient remains higher than for a plain nozzle and almost constant as the nozzle-to-plate distance ranges from 2 to 8. The secondary maximum heat transfer coefficient occurred at a distance from the stagnation point of 7 nozzle diameters, compared to around 2 when no turbulence was induced.

It was expected that the periodic destruction and reconstruction of thermal and hydrodynamic boundary layers would enhance impingement heat transfer when unsteady (pulsating) impinging jets were used. Nevins and Ball indicated that the Nusselt number was independent of the amplitude of pulsation and pulse frequency for both square and sinusoidal waveforms. Zumbrunnen and Aziz (1993) [69] argued that boundary layer response was sufficiently rapid to allow heat transfer enhancement when the frequency of pulsation was high enough to keep the time averaged thermal boundary layer thickness significantly thinner than steady jets. They found that significant heat transfer enhancements occurred at the stagnation point when the Strouhal number was much greater than 0.26 in Reynolds numbers ranging from 6,500 to 16,000. At the maximum Strouhal number of 0.365, and a Reynolds number of 9450, the local Nusselt number at the stagnation point was two times higher than corresponding steady jets. More recently, Camci and Herr (2002) [6] investigated the heat transfer enhancement of a self-oscillating impinging planar jet. They created a self-oscillating impingement jet by adding two communication ports at the throat section. A typical enhancement of the Nusselt number at the stagnation line of around 70% was observed with Re=14,000 and a nozzle-to-plate distance of 24 nozzle diameters. They indicated that oscillation of the jet increased convection and diffusion significantly. However, the kinetic energy production was only slightly modified.

The flow of a synthetic jet impinging orthogonally onto a plane surface may have different

characteristics because of its shorter developing zone compared to a conventional jet. When the synthetic jet was employed in thermal management applications, jet impingement was often confined to a small space. Although there are a great number of jet impingement studies, documented investigations on the detailed flow and heat transfer characteristics of synthetic jet impingement are rare.

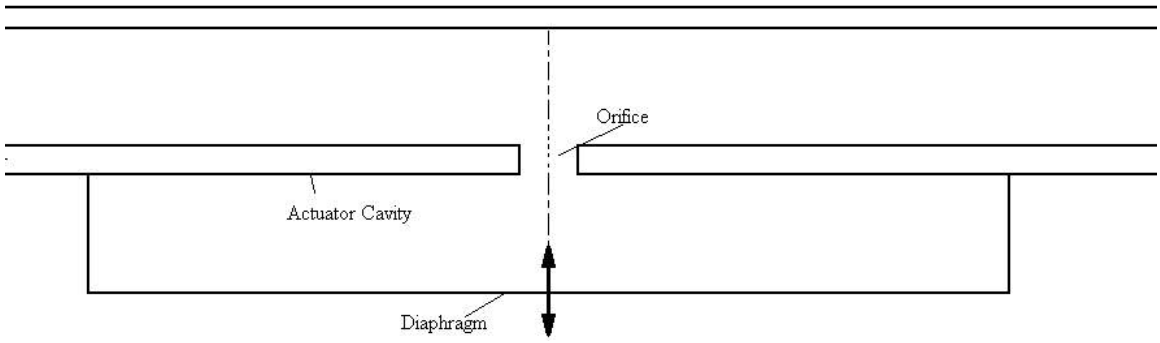

Figure 2.3: Axisymmetric synthetic jet impingement

Vukasinovic and Glezer (2001) [64] investigated the performance of a low-profile radial countercurrent heat sink driven by an integrated synthetic jet actuator. A sketch of an axisymmetric synthetic jet impingement configuration is shown in figure 2.3. In this work, two parallel disks were placed some distance apart, a synthetic jet was integrated into the bottom plate and was designed to cool the upper plate through normal impingement. The heat transfer and fluid dynamics of a normally impinging synthetic jet in this confined flow configuration were studied including the effect of some important parameters, such as the gap height to plate diameter ratio. A power dissipation of 50 W was accomplished at the nominal case temperature of $T_c = 70°C$. A radial countercurrent flow in the gap between the plates was observed. A hot air layer flowed radially outwards along the top plate and a layer of cooler ambient air entrained from the jet exit plane flowed inwards. A cooling effect could still be observed when the spacing between the two plates was of the order of the jet orifice diameter, although generally the global heat transfer coefficient decreased with decreasing gap height.

Tamburello (2003) [57] used the commercial CFD package FLUENT (v5.4) to analyze

the synthetic air jet used by Vukasinovic and Glezer [64]. He built an axisymmetric model of the experimental geometry. The flow domain extended three times farther from the centerline than the available experimental data to ensure that the location of the far-field boundary conditions did not affect the results of the simulation. Maximum velocity, pressure drop across the orifice, and the vorticity in the critical areas differed by less than 5%, 5%, and 11% when comparing this domain to a larger flow domain. Mesh refinement comparisons showed 3%, 4%, and 7% differences for the above parameters. One hundred and sixty oscillation cycles were simulated to ensure a fully developed, periodic flow. The working frequency was 80 Hz and LES was used to simulate turbulence. The motion of the diaphragm was not modeled as a physical moving component, instead a time dependent velocity boundary condition was used. The velocity profile varied in space as a Bessel function of the first type. In all cases, the velocity profiles from the simulations matched well in the shape and magnitude with the experimental data. The discrepancy between the simulation data and the experimental data were discussed as the results of three dimensional effects and resolution of PIV. Actuator diaphragm amplitude, jet-to-plate distance, cavity height, orifice thickness, and orifice diameter were varied to investigate the effects of different geometry designs and to find optimal parameters. It was found that the average centerline velocity over one full cycle increased with increasing actuator diaphragm amplitude, and target height, and with decreasing orifice diameter and orifice thickness. The average centerline pressure over one cycle changed very little throughout the flow field between the orifice plate and the target plate. The optimal parameters to produce a maximum averaged centerline velocity were found for this given actuator configuration. However, no heat transfer characteristics were discussed.

Russel (1999) [51] studied thermal management using synthetic jet technology on a flip-chip device based on single-level integrated module technology (SLIM). It was found that by using a synthetic jet, thermal resistance reductions as large as 87% occurred at the stagnation point on the heated surfaces compared with natural convection. Cooling effectiveness increased with both decreased radial distance from the centerline and with increased jet strength. Small-scale motion near the solid surface generated by the synthetic

jet enhanced the direct impingement heat transfer. The synthetic jet flow also provided efficient mixing with the global cross flow. The optimum nozzle-to-surface distance decreased with decreasing radial distance and increasing orifice diameter. He also found that changes in the working frequency didn't affect the thermal resistance significantly. Finally, a multi-jet actuator was shown to provide uniform lateral cooling. This was significant in that a reduction in lateral temperature gradients leads to significant improvements in mechanical reliability of the chip.

Mahalingam and Glezer (2001) [28] developed an active heat sink by integrating a synthetic jet actuator with a conventional heat sink (shown in figure /refch203). By exploiting the synthetic jet flow in the channels between the fins, they achieved heat dissipation rate

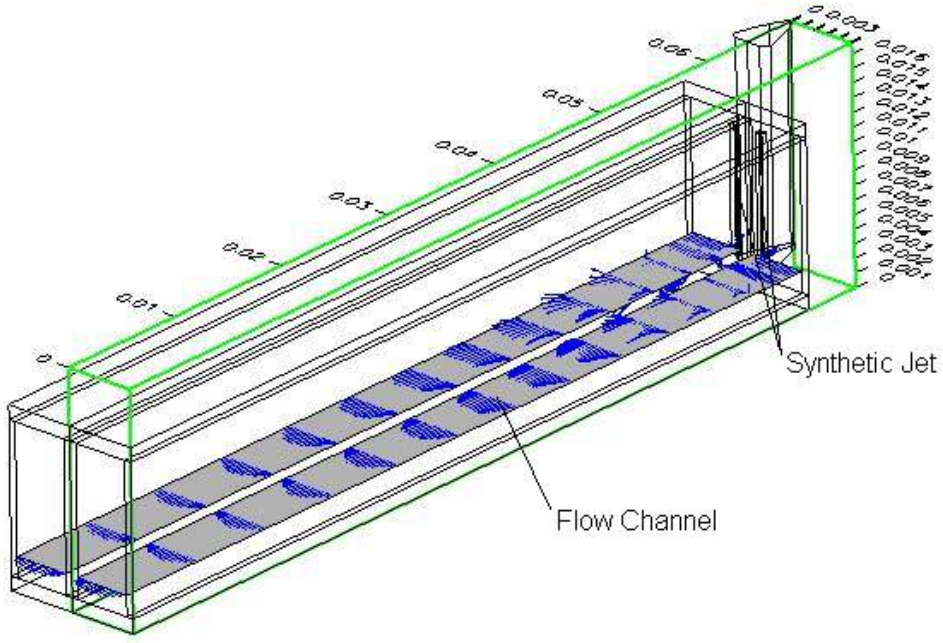

Figure 2.4: Geometry of a cell in an active heat sink

of 110W at 100°C in a package having a volume of 200 cm^3. This was 350% higher than natural convection. The Nusselt number was six to eight times larger than that of comparable forced, turbulent convection heat transfer. The thermal resistance of the active heat sink was $0.69°C/W$.

CHAPTER III

NUMERICAL STUDY OF FREE SYNTHETIC JET

The unique zero-mass-flux characteristic of a synthetic jet make it attractive for fluidic control and thermal management in microsystems. As discussed by Glezer et al.(2002) [19], plane and round synthetic jets have been investigated both experimentally and numerically, while the complex flow field within the actuator cavity has been primarily treated numerically. However, a systematic study on synthetic jet flows is still desired for in depth understanding of the flow characteristics. The synthetic jet flow formed by the time-periodic motion of air flowing through the orifice/nozzle of a sealed cavity forced by the time periodic motion of a diaphragm were studied numerically in this chapter (shown in Figure 3.1). The evolution of the synthetic jet, time-mean and instantaneous flow characteristics were identified and analyzed. Results were also used for the modeling of synthetic jet (Chapter 4).

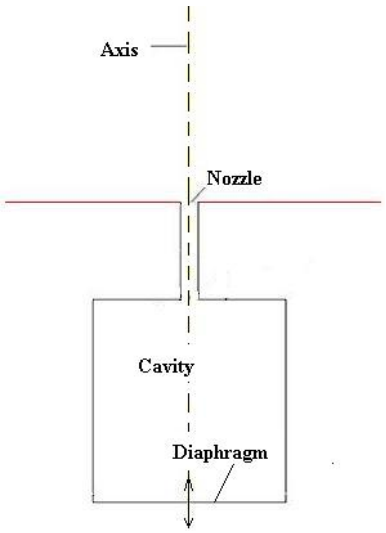

Figure 3.1: Schematic of synthetic jet

3.1 Numerical Approach

This study is limited to axisymmetric synthetic jet flow. Two commercial CFD packages were employed: Fluent and CFDACE+. As mentioned in the previous chapter, one challenging aspect of the numerical simulation of synthetic jet flow is to simulate the time dependent moving diaphragm of the cavity. Both of these two packages provide some sort of "moving grid" modeling capability.

In CFDACE+, the grid deformation over time in an unsteady simulation can be modeled by modifying the input file used by the CFDACE+ solver with CFDACE+ command language. The user provides the initial grid and identifies all regions that deform over time. For each deforming grid region, the point motion of one of more corner points is specified using command language. CFDACE+ automatically regenerates the grids in these deforming zones as following [1]:

1. First, the motion of the edge grid points is determined by an arclength-based linear interpolation of the corner points' motion;

2. All of the surface grids are regenerated using a transfinite interpolation (TFI) of the edge grid motion;

3. The volume grid is regenerated using TFI of the surface grid motion.

For more details, see the CFDACE+ user manual [1].

Fluent offers a "dynamic mesh" option since version 6.1, through which the user can model flows where the shape of the domain is changing with time due to motion of the domain boundaries. The motion could be predefined or determined by the solution at the current simulation time. The user needs to provide an initial volume mesh and the description of the motion of any moving zones in the model. Fluent allows the user to describe the motion using either boundary profiles or user-defined functions (UDFs). There are three different methods to update the mesh: spring-based smoothing, dynamic layering, and local remeshing. For details of these techniques and how to set up a problem using dynamic mesh, see the Fluent user manual [2]. In this study, the dynamic-layering technique is the method mainly used to model the piston-like motion of the diaphragm.

Second-order (the highest order available in FLUENT 6.1.18) discretization schemes were used for density, momentum, pressure, turbulence kinetic energy, specific dissipation rate and energy. QUICK or second order upwind scheme are mostly used. The SIMPLEC scheme was used for the pressure-velocity coupling. Under-Relaxation factors were set as follows: pressure 0.3, density 1, body force 1, momentum 0.7, turbulence kinetic energy 0.8, specific dissipation rate 0.8, turbulent viscosity 1 and energy 1. Air was modeled as an

ideal gas, C_p, thermal conductivity and viscosity were determined using a piece-linear table or kinetic theory. If no heat transfer was involved, constant C_p, thermal conductivity, and viscosity at the ambient temperature were used. All simulations were started using a first order discretization scheme for a couple of cycles to avoid the possible divergence problems associated with high-order schemes in the initial steps. Then the discretization scheme was set to second order as mentioned earlier in this paragraph. Due to the limitation of the dynamic mesh model in FLUENT, if this technique was used the temporal discretization scheme had to be set to first order. For those simulations with a modeled cavity, the temporal discretization was second-order upwind. The discretization schemes for the convective terms are the same as those schemes used in the full simulations.

Instead of directly setting the turbulence kinetic energy (k) and the specific dissipation rate (ω), we set the turbulence intensity and characteristic length or hydraulic diameters at the inlet or/and outlet boundaries. For simulations using the synthetic jet cavity model, a turbulence intensity of 10% was assumed at the velocity inlet and at the outlet, a turbulence intensity of 1% was assumed. For simulations with the full cavity, turbulence parameters were set only at the outlet.

The turbulence model is another concern when modeling synthetic jet flow, if turbulent flow exists in the flow field. It is known that the $k-\omega$ model performs better than the $k-\epsilon$ model in low Reynolds number, axisymmetric shear flows. The Shear-Stress-Transport (SST) $k-\omega$ turbulence model was proposed by Menter(1994) [32]. It combines the best elements of the $k-\epsilon$, and the $k-\omega$ model with a blending function. This function is one near the surface and zero in the outer part of boundary layer and for free shear flows. It activates the Wilcox model in the near-wall region and the $k-\epsilon$ model for the rest of the flow. Therefore, the attractive near-wall performance of the Wilcox model is utilized without the potential errors resulting from the free-stream sensitivity of that model. For further details of the SST model, see Menter(1994) [32]. Viesser et al. [67] compared the performance of several commonly used turbulence models in heat transfer problems, and concluded that the SST $k-\omega$ model "in combination with an optimal wall treatment, does provide highly accurate results for a wide variety of heat transfer test cases". Our numerical

studies with heat transfer (presented in Chapter 6) also support the use of SST $k-\omega$ model in 2d/axisymmetric simulations.

The near-wall modeling significantly impacts the fidelity of numerical solutions, inasmuch as walls are the main source of mean vorticity and turbulence. Accurate representation of the flow in the near-wall region determines successful predictions of wall-bounded turbulent flows. The $k-\omega$ model was designed to be applied throughout the boundary layer, provided that the near-wall mesh resolution is sufficient. Traditionally, there are two approaches to modeling the near-wall region: wall functions and near-wall model. In this study, the near-wall model was used in the $k-\omega$ SST model. The Transitional Flows option was enabled, low-Reynolds-number variants were used, and the mesh requirement was the same as for the enhanced wall treatment. The enhanced wall treatment was employed with the intention of resolving the laminar sublayer; y^+ at the wall-adjacent cell should be on the order of $y^+ = 1$. However, a higher y^+ is acceptable as long as it is well inside the viscous sublayer. At least 10 cells within the viscosity-affected near-wall region ($Re_y < 200$) were meshed to be able to resolve the mean velocity and turbulent quantities in that region. Because the $k-\omega$ model was designed to calculate the wall effect, it is not necessary to specify any turbulence boundary conditions on the wall. The grid requirement for $k-\omega$ model was satisfied for all simulations. The boundary layer mesh tool was used when meshing the models in this study. The first layer of node was within 30 μm from the wall and evolved 4 to 5 layers of nodes toward the outer layer.

Both body adapted structured mesh and unstructured mesh were used in this study. The structured mesh was mainly used in the cavity to easily utilize the dynamic-mesh method. A mesh study and a time-step-size study were performed to evaluate the quality of the numerical model used in this work. The validation of this axisymmetric simulation also includes comparison with the experimental data of jet impingement conducted by Vukasinovic et al. (2001) [64] (shown in Chapter 5).

Three meshes with sizes of $\sim 5,000$, $\sim 10,500$, and $\sim 22,000$ were used in the mesh study. Compared with the medium-sized mesh, the grid density in the strong non-linear region (the region near the nozzle) was tripled in the fine-sized mesh. For the medium-sized

mesh, 36 time steps per cycle and 108 time steps per cycle were used in the time-step-size study.

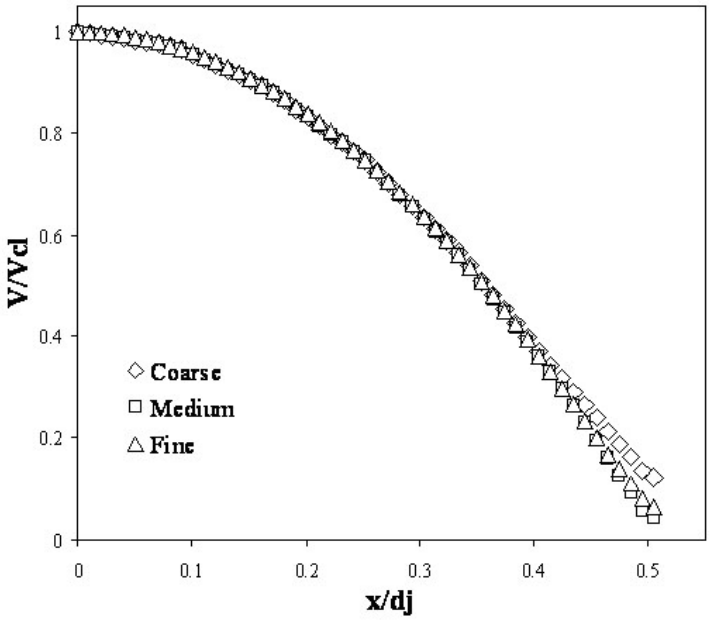

Figure 3.2: The velocity profile at the nozzle exit for different meshes

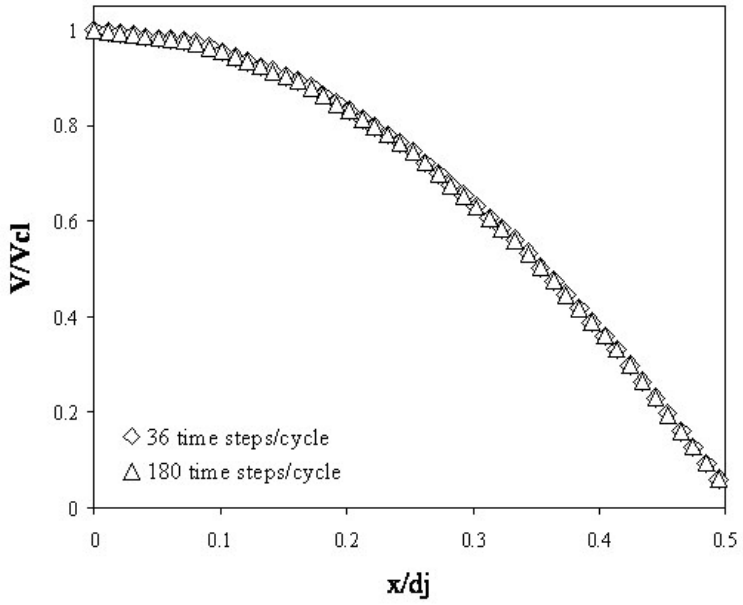

Figure 3.3: The velocity profile at the nozzle exit for different time-step sizes

In the mesh study, the RMS error of velocity between the fine and medium meshes was less than 2% (1.25%), and the RMS error between the fine and coarse meshes was around 8%. All three meshes can well resolve the vortex dynamics of the synthetic jet flow (not shown). The mesh study results showed that the medium mesh was sufficient to resolve the flow field with good accuracy. The simulation using 36 time steps per cycle yielded almost identical results to the simulation using 180 time steps per cycle. The time-step-size study results showed that 36 or more time step per cycle is sufficient to capture the transient characteristics of a synthetic jet with good accuracy. As examples, Figures 3.2 and 3.3 show the typical velocity profile at the nozzle exit from different meshes and time-step-sizes. The detailed results of the mesh study and the time-step-size study are not included in this dissertation.

In this study, meshes similar to or finer than the medium mesh were used to complete the numerical simulation. For most simulations, 36 time steps per cycle or 40 time steps per cycle were used.

It's also important to know that the computational domain was large enough so that the location of the outer boundaries does not affect the results. A series of numerical studies were designed to locate this boundary (see Figure 3.4). The smallest outer domain tested was $7.5d_j$(W)x$12.5d_j$(L) with a d_j=2 mm nozzle. The largest one was $350d_j$(W)x$750d_j$(L) with a d_j=0.1 mm nozzle. A quarter circle shaped domain with a radius of 150 d_j and d_j=0.5 mm was also tested. In most computational domains, the nozzle outlet plane was one of the boundaries of the outer domain. In other computational domains, the nozzle exit plane was inside the domain. In most cases, an outer domain of $20d_j$x$50d_j$ was found to be sufficiently large to eliminate the effect of the location of the outer boundary condition.

Utturkar et al.(2002) [62] examined the sensitivity of synthetic jets to the design of the jet cavity. They found for symmetrically placed diaphragms modifications in the cavity design had only limited effect on the jet exit flow. The diaphragm was placed at the bottom and side position of the cavity. The aspect ratios of examined cavity designs were in the range of h_c/d_c=1/5 $\sim$ 5. Therefore, the present study focused on the effect of the cavity volume, the displacement of the diaphragm, and the ratio of d_{cav}/d_{noz}.

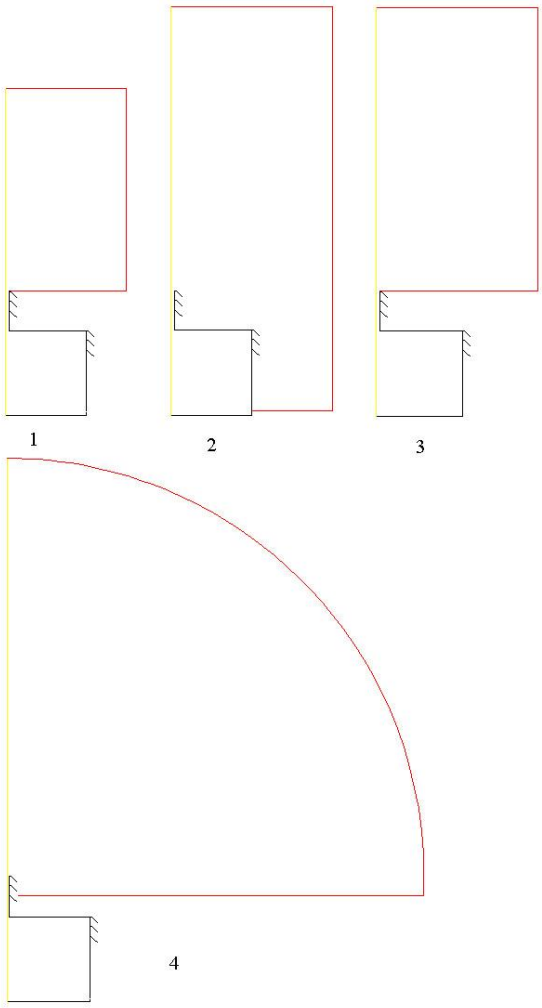

Figure 3.4: Computational domain study

An accurate simulation of the diaphragm motion would solve the fluid-structure interaction problem, which in turn involves the material mechanics and material properties of the diaphragm. This makes the simulation more difficult and limits the generality of the study. As mentioned in previous chapters, this study is an investigation of the effect of geometrical parameters on synthetic jet flow. Therefore, we would like to avoid this structural effect of the diaphragm.

To do this, we must know if the spatial profile of the diaphragm is important. If the answer is no, then we can use the simplest displacement profile to complete our study. To investigate this effect, we ran two simulations that were identical except for the diaphragm

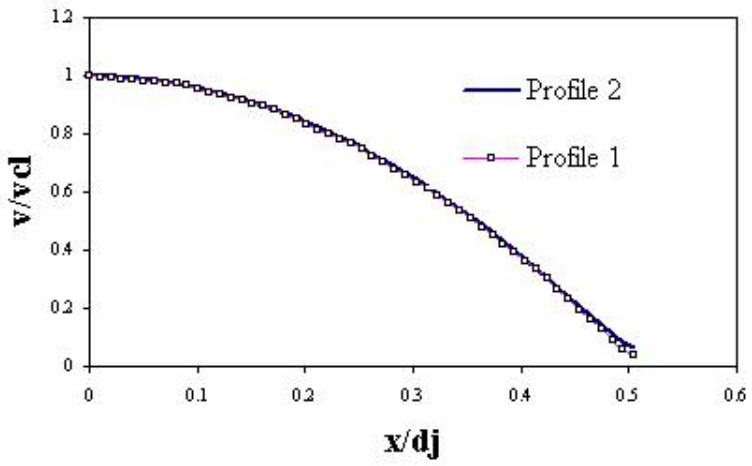

Figure 3.5: A comparison of the velocity profile at the jet exit for different diaphragm displacement profiles (blowing stroke)

spatial displacement profile. The volume displacements of these two profiles were set equal. One profile was uniform, i.e., the diaphragm moved like a piston. Real diaphragms used in experiments usually have a driven part at the center of the diaphragm with a flexible outer portion attached to the cavity. The second diaphragm displacement profile was designed to simulate such a diaphragm.

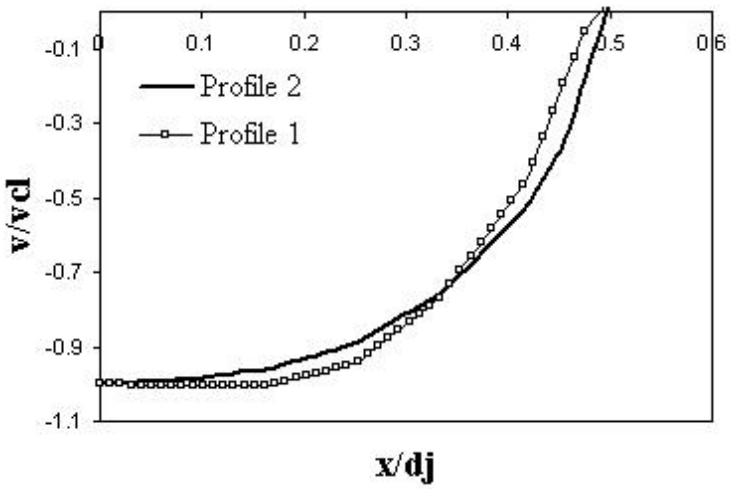

Figure 3.6: A comparison of the velocity profile at the jet exit for different diaphragm displacement profiles (suction phase)

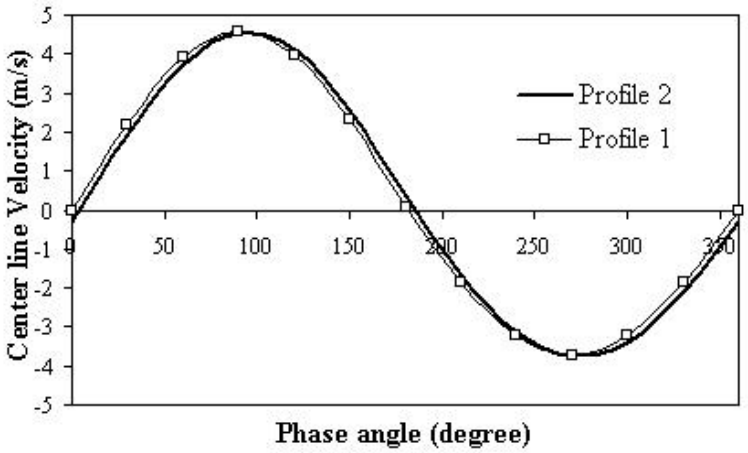

Figure 3.7: A comparison of the centerline velocity at the jet exit over one cycle for different diaphragm displacement profiles

The simulation results show that the effect of the diaphragm displacement profile on the synthetic jet flow was limited. Figures 3.5 and 3.6 show a comparison of the velocity profiles at the nozzle/orifice exit at the maximum stroke and suction phase. At the maximum blowing stroke, the velocity profiles are almost identical (RMS error 1.09%). There exists some difference at the maximum suction phase, but the difference is not significant (RMS error 4.94%). The centerline velocity at the jet exit over one cycle is shown in Figure 3.7. The difference between these two cases is small. The velocity vector fields of profile 2 are shown in Figures 3.8, 3.9.

It is reasonable to neglect the effect of the diaphragm displacement profile. In this study, all synthetic jet system simulations with a cavity used a simple, uniform displacement profile. Thus, the bottom wall of the cavity moved like a piston.

3.2 Procedures

The main purpose of this study was to investigate the synthetic jet flow under the effects of changes in the following parameters: cavity geometry (height, diameter), nozzle geometry (diameter, length), diaphragm displacement, and working frequency. The flow characteristics of interest include the velocity through the nozzle, pressure distribution in the nozzle, and the free-jet characteristics. The scope of investigated parameters is listed in Table 3.1.

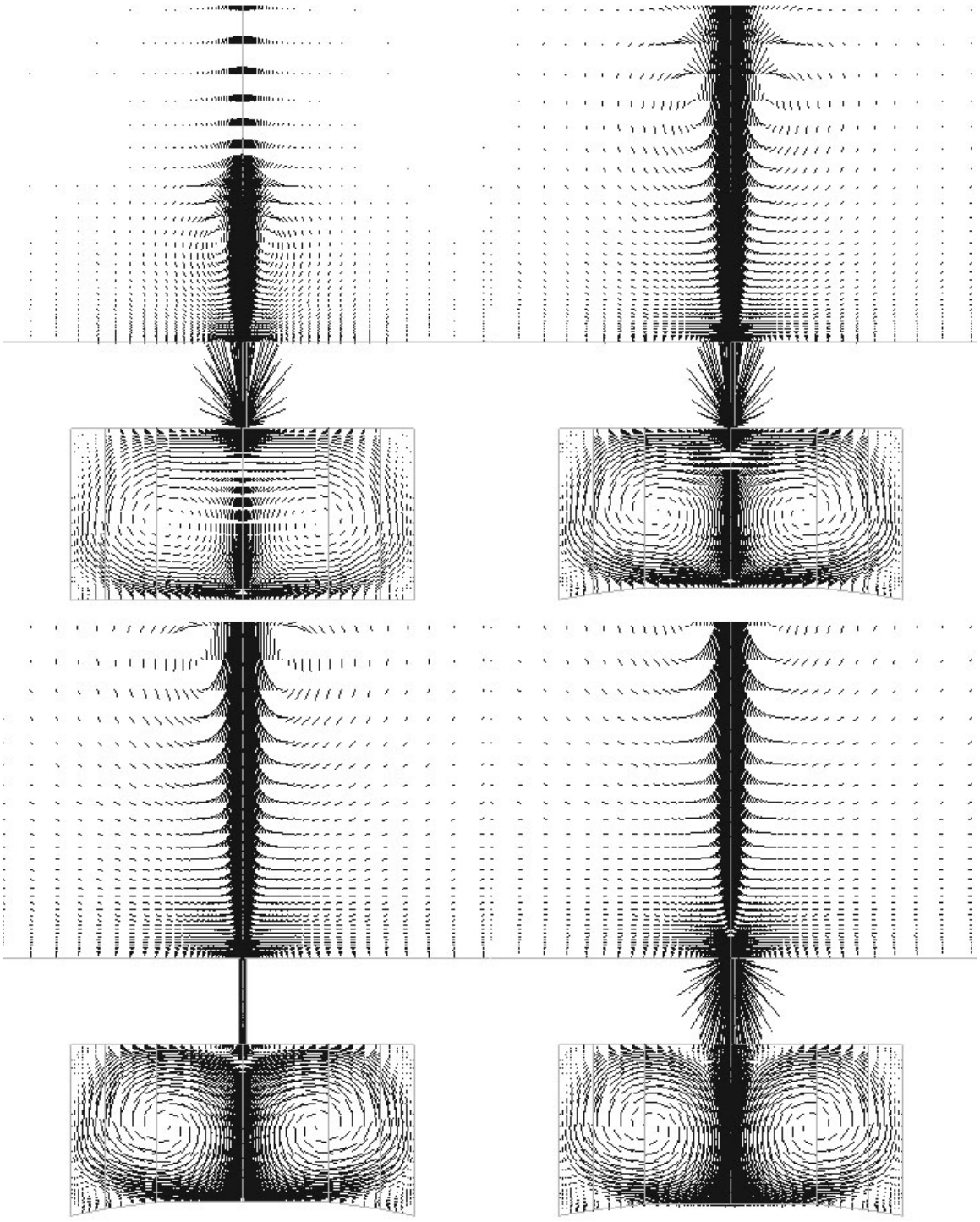

Figure 3.8: Diaphragm profile 2 and corresponding velocity field

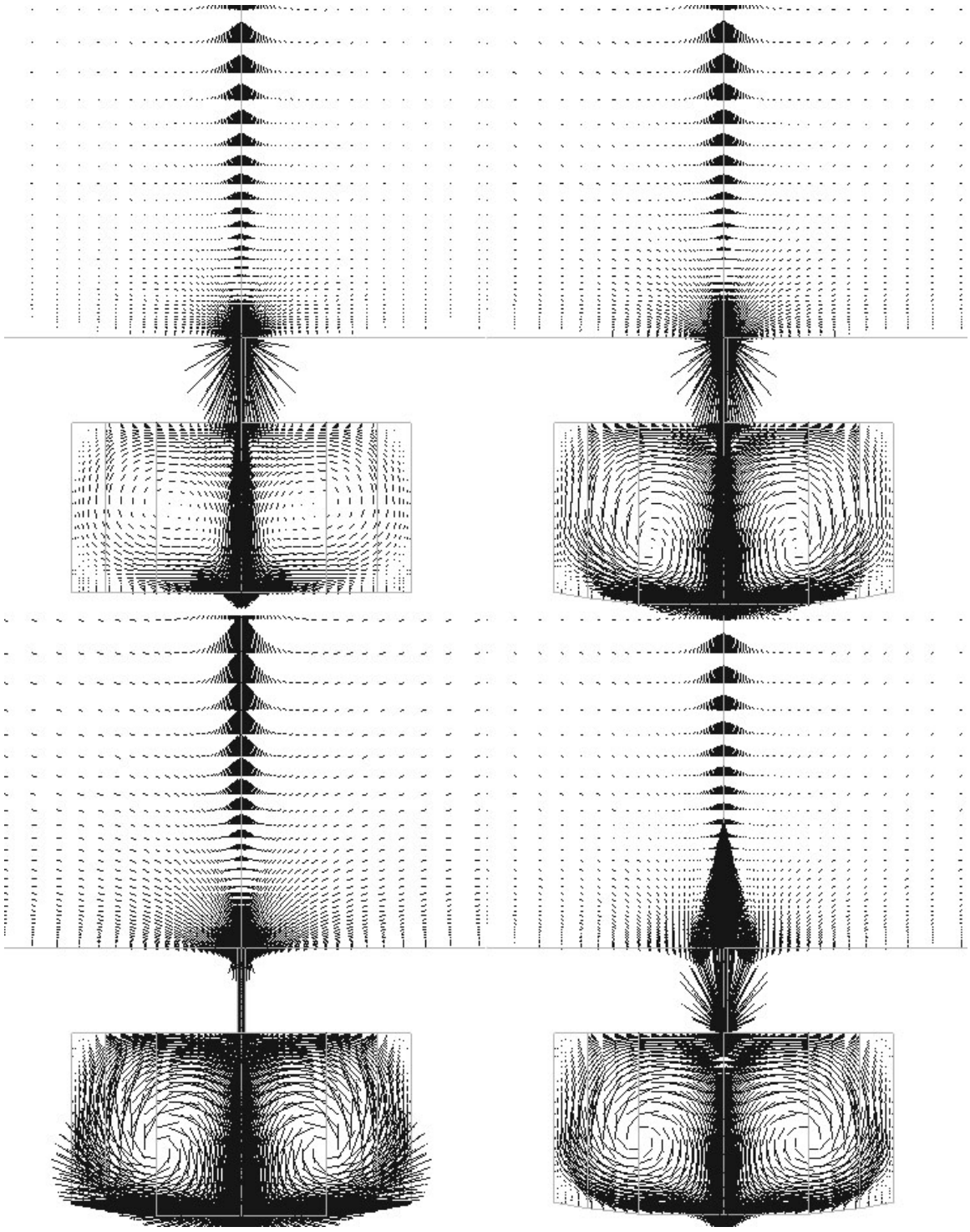

Figure 3.9: Diaphragm profile 2 and corresponding velocity field (continued)

Table 3.1: Summary of simulation parameters

Parameter	Range	Values
Nozzle diameter d_j (mm)	$0.1 \sim 2$	0.1, 0.5, 1, 2
Nozzle length l_j/d_j	$2.5 \sim 50$	2.5, 5, 10, 50
Cavity diameter d_c/d_j	$5 \sim 200$	5, 10, 20, 40, 200
Cavity height h_c/d_c	$\frac{1}{4} \sim 1$	$\frac{1}{4}$, $\frac{1}{3}$, $\frac{1}{2}$, 1
Frequency (Hz)	$80 \sim 1000$	80, 250, 500, 1000
Diaphragm displacement (mm)	$0.3 \sim 5$	0.3, 0.5, 1, 3, 5

In summary, we employed two commercial CFD packages, CFDACE+ and FLUENT, to complete the numerical simulations. In CFDACE+ the low Re turbulence model was used, and in FLUENT the SST $k-\omega$ turbulence model was used. The synthetic jet cavity was fully simulated with the diaphragm modeled as a piston-like moving wall.

To make sure a periodic state was reached, the velocity and pressure were checked at a point 10 d_j away from the nozzle exit and along the centerline. When these two values changed by less than 0.5% between two successive cycles, the simulation stopped. Typically, 20 cycles were simulated to reach a periodic state.

3.3 Formation and evolution of a synthetic jet

As its name implies, a synthetic jet is synthesized by a time-periodic flow. The jet cannot be formed if some criteria is not met. Several researchers have discussed possible criteria in their work. These criteria either are a threshold stroke length (Smith 2001 [55]), or a threshold Strouhal number (Utturkar 2003 [61]). Since the non-dimensional Stroke length is the inverse of the Strouhal number, these two criterion are in agreement on which key parameter determines the formation of a synthetic jet. However, it is not easy to tell whether a synthetic jet has formed or not, because it is quite different from a conventional jet in the developing region.

In this work, vortex dynamics was used to determine whether the jet formed or not. First, let's examine the vortex dynamics of a case in which no jet was synthesized. The geometry of this case was $d_j = 2$ mm, $d_c/d_j = 5$, $h_c/d_j = 5$, $l_j/d_j = 2.5$, the working frequency was 1 kHz, and the maximum diaphragm displacement was 0.3 mm. The non-dimensional stroke length was 0.35 and Re_{I_o} was 88. From the vorticity contours shown

in the Figures 3.10, and 3.11 the vortex pair formed at the edge of the nozzle during the blowing stroke does not move downstream and is sucked backed into the nozzle during the suction phrase. The-time-mean velocity vector field (Figure 3.12) shows no obvious jet flow. The time mean zero velocity line is located inside the nozzle.

The vortex dynamics of a synthetic jet flow is shown in Figure 3.13. This synthetic jet was of non-dimensional stroke length $L_{stroke}/d_j = 12.02$, Re_{I_o} of 1580, with geometry parameters of $d_j = 1$ mm, $h_c/d_c = 1$, $d_c/d_j = 10$, and working frequency 250 Hz. During the blowing stroke, the vortex pair generated at the nozzle exit moved downstream and dissipated. The vortex pair dissipated very quickly. Two to three vortex pairs could be identified in the flow field during any one cycle. It was observed that it takes approximately one tenth of a cycle to detach a vortex pair from the nozzle exit. During this time, the vortex core moved relatively slowly. Once the vortex pair detached from the nozzle, its velocity reached a peak and then decreased. The vortex pair velocity was estimated using an image processing technique to isolate the vortex core and measure the distance between the vortex core and the nozzle exit. The results are shown in Figure 3.14.

During the suction phase, a counter-rotating vortex pair is generated at the nozzle exit in the cavity. The vortex pair moves towards the diaphragm (bottom of the cavity) and then moves to the side. At last, it dissipates at the center of the cavity.

We can observe the difference of vortex dynamics between the synthetic jet formed case and the one with no jet flow formed. As other researchers suggested the non-dimensional stroke length or Strauhal number could be used as a criterion for jet formation. Utturkar (2003) [61] suggested a Strauhal number of two, which corresponds to a non-dimensional stroke length of 0.5. Above this length, the jet is formed.

The dynamics of the vortex pair in the cavity is similar. Figure 3.15 shows the vortex evolution in the cavity with h_c/d_c=1/4. It is interesting to observe that the vortex pair moves in a cylindrical domain with a radius approximately equal to the cavity height. This is also observed in h_c/d_c=1/3 cases (Figure 3.16), although not so clearly. The vortex dynamics for the cases h_c/d_c=1, and 4 are shown in Figure 3.17 through 3.20 respectively. When the cavity aspect ratio is large, the moving diaphragm is far away from the nozzle/orifice,

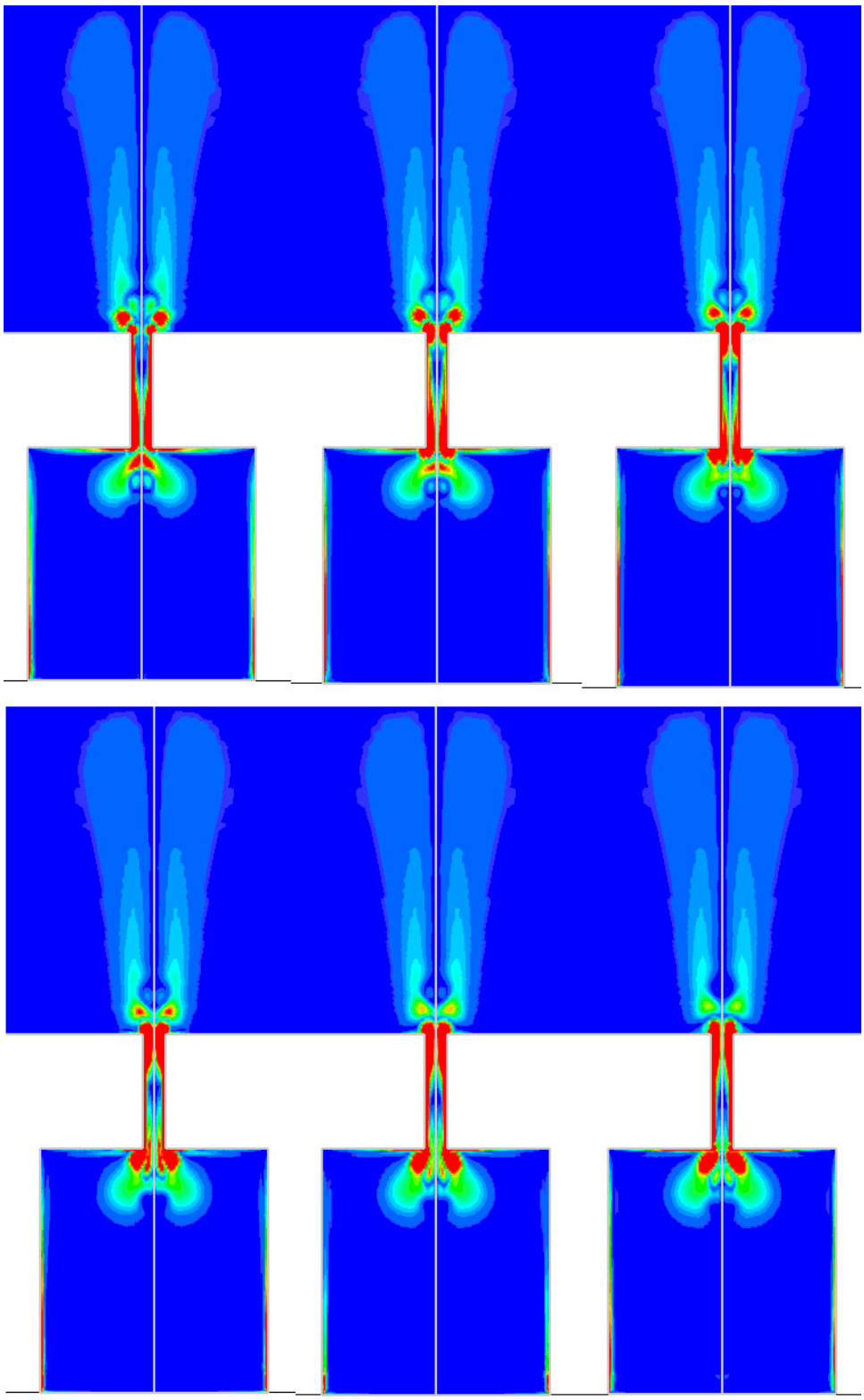

Figure 3.10: Vortex dynamics of a synthetic jet (not formed) with $h_c/d_c = 1$, f=1 kHz, d_j=2 mm

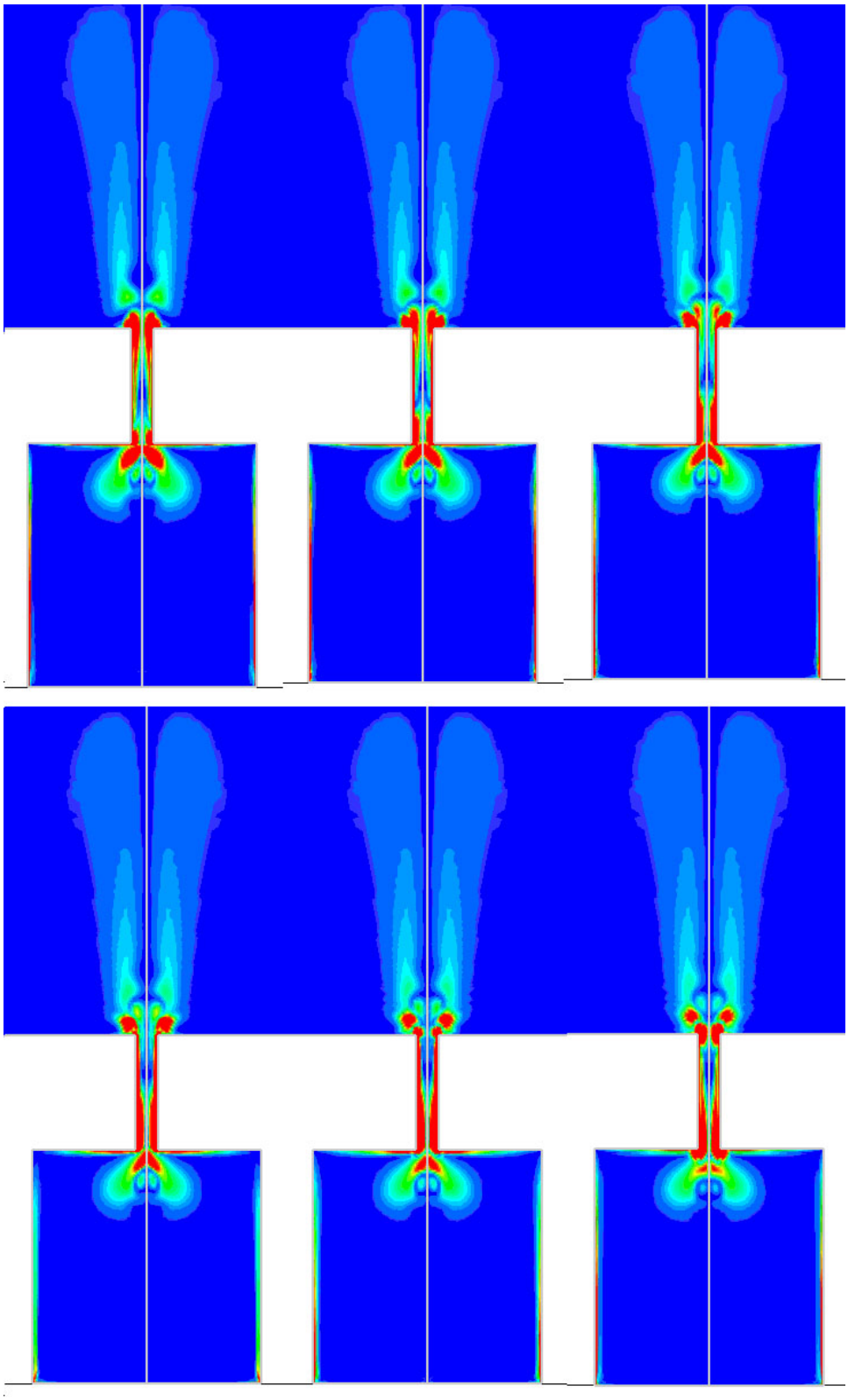

Figure 3.11: Vortex dynamics of a synthetic jet (not formed) with $h_c/d_c = 1$, f=1 kHz, d_j=2 mm (continued)

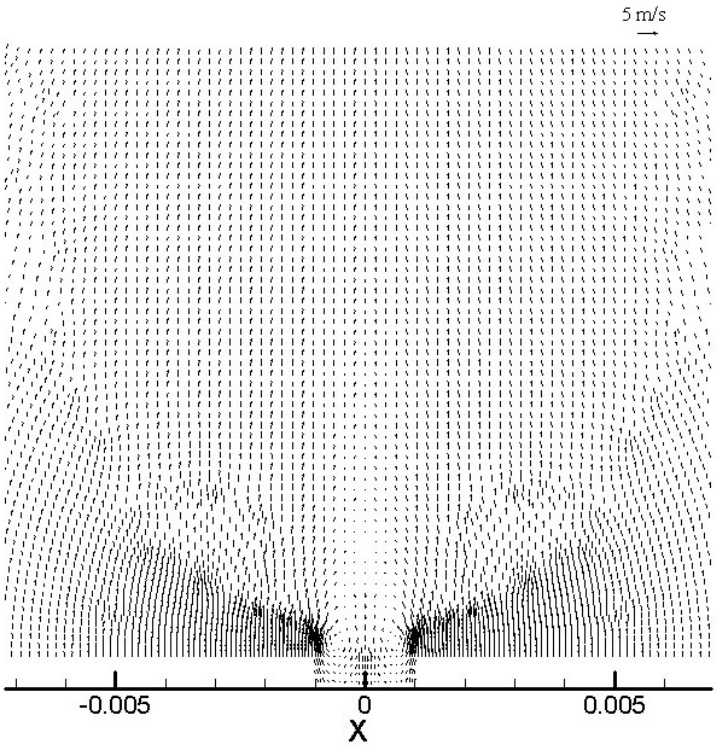

Figure 3.12: Time-mean velocity field near the nozzle exit from a case when no jet is formed ($L_{stroke}/d_j = 0.35$)

the motion of the vortex pair in the cavity is similar to that of the vortex dynamics outside of the cavity.

To examine the effect of the cavity geometry on the synthetic jet flow, simulations with a real speaker shaped cavity were conducted. The orifice geometry used in these simulations is d_j=6.35mm and l_j=3.175mm. The computational domain and mesh are shown in Figure 3.21. The dynamics of vortex of this case is shown in Figure 3.22 and 3.23.

The general vortex dynamics evolution is illustrated in these figures:

1. When the diaphragm begins to move down, a vortex pair was formed from the edge of the nozzle in the cavity. A high-vorticity region was observed near the center line and moved down towards the diaphragm. The vortex pair moved to the side at first and then detached the inner wall of the cavity moving towards the diaphragm at last; Outside of the cavity, the already detached vortex pair kept moving downstream and dissipated.

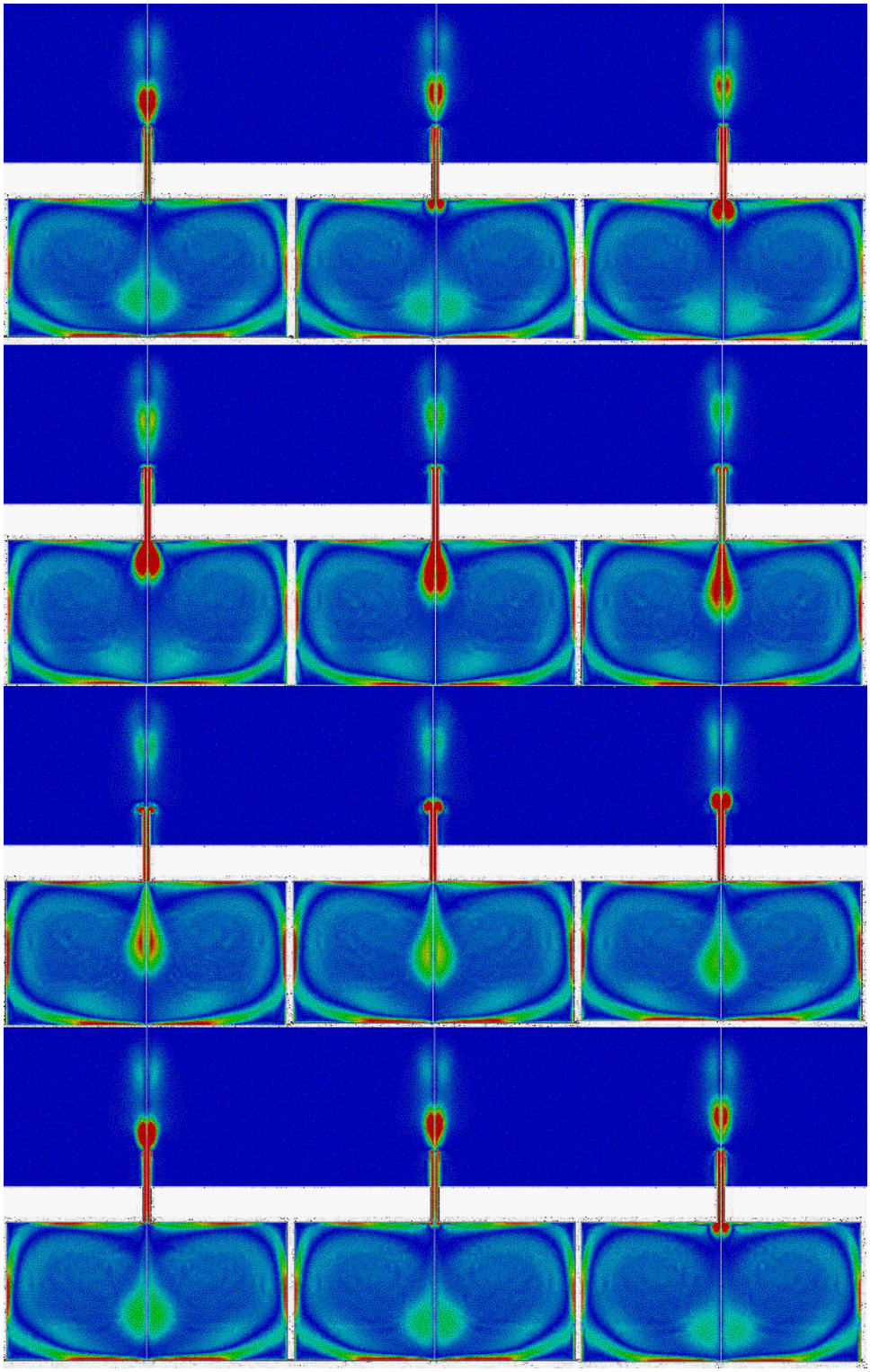

Figure 3.13: Vorticity contours over one cycle of a 250 Hz axisymmetric synthetic jet ($L_{stroke}/d_j = 12.02$)

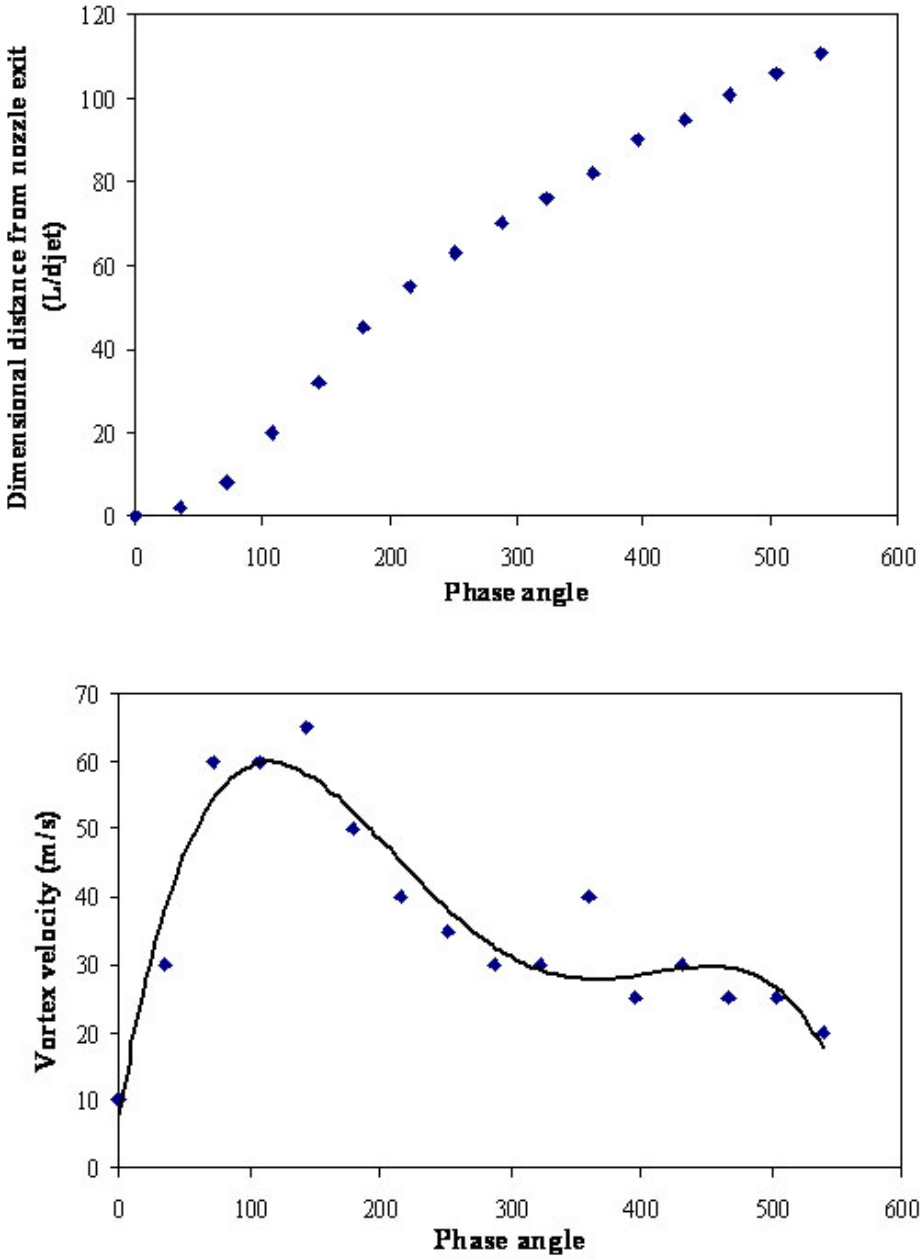

Figure 3.14: Vortex pair distance from nozzle exit(top), Vortex pair velocity(bottom), ($L_{stroke}/d_j = 12.02$)

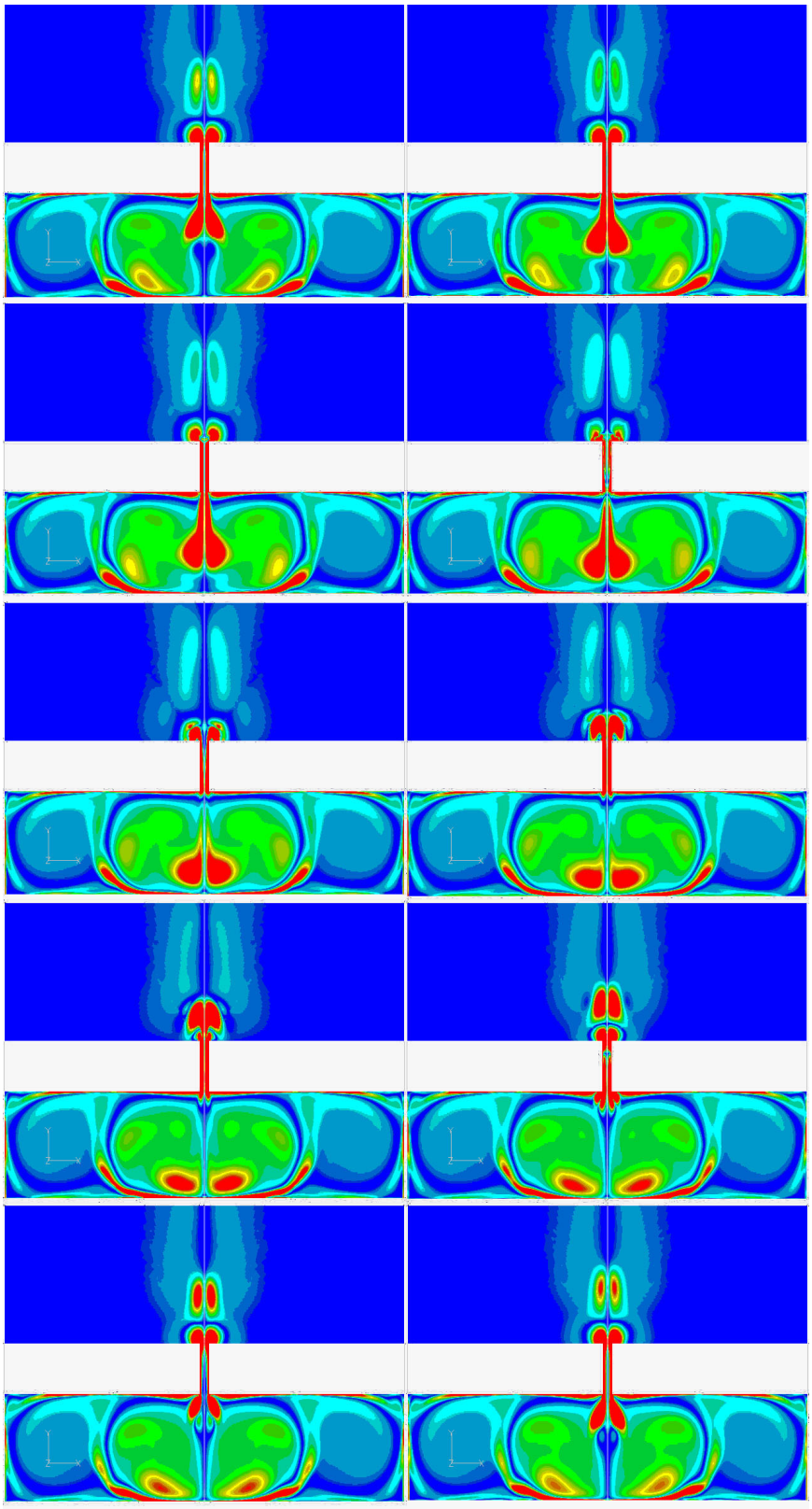

Figure 3.15: Vortex dynamics of a synthetic jet with $h_c/d_c = 1/4$, f=1 kHz, d_j=1 mm

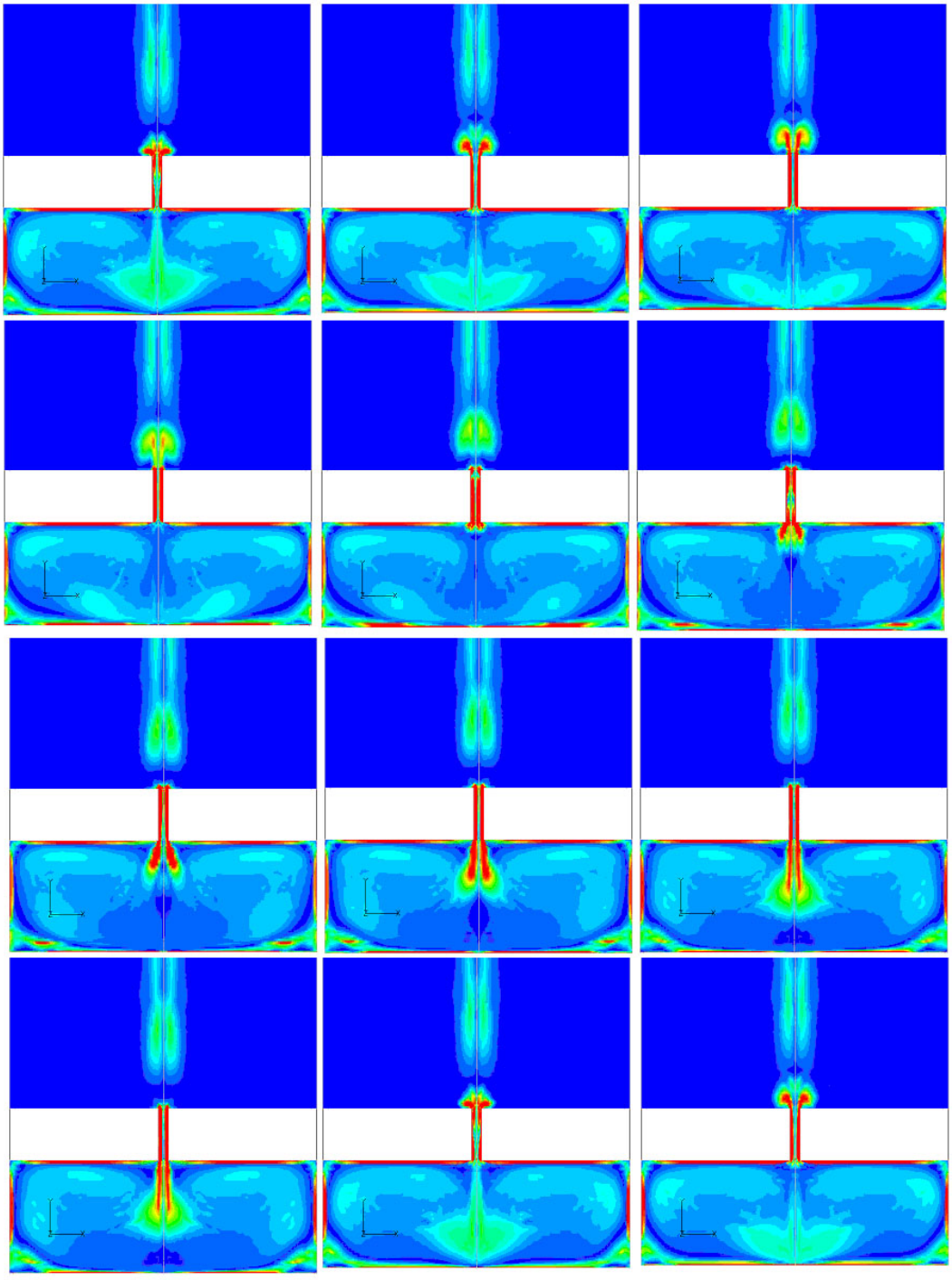

Figure 3.16: Vortex dynamics of a synthetic jet with $h_c/d_c = 1/3$, f=1 kHz, d_j=1 mm

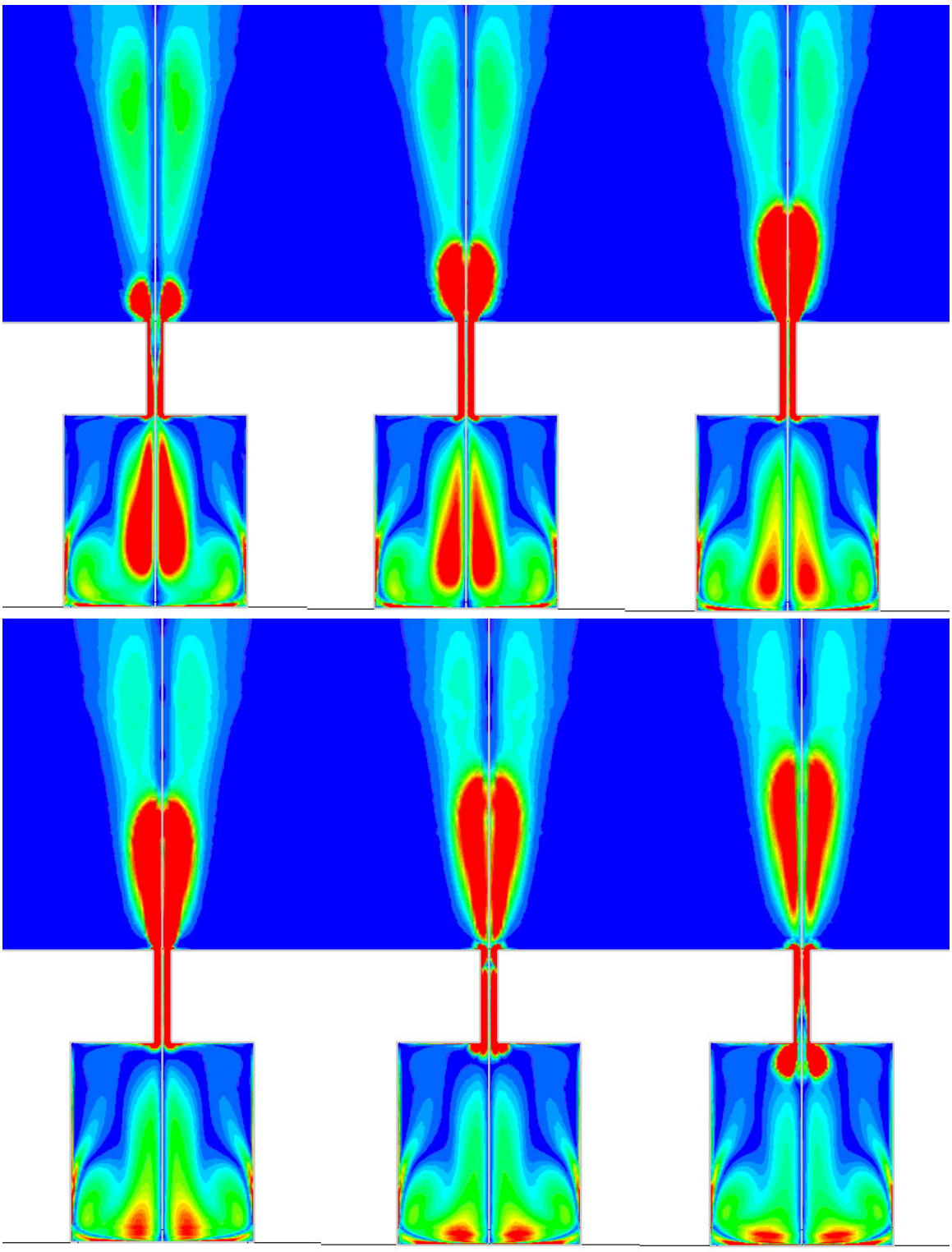

Figure 3.17: Vortex dynamics of a synthetic jet with $h_c/d_c = 1$, $L_{stroke}/d_j = 16.6$

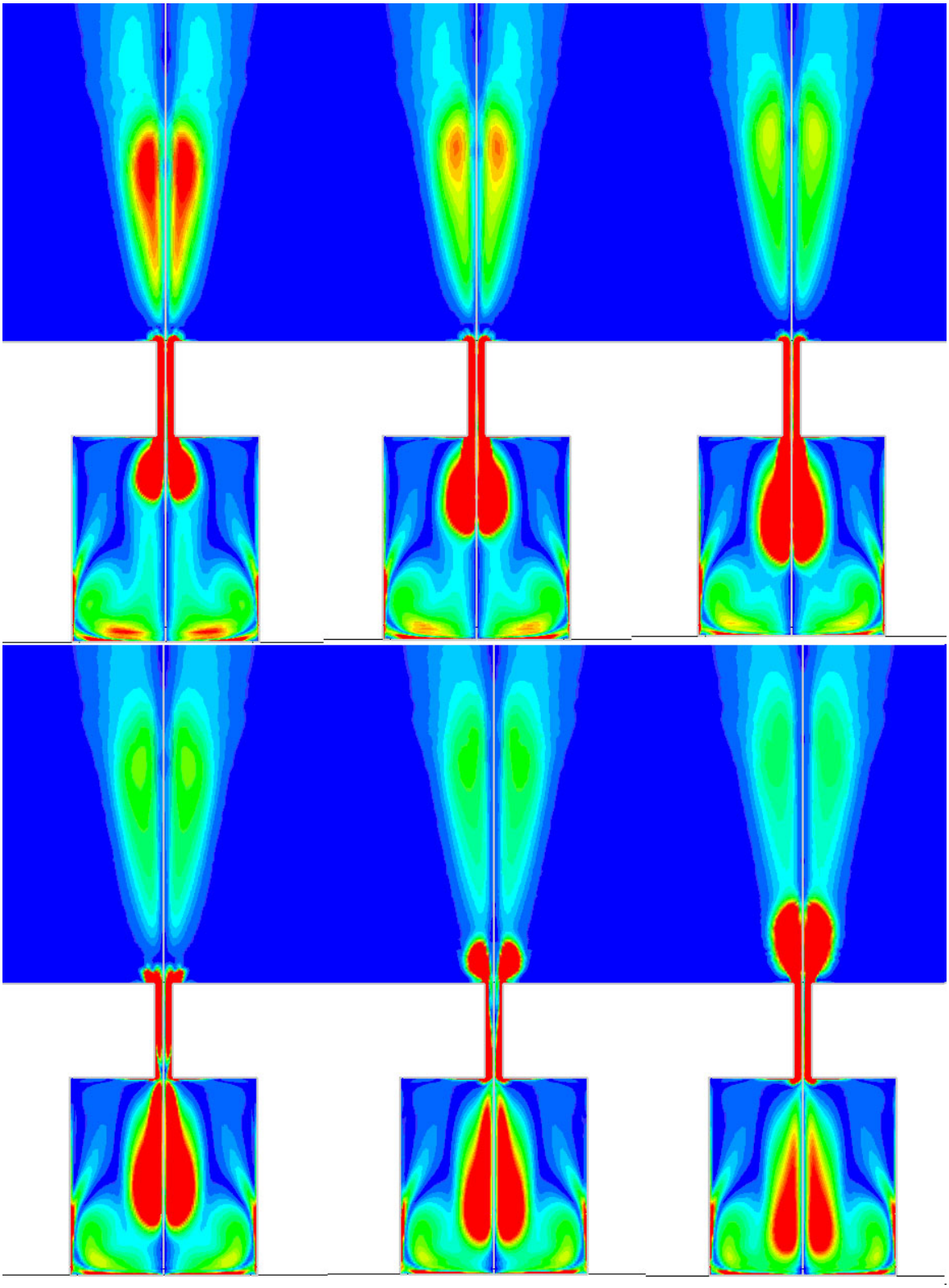

Figure 3.18: Vortex dynamics of a synthetic jet with $h_c/d_c = 1$, $L_{stroke}/d_j = 16.6$ (continued)

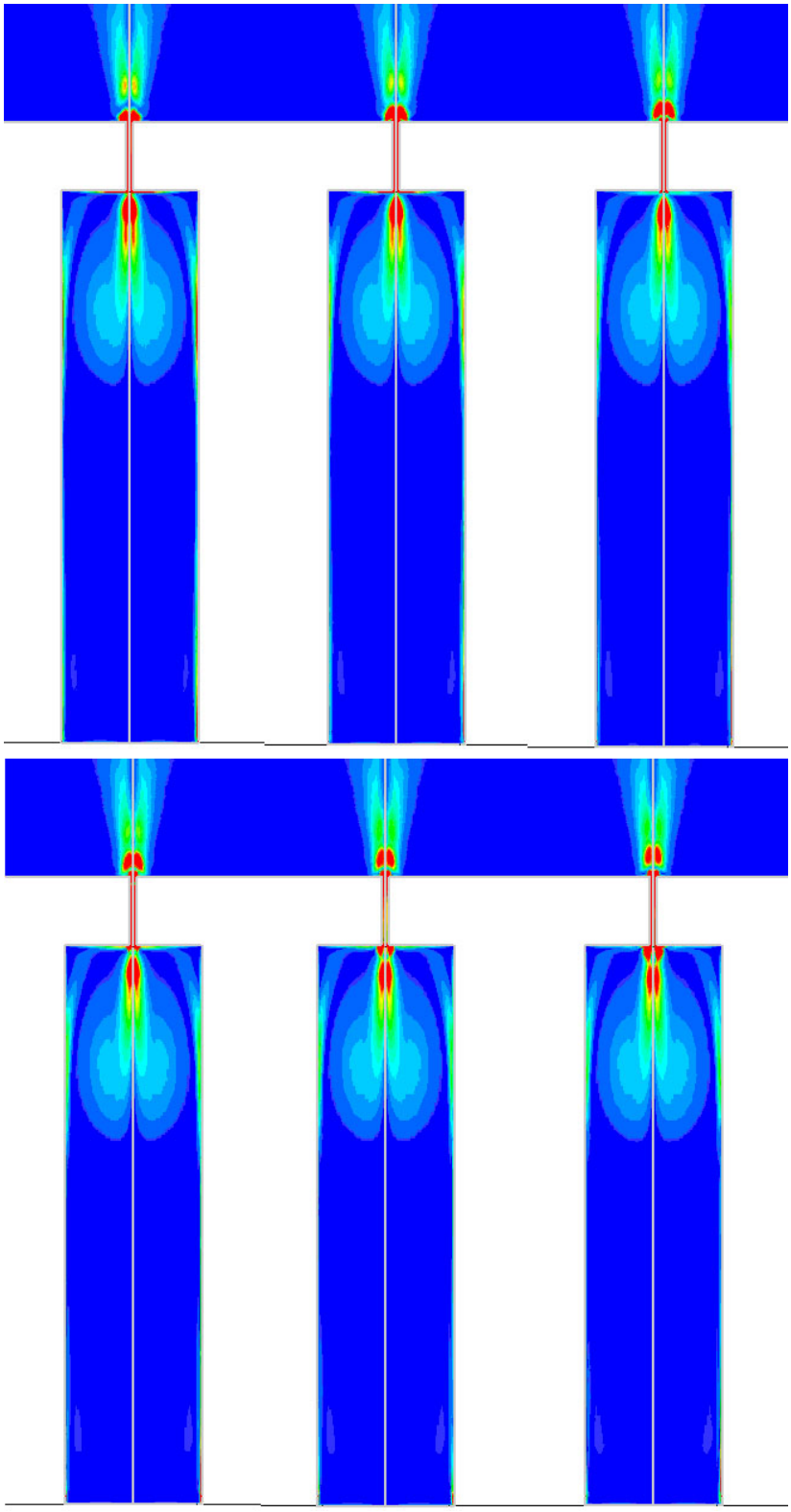

Figure 3.19: Vortex dynamics of a synthetic jet with $h_c/d_c = 4$, f=1 kHz, d_j=0.5 mm

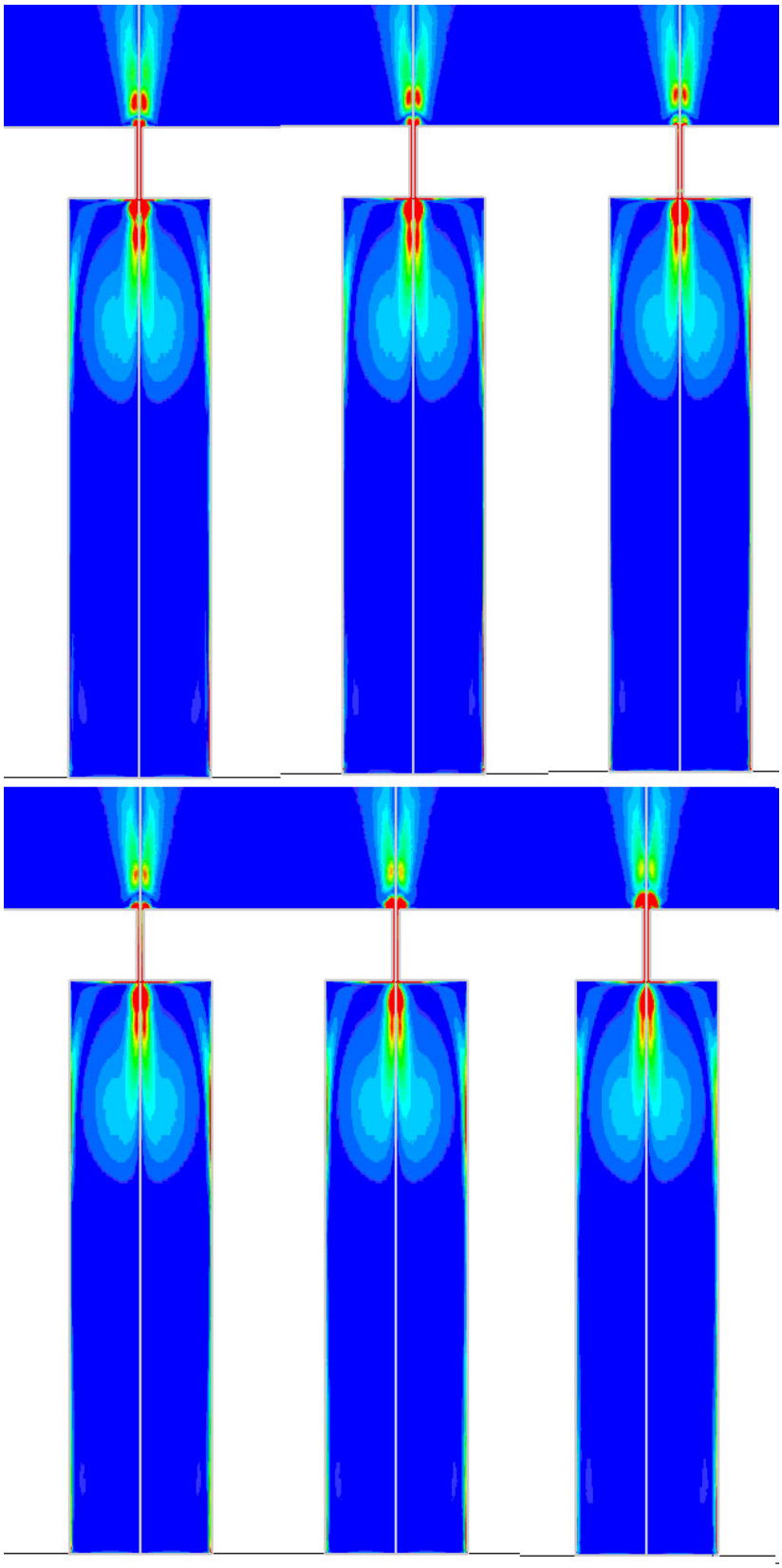

Figure 3.20: Vortex dynamics of a synthetic jet with $h_c/d_c = 4$, f=1 kHz, d_j=0.5 mm (continued)

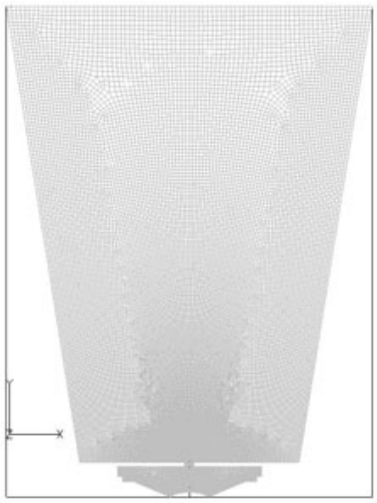

Figure 3.21: Computational domain of free speaker

2. When the diaphragm reached its largest displacement, the vortex pair reached its maximum strength too. The high vorticity region vanished because of dissipation.

3. As the diaphragm started to move upwards, the strength of the vortex in the cavity began to be reduced. At the same time, from the nozzle/orifice edge, a new vortex pair was generated.

4. As the diaphragm moved back to its largest upward displacement, the vortex pair detached from the nozzle/orifice edge. Three vortex pairs could be observed simultaneously.

In the above, we examined the vortex dynamics of different cavity geometry configurations and working frequencies. All of these parameters affect the non-dimensional stroke length L_{stroke}/d_j and Re of the synthetic jet. When L_{stroke}/d_j is smaller than some critical value, the vortex pair formed at the edge of the nozzle/orifice cannot detach, and so no jet is synthesized. Once L_{stroke}/d_j is larger than this critical value, the vortex pair moves downstream and dissipates. If L_{stroke}/d_j is relatively small, then the distance the vortex pair travels before it dissipates is also relatively small.

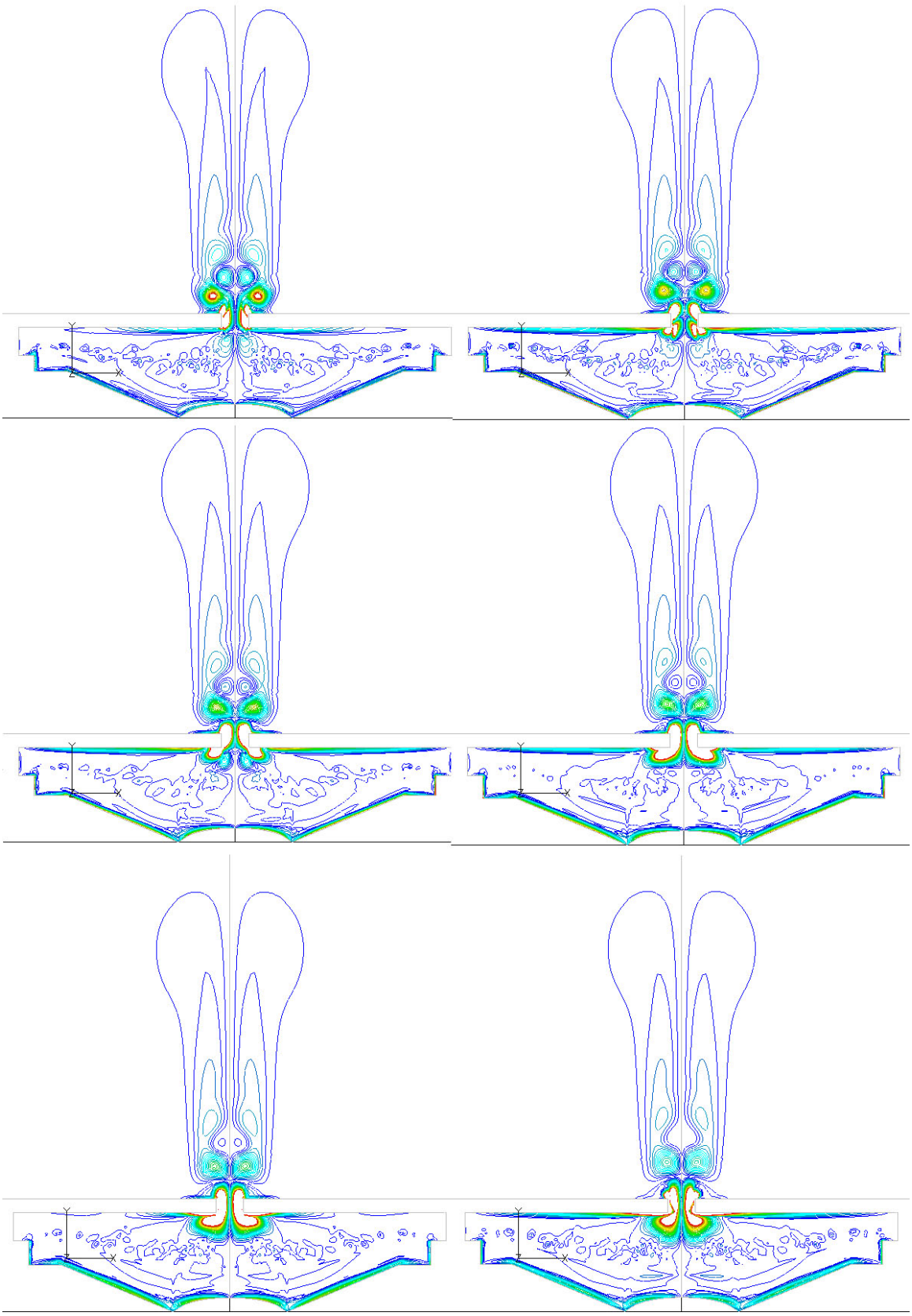

Figure 3.22: Vortex dynamics of speak shaped cavity (f=80, $A_m = 1$ mm, $d_j = 6.35$ mm)

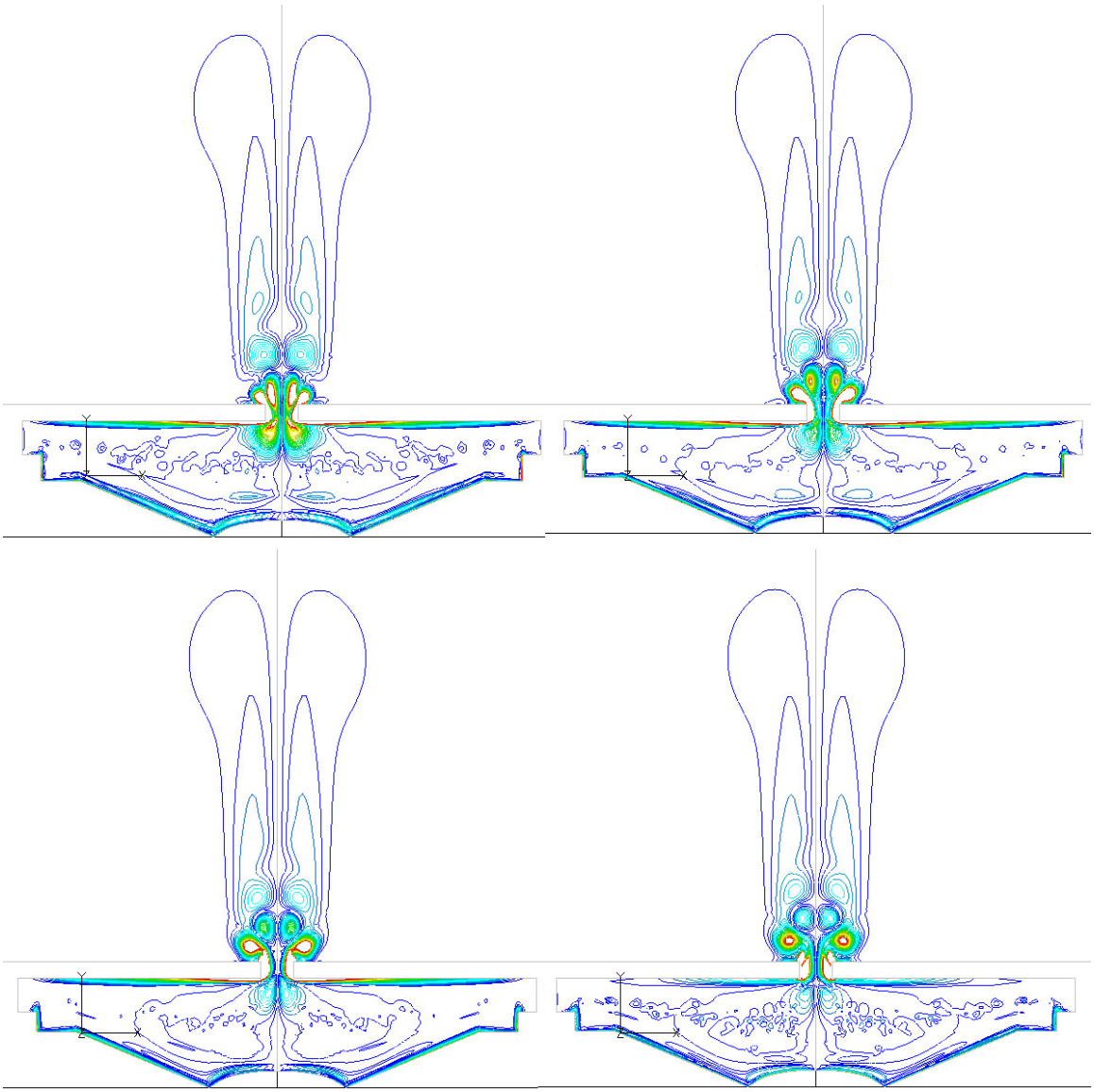

Figure 3.23: Vortex dynamics of speak shaped cavity (f=80, A_m = 1 mm, d_j = 6.35 mm) (continued)

3.4 Free jet characteristics

To characterize the synthetic jet, parameters representing the time dependent characteristics of a synthetic jet are required. Smith and Glezer (1997) [53] suggested the non-dimensional stroke length L_{stroke}/d_j and Reynolds number based on the downstream-directed momentum Re_{I_o} (Equation 2.22).

The time-mean velocity fields of synthetic jets are quite different from those of conventional jets. At the nozzle/orifice exit or in some region very close to the nozzle/orifice exit, the time-mean streamwise velocity is zero. This reflects the unique zero-mass-flux characteristic of a synthetic jet. However, this time-mean no-flux line is not necessarily exactly at the nozzle/orifice exit. This is one of the reasons for the poor near-field predictions of those simulations using a time dependent boundary condition at the nozzle/orifice exit. The time-mean velocity fields of synthetic jet flows with $L_{stroke}/d_j = 5.73$ and $L_{stroke}/d_j = 121.6$ are shown in the figures 3.26 $\sim$ 3.29. For the $L_{stroke}/d_j = 121.6$ case, the nozzle exit edge was rounded to avoid the sharp right angle because of the small nozzle diameter (100 μm).

From the time-mean velocity fields, shown in figures 3.24 $\sim$ 3.29, we see that the development of a synthetic jet flow is similar over a wide range of L_{stroke}/d_j and Re_{I_o}. Therefore it's helpful to analyze the typical characteristics of a synthetic jet flow. A synthetic jet with a 0.5 mm diameter nozzle, and with moderate values of $L_{stroke}/d_j = 8.9$ and $Re_{I_o} = 842$,

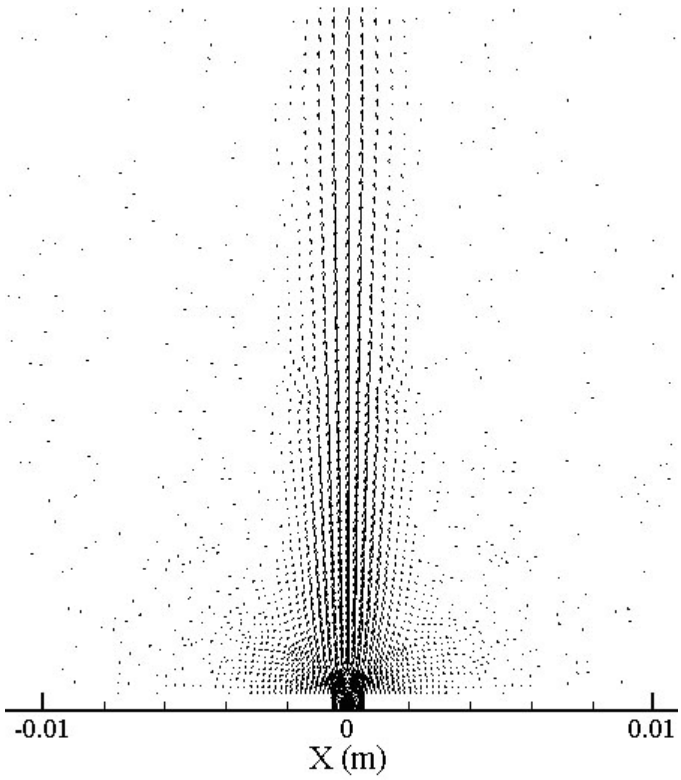

Figure 3.24: Time mean velocity field of synthetic jet with L_{Stroke}/d_j =1.2 and Re_{I_o}=213

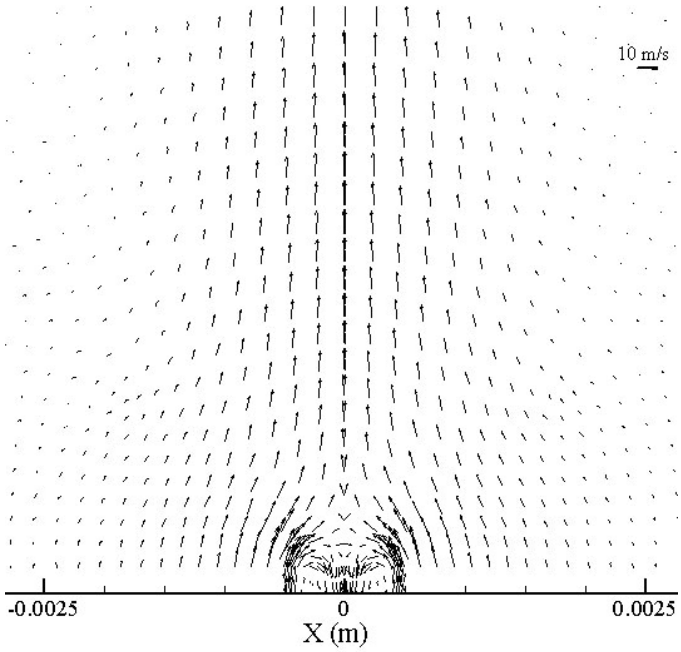

Figure 3.25: Time mean velocity field of synthetic jet with L_{Stroke}/d_j =1.2 and Re_{I_o}=213 (enlarged)

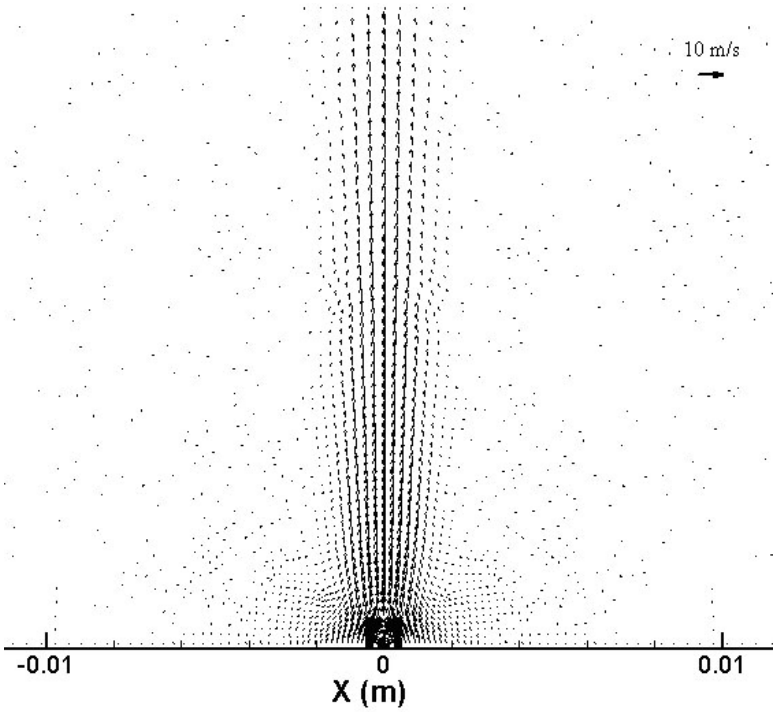

Figure 3.26: Time mean velocity field, L_{stroke}/d_j =5.73 and Re_{I_o}=5275

operating at 250 Hz is used for this purpose. The flow characteristics are expected to be typical.

First, the time mean characteristics are analyzed. Figures 3.30 to 3.33 show the time-mean and instantaneous pressure and velocity along the centerline. The pressure and streamwise velocity in the nozzle were almost linear. It is worth noting that there were two significant slope change at the entrance and exit of the nozzle.

The instantaneous pressure distribution along the centerline showed the same characteristics. The largest pressure difference was in the nozzle. The centerline pressure in the cavity ($y/d_j < -10$), stayed relatively constant. The pressure difference between $y/d_j = -11$ to $y/d_j = 1$ (one nozzle diameter on each side of nozzle) was over 85% of the total pressure difference from diaphragm to ambient. The pressure along the nozzle cross section was almost uniform.

The time-mean centerline velocity shown in Figure 3.32 was nearly zero. At the nozzle exit, the velocity increased to its maximum in a short distance and then dropped. The instantaneous centerline velocity, figure 3.33, showed similar trends.

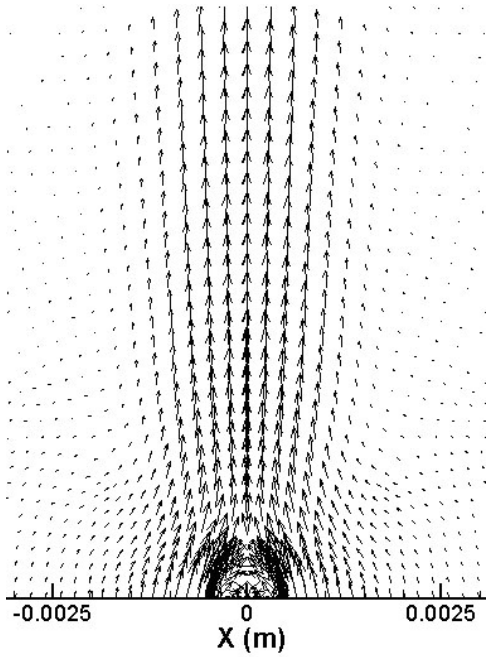

Figure 3.27: Time mean velocity field, L_{stroke}/d_j =5.73 and Re_{I_o}=5275 (enlarged)

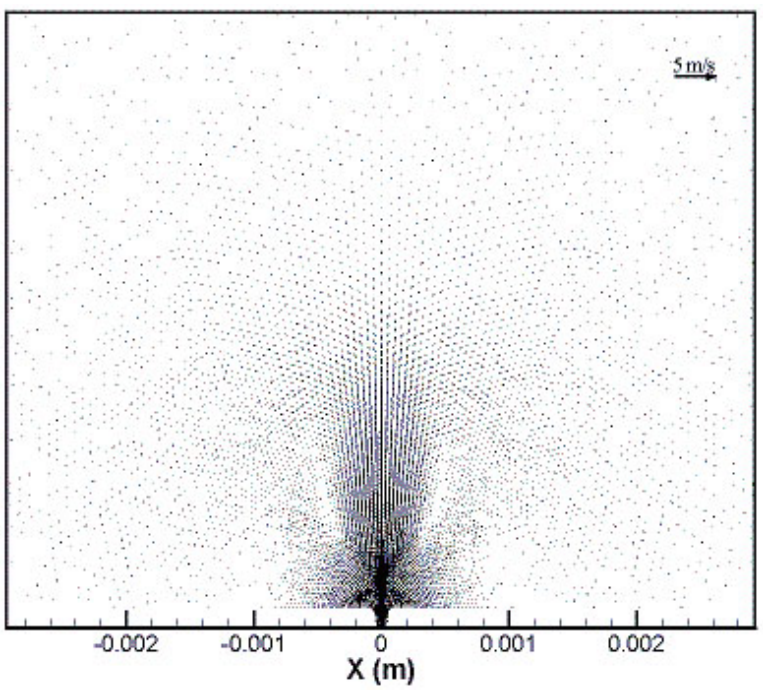

Figure 3.28: Time mean velocity field, L_{stroke}/d_j =121.6 and Re_{I_o}=5861

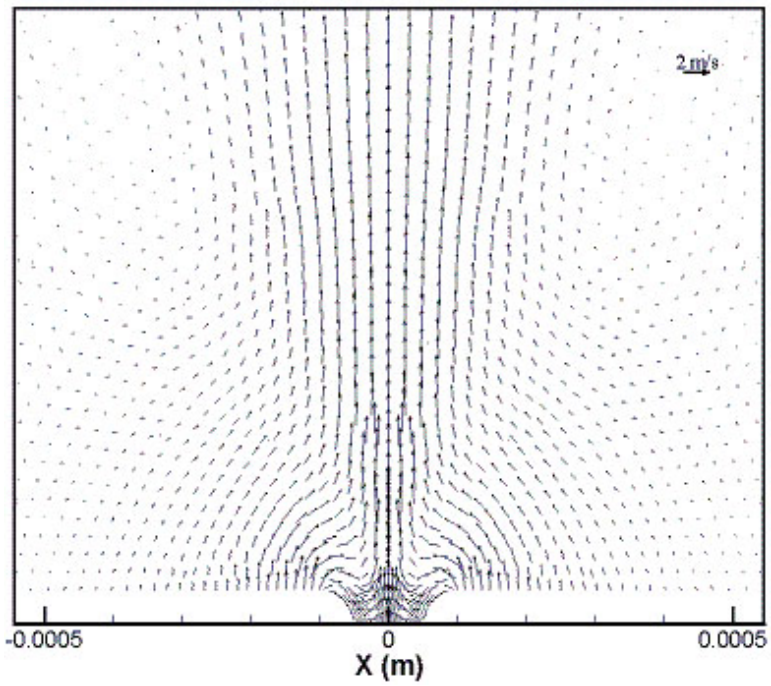

Figure 3.29: Time mean velocity field, L_{stroke}/d_j =121.6 and Re_{I_o}=5861 (enlarged)

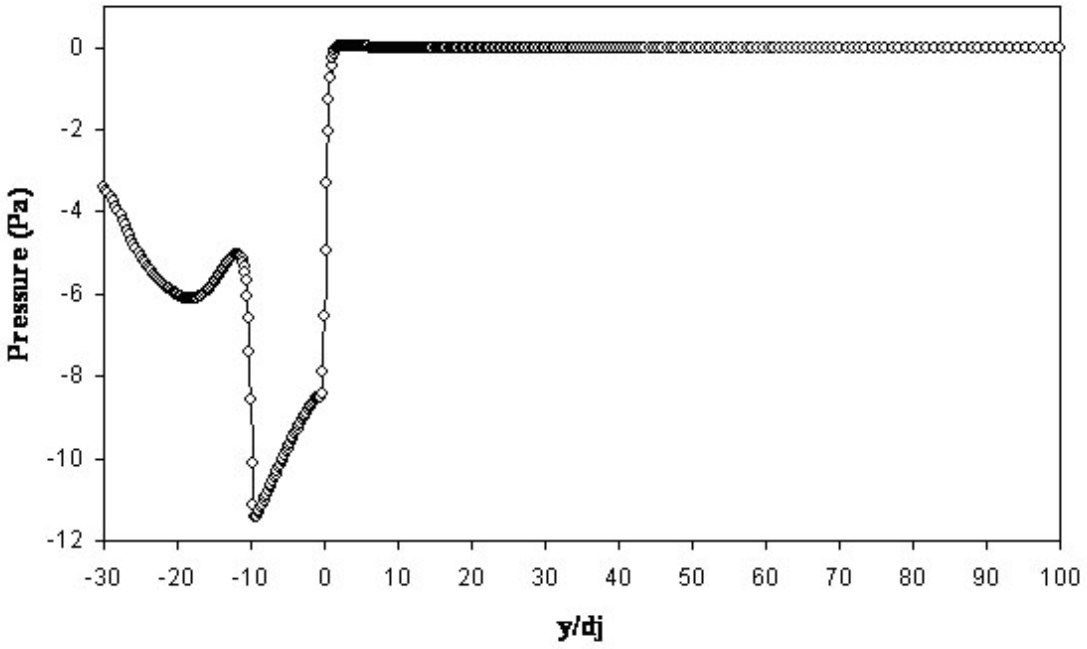

Figure 3.30: Time mean pressure distribution along the centerline

The streamwise velocity profiles at a cross-section located at the middle of the nozzle are shown in figure 3.34. This is similar to the velocity profile of an oscillating, pressure-driven pipe flow.

In conventional jets, when the potential core vanishes the jet is considered fully developed. In the potential core, the centerline velocity stays constant. So, the jet is considered fully developed when the centerline velocity starts to decay. At this point, the velocity profiles are also self similar. In synthetic jets, there is no potential core and the time-mean centerline velocity actually increases for a short distance past the nozzle exit. However, the velocity profiles show self similarity just like a conventional jet. Analogous to conventional jets, we consider the synthetic jet to be fully developed when the velocity profiles show self similarity. Other researchers have reported that the developing region of a synthetic jet is much shorter than a conventional jet. In this example, the velocity profile begins to show self similarity from $y/d_j = 12$ (Figure 3.36). However they are not well matched until y/d_j is larger than 20. Therefore, we conclude that this synthetic jet flow is self-similar and fully

developed at around $y/d_j = 20$.

The jet half-width b_j of a synthetic jet changes with distance from the nozzle exit as shown in Figure 3.37. As the distance increases, the jet half-width becomes more linearly related to y/b_j. A synthetic jet flow can be divided into several regions according to its velocity and vortex dynamics characteristics:

1. $y/d_j < (y/d_j)_{peak\_velocity}$, in this region the flow is dominated by the evolution of vortex pairs. The time mean centerline velocity increases from almost 0 to its maximal value;

2. $(y/d_j)_{peak\_velocity} < y/d_j < (y/d_j)_{self\_simlarity}$, this is the developing region of the synthetic jet. The jet entrains a large amount of surrounding fluid so the jet width grows significantly. The velocity begins to show self similarity from $y/d_j \sim 12$ for this case;

3. $y/d_j > (y/d_j)_{self\_simlarity}$, the synthetic jet is fully developed, jet half-width changes

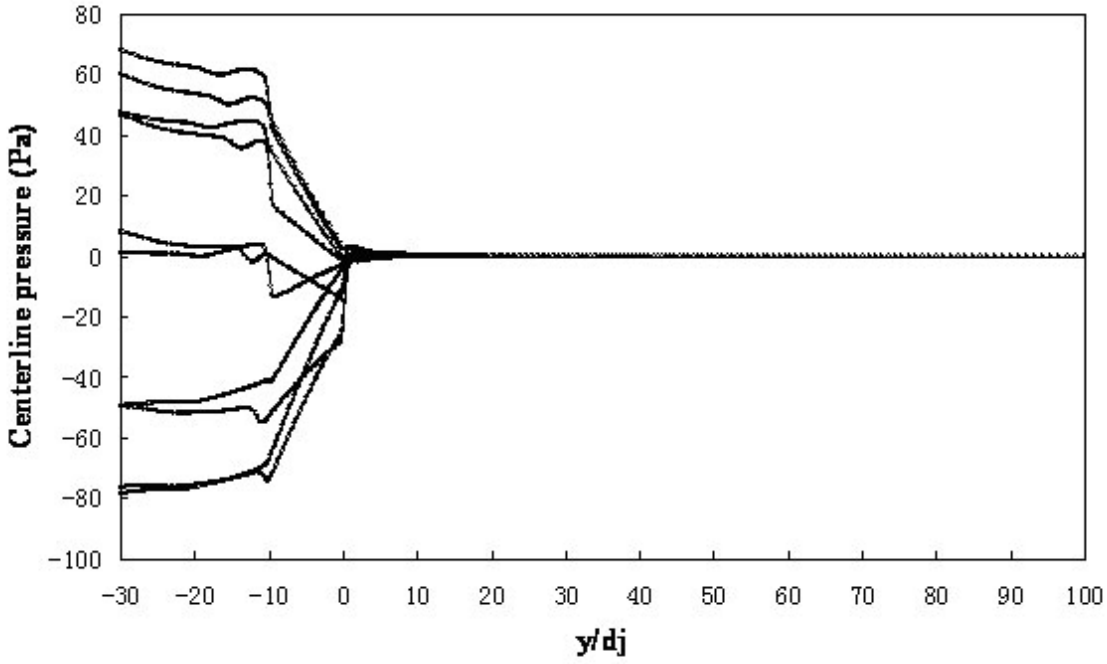

Figure 3.31: Instantaneous pressure distribution along the centerline

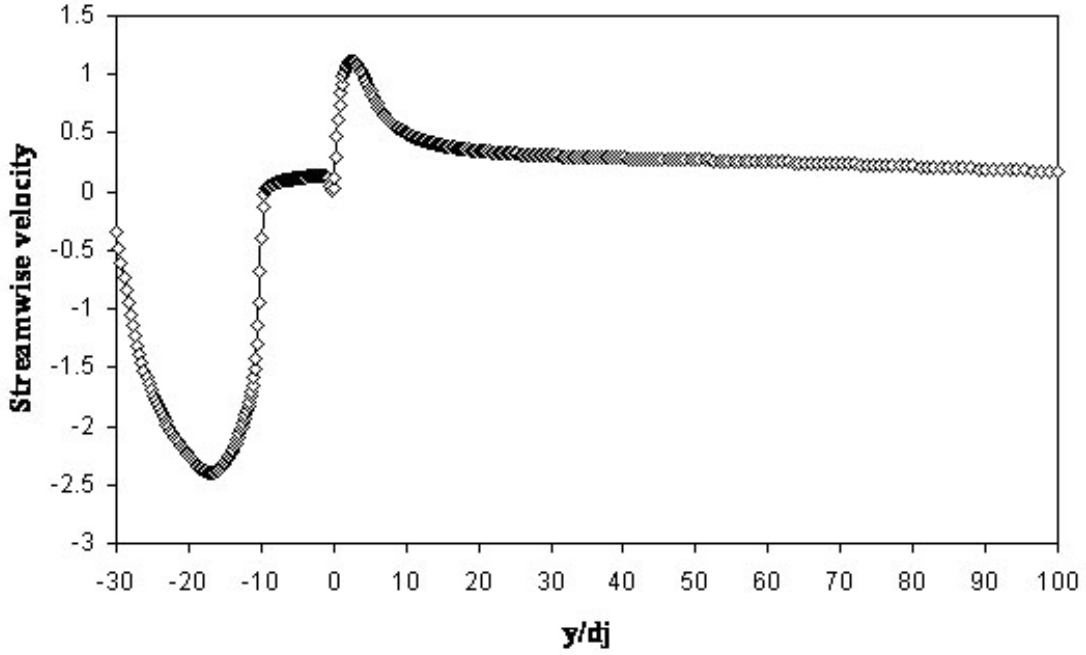

Figure 3.32: Time mean streamwise velocity along the centerline

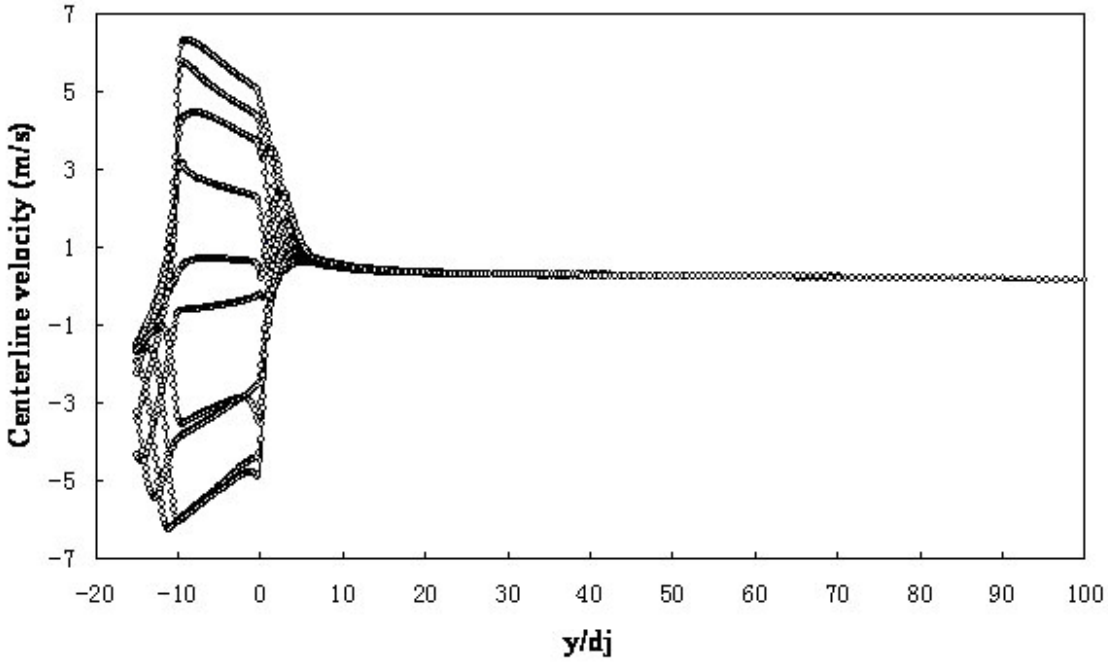

Figure 3.33: Instantaneous streamwise velocity along the centerline

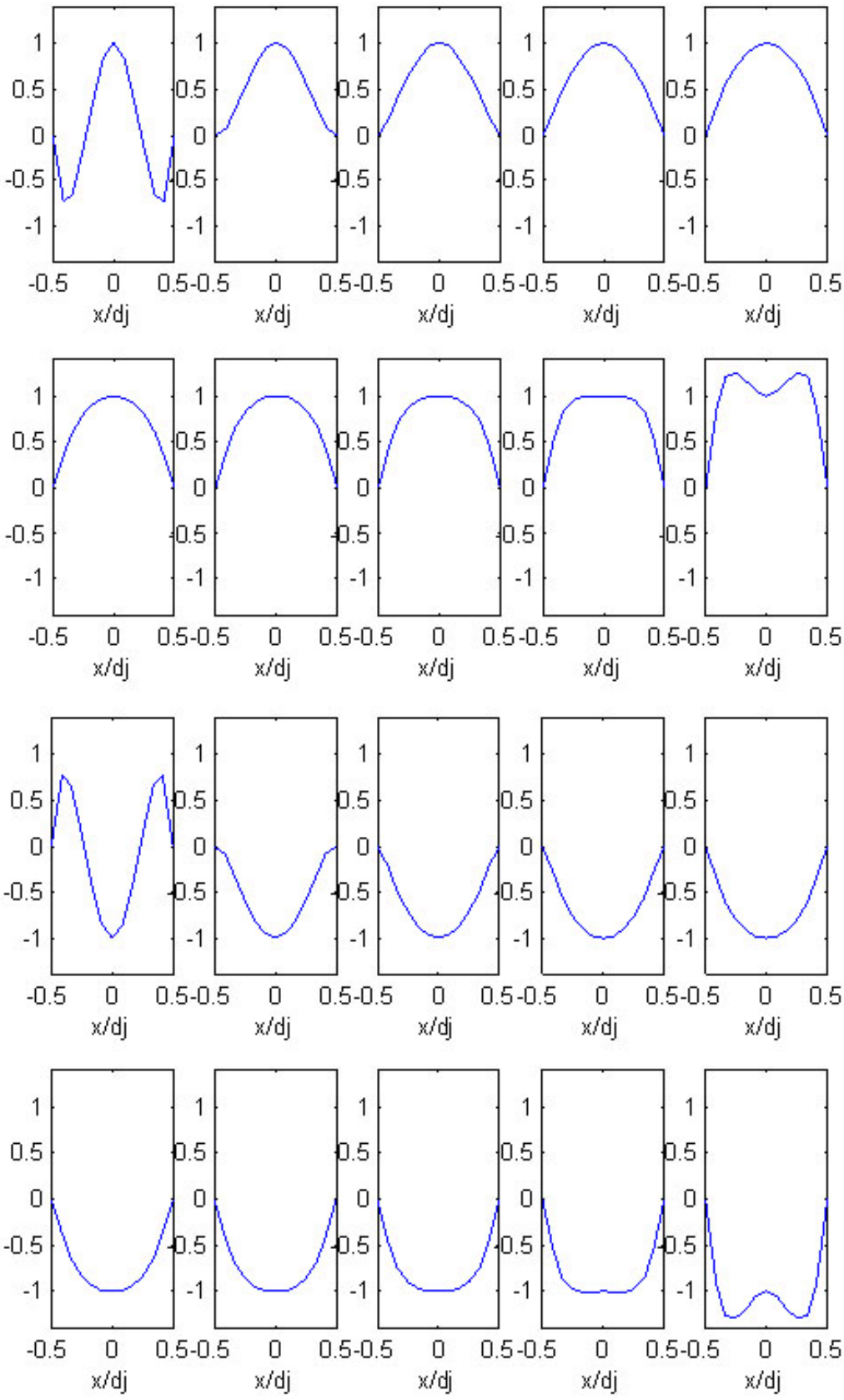

Figure 3.34: Middle nozzle streamwise velocity profile

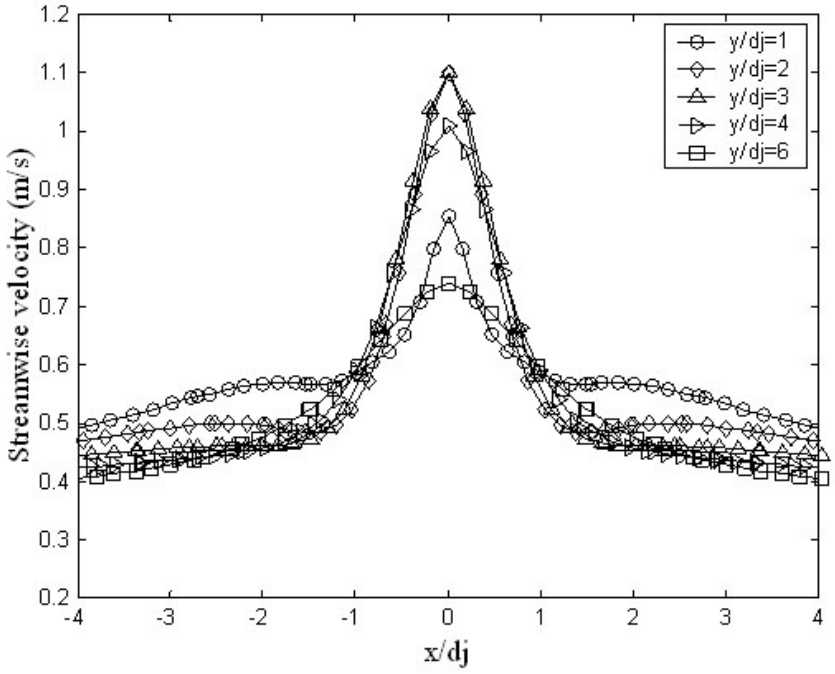

Figure 3.35: Streamwise velocity profile near nozzle exit

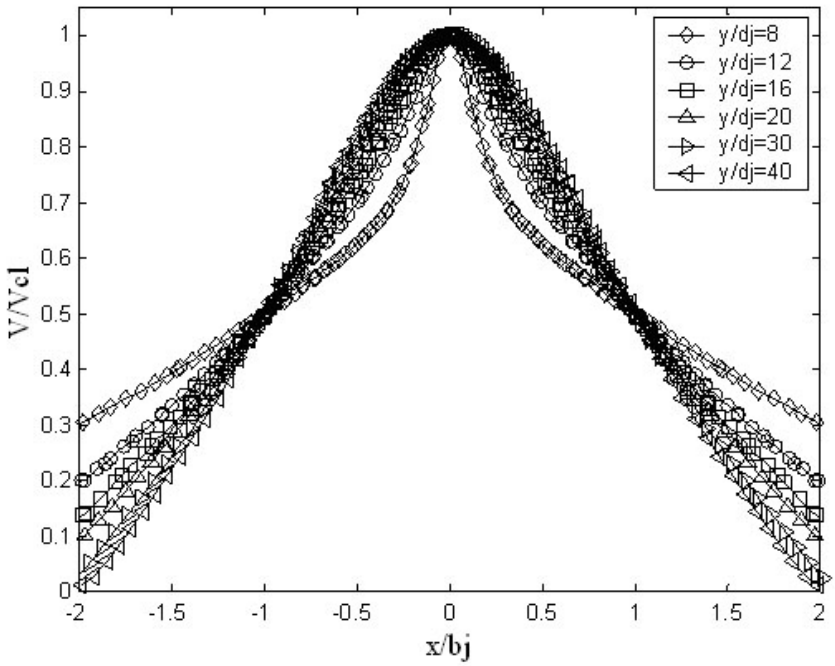

Figure 3.36: Normalized streamwise velocity profile versus downstream distance

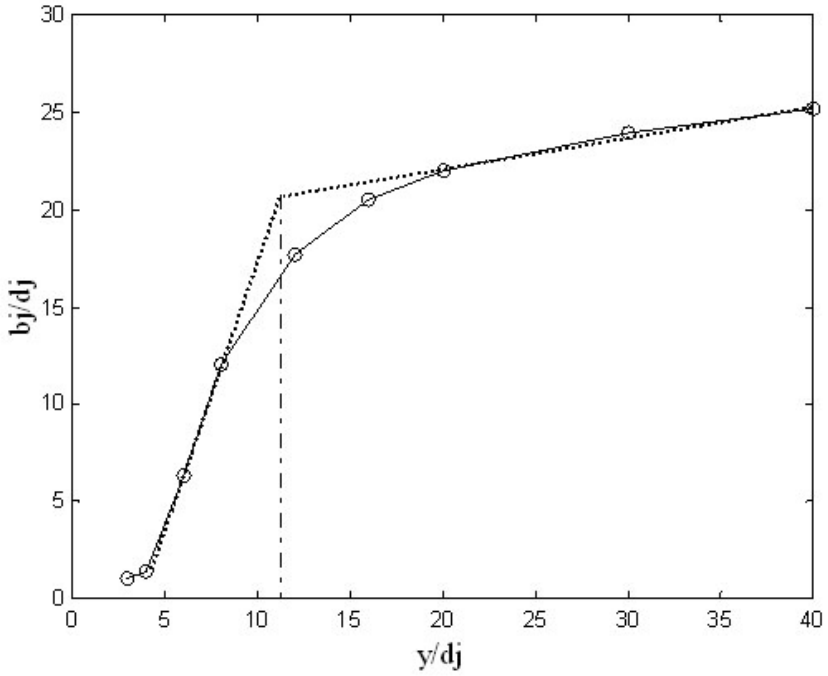

Figure 3.37: Jet half-width with downstream distance

linearly with the distance from nozzle.

For a large non-dimensional stroke length L_{stroke}/d_j case, the above observations are valid too. A synthetic jet with $L_{stroke}/d_j = 122$, $Re_{I_o} = 5861$, working frequency 250 Hz, d_j=100 μm are shown in figure 3.38 to 3.40. The centerline velocity reached a maximum at $y/d_j = 2.2$. The streamwise velocity profiles showed self similarity from $y/d_j = 20$. The time mean centerline velocity decayed to around 5% of its maximum value at $y/d_j = 40$, which means that a free synthetic jet could penetrate over 40 nozzle diameters into the ambient.

3.5 Developing Region

Some researchers have mentioned that the developing region of a synthetic jet is shorter than a conventional jet. To the author's knowledge, however, there is no detailed discussion on this issue. The length of the developing region is important in micro-system applications where the distance between the jet exit and the target surface is either small or strongly

affects the performance of the system.

In this study, parameters that affect the development length of the synthetic jet were varied, including working frequency, non dimensional stroke length, and the blowing stroke half-cycle average velocity.

Two series of simulations were conducted. On the first set, the geometry was h_c/d_c=1, $l_j/d_j = 5$, and $d_j = 1mm$. The working frequencies were: 160Hz, 500Hz and 1000Hz. The second set had $h_c/d_c = 0.5$, $l_j/d_j = 10$, and $d_j = 0.5$ mm, and the working frequencies were 250Hz, and 500Hz.

With a low working frequency (160Hz, Figure 3.41), the synthetic jet ($d_j = 1mm$) flow shows self similarity from $x/d_j = 4$ just like the case working at high frequency (1000Hz, Figure 3.43). The normalized velocity profiles of the synthetic jet working at 500Hz are shown in Figure 3.42. The non dimensional stroke lengths for these three cases are 63.2, 16.6 and 36.1 respectively. The stroke half cycle average velocities for these three cases are 20.2 m/s, 33.2 m/s and 36.1 m/s respectively. For all these cases, the normalized velocity

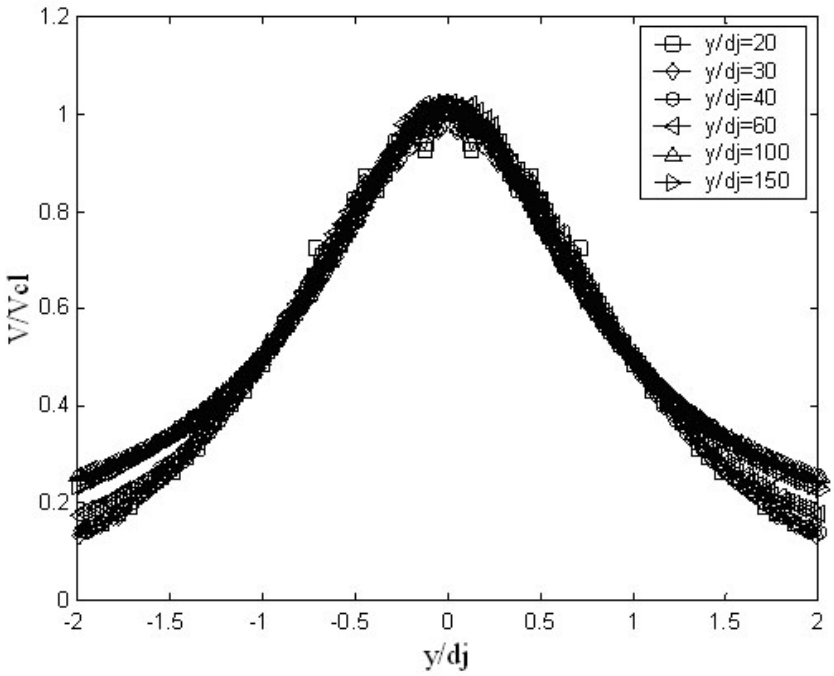

Figure 3.38: Normalized velocity profile of a synthetic jet ($d_j = 0.1$ mm $f = 250$ Hz)

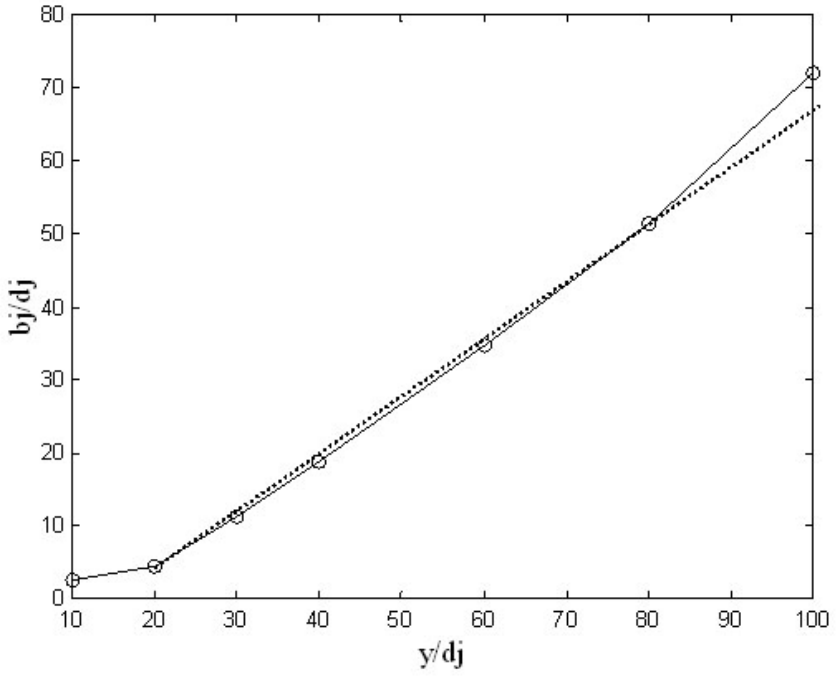

Figure 3.39: Jet half-width with downstream distance of a synthetic jet (d_j = 0.1 mm f = 250 Hz)

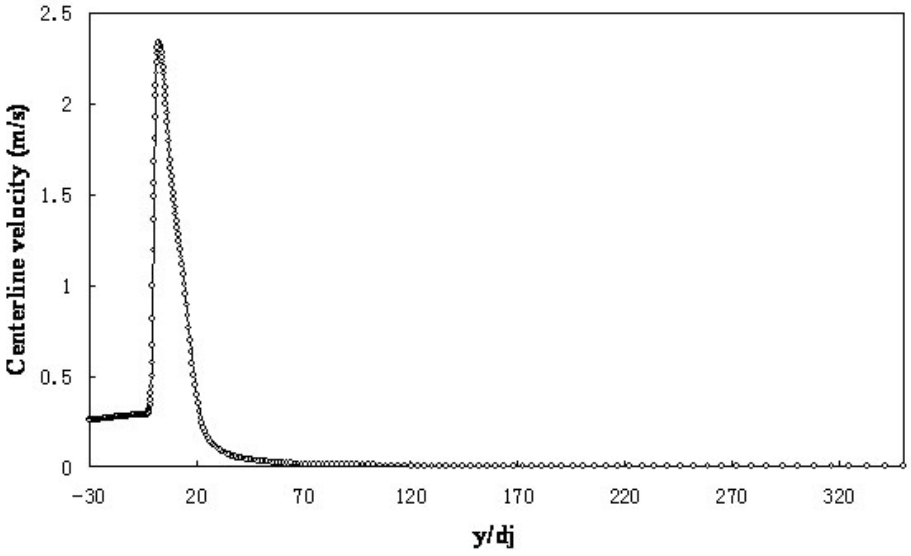

Figure 3.40: Time-mean centerline velocity of a synthetic jet (d_j = 0.1 mm f = 250 Hz)

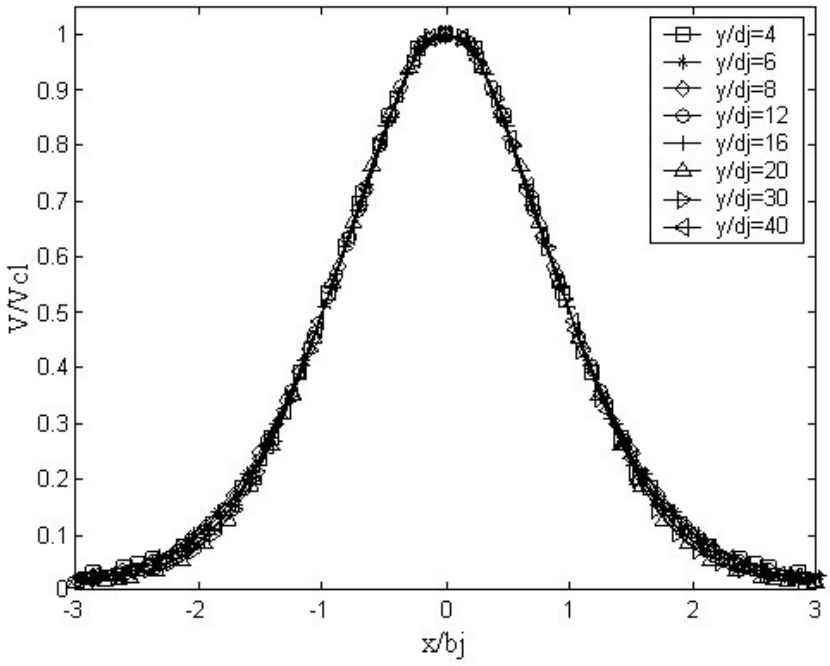

Figure 3.41: Velocity profile of a synthetic jet working at 160 Hz, $d_j = 1mm$

profiles show self similarity as close as $y/d_j = 4$ to the nozzle exit. Therefore, it is not the frequency that determines the length of the developing region.

For synthetic jets with $d_j = 0.5$ mm, a smaller cavity volume change rate ($\Delta V/V$) was used so that the non-dimensional stroke length and blowing stroke half-cycle average velocity were smaller. Corresponding to the working frequencies of 250 Hz and 500 Hz, the non dimensional stroke lengths were 12 and 13.5. The normalized velocity profiles are shown in the figures 3.44 and 3.45. For the $f = 250$ Hz case, the normalized velocity profiles don't show clear self similarity until around $y/d_j = 20$, so only normalized velocity profiles for $y/d_j > 20$ are shown. A working frequency of 1000 Hz case was also analyzed (not shown here), the jet showed self similarity at $y/d_j > 4$. This synthetic jet had a non-dimensional stroke length of 21.1.

We also examined two relatively extreme cases; one with a large non dimensional stroke length and a relatively small stroke half cycle average velocity, and the other with a small non dimensional stroke length and a relatively large stroke half-cycle average velocity. For

the first case, the synthetic jet operated at 80Hz, with a large non-dimensional stroke length of 76. Here, the stroke half cycle average nozzle exit velocity was only 6.1 m/s. The normalized velocity profiles of this synthetic jet flow are shown in Figure 3.46. In this case the normalized velocity profiles showed self-similarity for $y/d_j = 4$. For the second case the synthetic jet operated at 1000Hz, with a non-dimensional stroke length of 13.9. Here, the stroke half-cycle average velocity was 27.8 m/s. The normalized velocity profiles, shown in Figure 3.47, are not self-similar until $y/d_j > 10$.

Both the non-dimensional stroke length and the stroke half-average nozzle exit velocity, play an important role in determining the length of the developing region. With a larger nozzle exit velocity, the synthetic jet flow entrains more ambient fluid, so it needs less distance to reach a fully developed state. In general, a larger stroke half-cycle average velocity is often associated with a larger non dimensional stroke length. However, if the non dimensional stroke length is large enough (~ 16), the synthetic jet flow can become fully developed within four nozzle diameters downstream from the nozzle exit, even if the

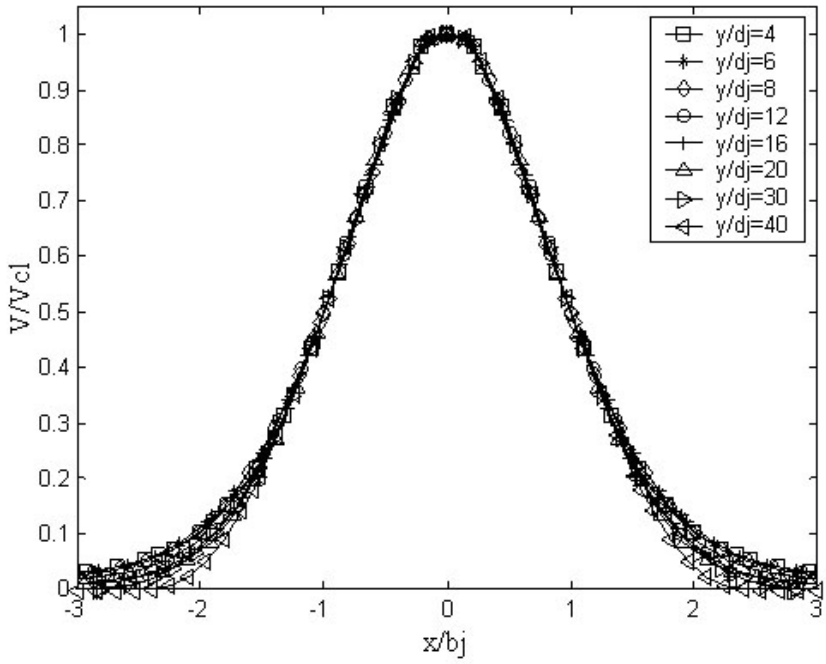

Figure 3.42: Velocity profile of a synthetic jet working at 500 Hz

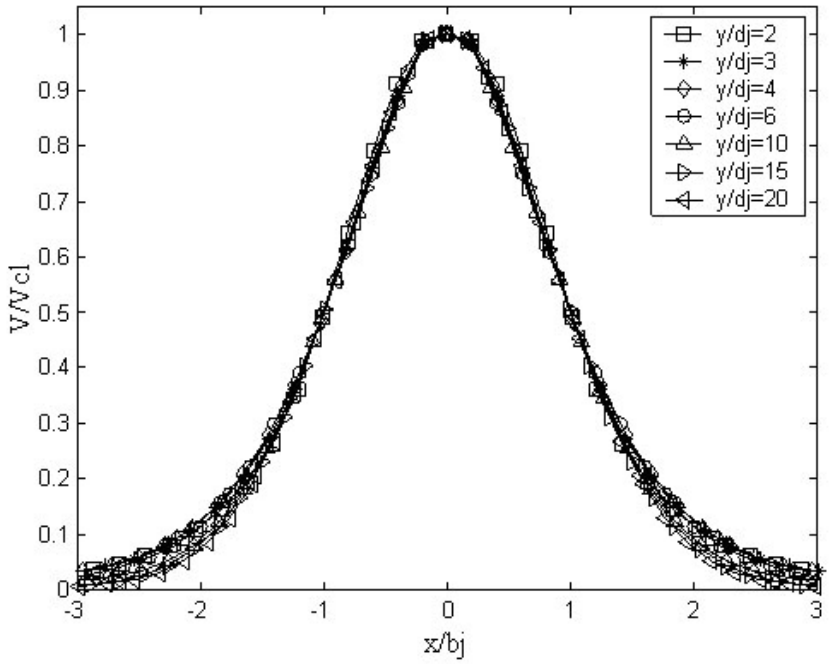

Figure 3.43: Velocity profile of a synthetic jet working at 1000 Hz

nozzle exit velocity is not large. If the non dimensional stroke length is small, and the stroke half cycle average velocity is large, the developing region of the synthetic jet flow is significantly longer (generally larger than 8).

3.6 Fully developed synthetic jet flow

When the synthetic jet flow is fully developed, the normalized velocity profiles show self similarity and the jet half-width grows linearly with the distance to the nozzle exit. Therefore, once this linear relation and the centerline velocity are determined, the synthetic jet flow is determined.

The normalized velocity profiles from the synthetic jet flows in this study are shown in Figures 3.48 to 3.50. These profiles don't change with the working frequency, the nozzle diameter, or the cavity geometry, although when the aspect ratio of the cavity is large, some differences do exist near the edge of the jet. These profiles are compared to the analytical solutions of conventional turbulent symmetrical jets by Goertler and Tollmien in Figure 3.51. The profiles are very close, although when $x/b_j < 1$ the synthetic jet velocity profile is closer

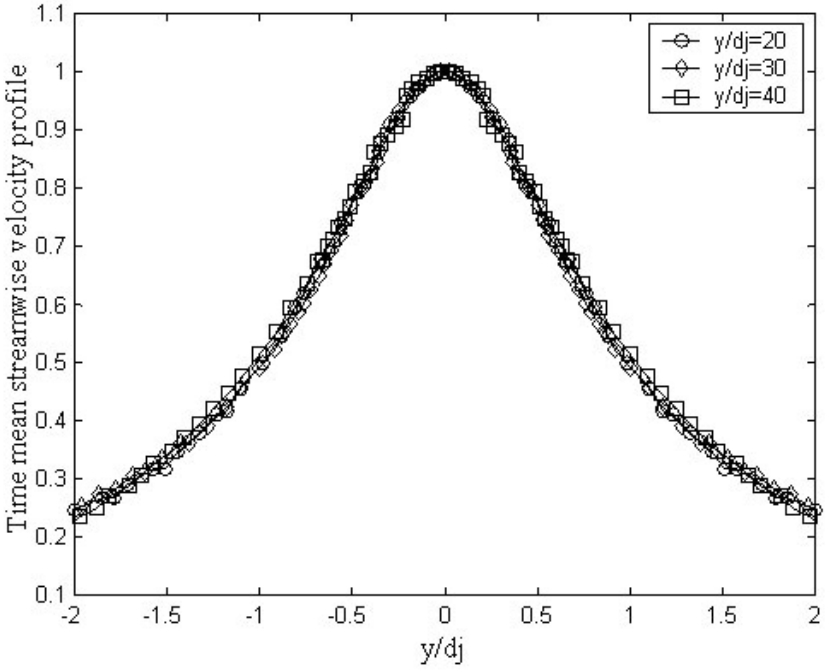

Figure 3.44: Normalized velocity profile $d_j = 0.5$ mm set ($f = 250$ Hz)

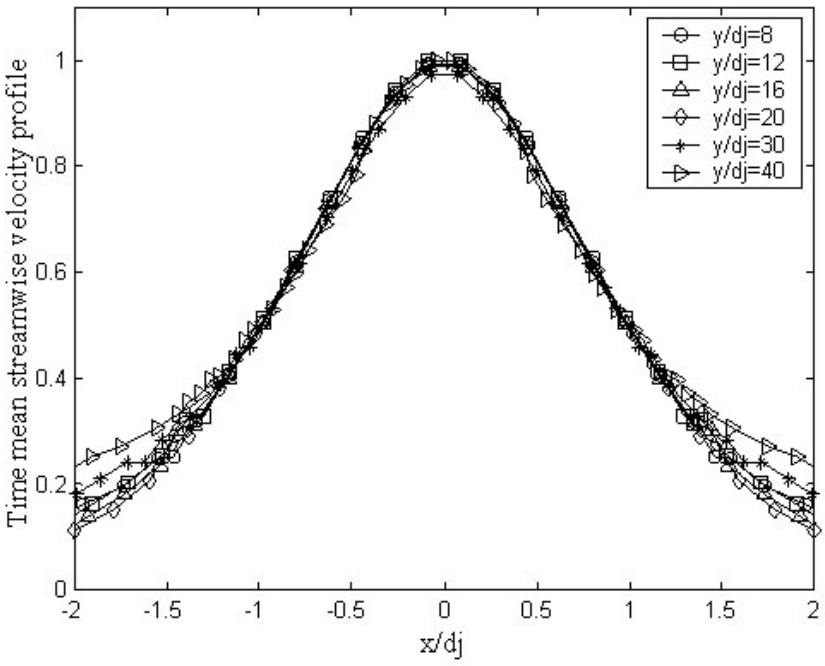

Figure 3.45: Normalized velocity profile $d_j = 0.5$ mm set ($f = 500$ Hz)

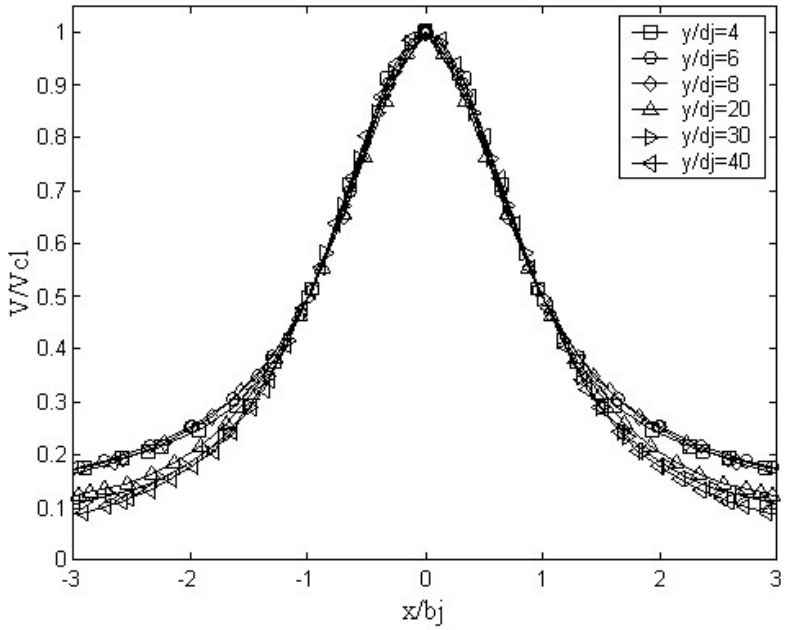

Figure 3.46: Normalized velocity profile ($f = 80$ Hz)

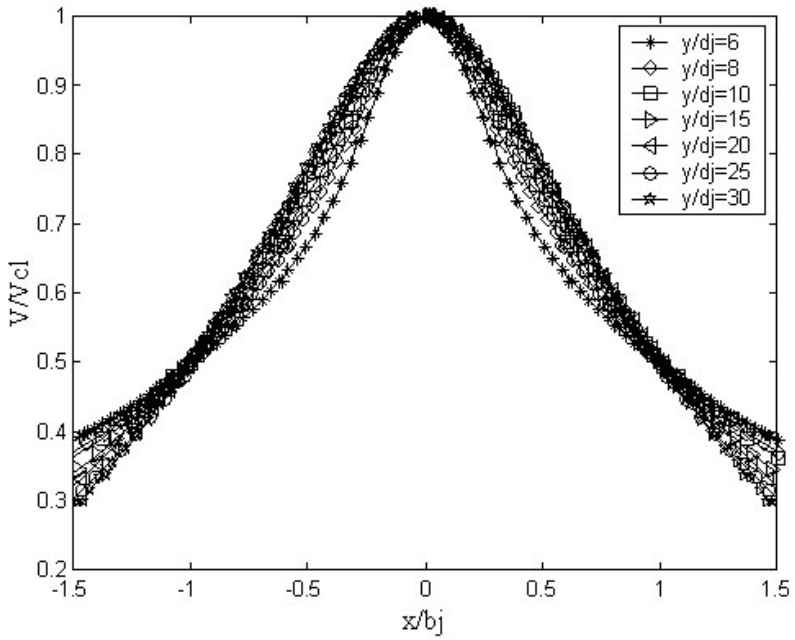

Figure 3.47: Normalized velocity profile ($f = 1000$ Hz)

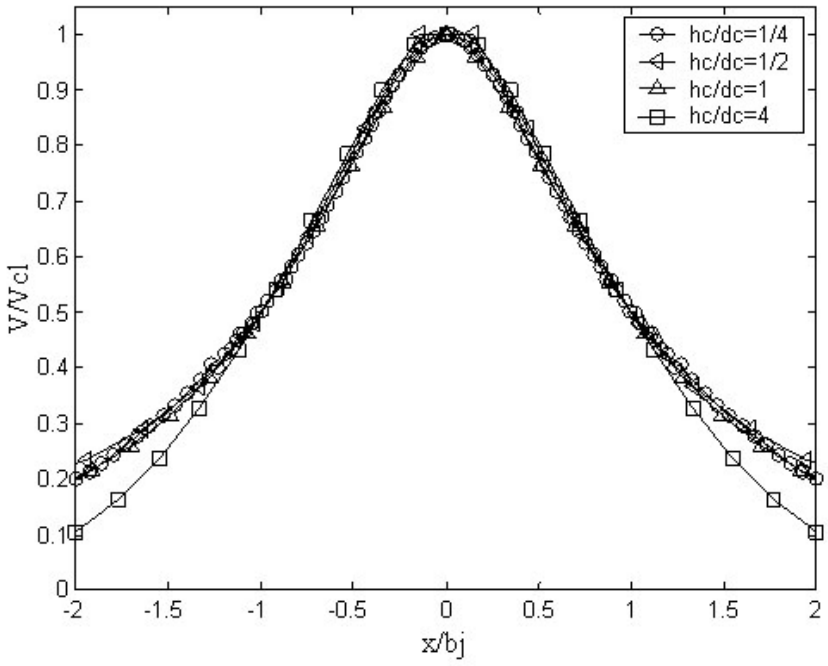

Figure 3.48: Self-similar velocity profiles for the synthetic jet with different cavity aspect ratios

to Goertler's solution, and when $x/b_j > 1$ the velocity profile is closer to Tollmien's. The velocity profile of fully developed turbulent jets show this same characteristic. Therefore in engineering applications, a combination of these two analytical solutions could be used to model the time-mean fully developed synthetic jet flow.

In Figure 3.52, 3.53, and 3.54, we observe that the jet half-width changes linearly with distance from the nozzle exit for synthetic jets working at different frequencies, for different sized nozzle, and for cavities with different aspect ratios. It is interesting that the slopes of these linear relations are very close except for the $h_c/d_c = 1/4$ case. For the cases with the non dimensional stroke length greater than 16, a data fit finds the following relation for the jet half-width.

$$\frac{b_j}{d_j} = 0.1246 \cdot \frac{y}{d_j} + 0.156 \tag{3.1}$$

However, cases with smaller non dimensional stroke length reveal different trends (Figure 3.54).

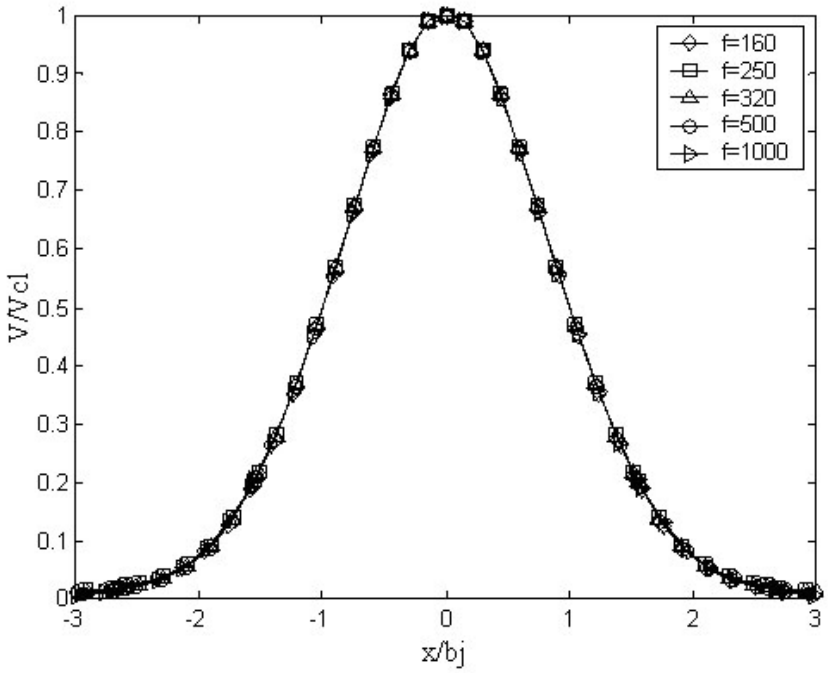

Figure 3.49: Self-similar velocity profiles for the synthetic jet with different working frequencies $d_j = 1$ mm

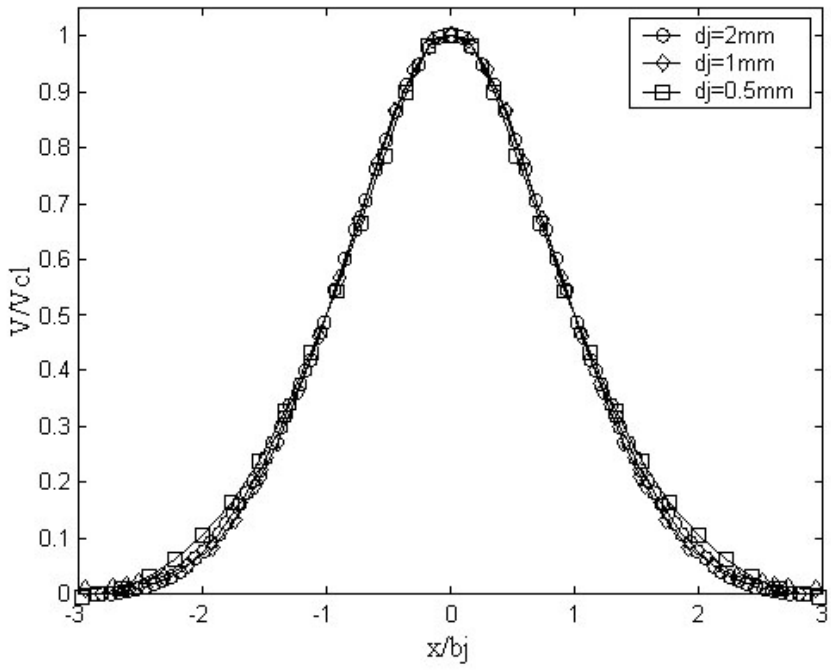

Figure 3.50: Self-similar velocity profiles for the synthetic jet with different nozzle diameters

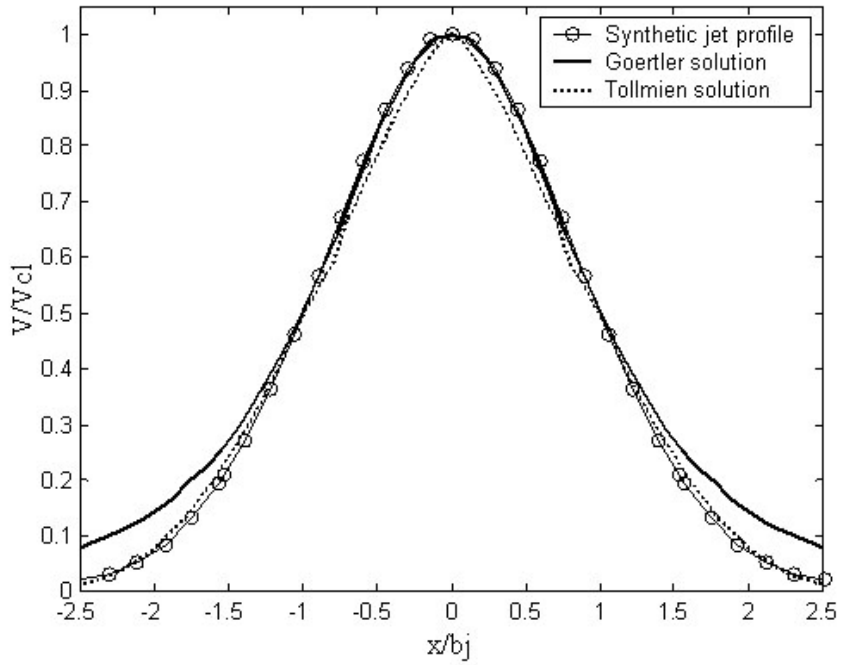

Figure 3.51: Comparison of the fully developed synthetic jet flow velocity profile with the analytical solutions of Goertler and Tollmien

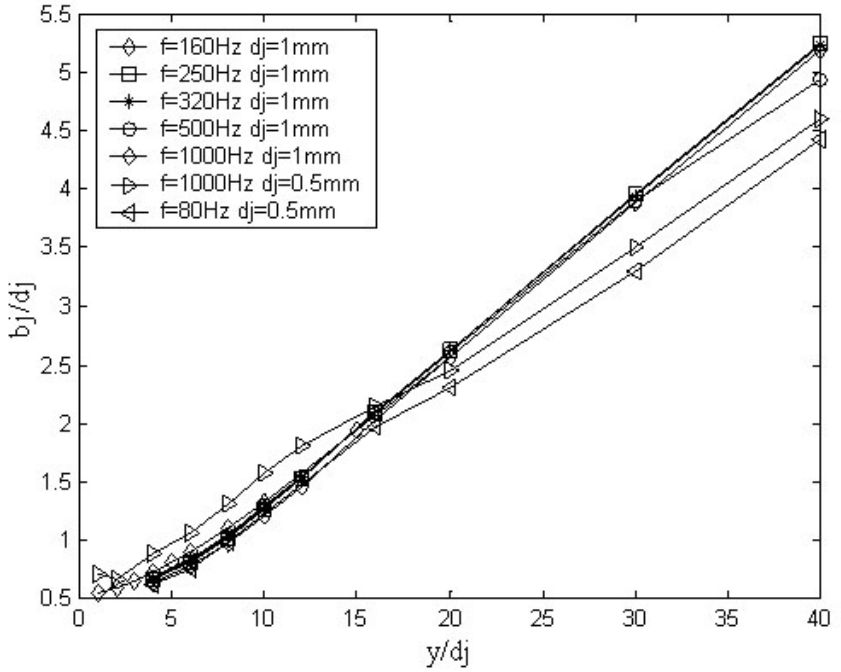

Figure 3.52: Synthetic jet half-width for different working frequencies

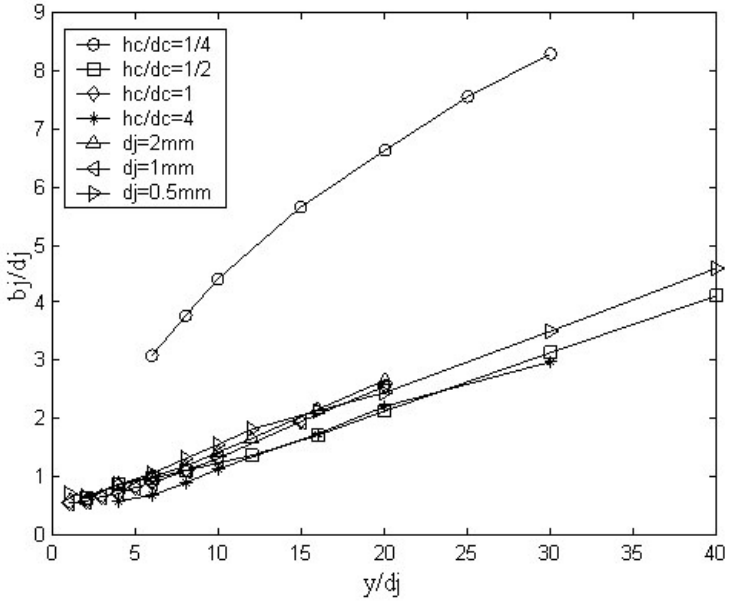

Figure 3.53: Synthetic jet half-width for different nozzle diameter and cavity aspect ratios

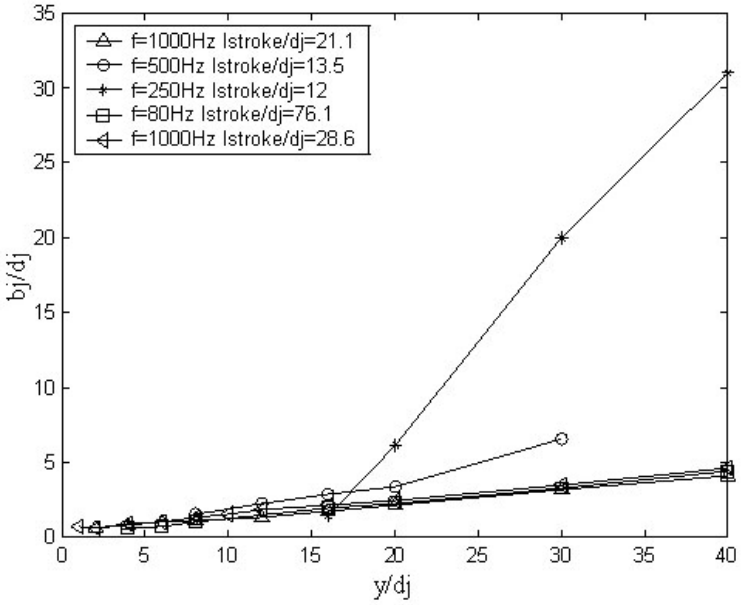

Figure 3.54: Synthetic jet half-width for different non dimensional stroke lengths L_{troke}/d_j

3.7 Summary

A numerical study of free synthetic jet flow was conducted. The synthetic jet cavity was modeled as a rigid chamber with a piston-like moving diaphragm at its bottom. For turbulent synthetic jets, the Shear Stress Transport (SST) $k-\omega$ model was used.

Typical vortex dynamics and flow patterns were identified. The time-mean jet flow characteristics were studied. The effect of working frequency, cavity geometry (mainly aspect ratio), and nozzle geometry (nozzle diameter) on the synthetic jet flow were investigated. The synthetic jet formation criterion was studied based on vortex dynamics. It is suggested that the synthetic jet flow can be divided into three regions, analogous to conventional jets, based on a time-mean velocity field analysis. The developing region was found to be much shorter than conventional jets if the non dimensional stroke length is sufficiently large ($L_{stroke}/d_j > 12$). In the fully developed region, the normalized velocity profile shows self similarity. This profile was found to be close to the analytical solution of conventional axisymmetric turbulent jets. A linear relation between jet half-width and distance from the nozzle exit was found when the non dimensional stroke length is large enough.

CHAPTER IV

MODELING OF SYNTHETIC JET CAVITY

Commercial and home made computational fluid dynamics (CFD) codes have been used to investigate the physics of engineering flows, conduct parametric studies, and evaluate device performance. The solver of these CFD codes often handles hundreds of equations and thousands of iterations, especially when a large number of variables are present. The computational cost is often very large for engineering applications. Extension of a CFD-based procedure to three dimensions to design a wing, for example, usually requires computer resources hundreds of times larger than in two dimensions, which is prohibitive, especially in an advanced design environment. To make the problem more tractable, the designer is often forced to limit the number of design variables, thereby compromising the size of the design space.

Recent advances in computer power allow us to complete large scale CFD simulations. However, in transient problems when the characterizing time of the target system is very small, the required computational cost is still unacceptably high. One example is the simulation of synthetic-jet impingement heat transfer. To fully resolve the time dependent characteristics of a synthetic jet, a time-step size of around $1/30 \sim 1/50$ of one period is required. Even for low frequency cases such as 200Hz, one second of real time CFD simulation requires around 10,000 time steps. In a typical experiment involving heat transfer, the actual time needed from initial state to steady state is about 15 to 20 minutes, which then requires approximately $12\text{x}10^6$ time steps. To complete the simulation for this number of time steps, days, weeks, or even more computational time is needed, even with a relatively coarse mesh. However, in engineering applications, a working frequency of several kHZ and mesh sizes of the order of a million nodes are not uncommon. As we can see, the computational cost is too high to be used effectively and comfortably in engineering works. So some sort of reduced-order models for these problems are not only desirable, but essential.

To numerically simulate synthetic jet flows, we will face even more challenges. A full simulation of a synthetic jet flow typically includes three domains: nozzle/orifice, actuator cavity, and the flow field (open or confined) where the synthetic jet flow evolutes. To simulate the actuator cavity, besides its own computational cost, engineers have to simulate the diaphragm as a moving boundary. As mentioned in Chapter 3, although this task

is currently doable using commercial CFD packages, the techniques implemented in these packages are not mature enough to fully satisfy what CFD engineers desire. The additional computational cost to remesh the grid is only part of the problem. It is quite common that the computer is simply not "smart" enough to generate a satisfying grid once a complex moving boundary is assigned.

In most engineering applications, the flow details in the synthetic jet actuator cavity are generally not of interest. But, resolving this flow field sometimes consumes nearly half of the computational resources.

On the one hand, it is difficult and costly to simulate a full synthetic jet system. On the other hand, flow details in the cavity are not of interest in most engineering applications. As a reasonable solution, researchers have proposed cavity models to replace the actual actuator cavity simulation. However, as reviewed in Chapter 2, current simplified models either perform poorly in the near field region (defined as the region less than 10 times nozzle/orifice diameter from nozzle/orifice exit) or are not easy to implement. In this study, we derived a model which can be easily used with any commercial CFD package or homemade code. This model has been shown to offer very good accuracy if proper parameters are selected.

The model is based on a control volume analysis of cavity. It generates boundary conditions for a CFD simulation of a synthetic jet flow. Because the nozzle geometry is crucial to the synthetic jet flow evolution, we derived this model without including the geometry of the nozzle (only some basic nozzle/orifice size characteristics). The nozzle/orifice geometry is included in the CFD geometry model instead.

As shown in the previous chapter, the vortex dynamics near the nozzle exit is complex. The two-vortex-pair structure of the evolution of a synthetic jet flow is hardly to be reproduced by just assigning a boundary condition at the nozzle exit. Thus, the present model has obvious advantages over those boundary-condition-type models that entirely eliminate the nozzle geometry from the simulation. Generally, the mesh of the nozzle/orifice domain is only a very small portion of the entire mesh, so the improvement in the accuracy of the simulation in the near-field region easily pays for the additional computational cost. In

addition, this model needs very few or even no modification to fit different nozzle designs.

Another feature of this model is that the two key parameters that characterize a synthetic jet flow, non dimensional stroke length L_{stroke}/d_j and stream-wise-momentum-based Reynolds number Re_{I_0}, can be obtained directly from model's output. The results from this model can be directly used, without further numerical simulation, if no flow details are needed.

Besides the commonly used reduced order modeling methods mentioned in Chapter 2, another effective way of improving the efficiency of CFD codes (based on either the Euler equations or the Navier-Stokes equations) is to reduce the overall number of grid points. This can be done by restricting the computational domain to the highly nonlinear region of the flow field and introducing improved boundary conditions on computational boundaries. The intermediate and far-field regions are replaced by an analytic/asymptotic model which provides for a smooth transition (e.g., mathematically correct) across the computational boundary to the true far field conditions of constant pressure, rectilinear flow at infinity. The synthetic jet cavity model presented in this chapter is derived using this logic and based on physical observations.

4.1 The temporal characteristics of synthetic jet flow

This model is based on the physical understanding of synthetic jet flows, so we first analyze the flow characteristics, especially in the cavity and the near-field region. We use the data from the numerical simulations described in the previous chapter.

The following is the analysis of a sample case, which is an axisymmetric synthetic jet with the nozzle diameter of 1 mm, $l_j/d_j = 5$, cavity aspect ratio of 1, $d_c/d_j = 5$, the displacement of the diaphragm is 0.3 mm or 3% of the cavity height (h_c).

In Figure 4.1, the pressure distribution in a synthetic jet cavity and through the nozzle are shown. It is quite clear that the major pressure change occurs in the nozzle. Regions with significant pressure difference in the cavity only occupy the area within several diameters from the nozzle entrance. The time-mean centerline pressure, shown in Figure 4.2, also indicates that the pressure in the cavity is relatively uniform except the region close to the

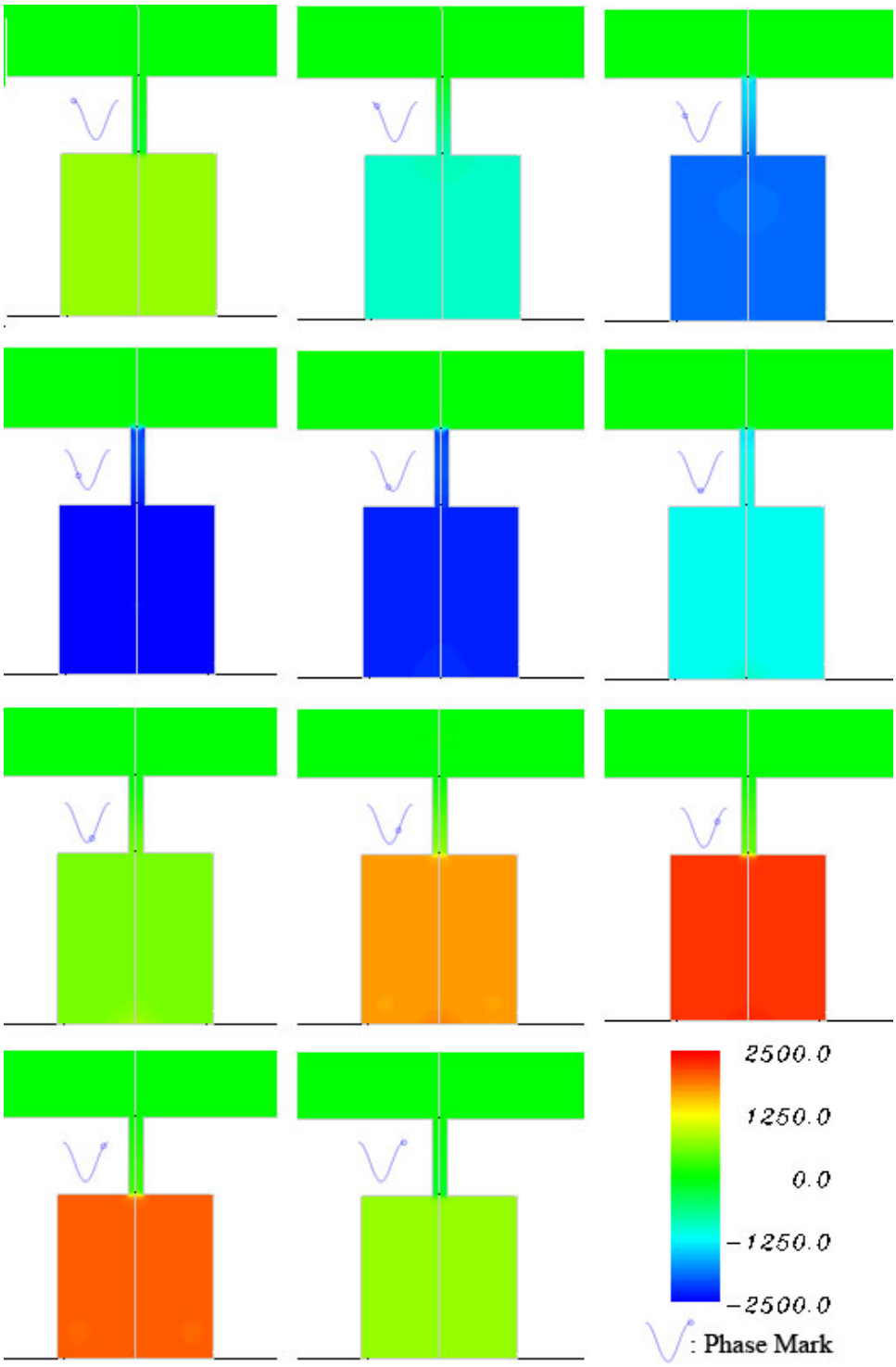

Figure 4.1: Typical pressure contours in an axisymmetric synthetic jet ($d_j = 1$ mm, $f = 250$ Hz)

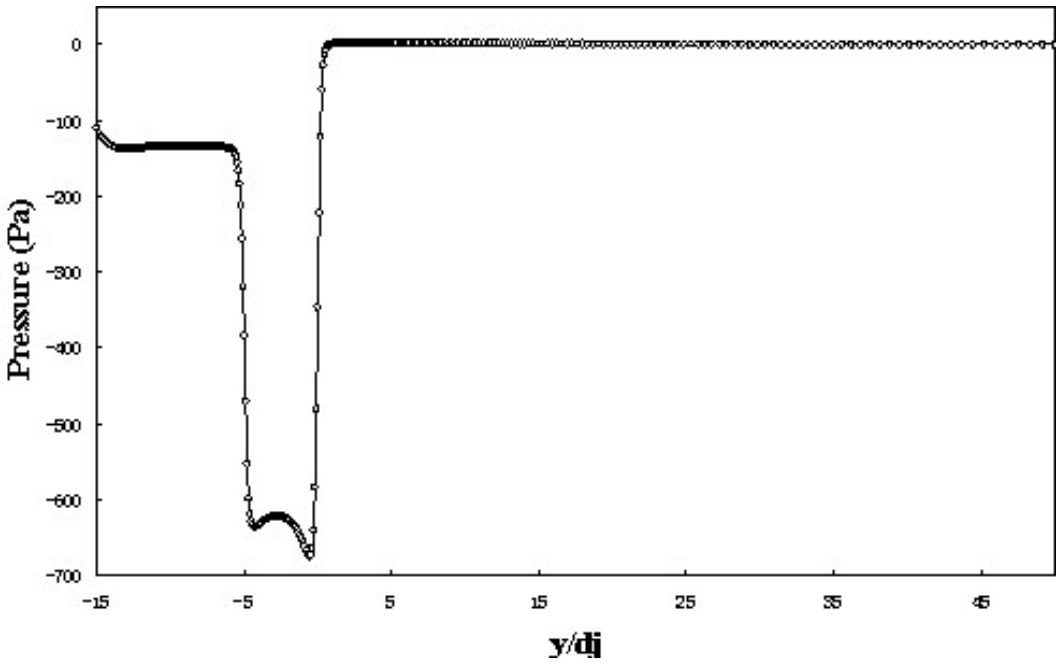

Figure 4.2: Typical time-mean centerline pressure distribution ($y/d_j = 0$ is nozzle exit)

nozzle. In addition, considering the large pressure difference between the two ends of the nozzle, assuming a uniform pressure distribution in the cavity is reasonable.

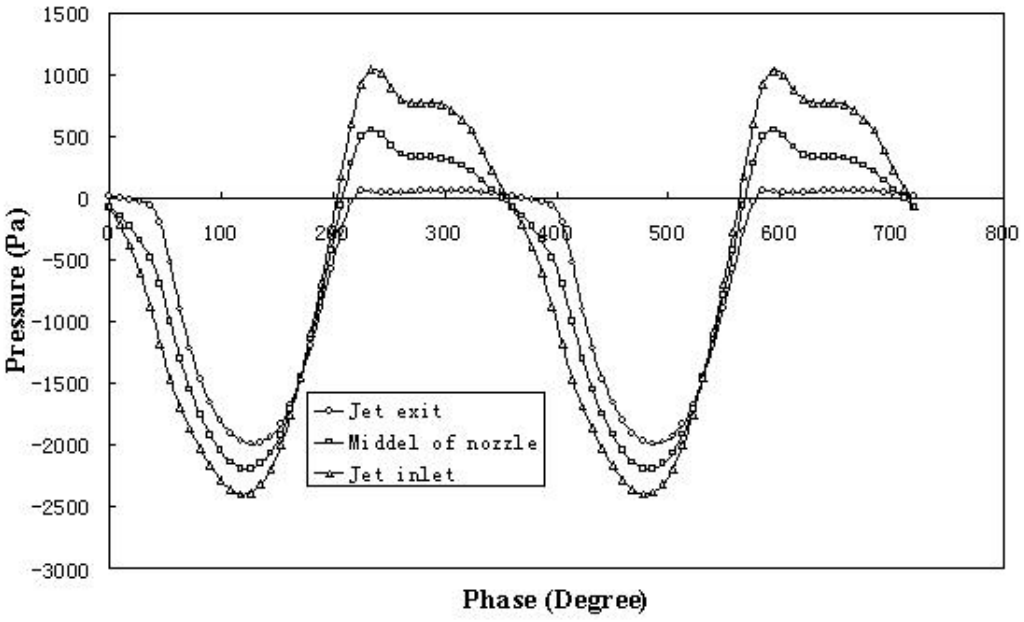

Figure 4.3: Pressure at nozzle exit, in the middle of nozzle and nozzle inlet

Figure 4.3 shows the instantaneous pressure at the nozzle exit ($1\mu m$, from the nozzle exit), in the middle of nozzle, and at the nozzle inlet ($1\mu m$ inside from the inlet). These pressures are not symmetric about the P=0 axis. During the blowing stroke, the pressure at the nozzle exit is almost zero. During the suction phase, the pressure at the nozzle exit is negative forming the pressure difference to accelerate the ambient fluid towards the nozzle/orifice. Specific points where the pressure was monitored are shown in the top half of Figure 4.4. In the bottom half of Figure 4.4, the pressure at these points are plotted. The pressure at the nozzle inlet is also shown as a reference. The pressure in the cavity doesn't show strong asymmetric about P=0. The time dependent pressure plots at the 6 points collapse into one curve. This again shows the pressure distribution in the cavity is quite uniform. The asymmetric pressure (about P=0) in the nozzle is believed due to the losses associated with friction and sudden cross-sectional area changes.

Some phase difference is observed when comparing the pressure in the nozzle and in the cavity. In the model, the phase lag was not included.

The velocity vector fields for this synthetic jet near the jet exit are shown in Figures 4.5 through 4.7. During the blowing stroke, the velocity fields are very similar to conventional jet flows only with different initial velocities from the nozzle at each time instant. During the suction phase, the conventional jet like flow remains in a region some distance from the nozzle. It was also found that the cross-sectional average velocity at different positions in the nozzle are nearly equal (Figure 4.8).

4.2 Reduced order modeling of the synthetic jet cavity

This model was derived based on the previous physical analysis and simplifications were based on physical observations. The model consists of two parts: a lumped parameter cavity and a channel (pipe) flow through the nozzle/orifice.

4.2.1 Cavity: conservation of mass

Observing the relatively uniform pressure distribution in the cavity, we assume the cavity is a lumped element device that is characterized by the following parameters: cavity volume (V_0), cavity volume change (ΔV), area ratio of cavity and nozzle (A_{cav}/A_{nozzle}), working

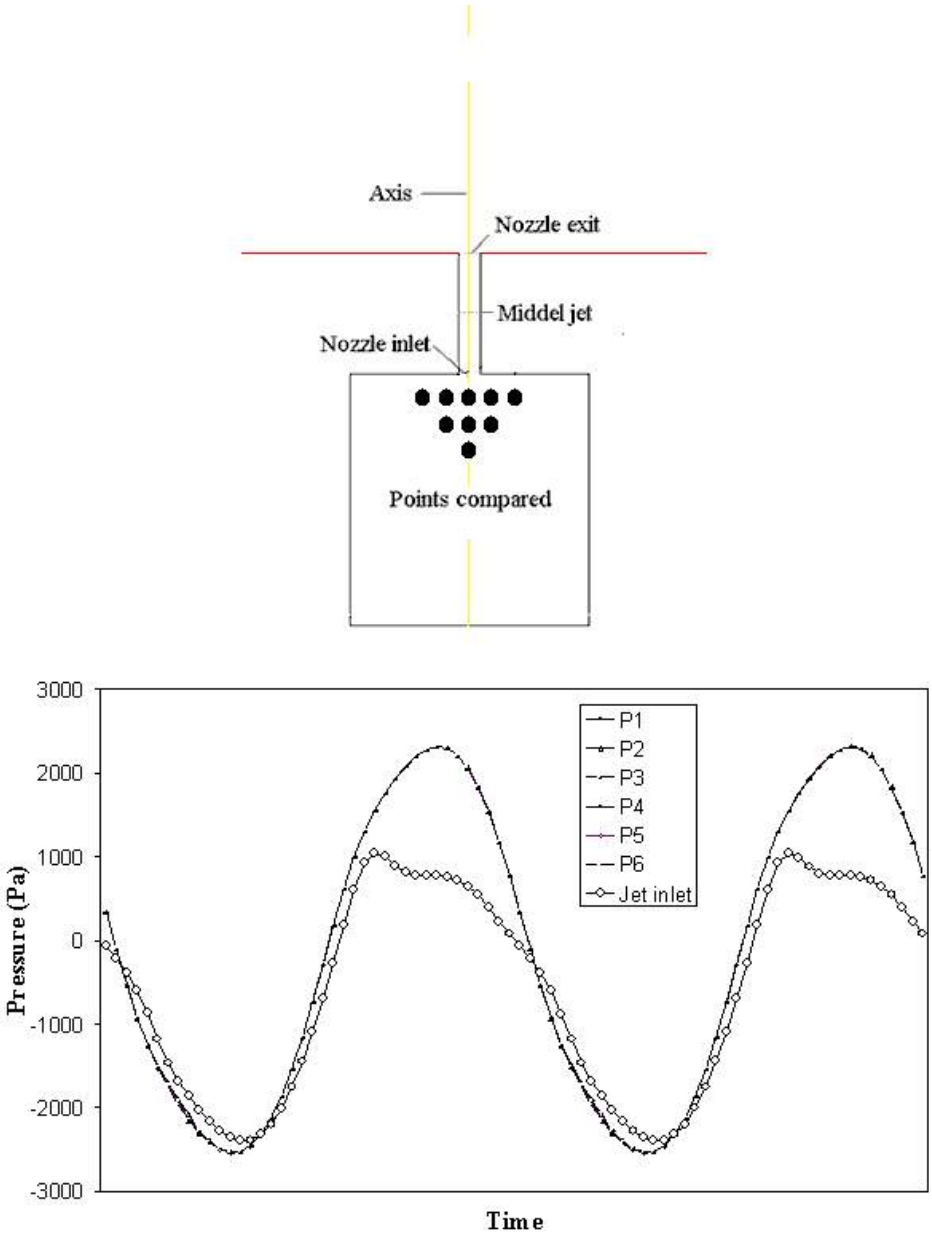

Figure 4.4: Pressure in the cavity at different positions

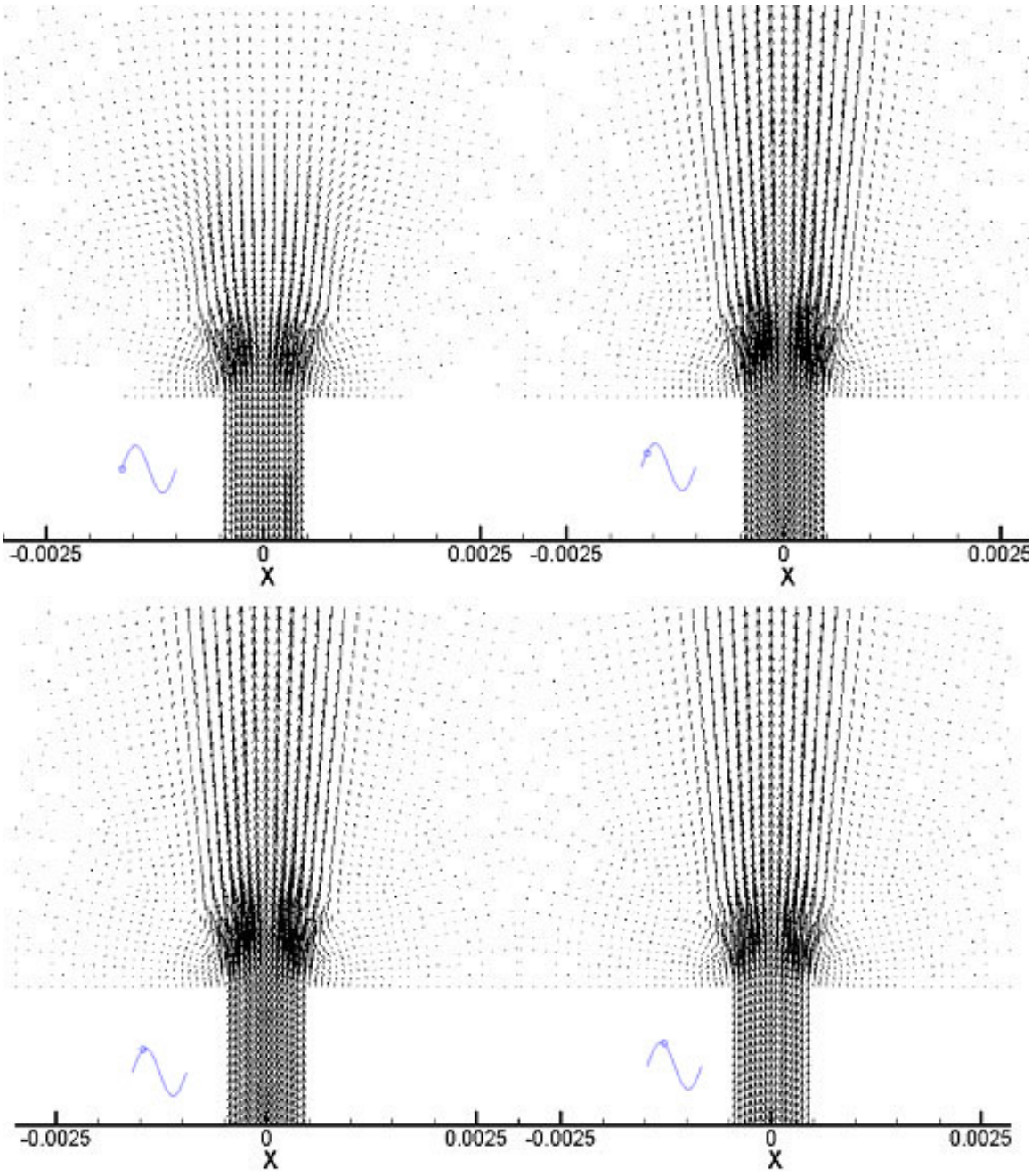

Figure 4.5: Velocity vector field in one cycle (in $\pi/5$ interval)

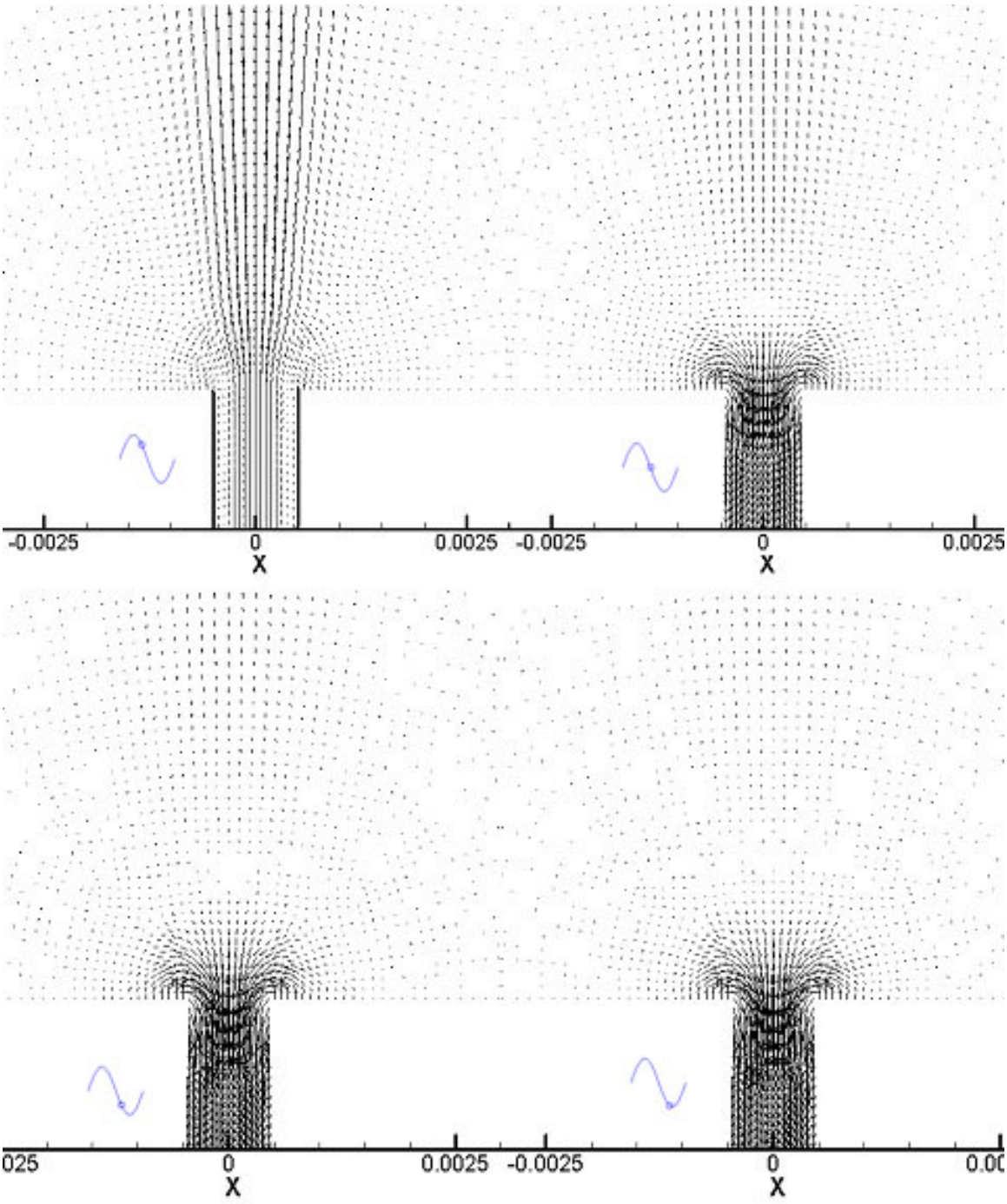

Figure 4.6: Velocity vector field in one cycle (in $\pi/5$ interval)(continued)

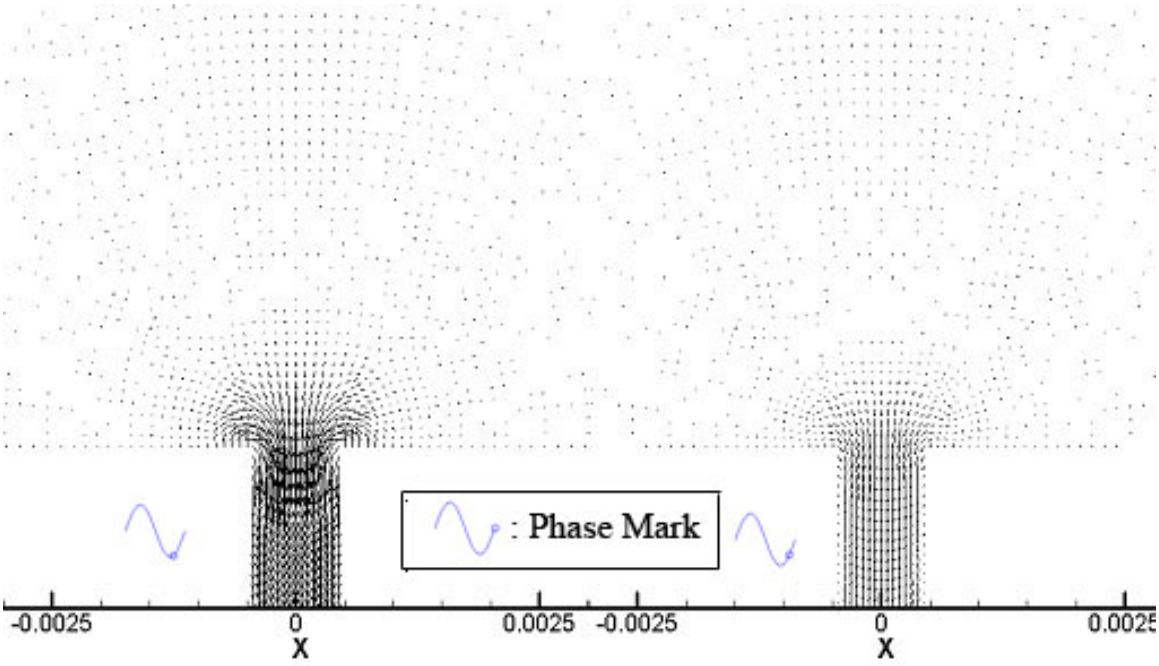

Figure 4.7: Velocity vector field in one cycle (in $\pi/5$ interval)(continued)

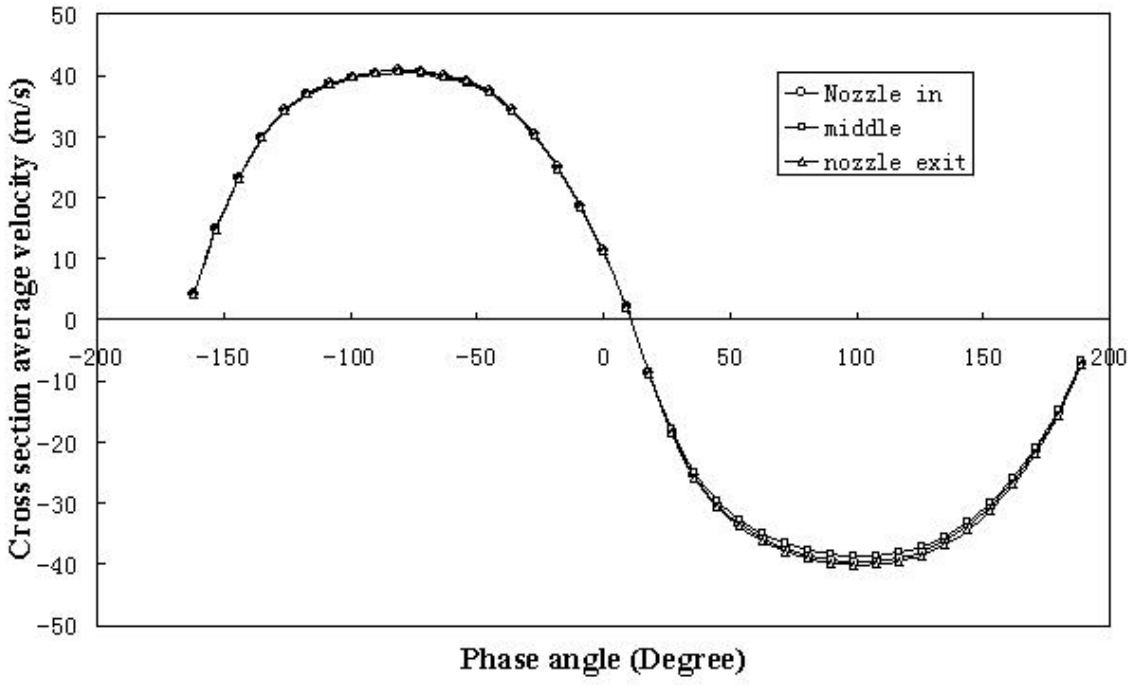

Figure 4.8: Cross section average velocities through the nozzle in one cycle

frequency (f), pressure in the cavity (P) and the velocity through the nozzle (u). In these parameters, V_0, ΔV, A_{cav}/A_{nozzle} and f are input parameters. P and u are output parameters.

Since the detailed velocity profile in the nozzle has to be determined by the nozzle geometry, the output velocity through the nozzle u in this model refers to the cross-sectional average velocity calculated from the flow rate through the nozzle. The synthetic jet flow can be characterized by two dimensionless parameters: the non dimensional stroke length L_{stroke}/d_j and the stream-wise-momentum-based Reynolds number Re_{I_0}. The cross-sectional average velocity determines both of the parameters once the geometry of the nozzle is known. Then, the output of this model could be used as a boundary condition to simulate the entire synthetic jet flow field.

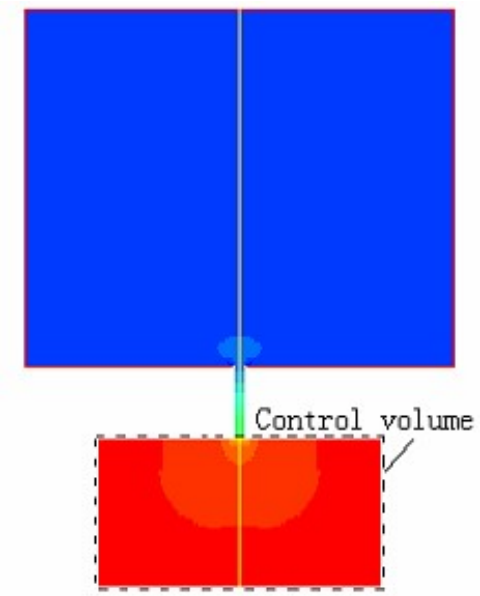

Figure 4.9: Scheme of the synthetic jet cavity modeling

If we apply the mass conservation law to the control volume shown in Figure 4.9, we have:

$$\frac{\partial}{\partial t}\int_{C.V} \rho \cdot dV + \int_{C.S} \rho \vec{v} \cdot \vec{n} dA = 0 \tag{4.1}$$

Assuming the density in the cavity is uniform, and because there is only one outlet, we

have:

$$\rho\frac{dV}{dt} + V\frac{d\rho}{dt} + \rho u A_{nozzle} = 0 \tag{4.2}$$

Now assume that the fluid inside cavity obeys a polytropic relation,

$$P \cdot \rho^{-n} = constant \ or \ d(P \cdot \rho^{-n}) = 0 \tag{4.3}$$

Expanding the differential yields,

$$d\rho = \frac{\rho}{n \cdot P} dP \tag{4.4}$$

and so

$$\frac{d\rho}{dt} = \frac{\rho}{P \cdot n}\frac{dP}{dt} \tag{4.5}$$

Substituting equation (4.5) into equation(4.2), we obtain,

$$\frac{dP}{dt} = -\frac{P \cdot n}{V}(\frac{dV}{dt} + uA_{nozzle}) \tag{4.6}$$

Now, we have one first-order ODE in the two dependent variables P and u. We need one more to close the problem.

4.2.2 Nozzle/orifice: conservation of mechanical energy

We apply the mechanical energy conservation equation to the flow in the nozzle (Figure 4.10). The flow is assumed to be compressible, losses due to friction and sudden flow area changes were considered, and the gravity potential was assumed to be negligible.

With these assumptions, the equation written between any two valid surfaces is:

$$\int_a^b \frac{\partial u}{\partial t} ds + \frac{u_b^2 - u_a^2}{2} + \int_a^b \frac{dP}{\rho} + \sum h_L = 0 \tag{4.7}$$

where, $\sum h_L$ represents the losses in the flow.

Again, assuming a polytropic process, $P \cdot \rho^{-n} = P_0 \cdot \rho_0^{-n}$, where P_0 and ρ_0 are atmospheric reference values, the above equation becomes:

$$\int_a^b \frac{\partial u}{\partial t} ds + \frac{u_b^2 - u_a^2}{2} + \int_a^b (\frac{P_0 \cdot \rho_0^{-n}}{P})^{\frac{1}{n}} dP + \sum h_L = 0 \tag{4.8}$$

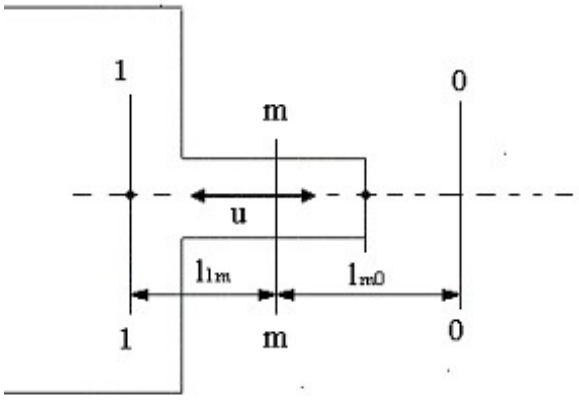

Figure 4.10: Scheme of modeling: nozzle subsystem

It was observed that the velocity in the nozzle doesn't vary much in the streamwise direction. Thus, we also assume that $\partial u/\partial t$ is constant along the streamwise direction. The integration in equation (4.8) can now be performed to yield:

$$\frac{\partial u}{\partial t} l_{a\to b} + \frac{u_b^2 - u_a^2}{2} + \frac{n}{n-1}\frac{P_0^{\frac{1}{n}}}{\rho_0}(P_b^{\frac{n-1}{n}} - P_a^{\frac{n-1}{n}}) + \sum h_L = 0 \tag{4.9}$$

The loss terms in equation (4.9) are to be determined once the nozzle/orifice geometry is known. For a pipe nozzle, we use the correlations from pipe flow to write the loss terms as:

$$\sum h_L = \frac{u^2}{2}(\frac{f \cdot l_j}{d_j} + \sum K) \tag{4.10}$$

where f is the friction factor and K represents various loss coefficients.

Since there are differences in the loss terms between the blowing stroke and the suction phase, we will need to write the loss terms in the above equation separately. The loss coefficients can be found in most mechanical engineering handbooks according to different cavity and nozzle geometries. For both strokes, we use calculate the friction factor using the laminar correlation $f_{lam} = 64/Re_d$ or H.Blasius' correlation $f = 0.316Re_d^{-1/4}$ once the flow is believed to be turbulent.

As shown in the Figure 4.10, we first apply the mechanical energy conservation equation

(4.9) from 1-1 line to m-m line to obtain,

$$\rho_0 \frac{\partial u}{\partial t} l_{1\to m} + \rho_0 \frac{u_m^2 - u_1^2}{2} + \frac{n}{n-1} P_0^{\frac{1}{n}} (P_m^{\frac{n-1}{n}} - P_1^{\frac{n-1}{n}}) + \rho_0 \cdot \sum h_{L_{1\to m}} = 0 \tag{4.11}$$

since $u_1 \ll u_m$, the equation becomes,

$$\rho_0 \frac{\partial u}{\partial t} l_{1\to m} + \rho_0 \frac{u_m^2}{2} + \frac{n}{n-1} P_0^{\frac{1}{n}} (P_m^{\frac{n-1}{n}} - P_1^{\frac{n-1}{n}}) + \rho_0 \cdot \sum h_{L_{1\to m}} = 0 \tag{4.12}$$

Now apply the mechanical energy conservation equation from m-m to 0-0:

$$\rho_0 \frac{\partial u}{\partial t} l_{m\to 0} - \rho_0 \frac{u_m^2}{2} + \frac{n}{n-1} P_0^{\frac{1}{n}} (P_0^{\frac{n-1}{n}} - P_m^{\frac{n-1}{n}}) + \rho_0 \cdot \sum h_{L_{m\to 0}} = 0 \tag{4.13}$$

Compiling equation (4.12) and (4.13), and noticing $P_1 = P$ yields:

$$\rho_0 \frac{\partial u}{\partial t} l_{1\to 0} + \frac{n}{n-1} P_0^{\frac{1}{n}} (P_0^{\frac{n-1}{n}} - P_1^{\frac{n-1}{n}}) + \rho_0 \cdot \sum h_{L_{1\to 0}} = 0 \tag{4.14}$$

which can be written as,

$$\frac{\partial u}{\partial t} = \frac{-1}{l_{1\to 0}} \{ \frac{n}{n-1} \frac{P_0^{\frac{1}{n}}}{\rho_0} (P_0^{\frac{n-1}{n}} - P_1^{\frac{n-1}{n}}) + \sum h_{L_{1\to 0}} \} \tag{4.15}$$

This is the second first-order ODE with the dependent variable u and P that we needed.

In summary, we applied the conservation of mass equation and mechanical energy equation to obtain two first-order ODEs in the dependent variables u and P, where u is the average velocity in the nozzle and P is the uniform cavity pressure.

$$\frac{\partial u}{\partial t} = \frac{-1}{l_{1\to 0}} \{ \frac{n}{n-1} \frac{P_0^{\frac{1}{n}}}{\rho_0} (P_0^{\frac{n-1}{n}} - P_1^{\frac{n-1}{n}}) + \sum h_{L_{1\to 0}} \} \tag{4.16}$$

The derivation of the above model is general; all the assumptions were based on physical simplifications and observations from CFD simulations. The loss term in the model was evaluated using general pipe flow correlations. There are two undetermined parameters: n and l. They are determined by matching model results to those of a full CFD simulation. If physics of the two subsystems is clear, they are determined by their physical significance.

4.3 Model of an axisymmetric cylindrical cavity and nozzle

To evaluate this reduced-order model, we used an axisymmetric synthetic jet with a cylindrically shaped cavity and nozzle. The piston-like moving diaphragm had a maximum displacement of 0.3 mm. The geometry of the synthetic jet is summarized in Table 4.1. We used a working frequency of 250Hz.

Table 4.1: Geometry of the modeled synthetic jet (mm)

	Height (Length)	Diameter
Cavity	10.5	10
Nozzle	5	1

With a sinusoidal piston motion,

$$V = V_0 + \Delta V \sin(2\pi f t) \tag{4.17}$$

So that

$$\frac{dV}{dt} = 2\pi f \Delta V \cos(2\pi f t) \tag{4.18}$$

The first ODE becomes

$$\frac{dP}{dt} = -\frac{Pn}{V_0 + \Delta V \sin(2\pi f t)} \left(2\pi f \Delta V \cos(2\pi f t) + u A_{nozzle} \right) \tag{4.19}$$

The second ODE, equation (4.16) is treated differently for blowing stroke ($u \geq 0$) and suction phase ($u < 0$).

For the blowing stroke, minor losses include a sudden contraction from the cavity area to the nozzle area and an exit. So that

$$\sum h_{L,1\to 0} = \frac{u^2}{2} \left(\frac{f \cdot l_j}{d_j} + K_{contraction} + K_{exit} \right) \tag{4.20}$$

in which $K_{contraction} = 0.4$ and $K_{exit} = 1$

During the suction phase, minor losses include a pipe entrance and a sudden expansion from the nozzle area to the cavity area.

$$\sum h_{L,1\to 0} = \frac{u^2}{2} \left(\frac{f \cdot l_j}{d_j} + K_{expansion} + K_{entrance} \right) \tag{4.21}$$

in which $K_{expansion} = 0.98$ and $K_{entrance} = 0.78$.

For both strokes, the friction factor was computated using the laminar correlation $f_{lam} = 64/Re_d$ or Blasius' turbulent flow correlation $f = 0.316Re_d^{-1/4}$. However, as mentioned in Chapter 2, oscillating flows become turbulent earlier than steady pipe flows. To the author's knowledge, there is no documented correlation available for oscillating pipe flows. We used the critical Re number summarized by Ohmi et.al (1982) [39] instead of $Re = 2300$ to determine the flow is laminar or turbulent.

The two ODEs were solved numerically using a MATLAB program, in which a fourth-order Runge-Kutta integration algorithm was used.

For the two subsystems where two ODEs were derived, the two ploytropic exponents (n) are not necessarily equal. Because the process in the cavity is different from the process in the nozzle, the n values could be significantly different. The value of l was assume as the length of the nozzle plus four nozzle diameters ($l = l_j + 4d_j$).

In the cavity, n value is determined by the physical process, such as isentropic, isothermal, etc. This polytropic exponent is the one that needs carefully analysis. In this particular case, n was set to be 0.865.

The polytropic exponent n in the second ODE mainly represents the compressibility. During the low velocity, compressibility is negligible and the value of n should be large. When velocity is large, compressibility is significant, and we shall assume $n = 1.4$ to represent an adiabatic process. Under this consideration, if the nozzle velocity is greater than 0.3 V_{sound}, where V_{sound} is the local sound speed ate atmospheric conditions, compressibility is fully considered and $n = 1.4$ was used. If velocity is less than 0.3 times sound speed, $n = 1.4 \cdot (0.3 \cdot V_{sound}/u)$ is used to ensure the smooth transition of the velocity curve. Upon this manipulation, the RMS error for the velocity is 4.8%, and the RMS error for the cavity pressure is 8%. In Figure 4.11, the calculated average velocity and cavity pressure are compared with simulation results. The corresponding curves are quite close to each other. Since the parameters l and n and the system losses were chosen based on physical ground, and not mathematic matching, the good agreement between the simulation and the proposed model is very good.

To examine the robust of this model, the modeling results were compared to simulation

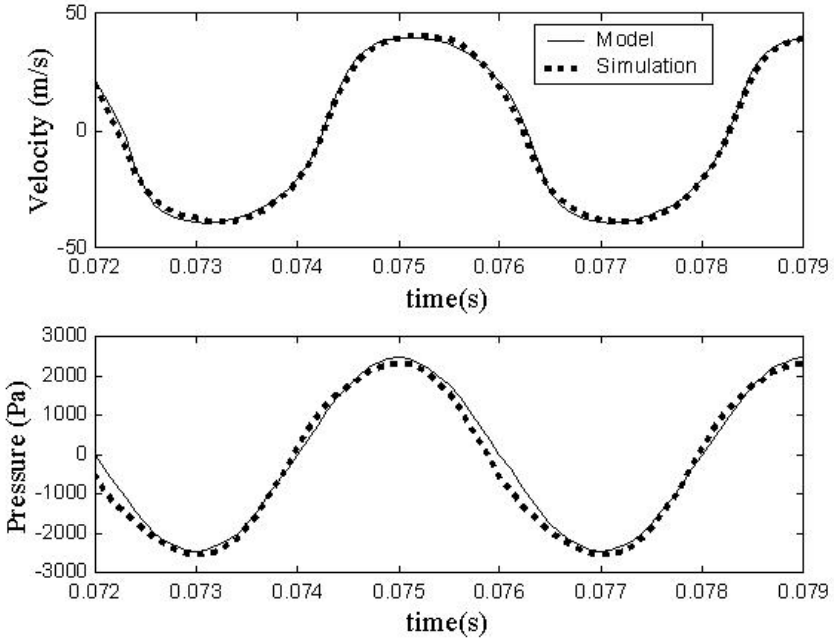

Figure 4.11: Synthetic jet model compared with simulation results (d_j=1 mm, f = 250 Hz)

results for other synthetic jet configurations.

For the second ODE, the n value needs adjusting when working frequency increases. Physically, this adjustment is related to how to estimate the compressibility. Therefore same synthetic jet works at different frequencies were examined to evaluate this dependence. We have examined the synthetic jets working at 250 Hz and 1000 Hz.

For the same synthetic jet working at a frequency of 500 Hz, the model predicts the pressure with a RMS error of 6.9% and the RMS error of the velocity is 5.9% with all parameters kept same (Figure 4.12).

For the same geometry as the above case, but with $f = 1000Hz$, the comparison is shown in Figure 4.13. The RMS error for the pressure is 11% and the RMS error for the velocity is 5.5%.

For a smaller nozzle diameter, ($d_j = 0.5mm$ and $l_j/d_j = 10$), the RMS error for the pressure is 12.5% and for the velocity is 8.9%, if the air in the cavity was assumed to be isentropic ($n = 1.4$). If the polytropic exponent was reduced to $n = 1.2$, the errors were reduced to 9.7% and 5.5% for pressure and velocity respectively. (see Figure 4.14)

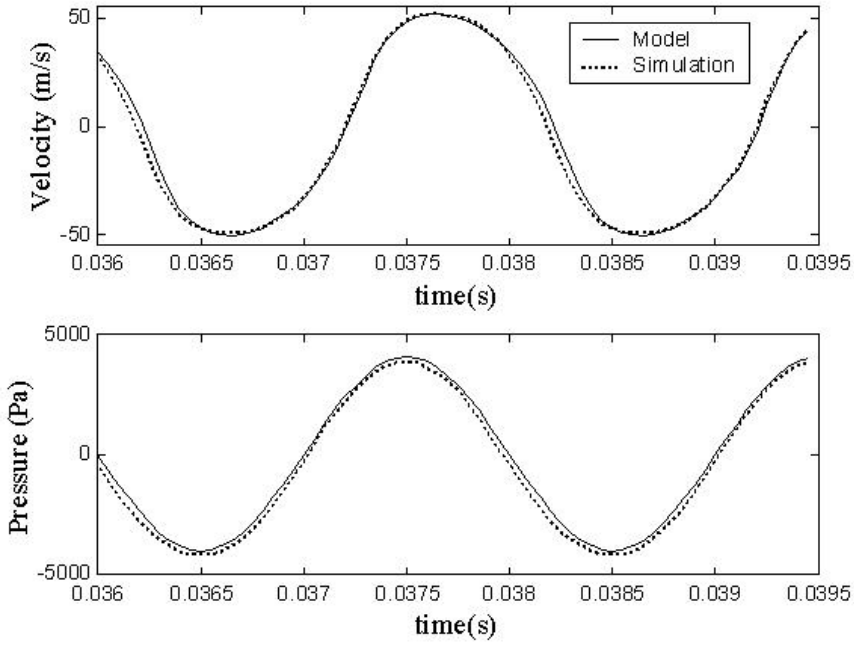

Figure 4.12: Synthetic jet model compared with simulation results (f =500 Hz, d_j=1 mm, h_c/d_c =1)

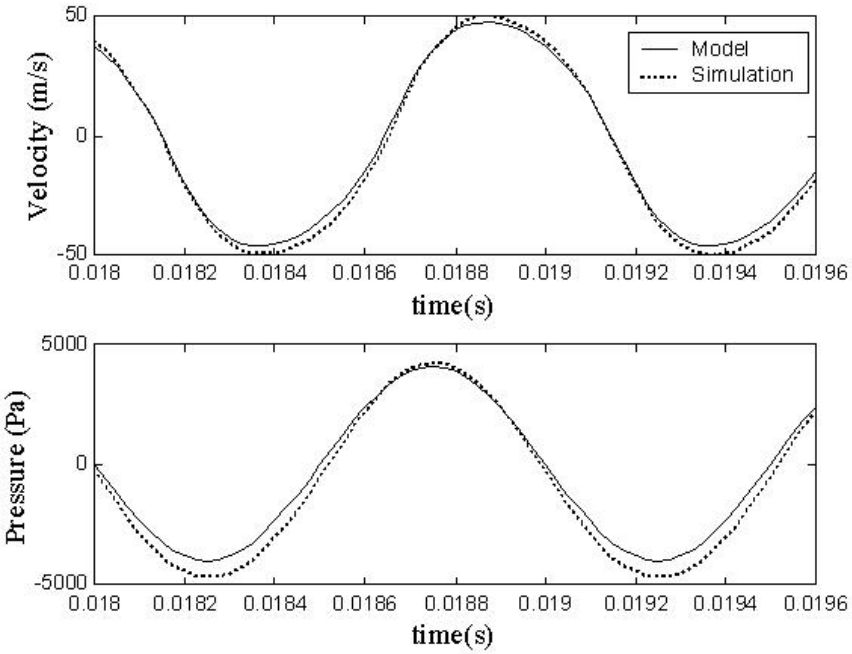

Figure 4.13: Synthetic jet model compared with simulation results (d_j=1 mm, f = 1000 Hz)

For a synthetic jet with a large diameter (d_j = 2 mm), l_j/d_j= 2.5, and assuming an isentropic process in the cavity (n = 1.4), the RMS error for the pressure is 24% and for the velocity it is 14.3%. As the opening is larger, it is expected that the polytropic process is closer to iso-volume, so $n > 1.4$. If we assume $n = 1.8$, the RMS errors are reduced to 9.7% and 5.4% for pressure and velocity respectively. (see Figure 4.15)

Configurations with different cavity geometries were also examined. For a configuration with an aspect ratio of $h_c/d_c = 4$ (d_j=1 mm), working at 1000 Hz, the model predicted the pressure in the cavity is with a RMS error of 9.4% and the velocity with a RMS error of 3%, if an isentropic process in the cavity was assumed. (Figure 4.16) Since the volume change $\Delta V/V$ is one fourth of the previous cases and the synthetic jet works at high frequency, the flow in the cavity is reasonably to be assumed as isentropic. And the model prediction matches the CFD simulation well means the model well captures the physics of the synthetic jet flow.

A cavity with a smaller aspect ratio, $h_c/d_c = 1/4$, and a nozzle diameter $d_j = 0.5$ mm is shown in Figure 4.17. n this case, the area ratio of $A_{cav}/A_{nozzle} = 400$, it is expected the process in the cavity is close to isentropic, due to the large pressure variation generated by the larger area ratio. With the polytropic exponent n =1.4, the model predicted pressure within 8% RMS error and velocity within 4.2% RMS error.

For extreme case in the nozzle diameter, this model also yield reasonably good results. One extreme case is the infinitely small nozzle, or in other word, the cavity is closed. The corresponding model now becomes:

$$\frac{dP}{dt} = -\frac{P \cdot n}{V}\left(\frac{dV}{dt}\right) \tag{4.22}$$

This is simply the equation describing the polytropic gas behavior in a closed system. The second ODE doesn't contribute to this case since u=0.

In the above examples, we used our reduced-order model to predict the pressure in the cavity and the average velocity through the nozzle successfully. Tested cases (not limited to the examples shown above) covered a range of nozzle diameter d_j from 0.5 mm to 6.35 mm, working frequency f from 80 Hz to 1000 Hz, cavity aspect ratio h_c/d_c from 1/4 to 4, area

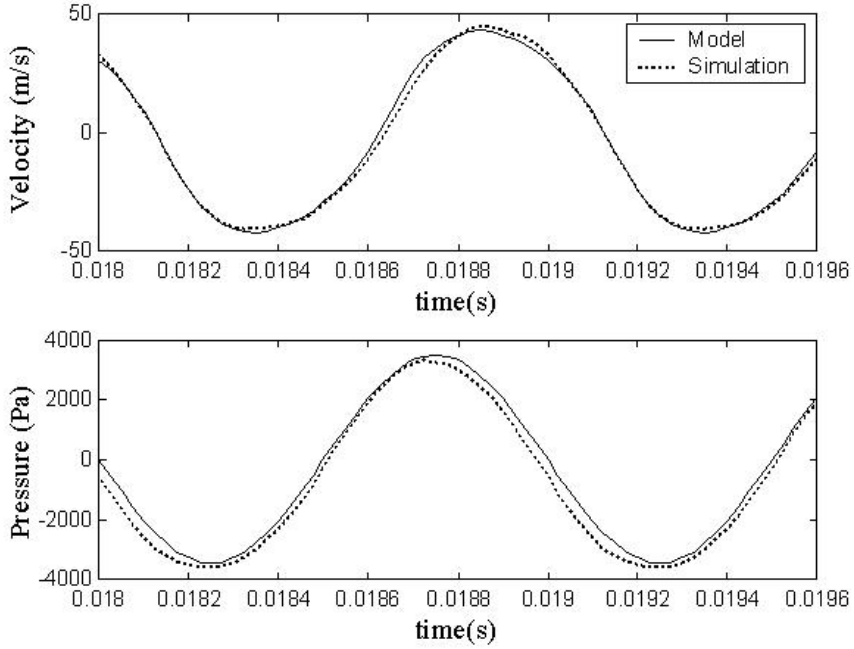

Figure 4.14: Synthetic jet model compared with simulation results (f =1000 Hz, d_j=0.5 mm)

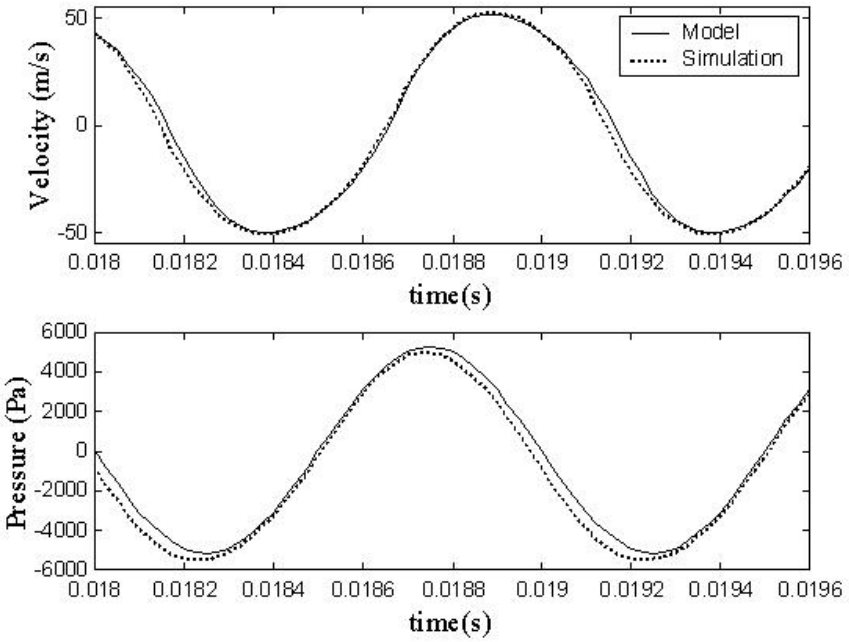

Figure 4.15: Synthetic jet model compared with simulation results (f =1000 Hz, d_j=2 mm)

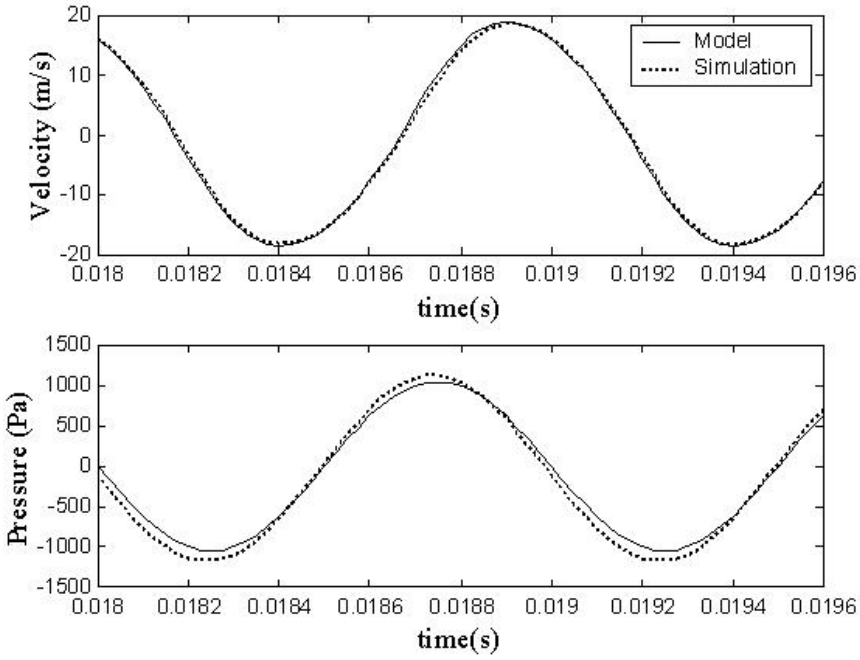

Figure 4.16: Synthetic jet model compared with simulation results (f =1000 Hz, d_j=0.5 mm, h_c/d_c =4)

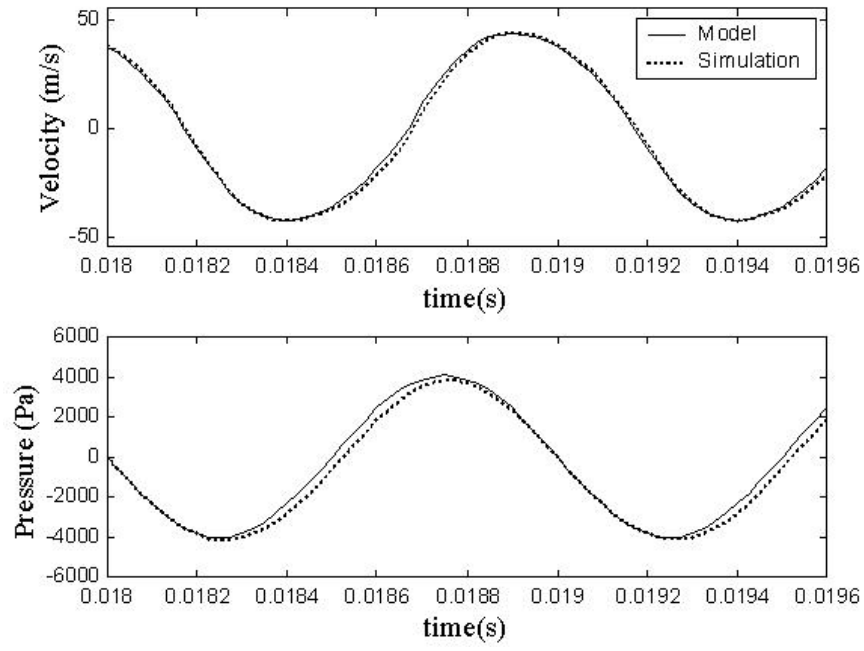

Figure 4.17: Synthetic jet model compared with simulation results (f =1000 Hz, d_j=1 mm, h_c/d_c =1/4)

ratio Acav/Anozzle from 25 to 1600, and volume change $\Delta V/V$ from 0.75% to 10%. The parameters in the model could be determined by matching the model prediction with CFD simulation results. However, since the physical significance of the parameters n are clear, if the physics of the flow in the cavity and through the nozzle are known, their value could be determined without any matching. The model predicted cavity pressure and average velocity through the nozzle are in good agreement with the CFD simulation. Generally, predictions of the model with n determined based on physical analysis, are within 10% RMS error. If n was varied by matching, the RMS error could be reduced to around 5%.

4.4 Full simulation with a modeled cavity

The following is an example of the application of the cavity model to a full CFD simulation of a synthetic jet. The model parameters are an aspect ratio $h_c/d_c = 1$, d_j=1 mm, $\Delta V/V$ = 3%, A_{cav}/A_{nozzle}=100, and a working frequency of 250 Hz. The predicted average velocity was assigned as the inlet boundary condition to the geometry model without a cavity but with half of the nozzle. The meshes are shown in the Figure 4.18, the top mesh contains the full cavity model; the bottom mesh eliminates the cavity and contains only the top half of the nozzle. The mesh size of these two meshes were 10671 nodes (without counting nodes associated with the moving diaphragm) and 5796 nodes respectively. The saving in computer resources for this example was 46%.

The near fields simulated were compared intensively. To avoid an overwhelming number of images, the Figures 4.19 through 4.28 only show the comparison at $1d_j$, $2d_j$, $3d_j$, $4d_j$, $5d_j$, $6d_j$, $8d_j$, $10d_j$, $20d_j$ and $30d_j$ from the nozzle exit at phase of maximum velocity fo the blowing stroke and suction phase. Because they represent the largest velocity, the errors are expected to have the largest magnitude also. The RMS errors of axial velocity and radial velocity at these positions are summarized in Table 4.2.

The simulation with the cavity model is of satisfying accuracy when compared to the full simulation results. The overall RMS errors for the axial velocity are less than 3%. The overall RMS errors for the radial velocity are less than 12%. But, considering that the magnitude of the radial velocity is significantly smaller than the axial velocity, the greater

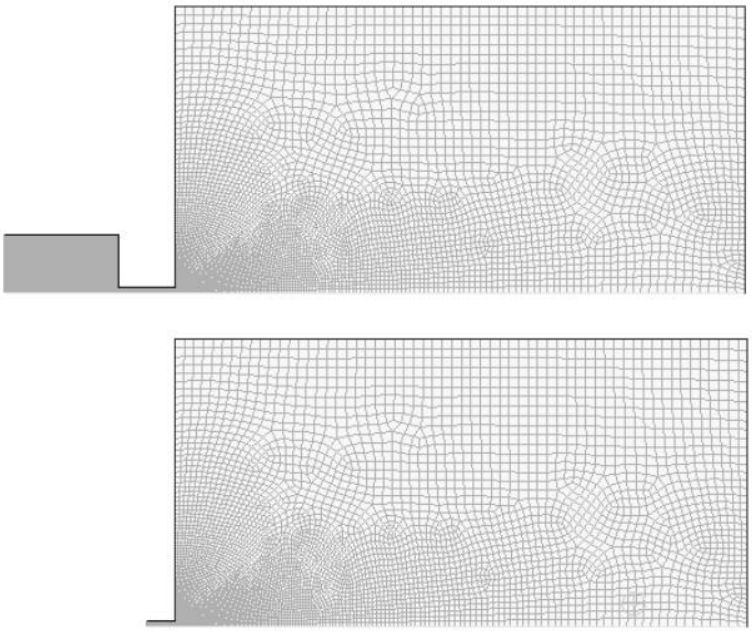

Figure 4.18: Meshes in example (top: with cavity, bottom: with cavity model)

Table 4.2: RMS error (in %) summary

	d_j	$2d_j$	$3d_j$	$4d_j$	$5d_j$	$6d_j$	$8d_j$	$10d_j$	$20d_j$	$30d_j$
$u_{Z,blowing}$	0.56	0.34	0.57	0.89	1.2	1.46	1.77	1.74	1.77	2.3
$u_{r,blowing}$	3.54	3.92	3.98	4.5	5.9	9.57	4.5	2.56	3.09	6.47
$u_{Z,suction}$	2.56	4.4	3.01	2.69	2.55	2.43	2.26	2.43	2.49	1.5
$u_{r,suction}$	0.44	2.08	3.51	3.86	3.69	3.36	3.23	3.84	19.1	11.6

errors are acceptable.

The vortex dynamics are simulated as well. Figures 4.29 and 4.30 are the vortex evolution of both cases. The left image is the vorticity contours for the full cavity simulation, and the right image is the vorticity contours for the cavity model simulation. The differences between the contours is minor.

As this is only a randomly selected example, it is expected that using the model predicted velocity as the boundary condition could well reproduce the origin synthetic jet flow. The methodology proposed in this chapter is proved to be functional and accurate.

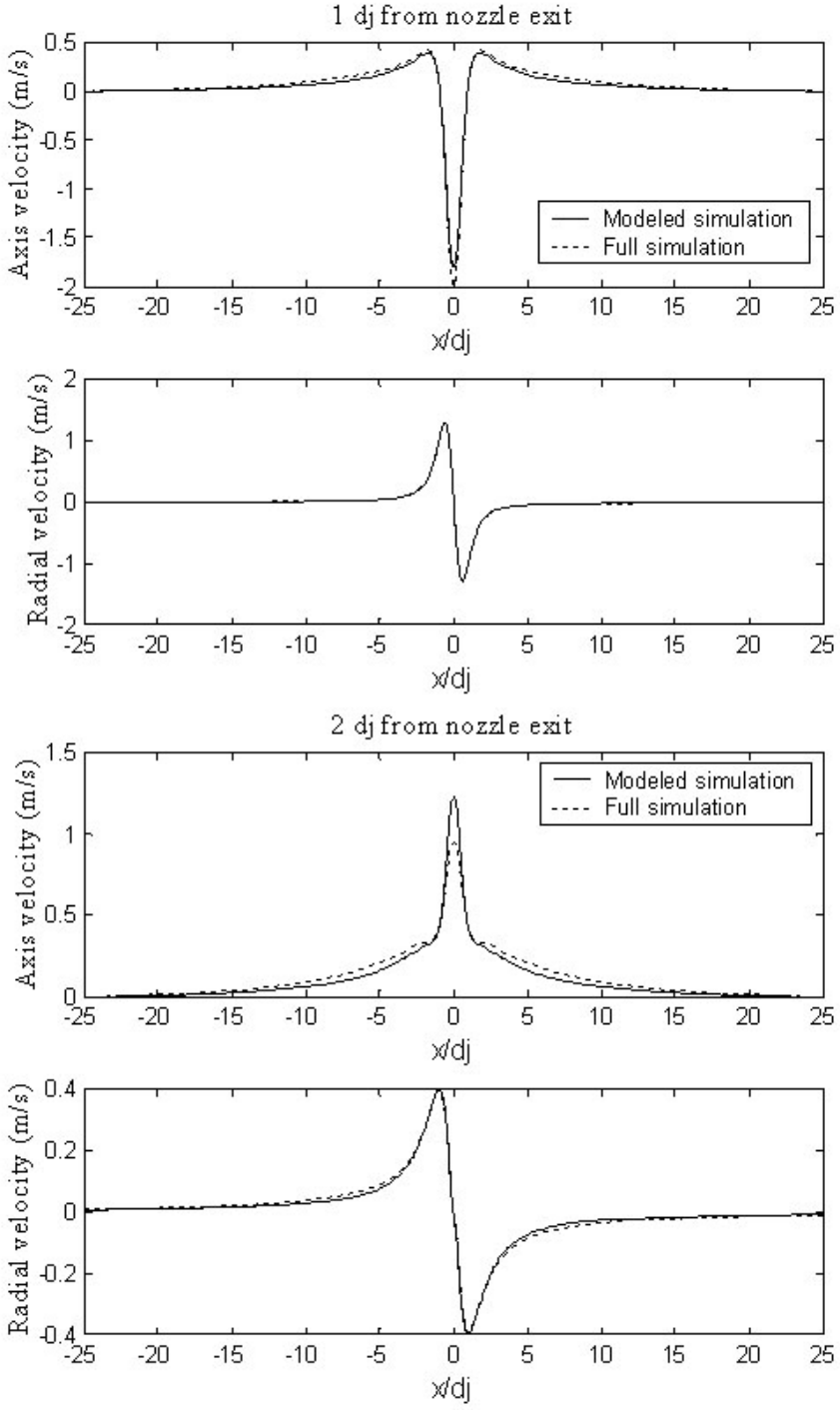

Figure 4.19: Axial velocity and radial velocity comparison, $h_c/d_c = 1$, d_j=1 mm, f =250 Hz (Max suction phase)

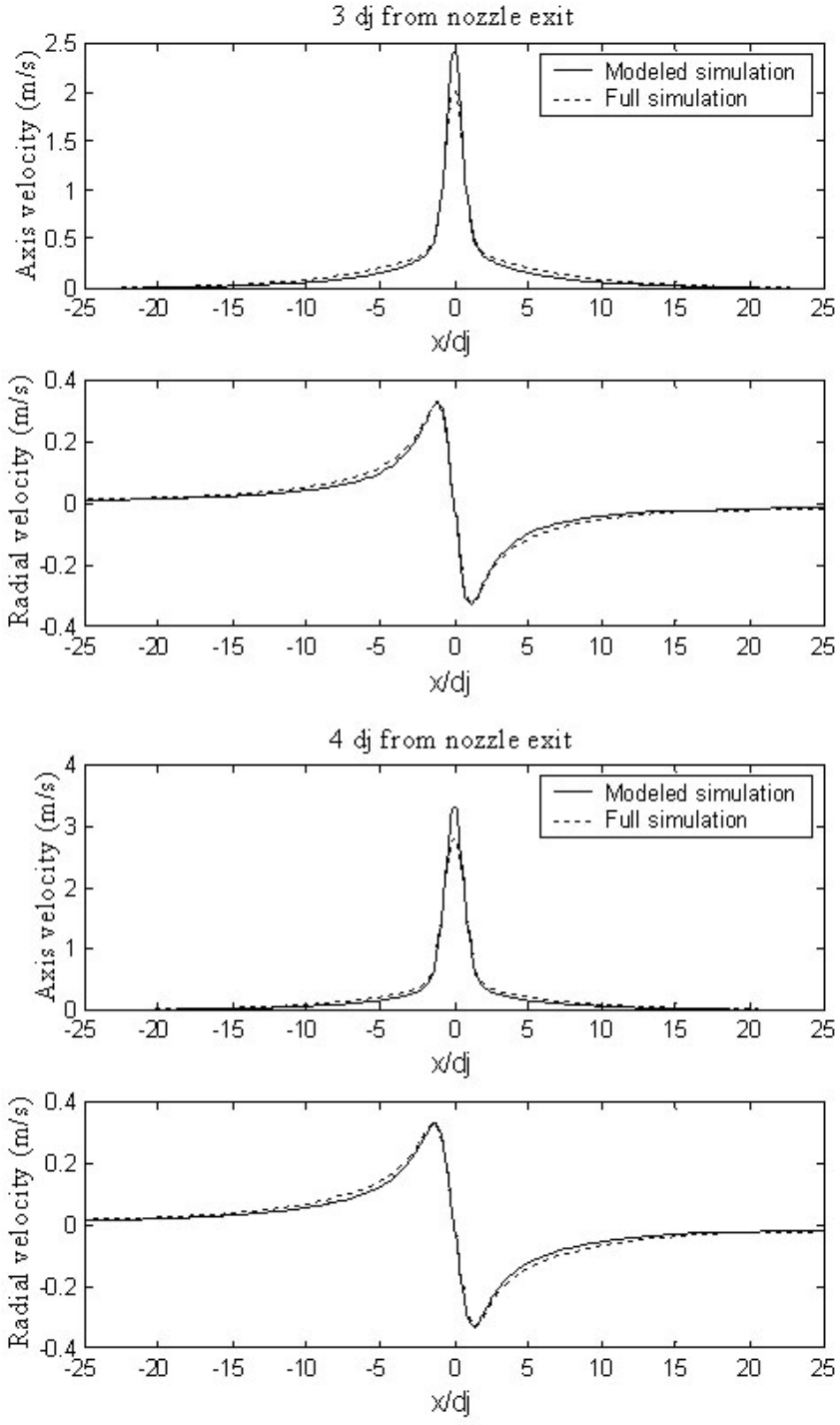

Figure 4.20: Axial velocity and radial velocity comparison (Max suction phase) (continued)

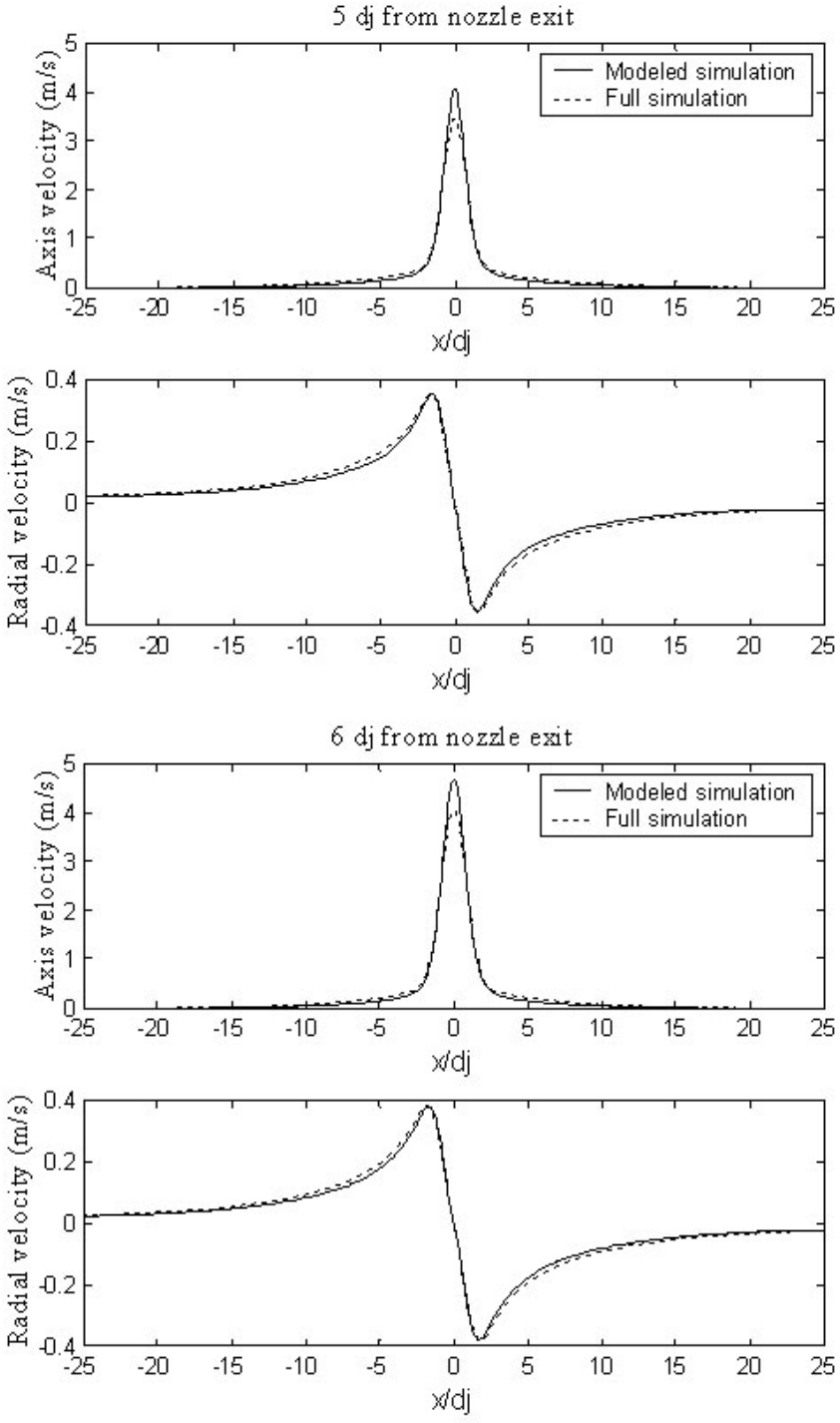

Figure 4.21: Axial velocity and radial velocity comparison (Max suction phase) (continued)

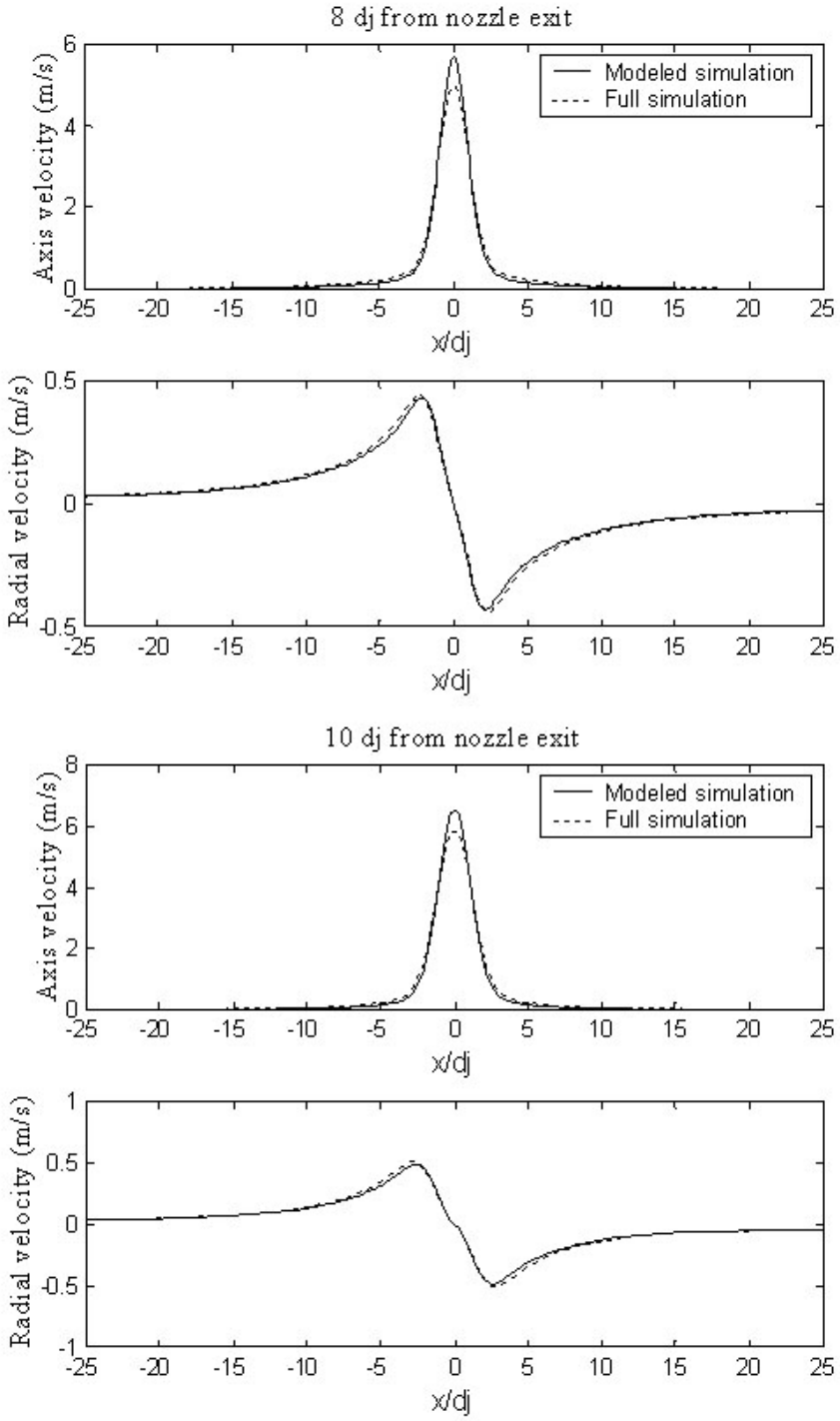

Figure 4.22: Axial velocity and radial velocity comparison (Max suction phase) (continued)

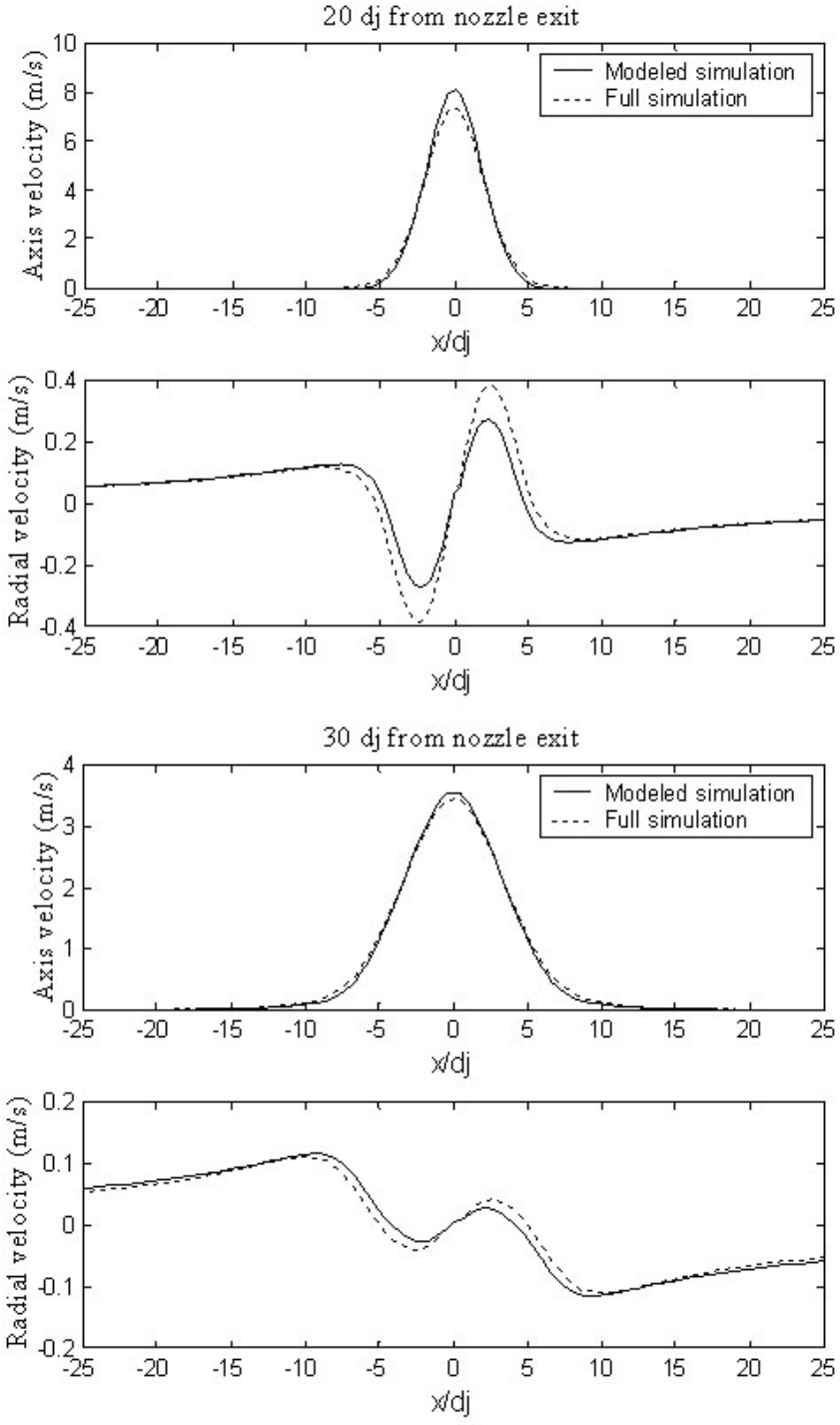

Figure 4.23: Axial velocity and radial velocity comparison (Max suction phase) (continued)

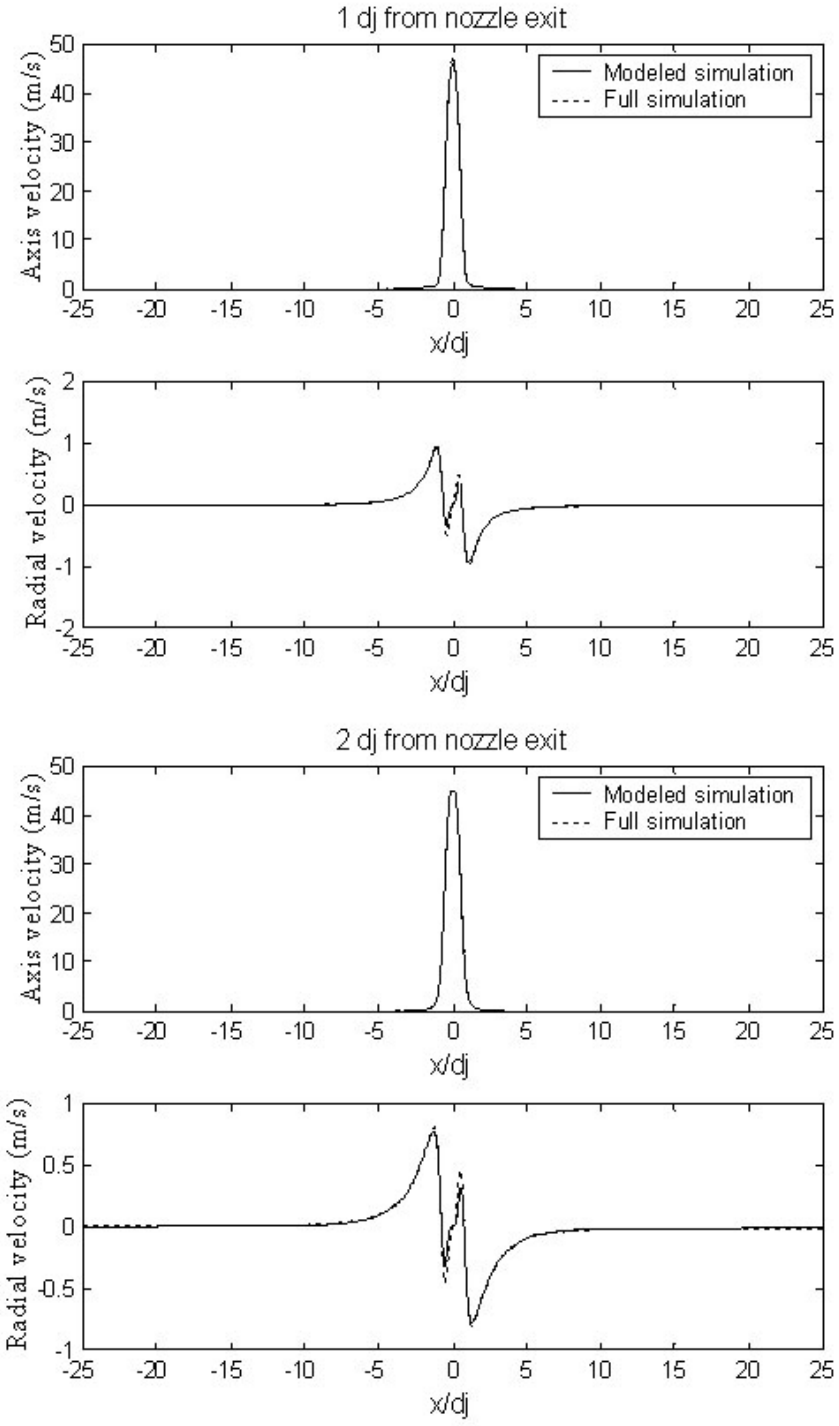

Figure 4.24: Axial velocity and radial velocity comparison, $h_c/d_c = 1$, d_j=1 mm, f =250 Hz (Max blowing stroke)

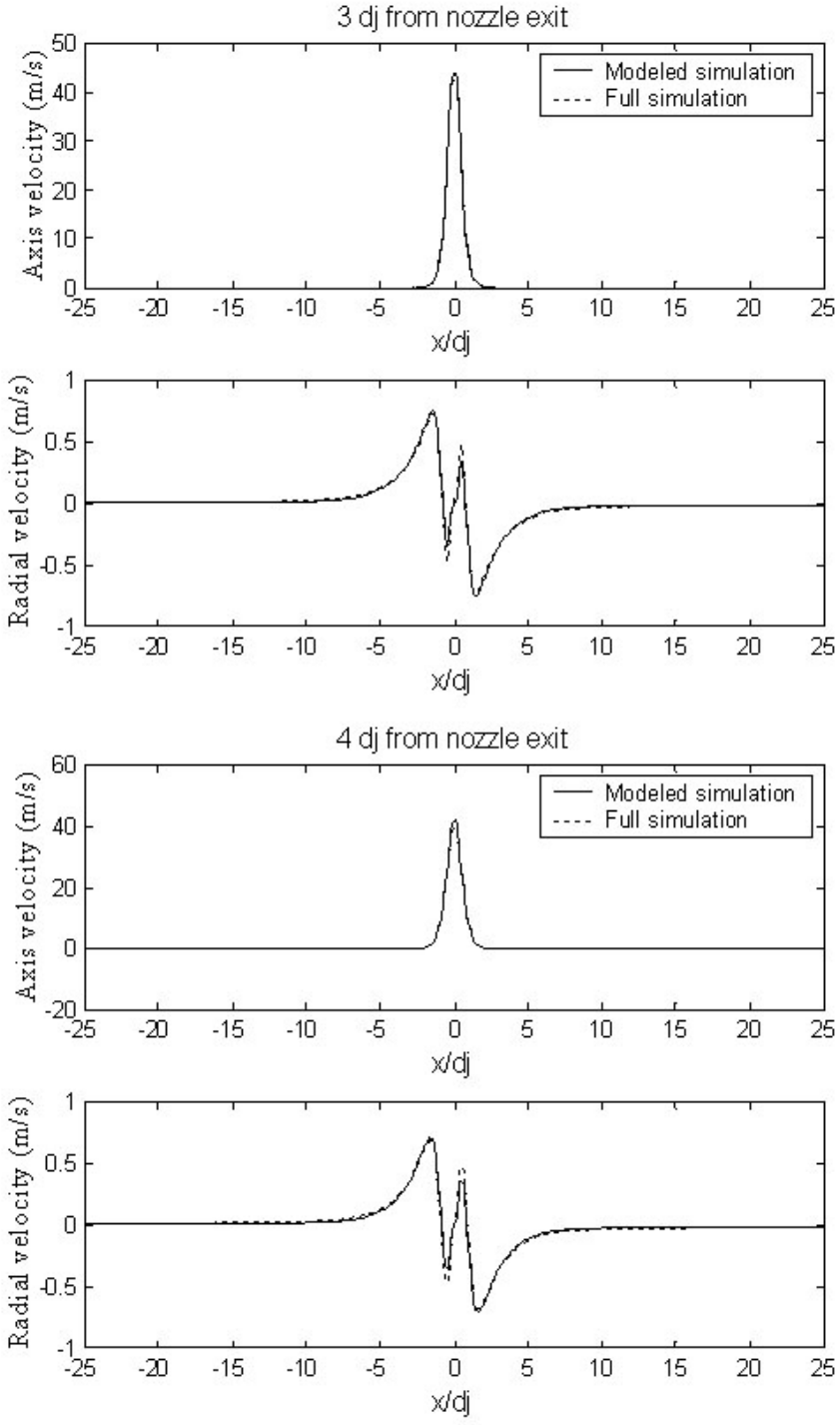

Figure 4.25: Axial velocity and radial velocity comparison (Max blowing stroke) (continued)

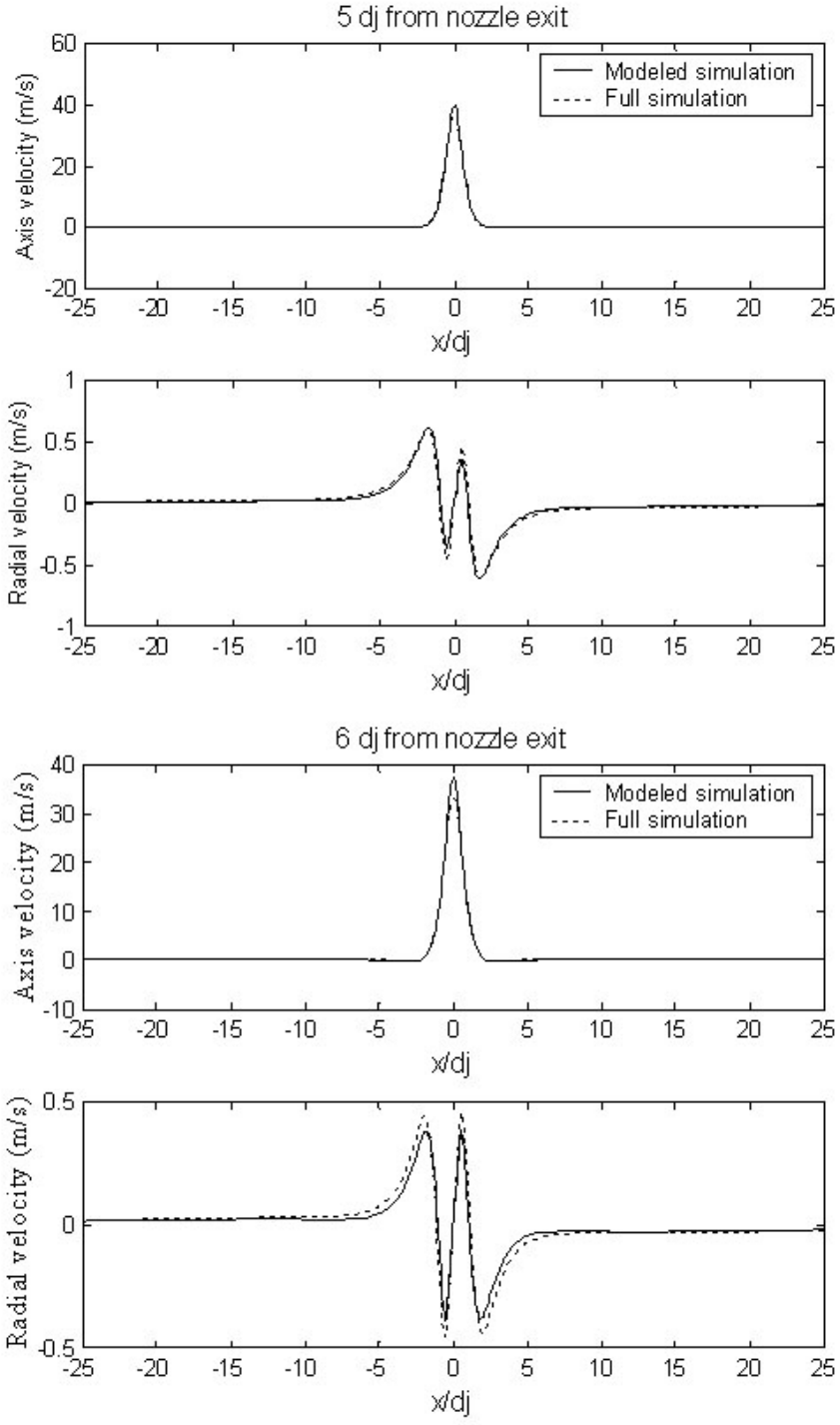

Figure 4.26: Axial velocity and radial velocity comparison (Max blowing stroke) (continued)

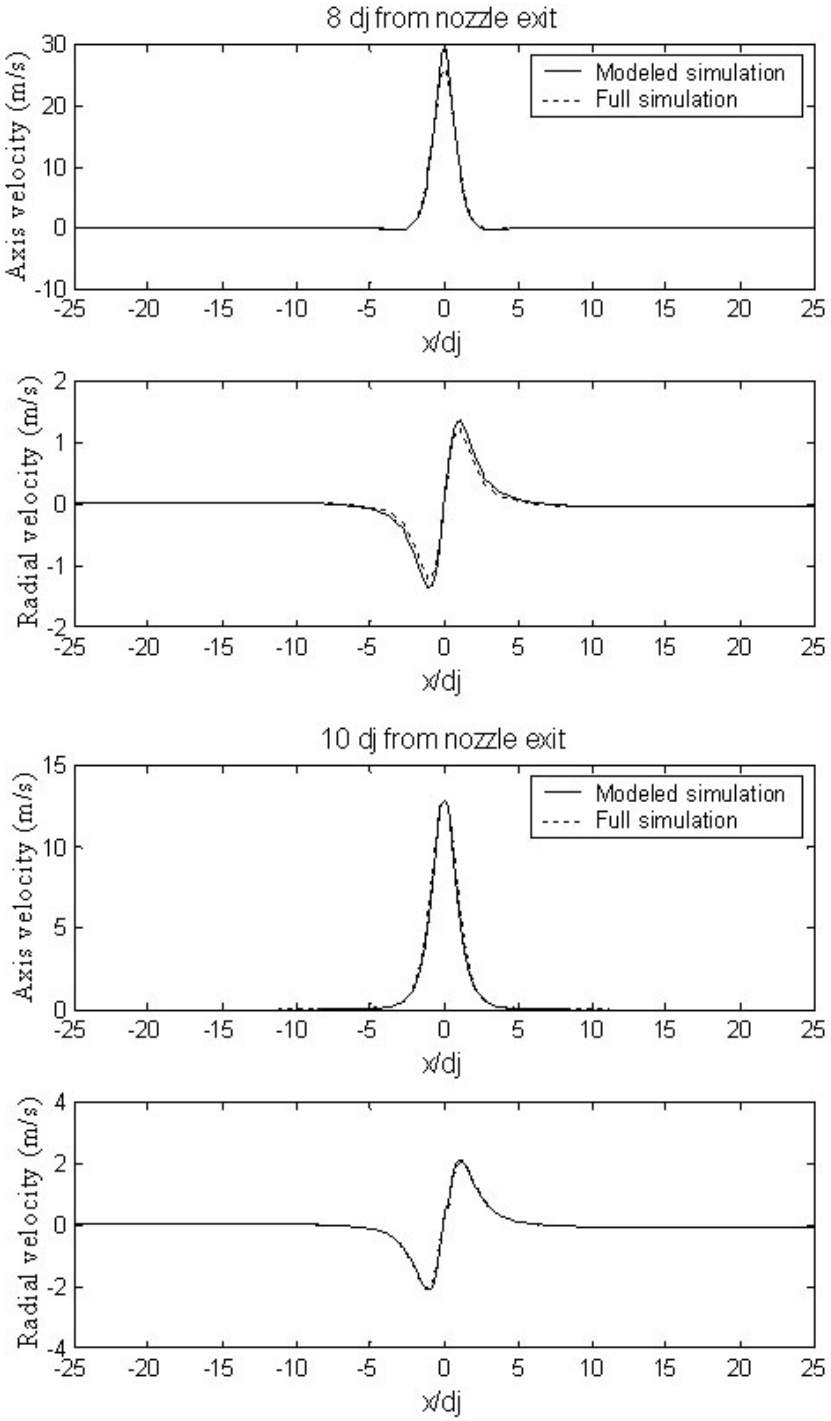

Figure 4.27: Axial velocity and radial velocity comparison (Max blowing stroke) (continued)

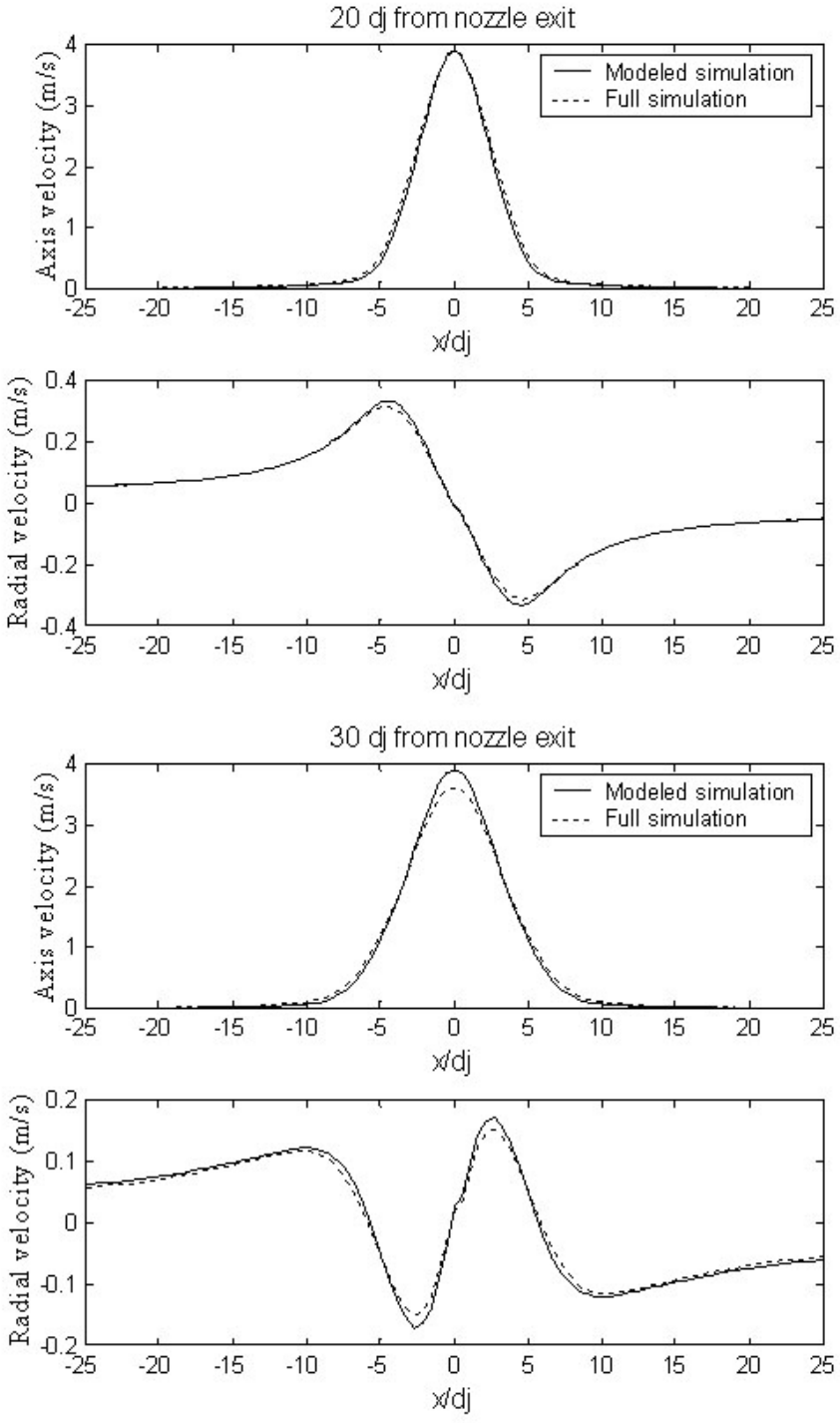

Figure 4.28: Axial velocity and radial velocity comparison (Max blowing stroke) (continued)

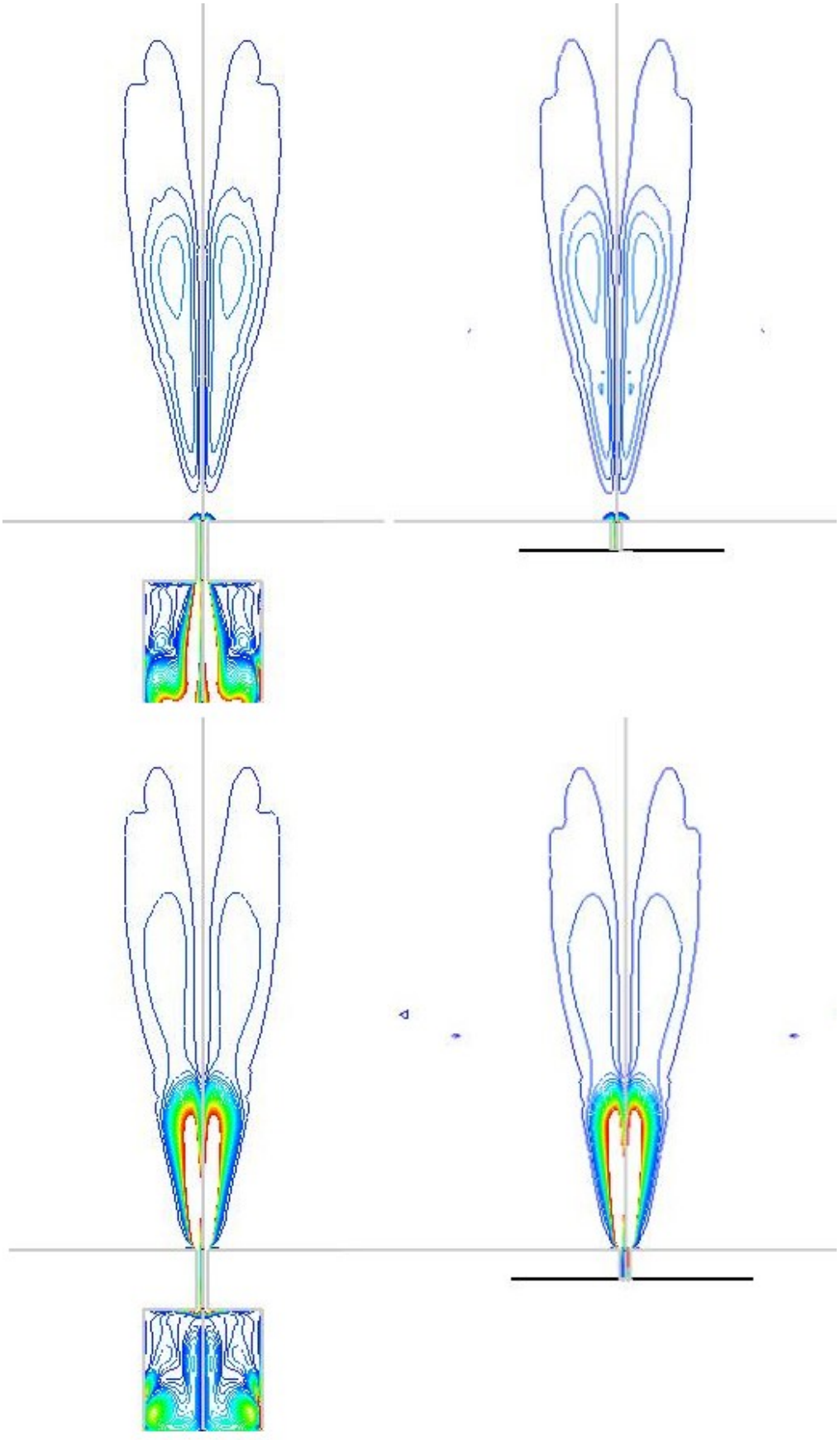

Figure 4.29: Comparison of vortex evolution in one cycle

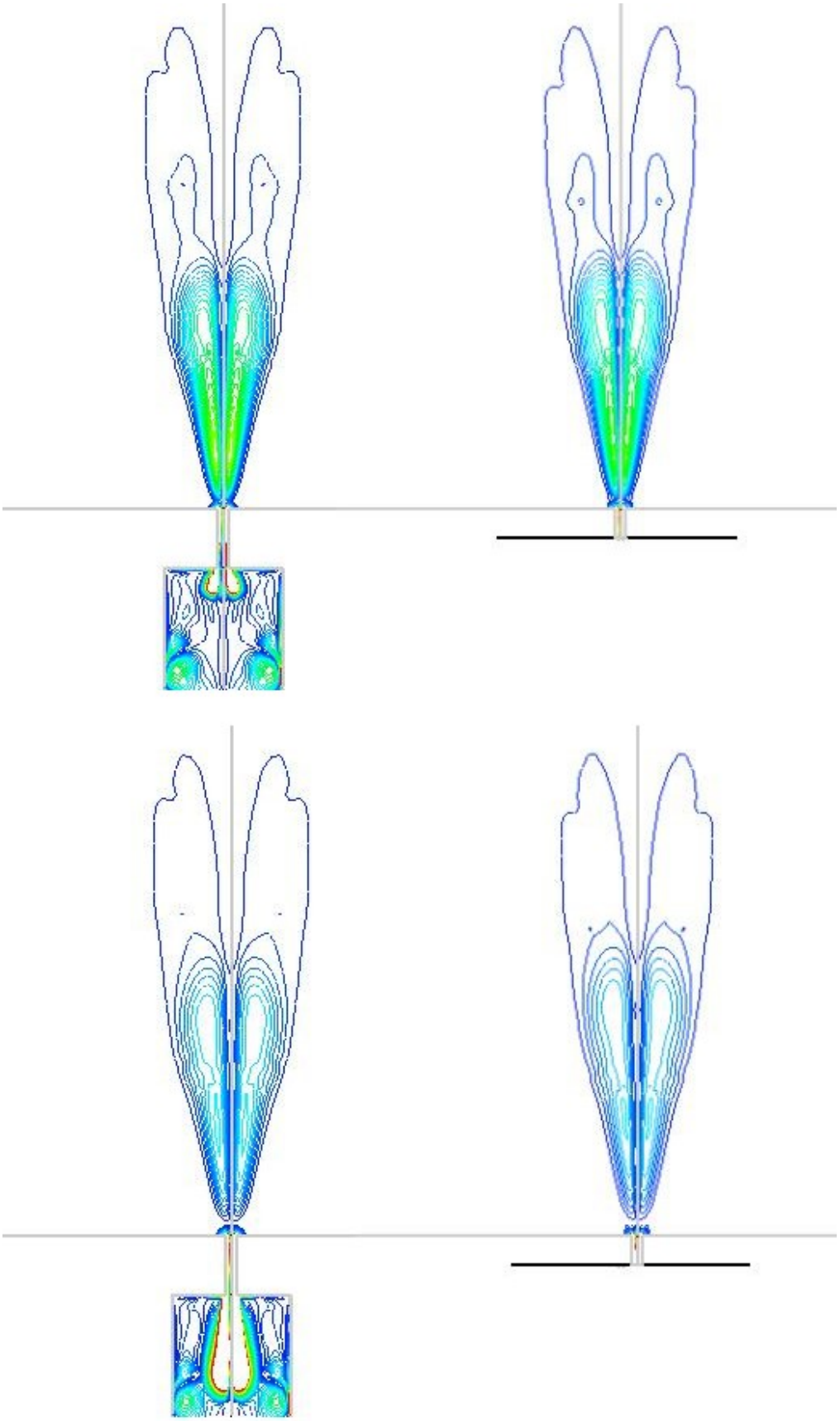

Figure 4.30: Comparison of vortex evolution in one cycle (continued)

4.5 Summary

In this chapter, a synthetic jet cavity model was derived based on the numerical study of free synthetic jet flows.

It was found that the pressure change mainly occurs in the nozzle/orifice, and that the pressure in the cavity is reasonably uniform. With this observation, the synthetic jet cavity was assumed as a lumped element device. The mass conservation equation was applied to the control volume including the cavity and the nozzle with an opening in the top wall. By assuming that the air in this system behaved as in a polytropic process, a first-order ODE in time with the cavity pressure the average velocity through nozzle/orifice as dependent variables was derived.

Another ODE was obtained by applying the mechanical energy conservation equation to the flow along the nozzle. By assuming the average velocity remained constant along the nozzle at any time instant, another first-order ODE coupling the nozzle average velocity and the cavity pressure was derived. The loss terms were calculated using pipe flows correlations.

The inputs for this model are the volume change in time, the working frequency, and the geometries of the cavity and nozzle. This system of ODE, is solved numerically to determine the cavity pressure and the average velocity through the nozzle/orifice. The solution can be used to determine the key parameters characterizing synthetic jet flow: the non-dimensional stroke length L_{stroke}/d_j and Re_{I_0}. In other words, once the design and operating parameters for the cavity are known, the synthetic jet flow is fully characterized by this model.

The performance of this model was examined. The testing examples covered nozzle diameter d_j from 0.5mm to 6.35 mm, working frequency f from 80Hz to 1000 Hz, cavity aspect ratio h_c/d_c from 1/4 to 4, area ratio A_{cav}/A_{nozzle} from 25 to 1600, and volume change $\Delta V/V$ from 0.75% to 10%. The proposed model accurately predicted the cavity pressure and the average nozzle velocity when the model parameters were determined by simple physical analysis or numerical matching. The overall RMS error of the cavity pressure and the average velocity was within 10% and 6% respectively.

This model is proposed to replace the fully simulated cavity. By assigning the average

velocity as the inlet boundary condition for an appropriate cross section of the nozzle, the synthetic jet flow could be resolved without simulating the cavity. One example presented in this chapter demonstrated the performance of this methodology. The modeled simulation well resolved the vortex dynamics of the synthetic jet flow compared to the full simulation. The flow field was well resolved too, with the RMS error of axial velocity less than 3% from one diameter from the nozzle to 40 diameters from the nozzle. The RMS error of the radial velocity was less than 10% in the near field and 20% in the far field. The increased error is believed due to mathematics involving the small magnitude of the radial velocity.

The model proposed in this chapter was derived from basic physical assumptions and simplifications. The governing equations used were mass and mechanical energy conservation. The parameters in the model can be determined by physical analysis or/and observations. From the results of testing examples, this model functions excellently. It can predict the pressure in the cavity and the average velocity through the nozzle with good accuracy. When the output of this model was assigned as the boundary condition to simulate synthetic jet flow, the flow field and vortex structure were well resolved.

In short, with properly chosen model parameters, this model can replace a simulation of the full cavity without losing much accuracy. The savings in computational resources are significant.

CHAPTER V

NUMERICAL STUDY OF SYNTHETIC JET IMPINGEMENT

Jet impingement is usually used where high heat transfer rates are desired. Similarly, synthetic-jet impingement heat transfer is promising in thermal management of micro-electronic systems.

Qualitatively, jet impingement heat transfer is improved with increased flow rate, turbulence, and decreased boundary layer thickness. Compared to conventional jet impingement, synthetic jets induce strong oscillation to the wall jets generated after impingement. This disturbance of the boundary layer enhances the heat transfer significantly. Thus, an in depth understanding of the flow and heat transfer characteristics of synthetic-jet impingement is desired.

Vukasinovic et al. (2001) [64] developed an active radial countercurrent heat sink driven by a synthetic jet actuator (Figure 5.1). Their experiments showed that this low-profile normal-impingement actuator provided efficient, localized, on-demand cooling in both open and closed test-section designs. Synthetic jet actuator technology also allows for efficient coupling between the local (device level) and global (system level) cooling processes. The heat sink showed a four-fold improvement in heat transfer compared to natural convection cooling. A 50 W heat dissipation was achieved at a case to ambient temperature difference of $T_{ca} = 50°\text{C}$.

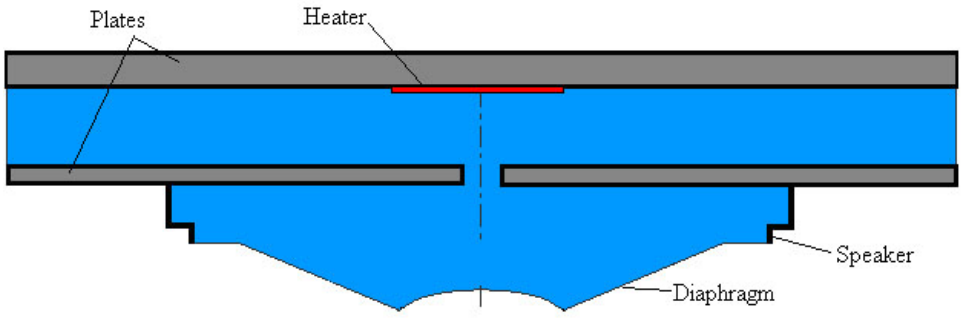

Figure 5.1: Synthetic-jet impingement heat transfer application

Tamburello (2003) [57] conducted a numerical study on a similar device to find the optimal design parameters, however heat transfer was not studied. His study was limited to the scaled geometry model used by Vukasinovic (2001) [64]. The nozzle/orifice diameter

in their studies was 6.35mm, which is significantly larger than those actually used in micro synthetic jet systems.

In this study, we employed CFD tools to investigate more general configurations of micro synthetic jets to understand the mechanism of synthetic-jet-impingement heat transfer.

5.1 Numerical Approaches

In this study, axisymmetric synthetic jet impingement was investigated numerically using the commercial CFD package FLUENT and CFDACE+. The synthetic jet flow was simulated by either one of the two approaches: full simulation with cavity included and/or simulation with a modeled cavity.

For the full-cavity simulations, the cavity was fully modeled with a piston-like moving diaphragm at the bottom. The dynamic mesh technique in FLUENT was employed to model the moving diaphragm. In the CFDACE+ simulations, the mesh-morphing technique was used. Air was modeled as an ideal gas, C_p, thermal conductivity, and viscosity were determined using piece-linear table or kinetic theory. If no heat transfer was involved, constant C_p, thermal conductivity, and viscosity at ambient temperature were used. The SST $k-\omega$ turbulent model was selected to simulate the turbulent flow. Details of these techniques and models have been discussed in previous chapters.

For those simulations with a modeled cavity, the cavity model introduced in Chapter 4 was used to generate the boundary condition in the middle of nozzle: the cavity and half of the nozzle were excluded from the geometry in these simulations. The turbulent flow was modeled using the SST $k-\omega$ equations. Material properties and other boundary conditions were the same as those in the full-cavity simulations.

In this study, both confined-synthetic-jet impingement and free-synthetic-jet impingement were investigated. Confined-synthetic-jet impingement refers to the configuration shown in Figure 5.1 with the bottom wall, and free-synthetic-jet impingement refers to the configuration without the bottom wall. The effects of synthetic-jet parameters, including nozzle diameter d_j, nozzle-to-impingement-plate distance H/d_j, working frequency f, non-dimensional stroke length L_{stroke}/d_j, and Re_{I_0} on the vortex dynamics, fluid flow, and heat

transfer characteristics were studied. Since jet-impingement heat transfer is usually more effective in the near field ($L/d_j < 10$), the near-field characteristics were analyzed more intensively.

5.2 Validation

To validate the numerical techniques used in this study, a mesh study and a time-step study were performed and the results of the numerical simulations were compared to experimental measurements (PIV) of the velocity field by Vukasinovic et al. (2001) [64]. The geometry of the synthetic jet used in the computational model (Figure 5.1) is exactly the same as the geometry used in the experiment. It consisted of a speaker-shaped cavity and a 1/4 inch diameter orifice. The thickness of the plate where the orifice is embedded was 1/8 inch. The diameter of the plates was 6 inches or 152.4 mm.

Because of the difficulty in measuring the motion of the speaker diaphragm, there is no measured data for the spatial profile of the speaker-shaped diaphragm. Only the displacement in the center was known. Therefore, the amplitude of the diaphragm in these simulations was determined by matching the volume change. In the simulation, the speaker diaphragm was modeled as a rigid moving wall, which is reasonable if the speaker works in its linear mode. Cases with plates distance of $2d_j$ and $4d_j$ (d_j is the diameter of the orifice) were selected to be shown here.

In Figures 5.2 to 5.5, the velocity profiles (maximum blowing stroke and suction stroke) at 16 vertical positions in the flow field of $H/d_j = 2$ case were compared to experiments. These are not normalized profiles, so the magnitudes of the velocity were compared too. The synthetic jet cavity was fully simulated. The numerical simulation resolved the velocity magnitude and profile reasonably well. There exists some discrepancies in the position near the impingement plate: the experimental data showed stronger disturbances in this region.

By examining the velocity vector plots of both CFD simulations (left) and PIV measurement (right) side by side (Figure 5.6 through Figure 5.7); we can conclude that the CFD simulation results agree with PIV measurement. The basic flow structures were resolved. The time-mean velocity fields from experimental measurement and CFD simulation were

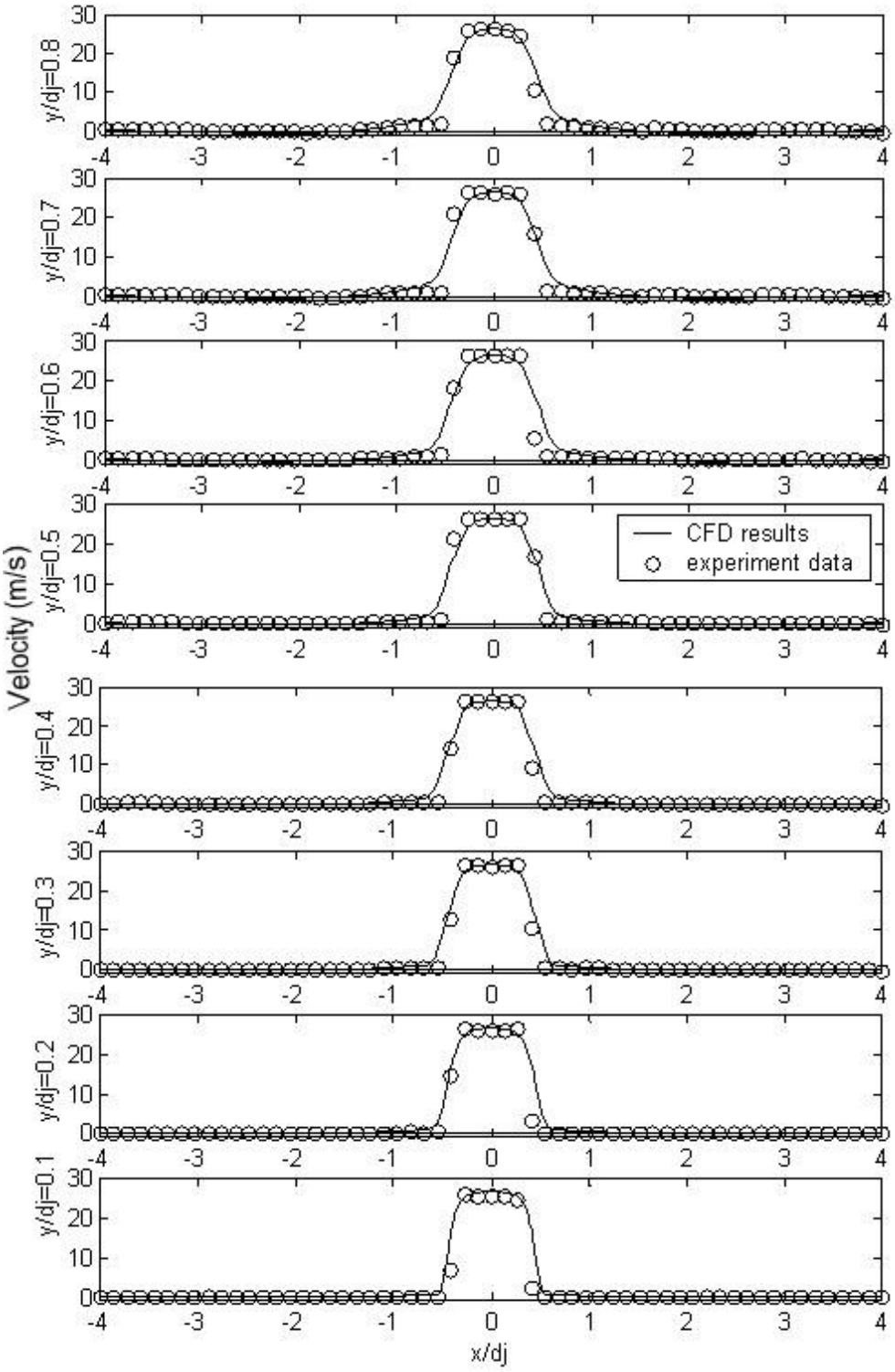

Figure 5.2: H/d_j=2 blowing stroke, f=80 Hz, d_j=6.35 mm

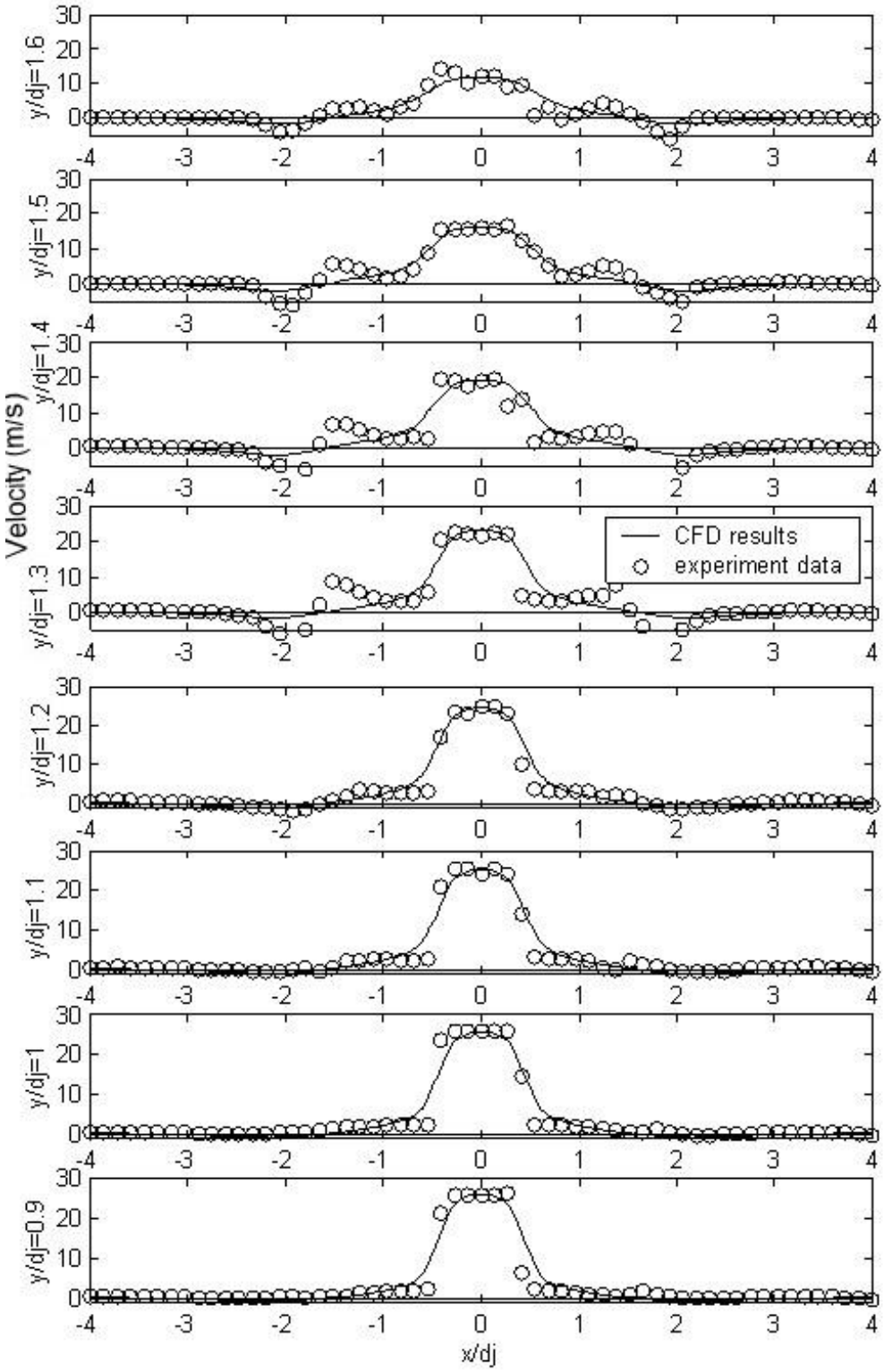

Figure 5.3: H/d_j=2 blowing stroke, f=80 Hz, d_j=6.35 mm (continued)

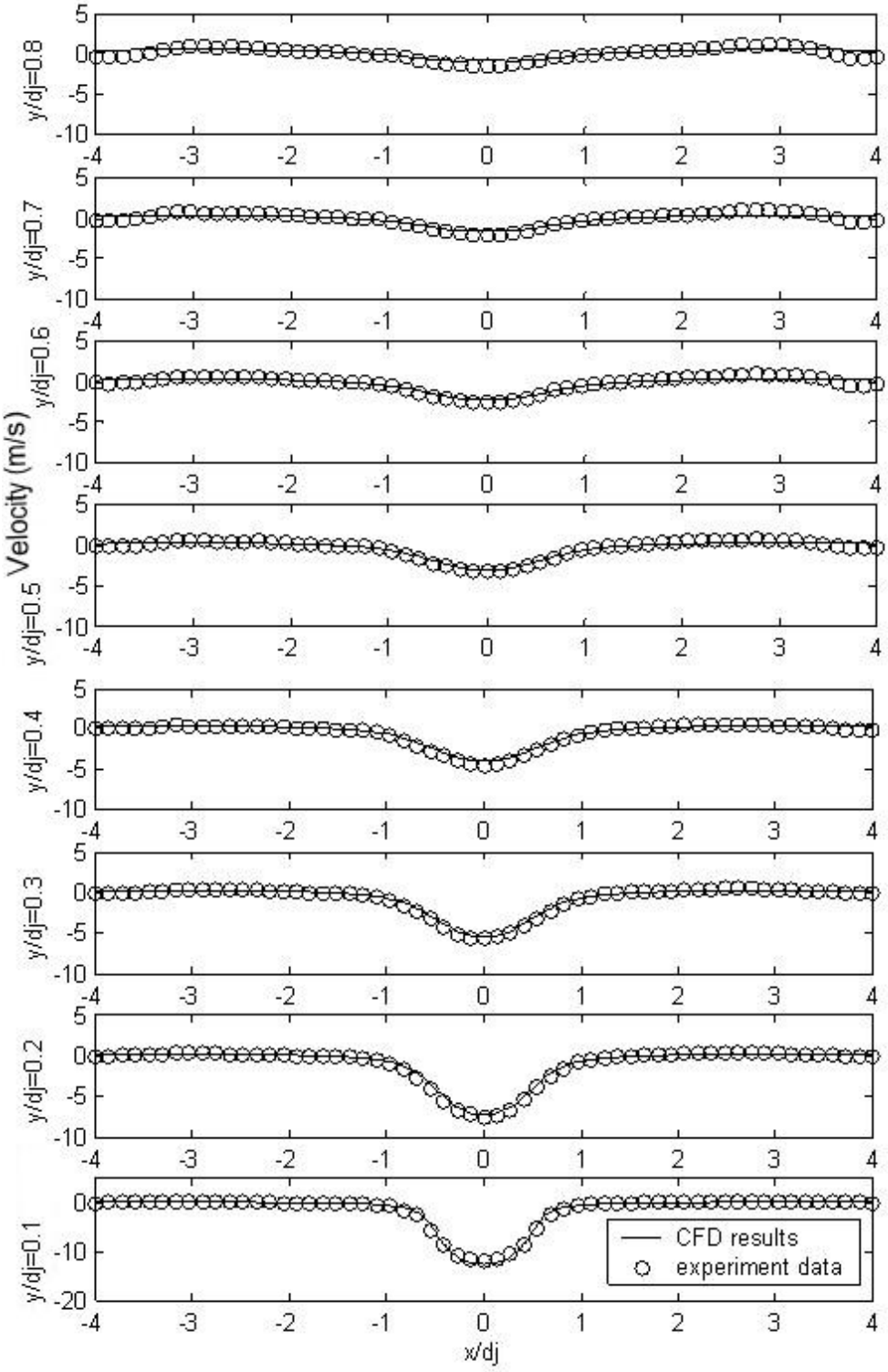

Figure 5.4: H/d_j=2 suction phase, f=80 Hz, d_j=6.35 mm

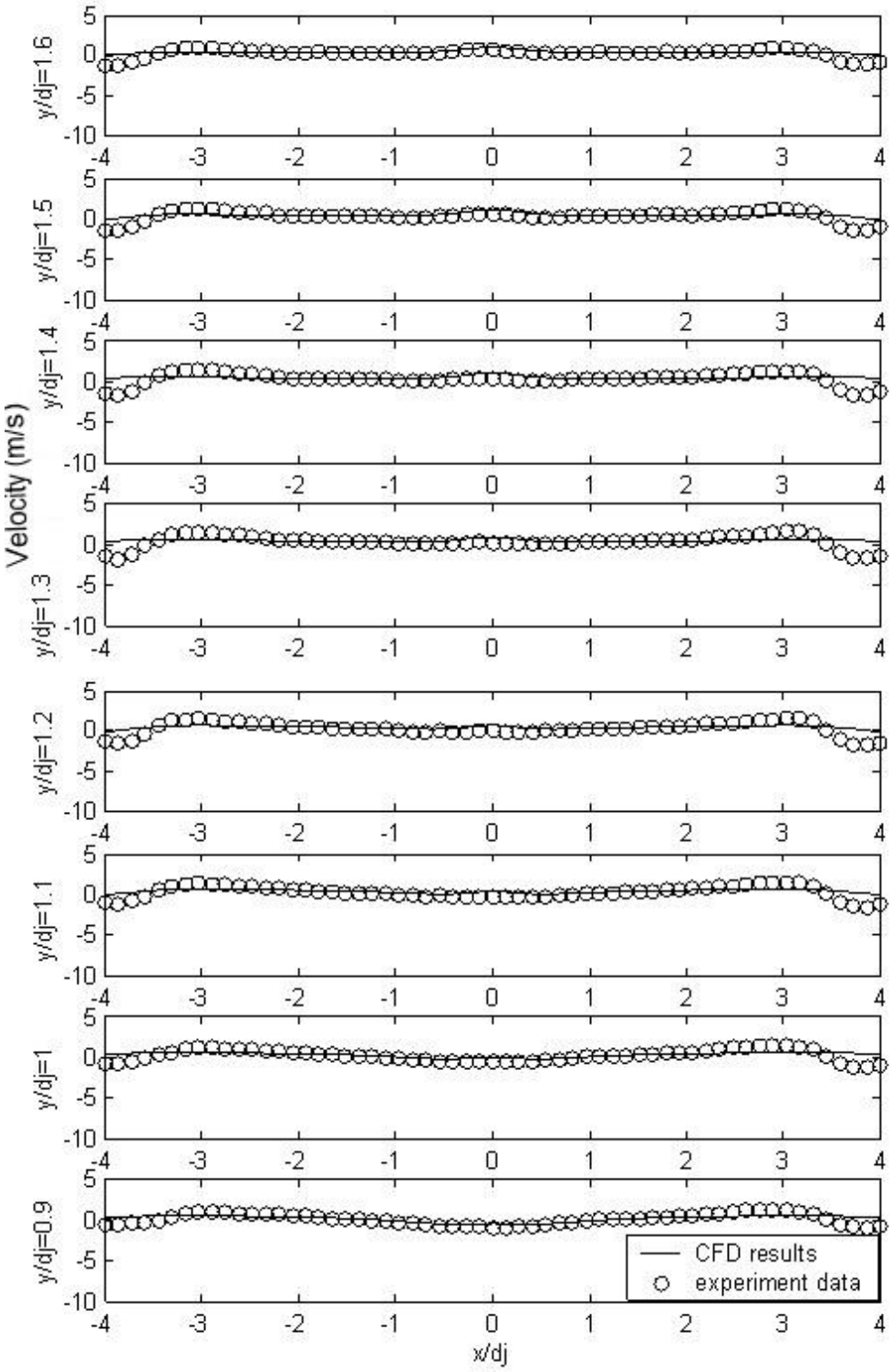

Figure 5.5: H/d_j=2 suction phase, f=80 Hz, d_j=6.35 mm (continued)

compared in Figure 5.8, the RMS error of axis-velocity is 13% and RMS error of radial-velocity is 10%. Although the overall vortex dynamics shows similar characteristics, there are discrepancies between the CFD simulation and PIV measurements. For better comparison, the CFD simulation results were interpolated onto the measurement points and a simple method of vortex tracking by checking the velocity direction change was used to automatically find the vortex ring trajectory. We found the vortex trajectory is closer to the centerline (axis) in the PIV measurement than in the simulations (Figure 5.9).

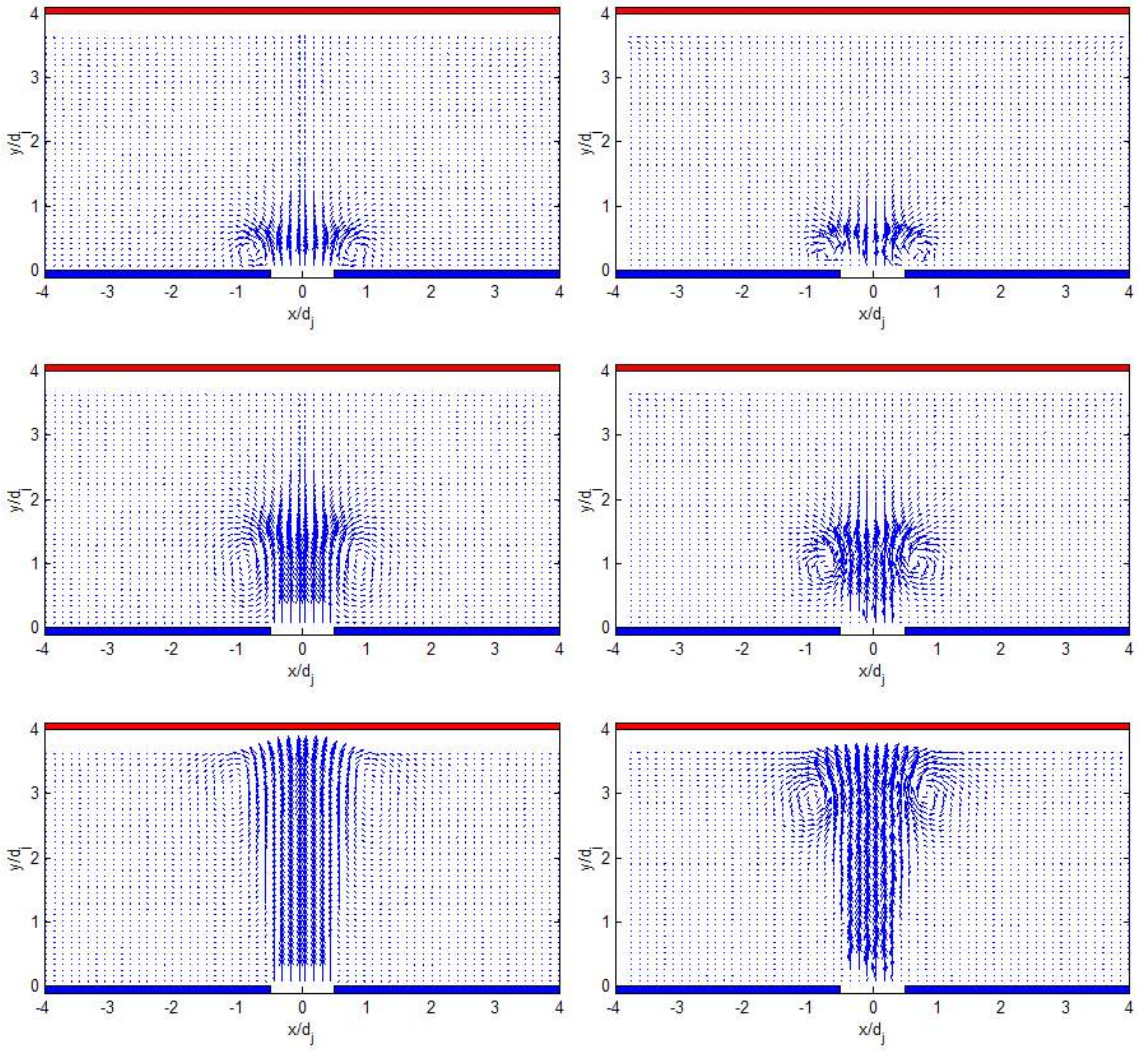

Figure 5.6: Velocity vector plots of PIV (right) and CFD simulation (left) H/d_j=4, f=80 Hz, d_j=6.35 mm

We examined the possible error that numerical techniques may induce. We tried to

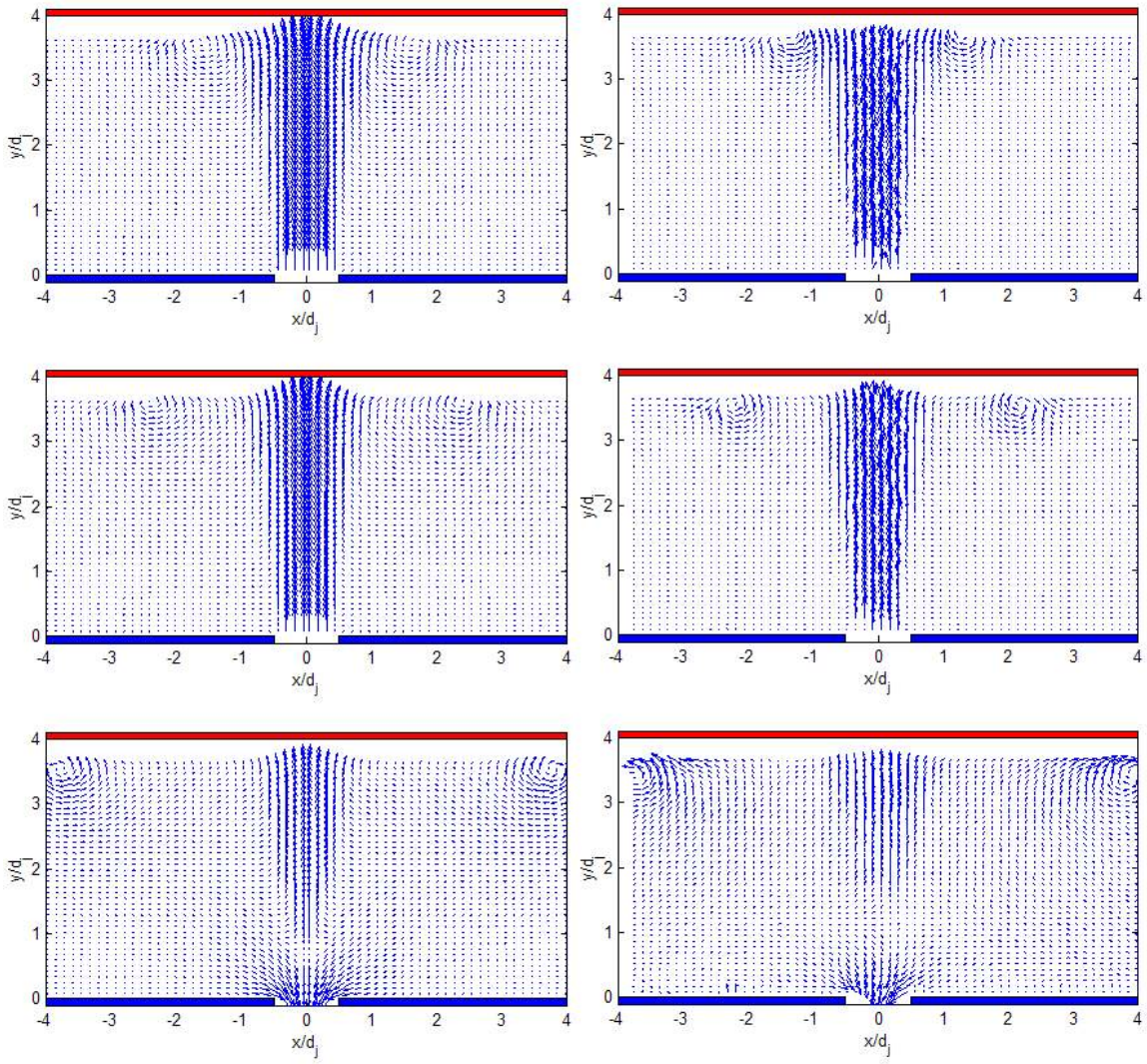

Figure 5.7: Velocity vector plots of PIV (right) and CFD simulation (left) H/d_j=4, f=80 Hz, d_j=6.35 mm (continued)

change the turbulence model setting (including $k-\epsilon$, SST $k-\omega$, laminar, and inviscid model) and mesh to reduce the difference. However, the results still showed similar discrepancy. However, in general, those numerical simulations did a reasonably good job on the overall flow field. The reason for the discrepancy may be the natural weakness of the numerical techniques. The simplifications in the cavity diaphragm modeling and cavity model itself induced errors. Some of the 3D effects of the system are hard to resolve using axisymmetric simulations. The reasons for the discrepancy may also come from the experimental uncertainty and resolution of PIV. The measurement plane not containing the

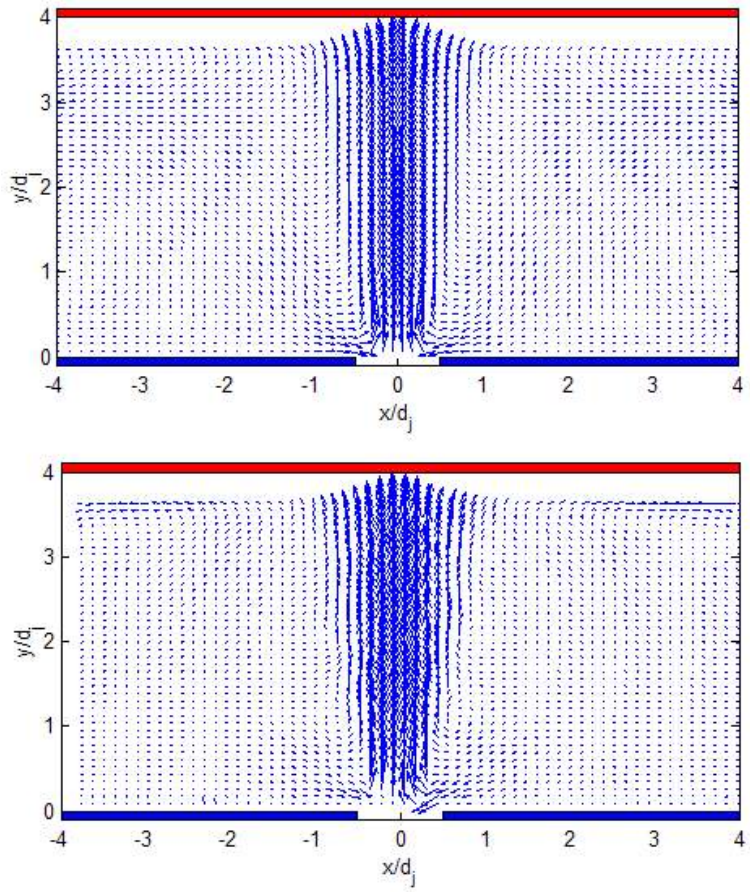

Figure 5.8: Velocity vector plots of PIV (bottom) and CFD simulation (top) H/d_j=4, f=80 Hz, d_j=6.35 mm

symmetry axis is another possible reason.

The geometry of the synthetic jet system used in the heat transfer validation is shown in Figure 5.10, which is same as that in experiment ([65]). The bottom surface is made out of two delrin pieces so that the contact thermal resistance between the disk (with mounted heater) and the ring in which the disk is inserted reduces radial conduction losses through the disk. A thick layer of foam insulation, placed underneath both the disk and the ring minimizes normal conduction losses. When the temperature at the center of the heater reaches 100°C, the disk underneath the heater expands to achieve a snug fit with the ring, thus providing a flat and impermeable impingement surface. A circular kapton heater (d_h/d_j = 13.6) with a cupronickel heating element is attached to the top of the delrin disk.

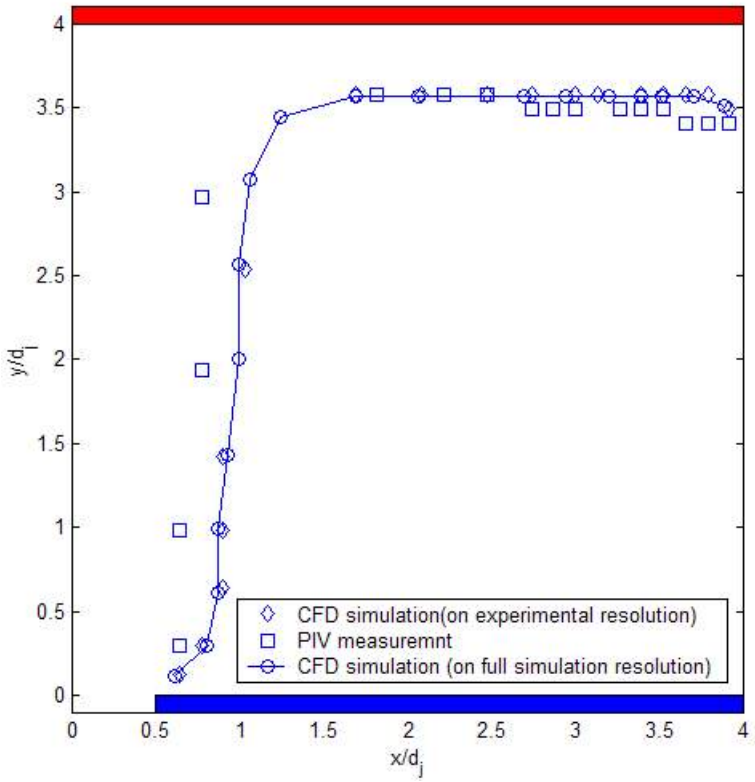

Figure 5.9: Vortex trace comparison of PIV and CFD simulation H/d_j=4, f=80 Hz, d_j=6.35 mm

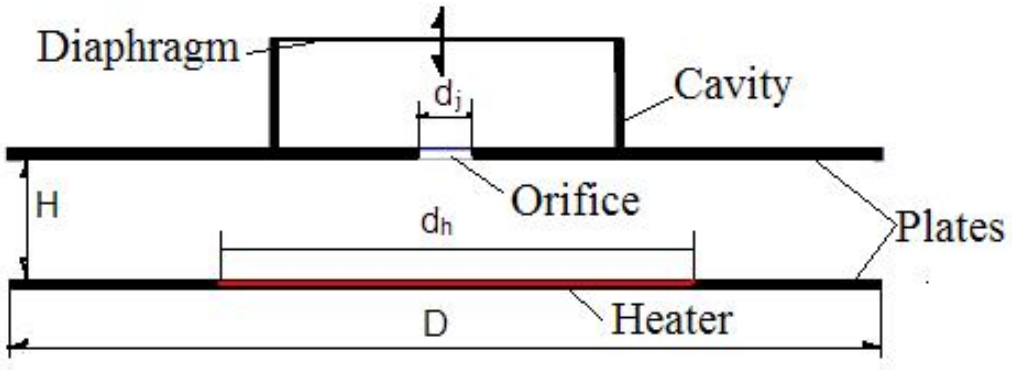

Figure 5.10: Geometry of synthetic jet impingement heat transfer validation

The heating element is sandwiched between two 51 μm thick kapton layers that are bonded to the heating element via 25 μm layers of adhesive. Due to the small thickness and low conductivity of these layers the lateral conduction losses through the heater are minimal and amount to at most 0.2% of the input power. The heater is assumed to yield a uniform heat flux. From experimental measurement, the amount of heat dissipated is 18W. It was estimated that 9% $\sim$ 16% of the total heat removed is through conduction from the top plate and radiation. The heat flux in the simulation was corrected accordingly.

The simulation was completed using FLUENT, the cavity was not included in the CFD simulation, and instead, the cavity model was used. A periodic velocity boundary condition was assigned to the inlet, which was in the middle of the nozzle. In the simulation, half of the nozzle geometry was included. The spatial distributions of temperature and heat transfer coefficient on the heater were available for comparison. In the experiment setup described above, no conjugate heat transfer simulation is necessary. Uniform heat flux boundary condition was assigned to the heater surface. The rest of the impingement plate was set as adiabatic. This was realized by applying a heat flux profile on the heater. The temperature of the inlet flow boundary was set to 340K, which was 42 degrees higher than the ambient(298K). The simulation configuration corresponded to the configuration of Jet III in the experiment: H/D=0.16, f=80 Hz, L_{stroke}/d_j=15.6. (Vukasinovic 2003 [65]) The results showed satisfying agreement. The CFD result for the temperature of the entire heater surface was 2.1% RMS error compared to experiment.

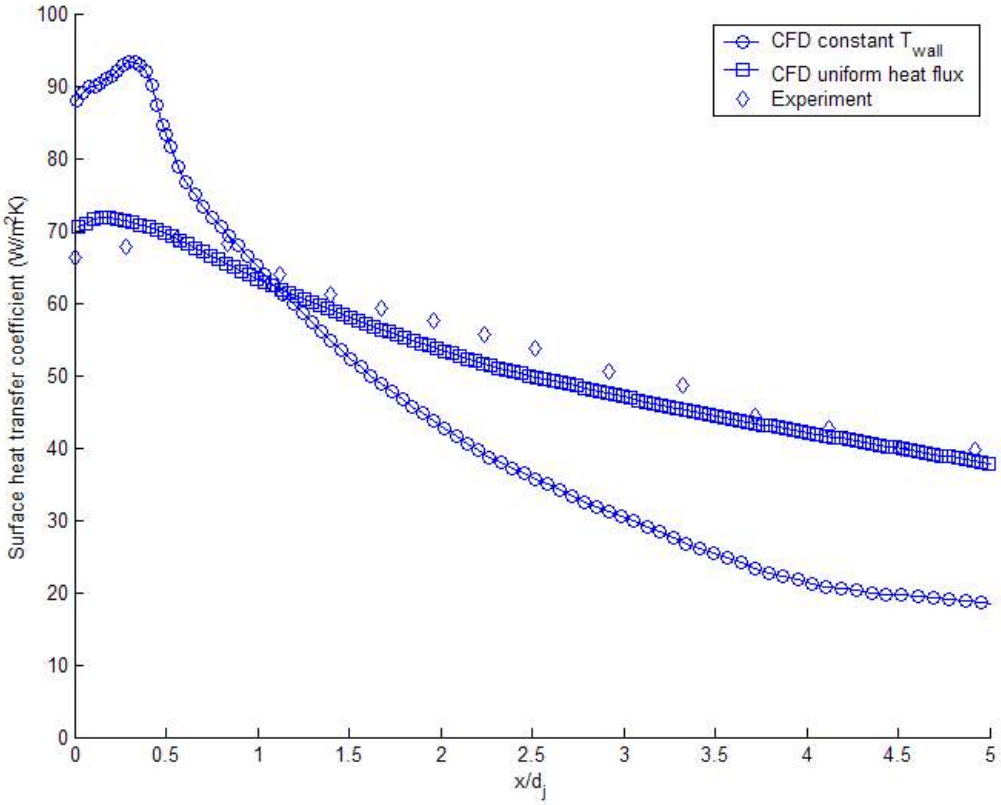

Figure 5.11: Surface Heat Transfer Coefficient Comparison

Heat transfer coefficient results were computed using the same method as in the experiment: $h_a = q/(T_h - T_a)$, ambient temperature(T_a) was selected as reference temperature.

The comparison of the surface heat transfer coefficient (SHTCO) is shown in Figure 5.11. The RMS errors for the ambient temperature based SHTCO is 3.71% (entire heater). Although the experiment set up is closer to the configuration using uniform heat flux, for comparison, we also plot the results from a constant temperature boundary condition simulation. The top plate was set at 390K and with an average jet temperature of 330K. The difference between using these two boundary conditions is significant.

The CFD results showed satisfying agreement with experiment, considering the synthetic jet characteristics were somewhat different from the experiment and the radiation and conduction heat transfer were not included in the simulation (only the heat flux was corrected correspondingly). Considering there was an approximately 10% uncertainty in the heat transfer coefficient measurement, the CFD results showed encouraging overall accuracy.

Although there were some discrepancies between simulation results and experimental measurement, the agreement is sufficiently good to validate the numerical approaches used. In the above validation process, we used both a full-cavity simulation and a modeled cavity simulation to simulate the synthetic jet. The results made us confident that the numerical approaches used in this study (and the entire work) are sufficiently accurate to yield physically realistic results for a synthetic jet flow and its applications.

5.3 Computational domain study

The effect of different computational domains at the outlet of this confined synthetic-jet impingement simulation was examined. The two different geometry models studied are shown in Figure 5.12. In computational domain 1, the real thickness of the top and bottom plates were modeled, and the computational domain was extends to at least 1.5H away from end of the channel to absorb the boundary effect of the corners and edges. In both cases, a pressure outlet boundary condition was assigned, i.e. P=0.

The pressure and velocity were compared at the orifice exit and a near-field plane located 1.425 mm above the jet exit. The centerline velocity and pressure are compared in

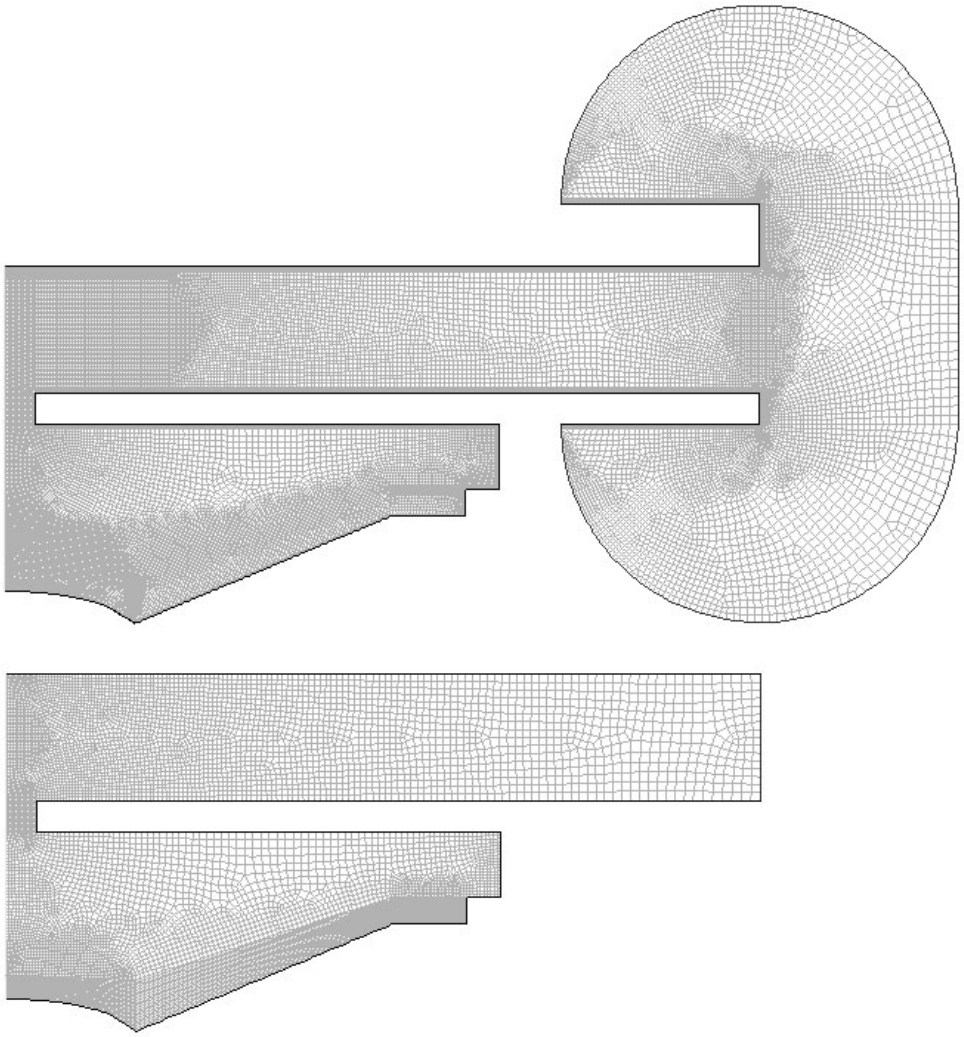

Figure 5.12: Typical meshes in computational domain study, domain 1(top), domain 2(bottom)

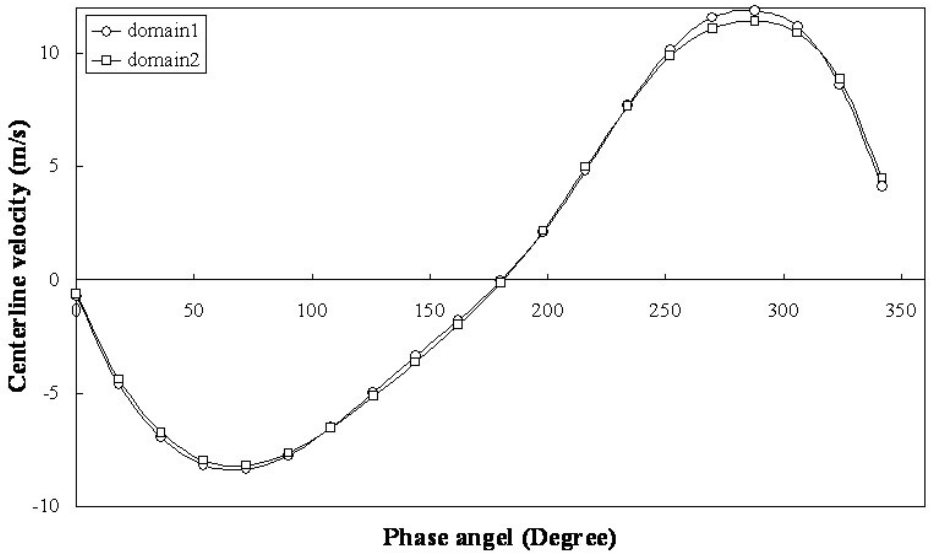

Figure 5.13: Streamwise velocity comparison in the middle of nozzle

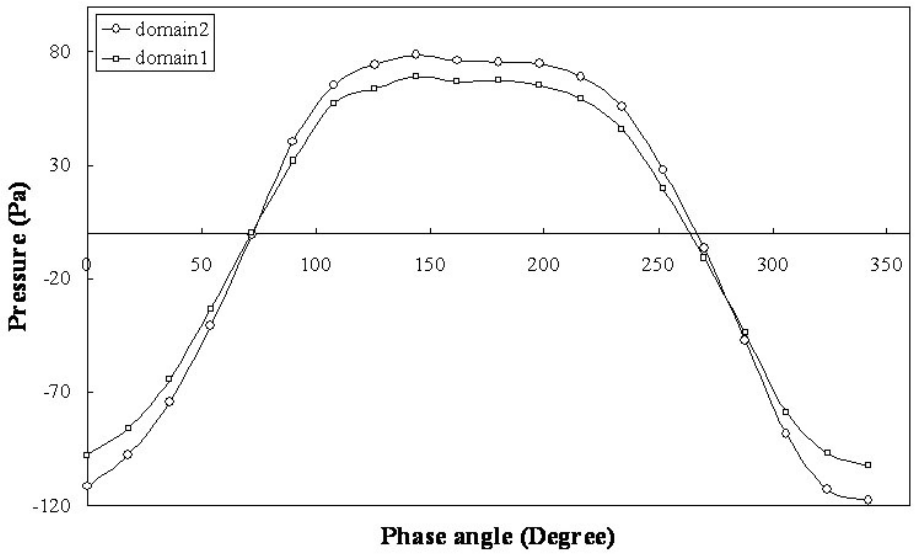

Figure 5.14: Centerline pressure in one period at a near field position (1.425mm from nozzle)

Figures 5.13 and 5.14. Figures 5.15 and 5.16 show the axial velocity and pressure along the horizontal, near-field plane. The RMS error of the centerline velocity in the near field above the jet exit over one period was 2.05%. The RMS error of the centerline pressure at this same point was 8.4%.

The results show that the extended computational domain is not as important as expected. The simpler domain 2 is sufficient to resolve the flow field. The pressure outlet boundary condition at the edge of channel is valid. Therefore, further simulations in this study use domain 2, and a pressure outlet boundary condition (P=0) was assigned.

5.4 Procedure

The convergence criterion was set at 10^{-3} for continuity, velocity components, k, and ω, and 10^{-6} for energy. Since the dynamic mesh technique in Fluent only works with the first-order implicit unsteady formulation, to be consistent, all simulations were performed using this scheme. The pressure-velocity coupling was SIMPLE in all cases. In all simulations, the results were considered periodic when the RMS error for certain monitored parameters during the last two periods were less than 0.5%. In impingement heat transfer simulations, the average top wall surface heat transfer coefficient, Nu, and the total heat transfer rate were monitored. The pressure and velocity at selected points representing both far-field and near-field positions were also monitored.

5.5 Vortex dynamics and the flow field

In synthetic-jet flows, the vortex dynamics well represents the flow fields and its characteristics directly affect the heat transfer. In this section, the vortex dynamics of an isothermal synthetic jet impinging on an isothermal plate are presented.

In a typical synthetic-jet impingement flow, the general characteristics of the vortex dynamics are the same even for different configurations. At first, the vortex pair generated from the nozzle/orifice moves towards the target plate, just like a free synthetic jet. After the vortex pair hits the top wall, two different phenomena were observed. If the non-dimensional stroke length L_{stroke}/d_j was sufficiently large, the vortex pair moved in the

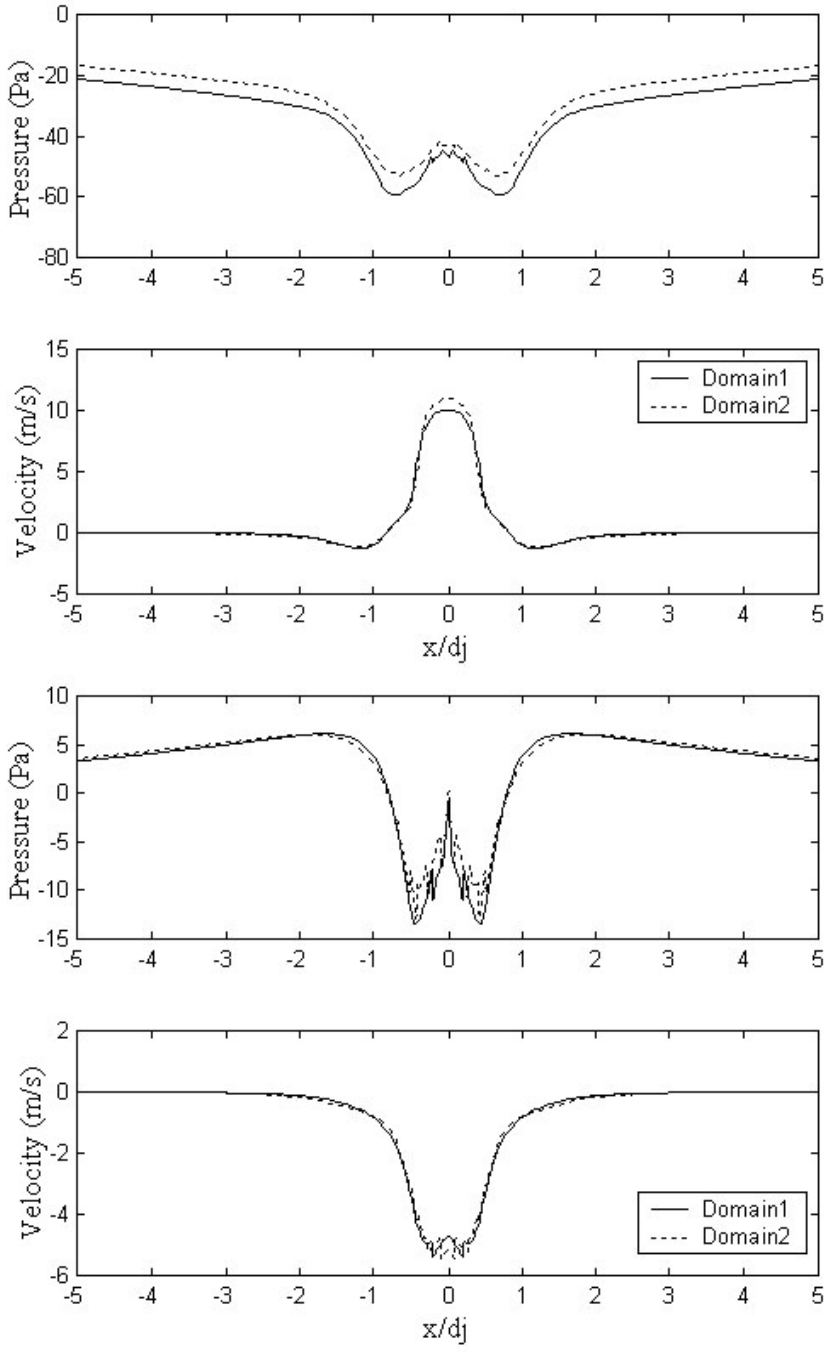

Figure 5.15: Comparison of axis velocity and pressure at blowing stroke (top) and suction stroke (bottom), d_j=6.35 mm, f=80 Hz

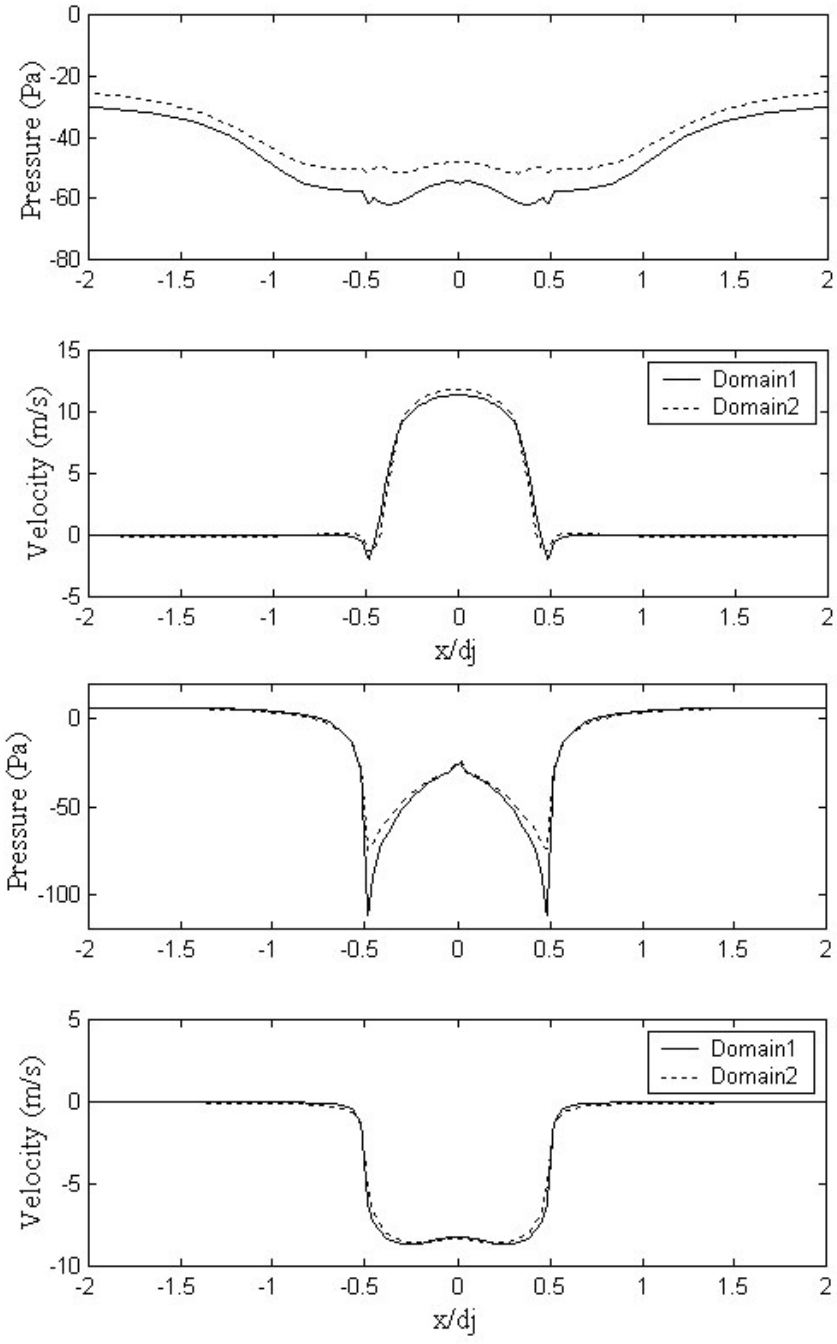

Figure 5.16: Pressure and axis velocity comparison at jet exit, blowing stroke(top), suction stroke(bottom), d_j=6.35 mm, f=80 Hz

radial direction and dissipated somewhere in the channel. Otherwise, the vortex pair stayed near the stagnation region or even moved a little back towards the orifice and dissipated some before it was sucked back into the cavity.

In Vukasinovic (2001) [64], it was found that a non-dimensional stroke length of at least 15 was needed in order to achieve meaningful heat dissipation. Our observations lead to similar conclusions. The vortex dynamics may well explain this heat transfer performance. When the non-dimensional stroke length is sufficiently large, for example over 12, the primary vortex pair impinges on the top wall and moves radially outward toward a large residual vortex pair located approximately $7d_j$ from the centerline. Simultaneously, two vortex pairs could be identified during one period.

The primary vortex pair merges into the residual pair just before a new primary pair emerges from the nozzle exit.

From Vukasinovic (2001) [64], a radial countercurrent flow between the plates entrains low temperature air from the ambient to help remove the heat. If the residual vortex is located close to the jet exit, it blocks this countercurrent flow and the overall heat transfer is poor. If the residual vortex moves closer to the outlet, the countercurrent works effectively to entrain low-temperature ambient air and the heat transfer improves. Also as the primary vortex pair moves radially outward along the impingement plate toward the residual vortex, it induces large velocity perturbations that enhance convective heat transfer. So when the residual vortex is located closer to the outlet, the region affected by the motion of the primary vortex is larger and the heat transfer performance is improved.

The flow field of synthetic-jet impingement with a speaker-shaped cavity is illustrated by streamfunction contours in Figures 5.17 and 5.18. In this case, the distance between the two plates is $2d_j$ and the non-dimensional stroke length is 13.3. Vorticity contours are shown in Figure 5.19.

Streamfunction contours and vorticity contours of configuration with H/d_j =4, 6, and 8 are shown in Figures 5.20 through 5.29. In these cases, the synthetic jet cavity is the same, and so the average jet exit velocities are equal. Therefore, the change in flow characteristics is the result of the change in the nozzle-to-impingement-plate distance H/d_j.

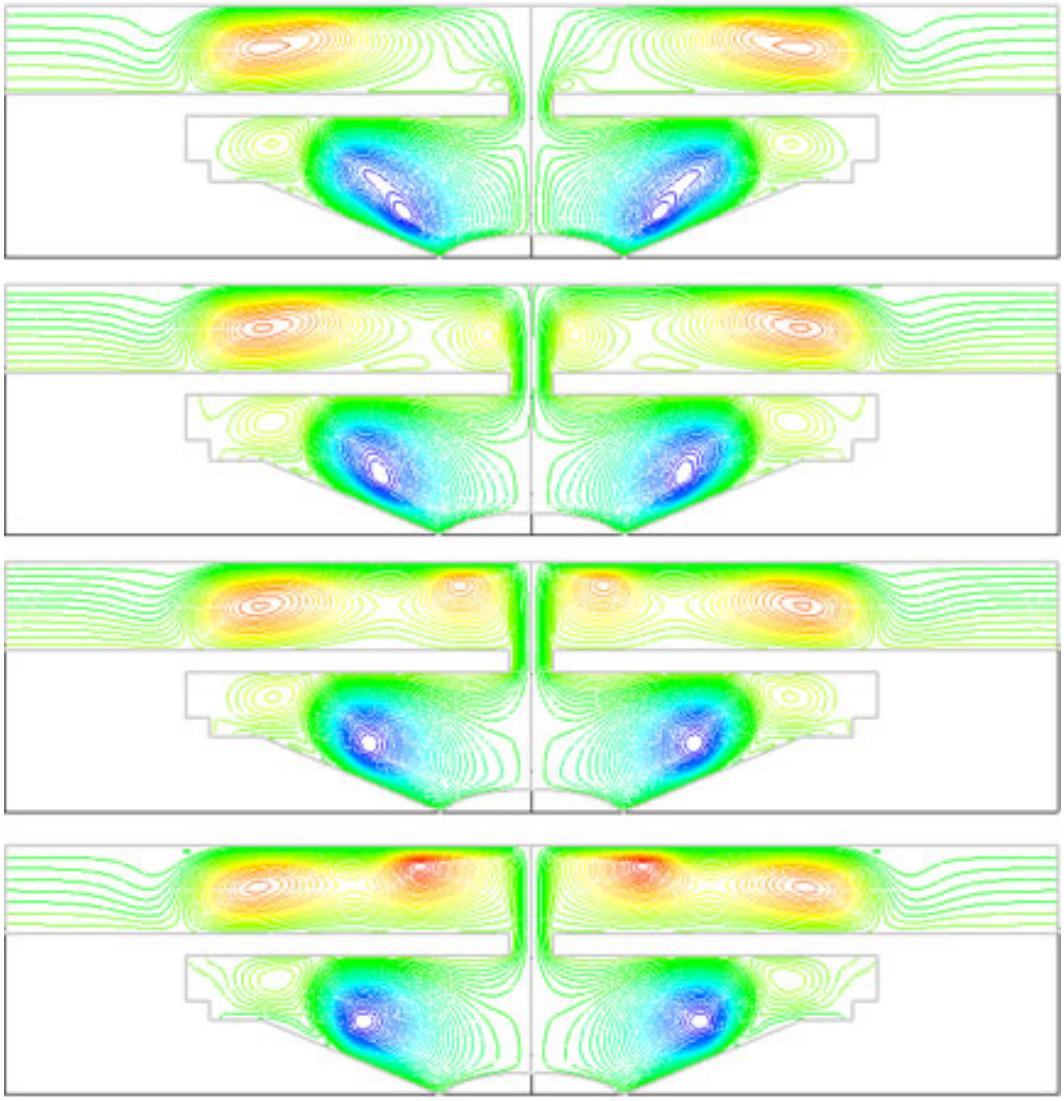

Figure 5.17: Stream function contours in one cycle (H/d_j=2)

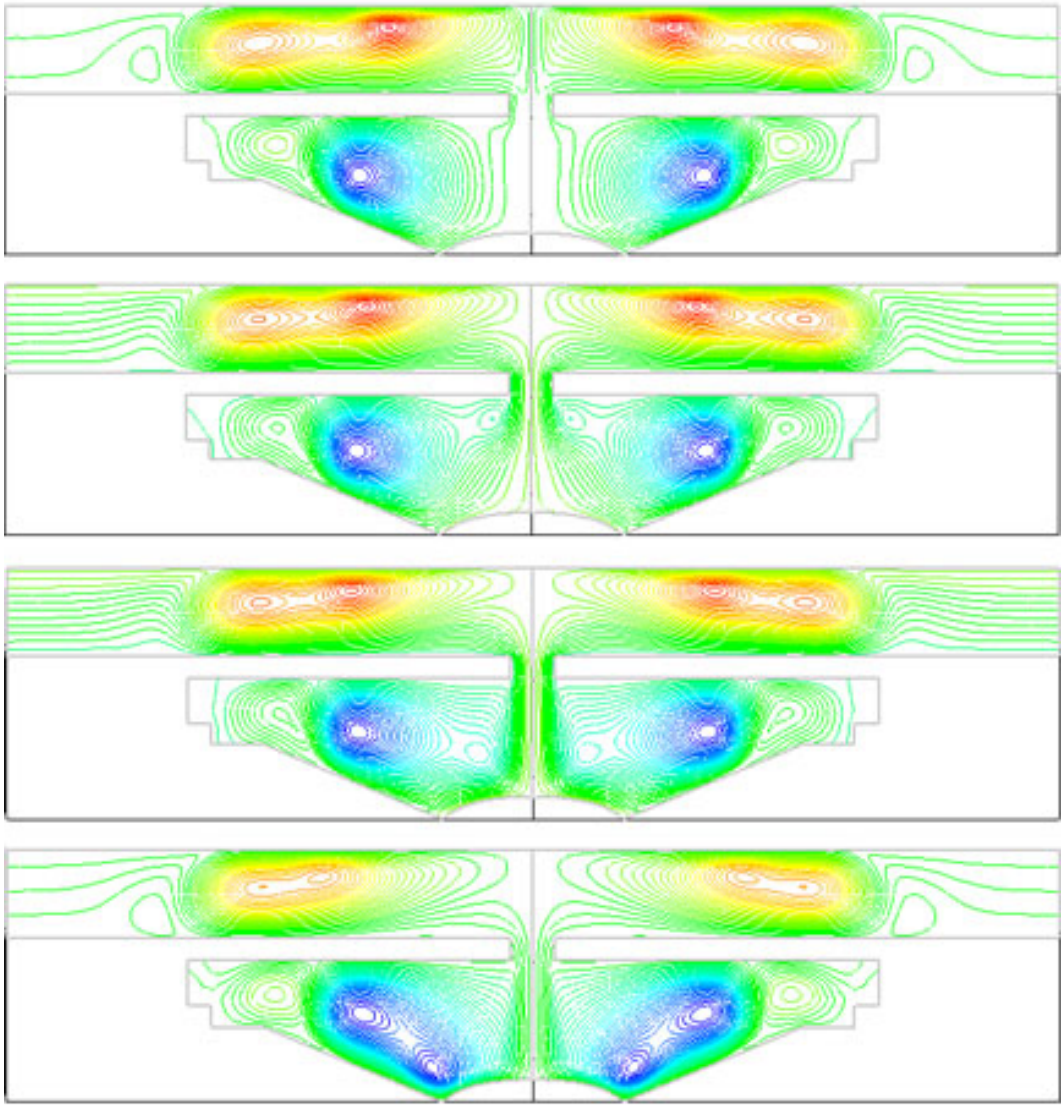

Figure 5.18: Stream function contours in one cycle (H/d_j=2, continued)

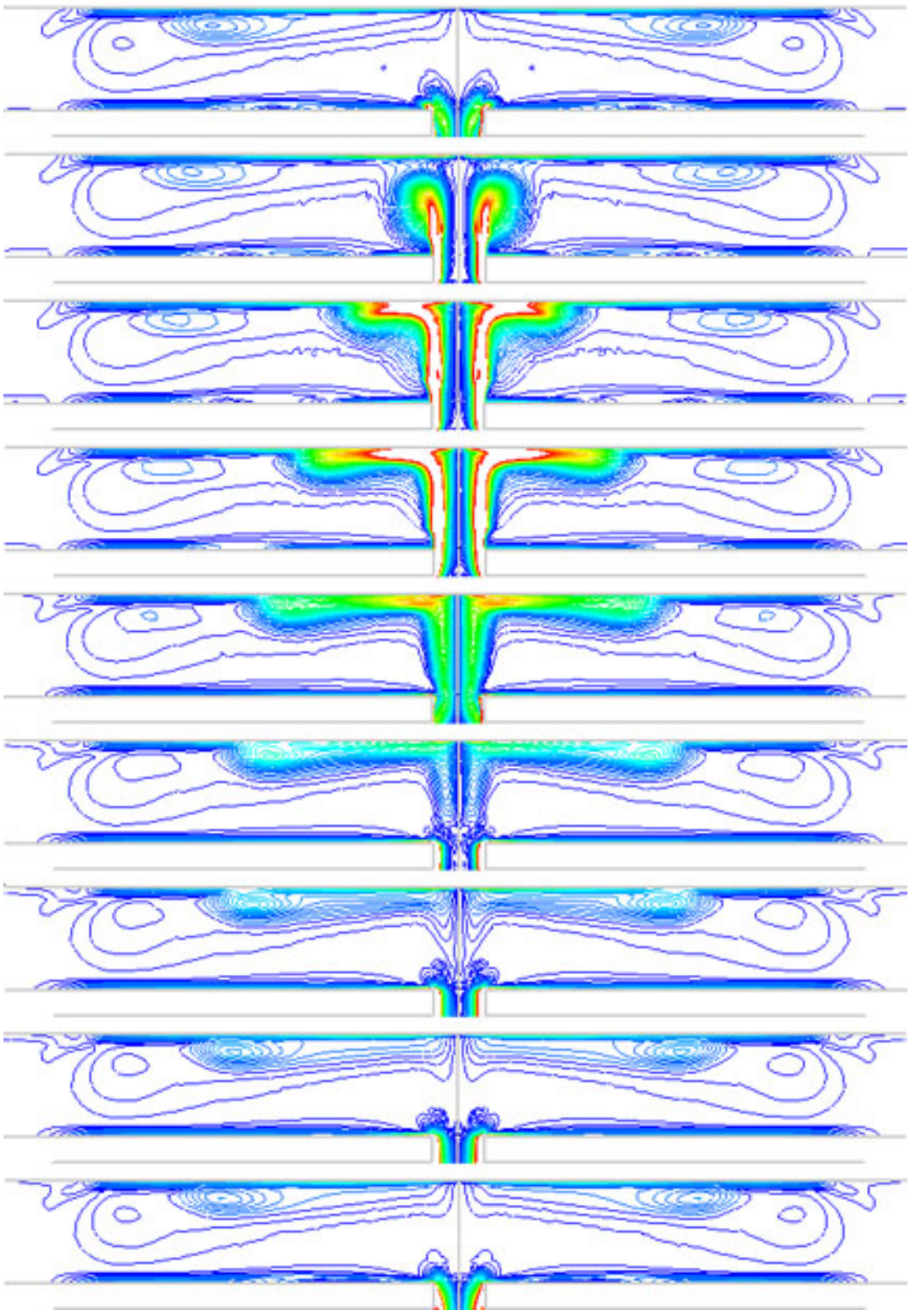

Figure 5.19: Vorticity contours in one cycle (H/d_j=2)

Although the flow pattern doesn't change when the distance between the plates increases, it is observed that the residual vortex pair moves further from the centerline. This implies that the highly disturbed flow region covers more area on the top plate, which improves heat transfer. However, at the same time the top wall is further from the nozzle/orifice and so the jet-impingement velocity decreases. Therefore, there exists an optimal distance that yields the best heat transfer performance. The heat transfer performance will be analyzed in detail in the next section.

The synthetic-jet impingement configurations studied in the experiments and in these numerical simulations are confined jets. It is known from conventional jet impingement studies that the heat transfer of confined-jet impingement is weaker than the corresponding free-jet impingement. To compare the difference in synthetic-jet flow characteristics, we also considered free synthetic-jet impingement. In Figures 5.31 and 5.32, we show the stream function and vorticity contours of synthetic-jet impingement with the same geometry as the $H/d_j = 8$ case, but with no bottom plate. The flow patterns are similar, but because there is no bottom plate, the residual vortex pair moves a little bit further from the top plate and it is larger.

Free synthetic-jet impingement with a nozzle/orifice diameter of 1 mm was also studied. The flow patterns with H/d_j =2, 4, 6, 8, and 10 are similar to the previous case. In Figures 5.33 through 5.36, vorticity contours for the cases with H/d_j =2, 4, and 8 are shown.

5.6 General heat transfer characteristics and comparison with conventional jet impingement

The heat transfer performance was evaluated by means of the total heat transfer rate, the surface heat transfer coefficient, and Nu. To illustrate the general heat transfer characteristics of synthetic jet impingement, both confined impingement (with a speaker-shaped cavity) and a free synthetic-jet impingement were analyzed. Next the heat transfer performances

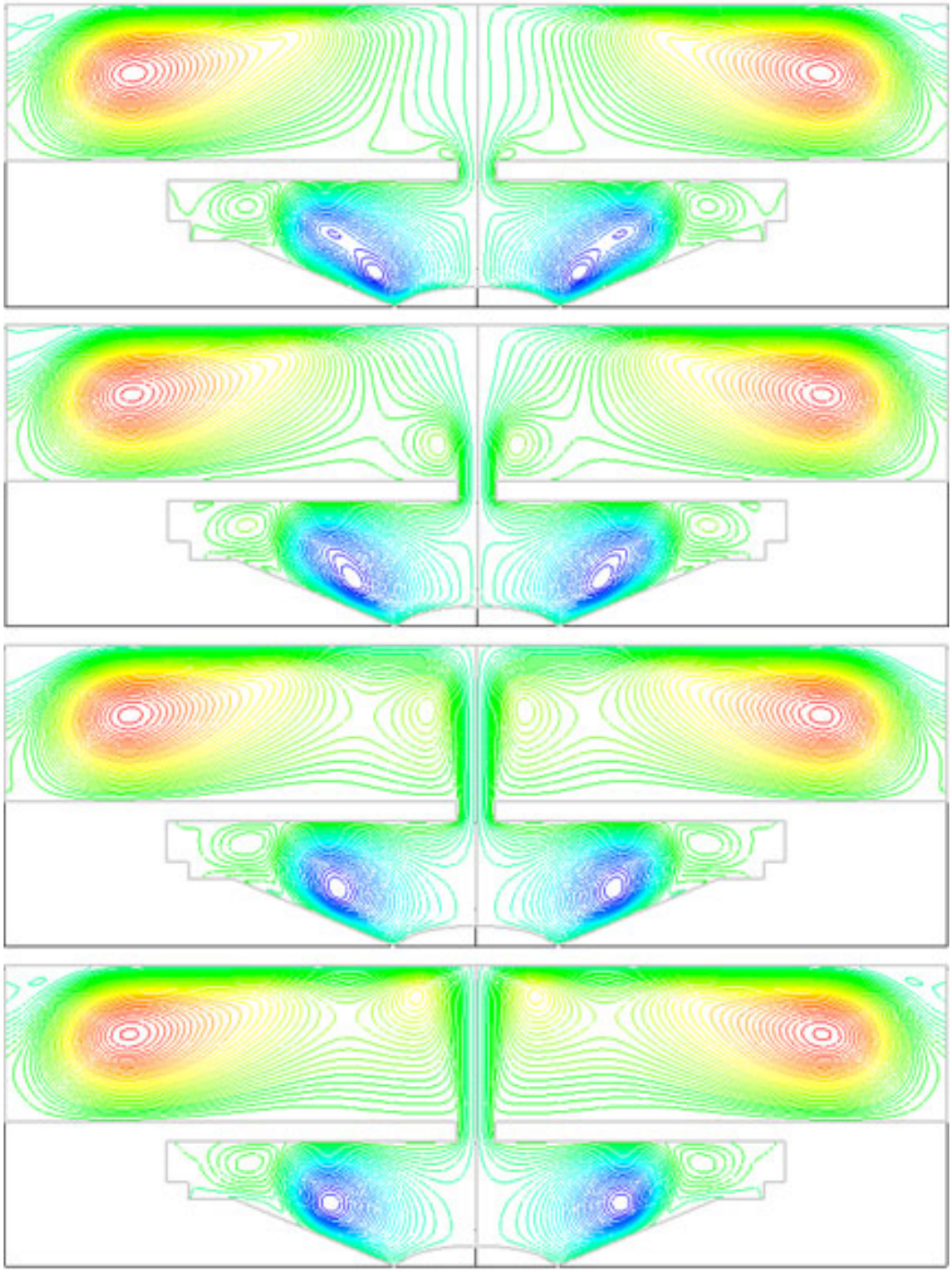

Figure 5.20: Stream function contours in one cycle (H/d_j=4)

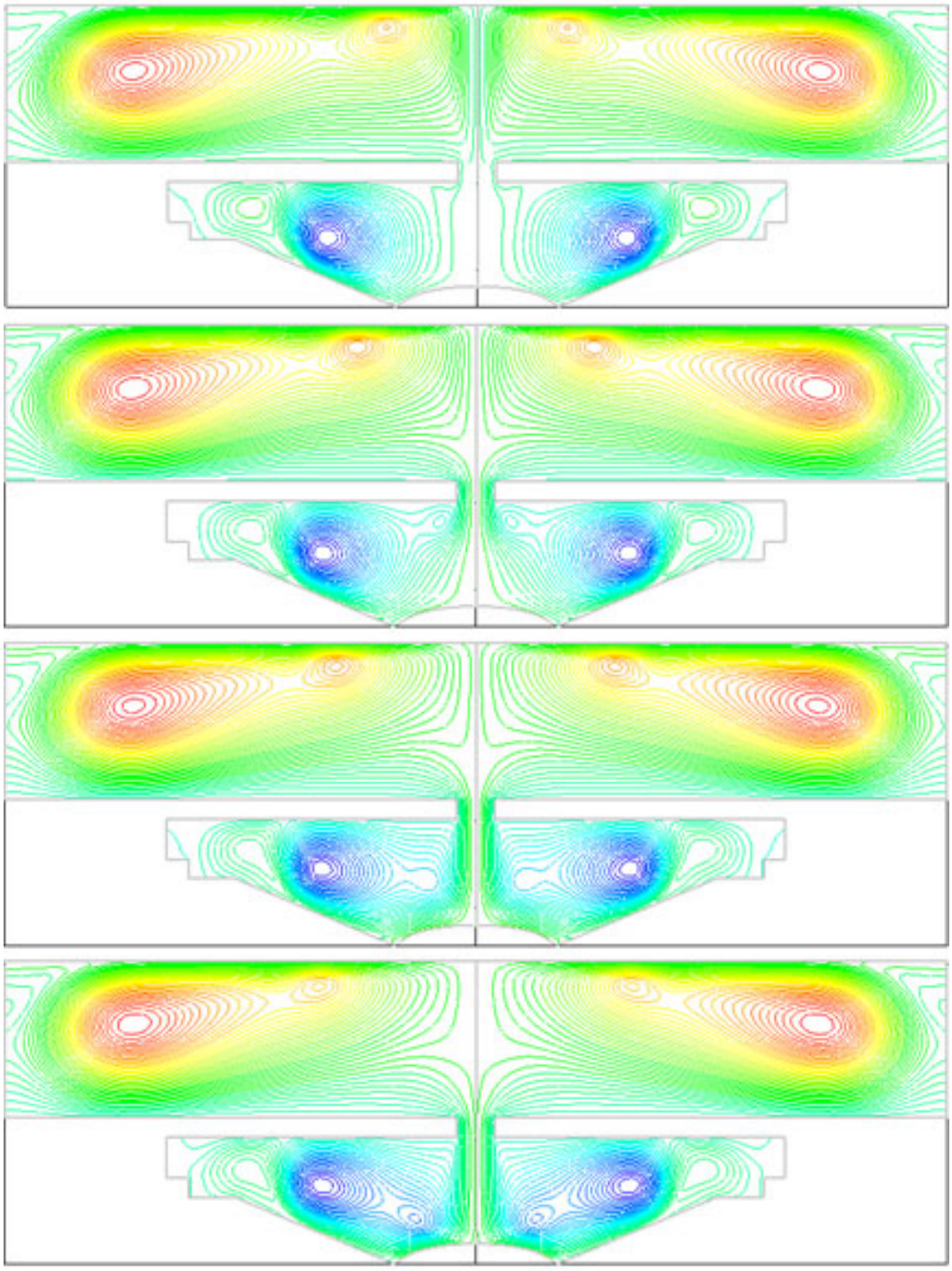

Figure 5.21: Stream function contours in one cycle (H/d_j=4, continued)

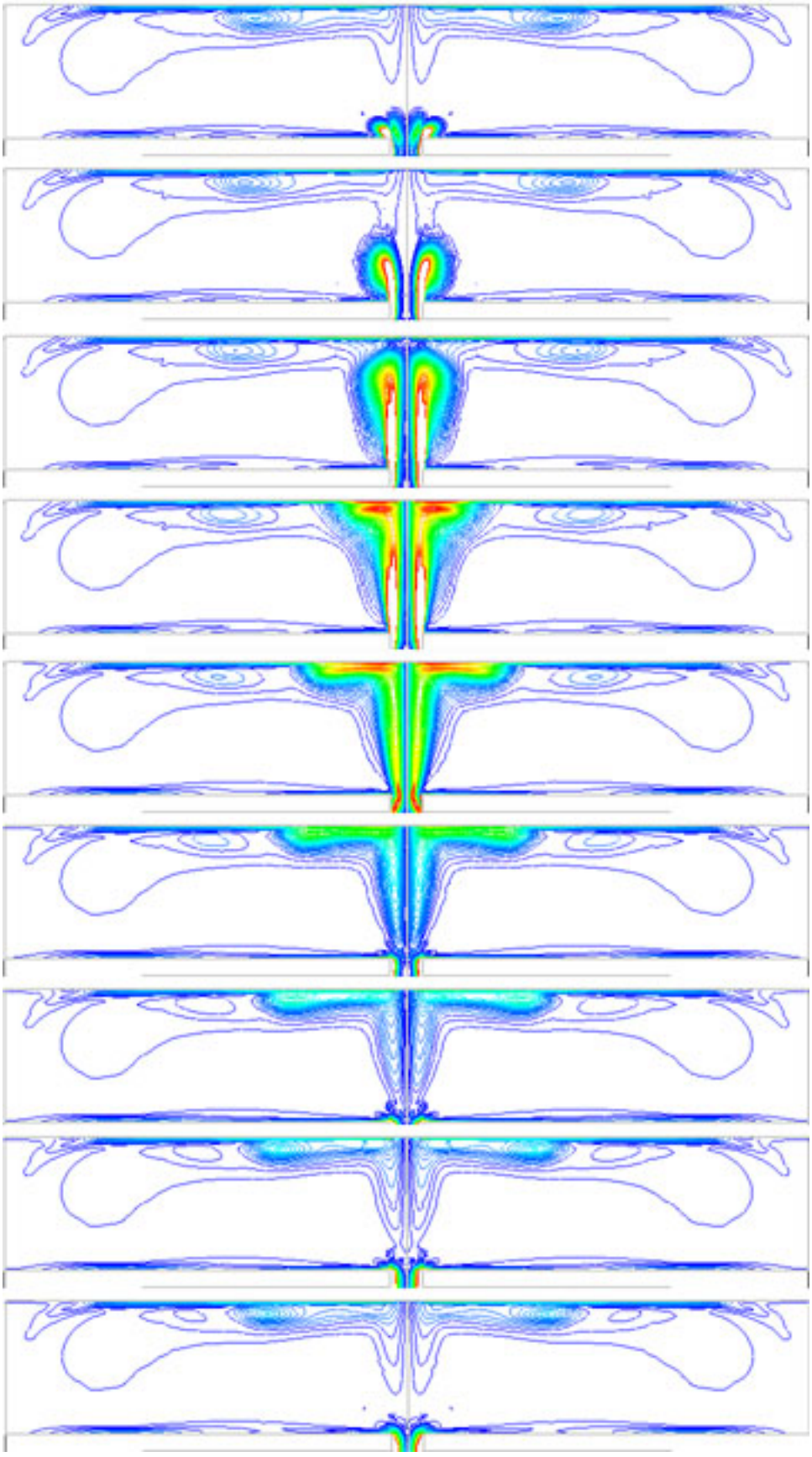

Figure 5.22: Vorticity contours in one cycle (H/d_j=4)

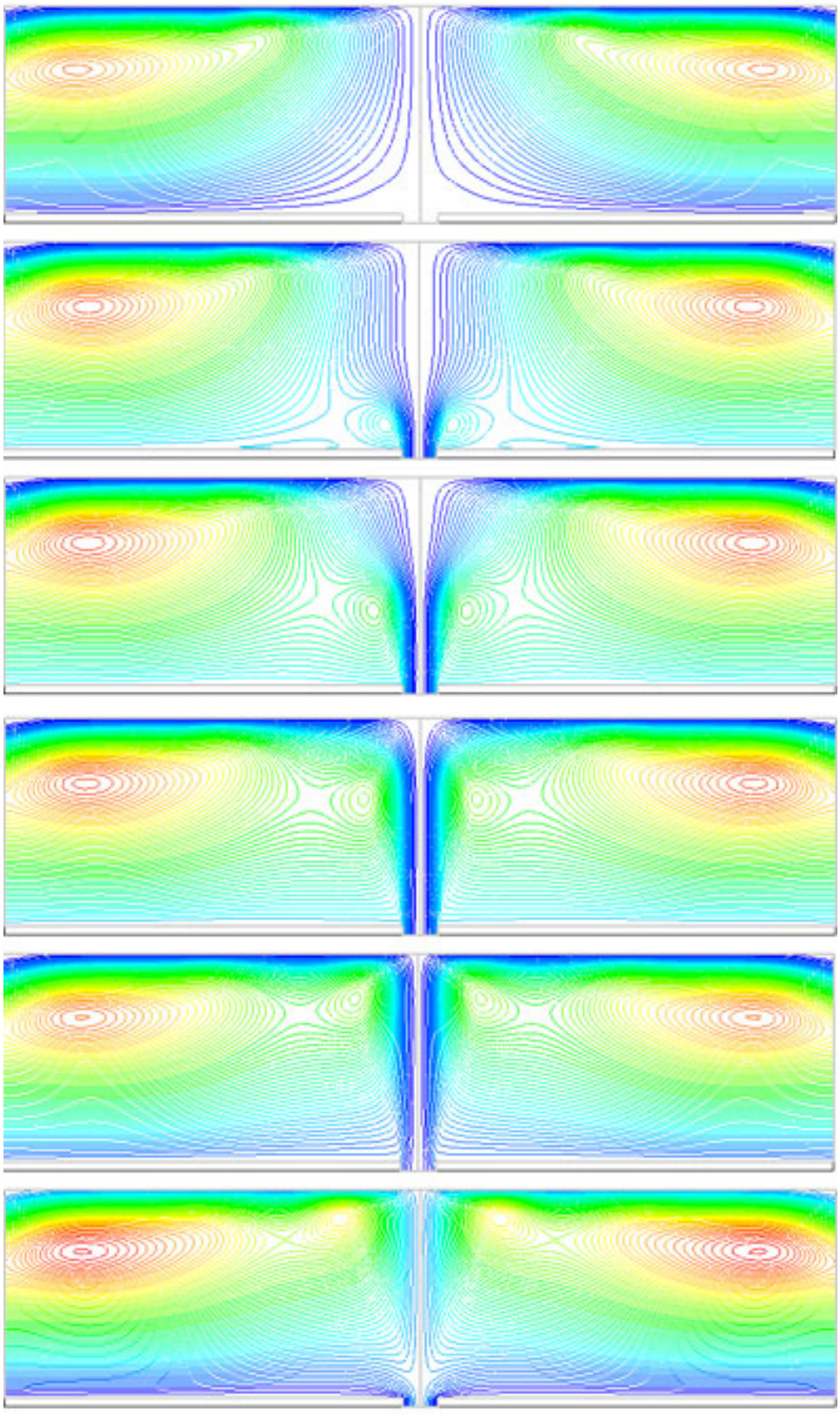

Figure 5.23: Stream function contours in one cycle (H/d_j=6)

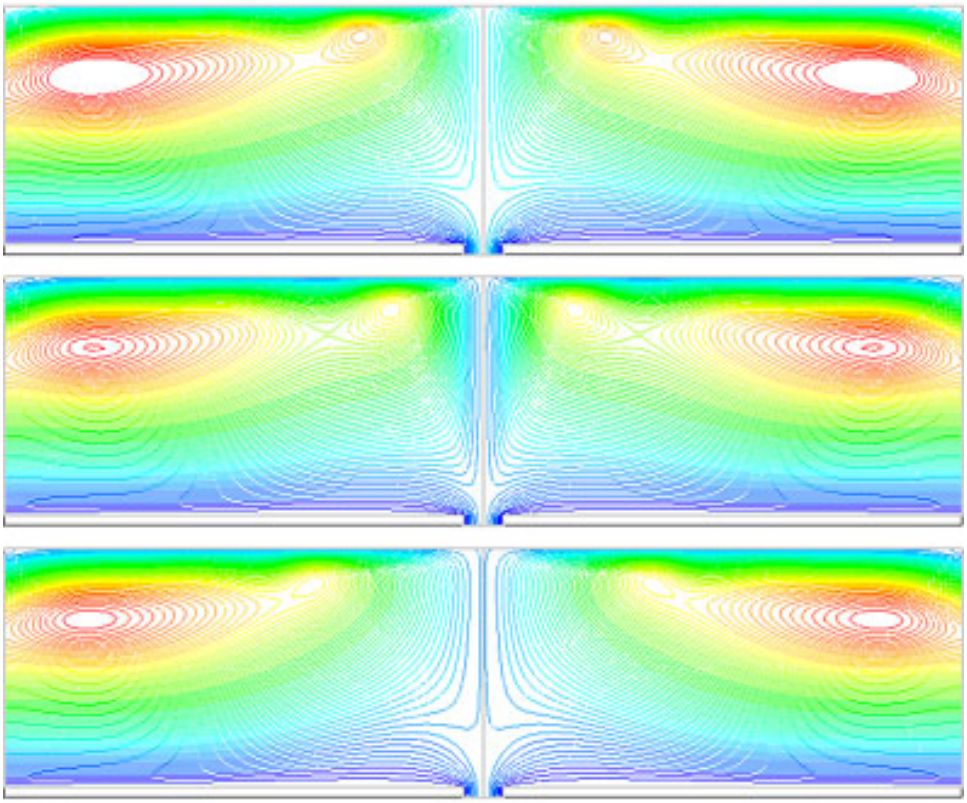

Figure 5.24: Stream function contours in one cycle (H/d_j=6, continued)

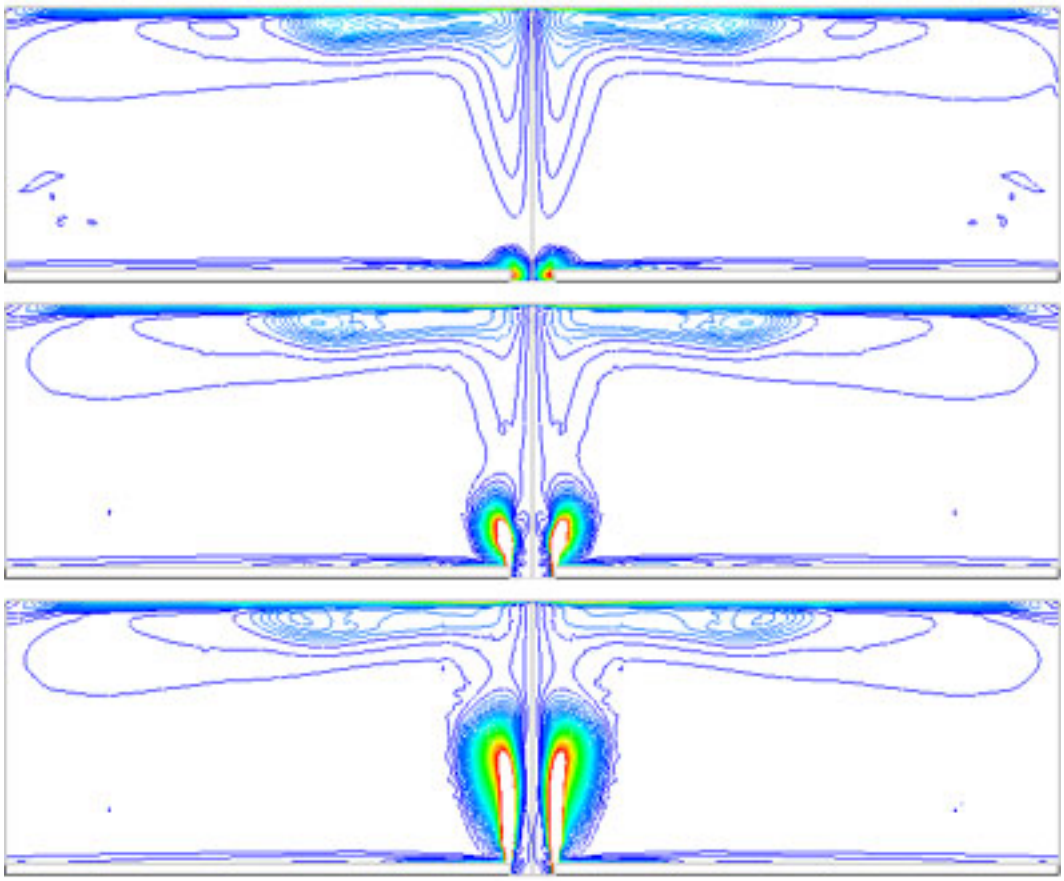

Figure 5.25: Vorticity contours in one cycle (H/d_j=6)

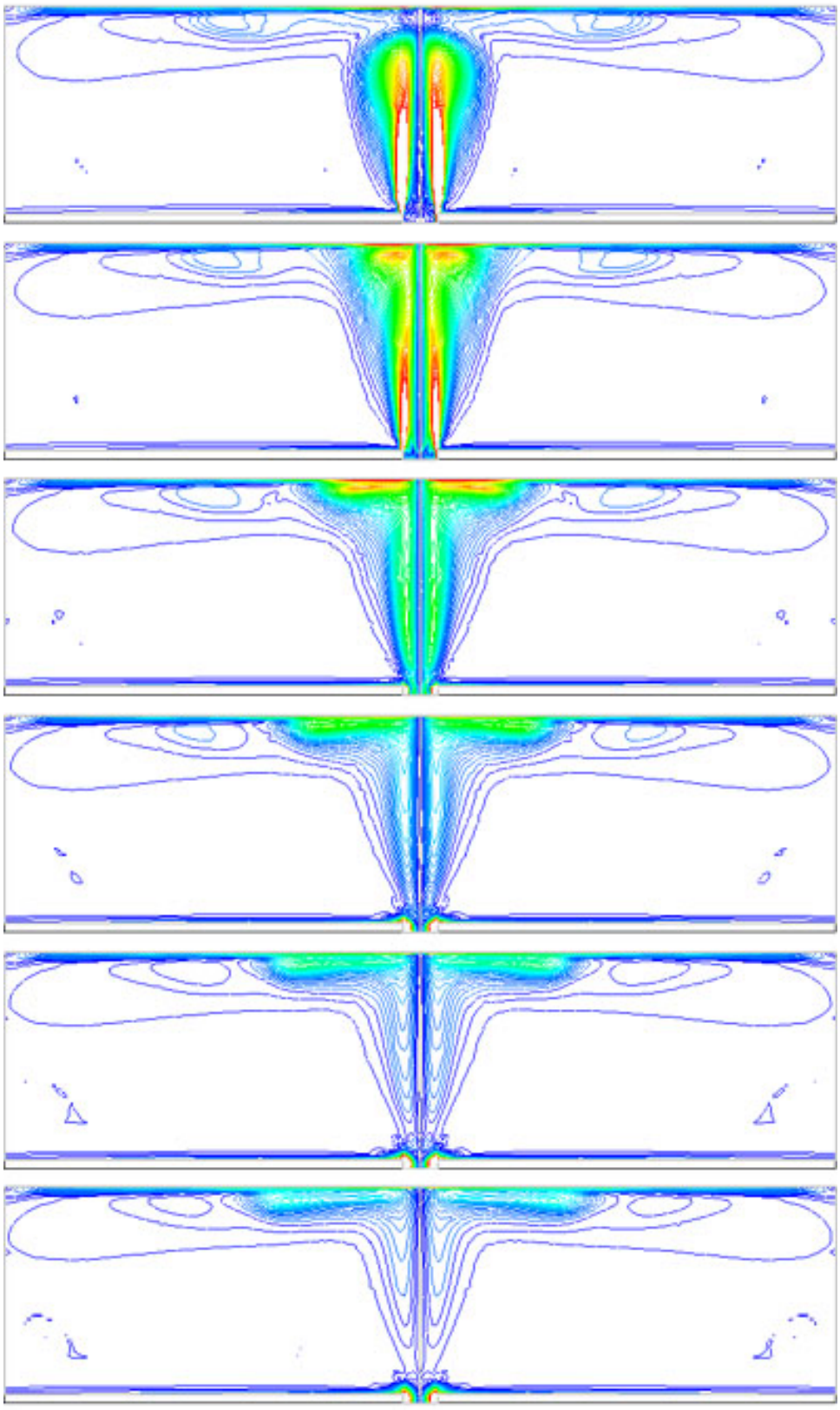

Figure 5.26: Vorticity contours in one cycle (H/d_j=6, continued)

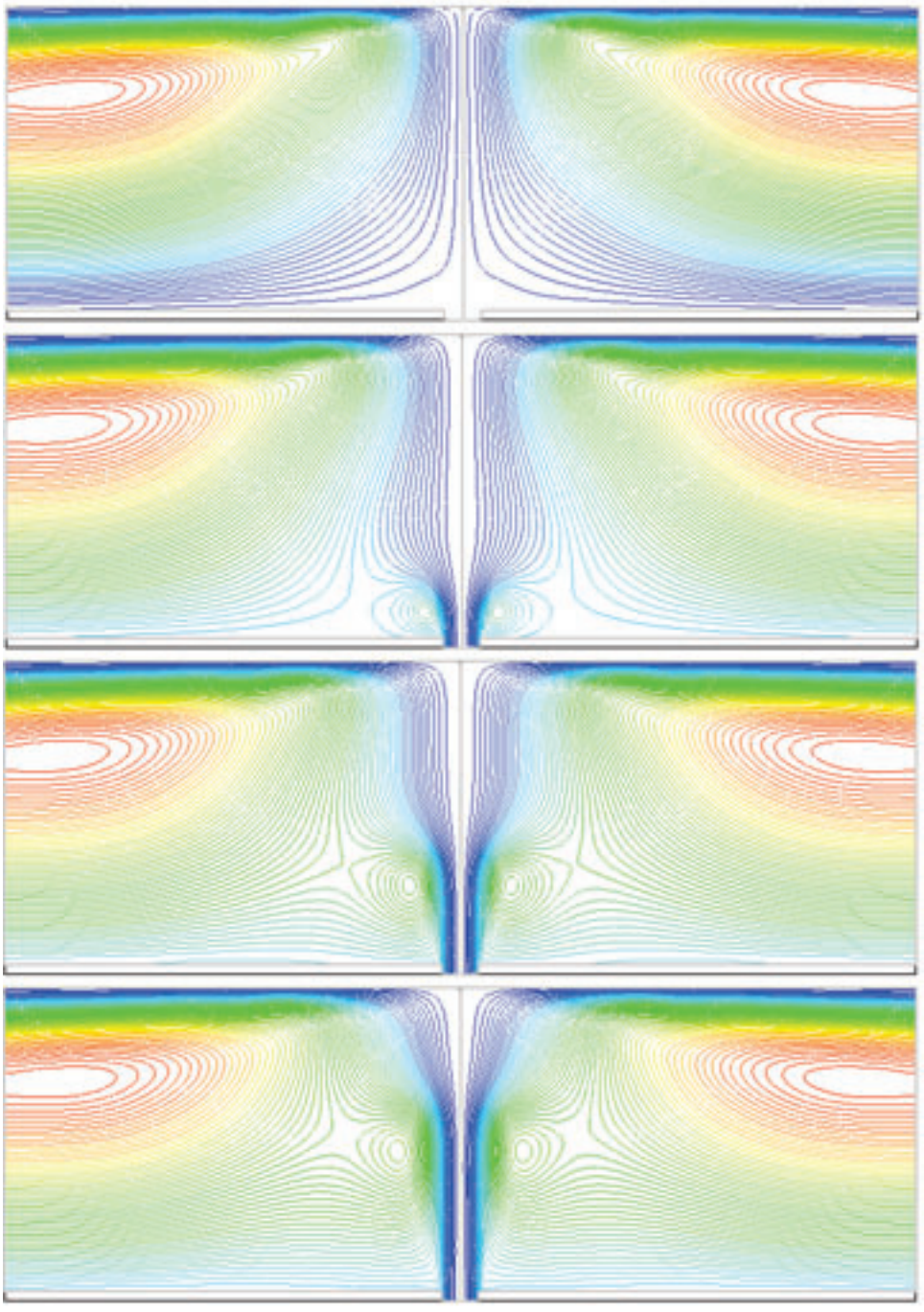

Figure 5.27: Stream function contours in one cycle (H/d_j=8)

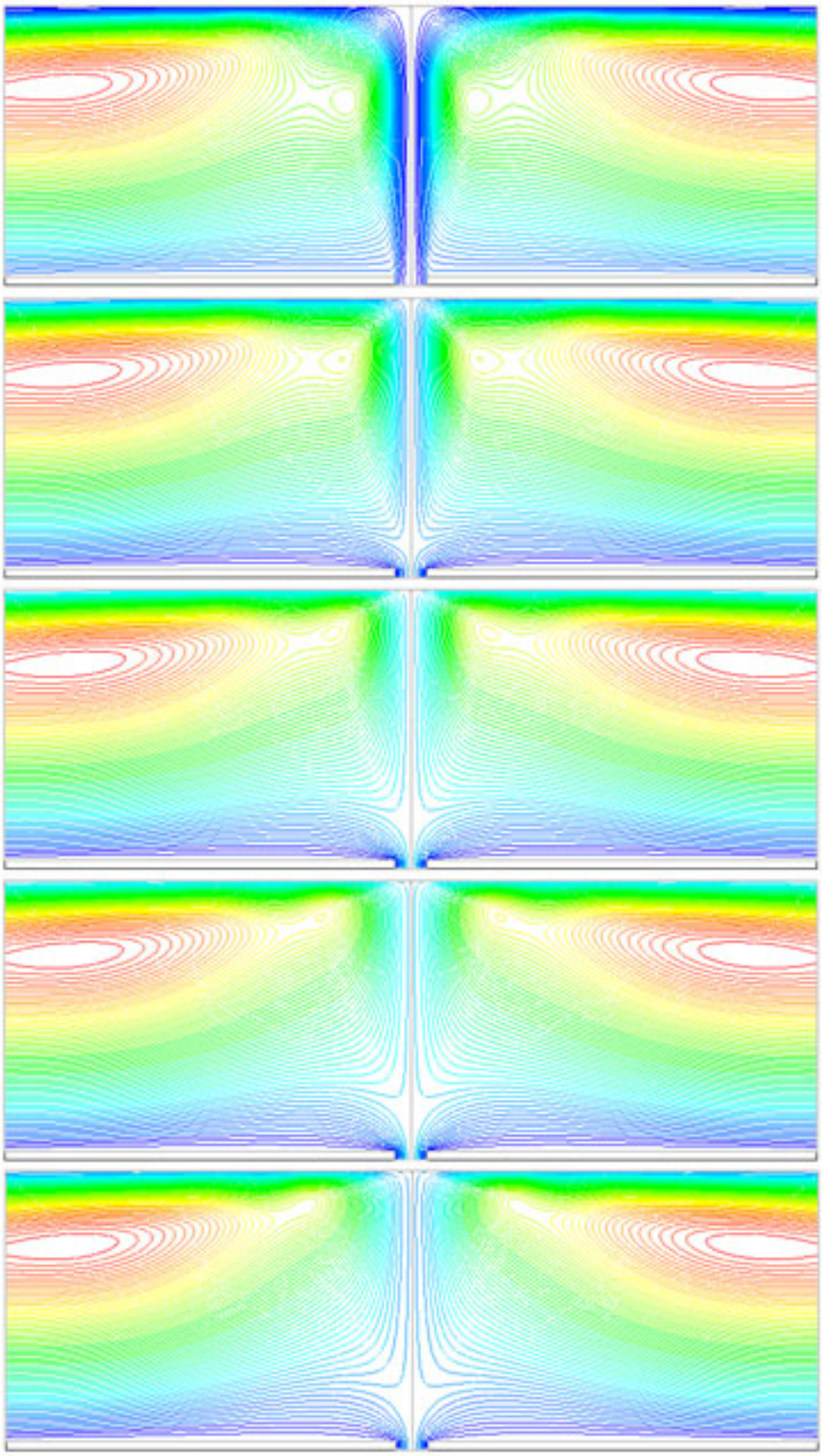

Figure 5.28: Stream function contours in one cycle (H/d_j=8)(continued)

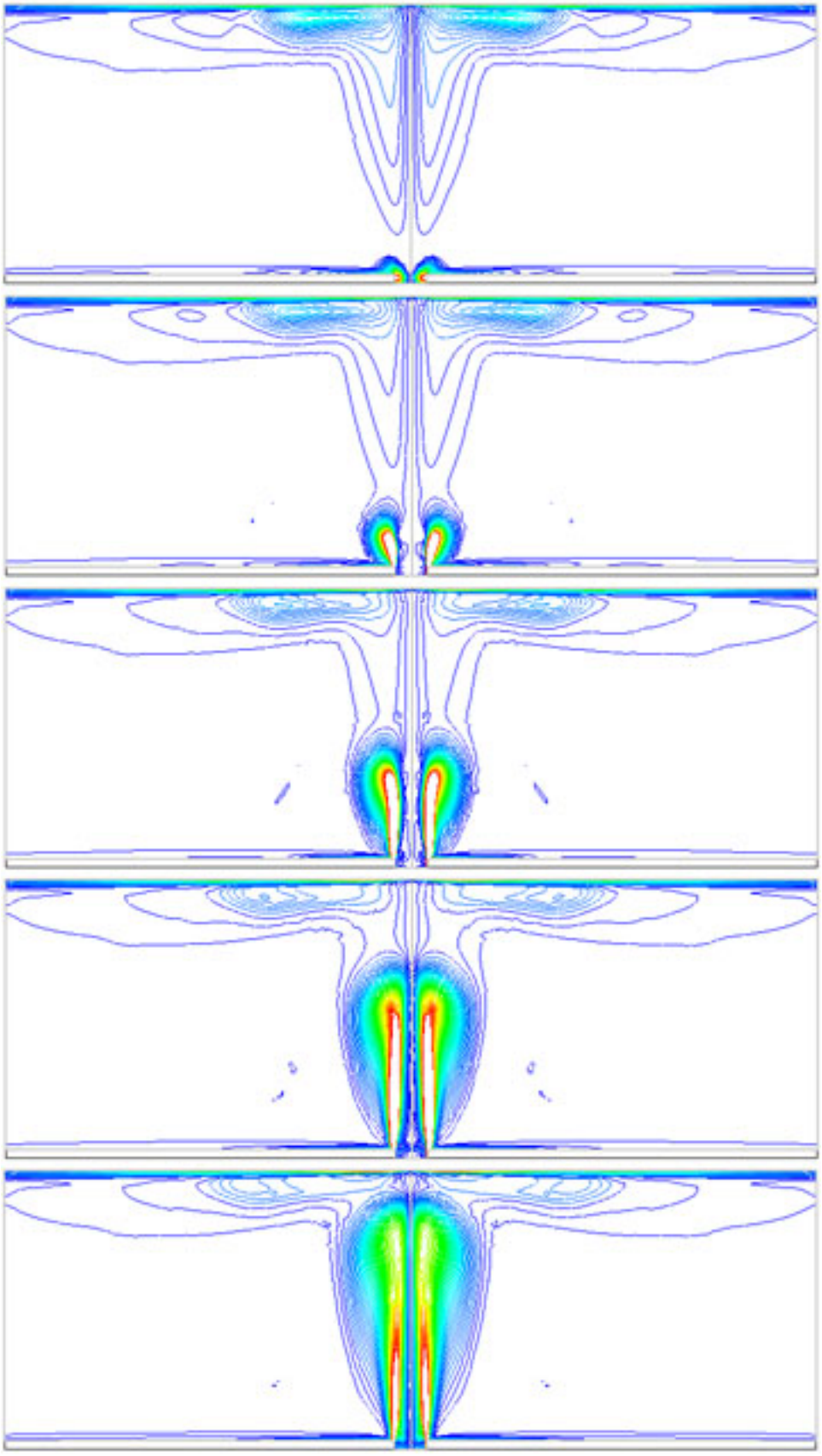

Figure 5.29: Vorticity contours in one cycle (H/d_j=8)

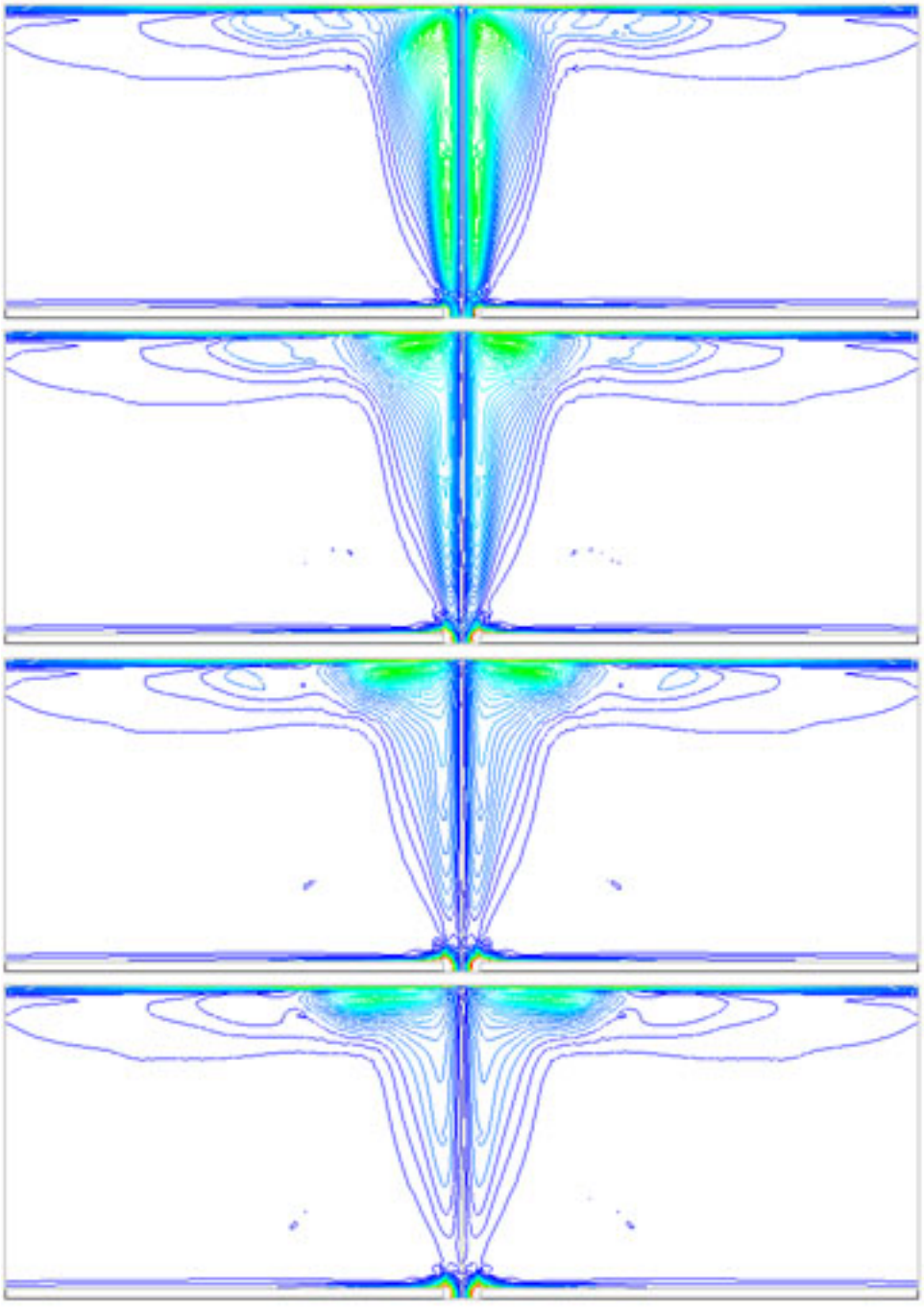

Figure 5.30: Vorticity contours in one cycle (H/d_j=8)(continued)

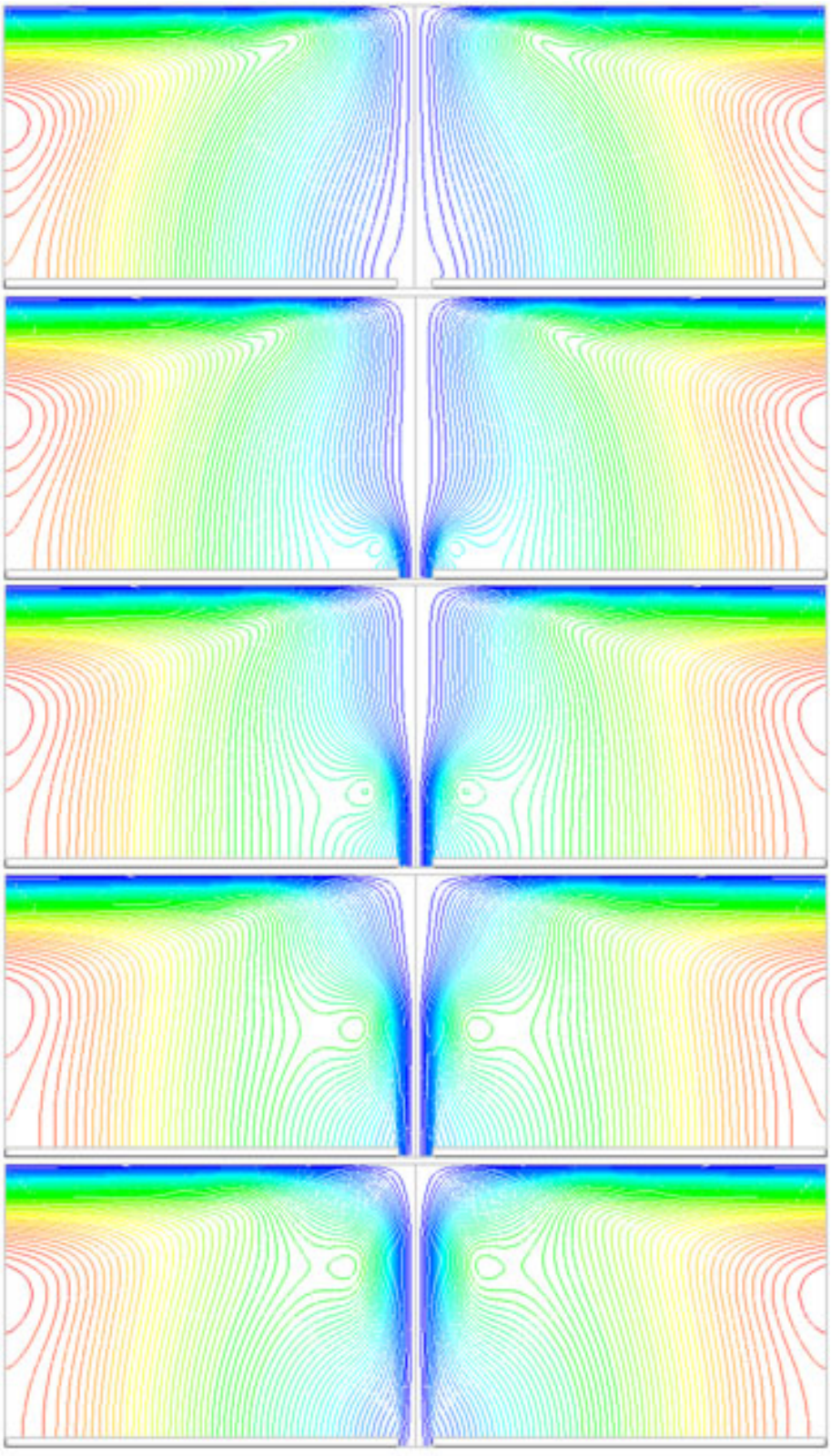

Figure 5.31: Stream function contours in one cycle (H/d_j=8, freejet)

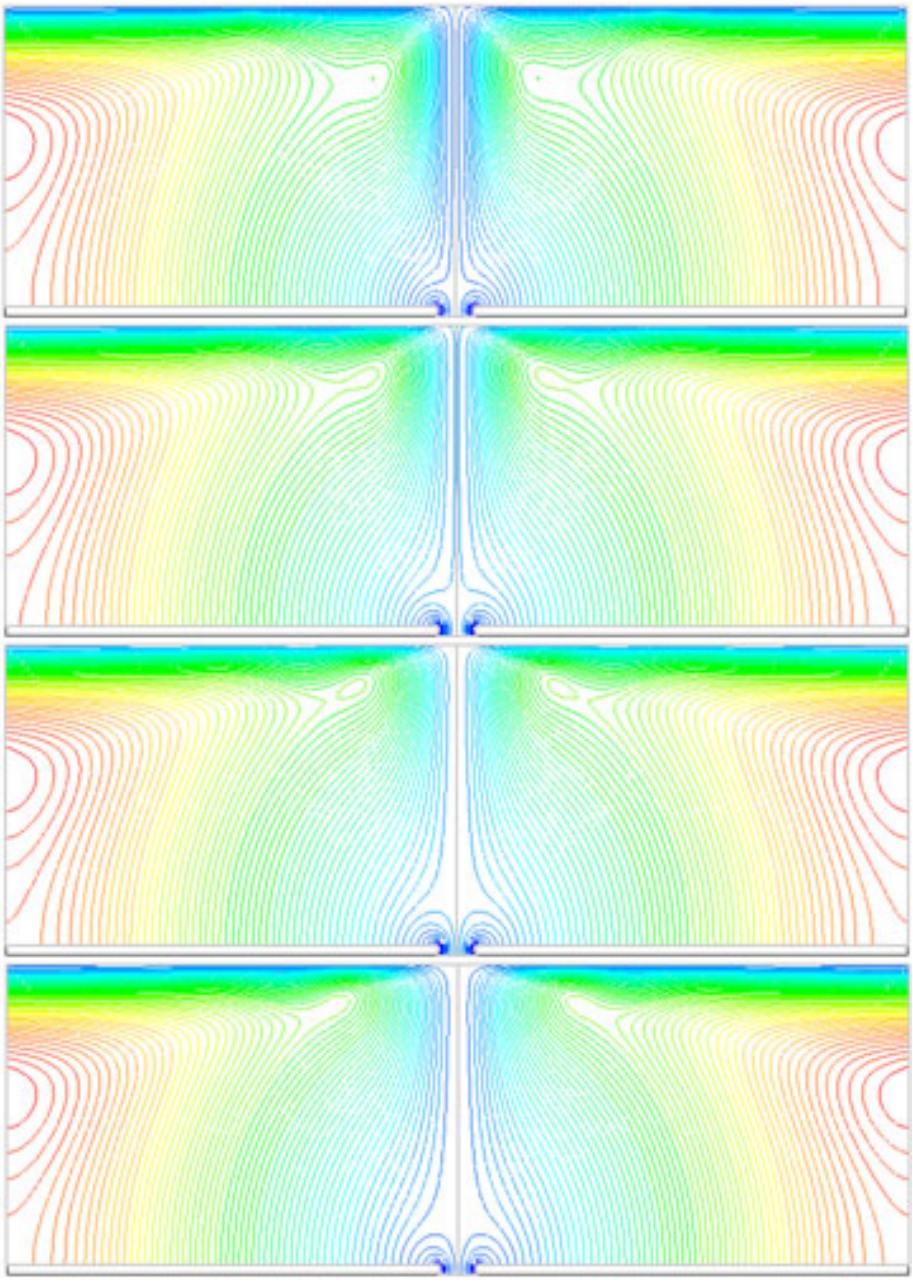

Figure 5.32: Stream function contours in one cycle (H/d_j=8, freejet continued)

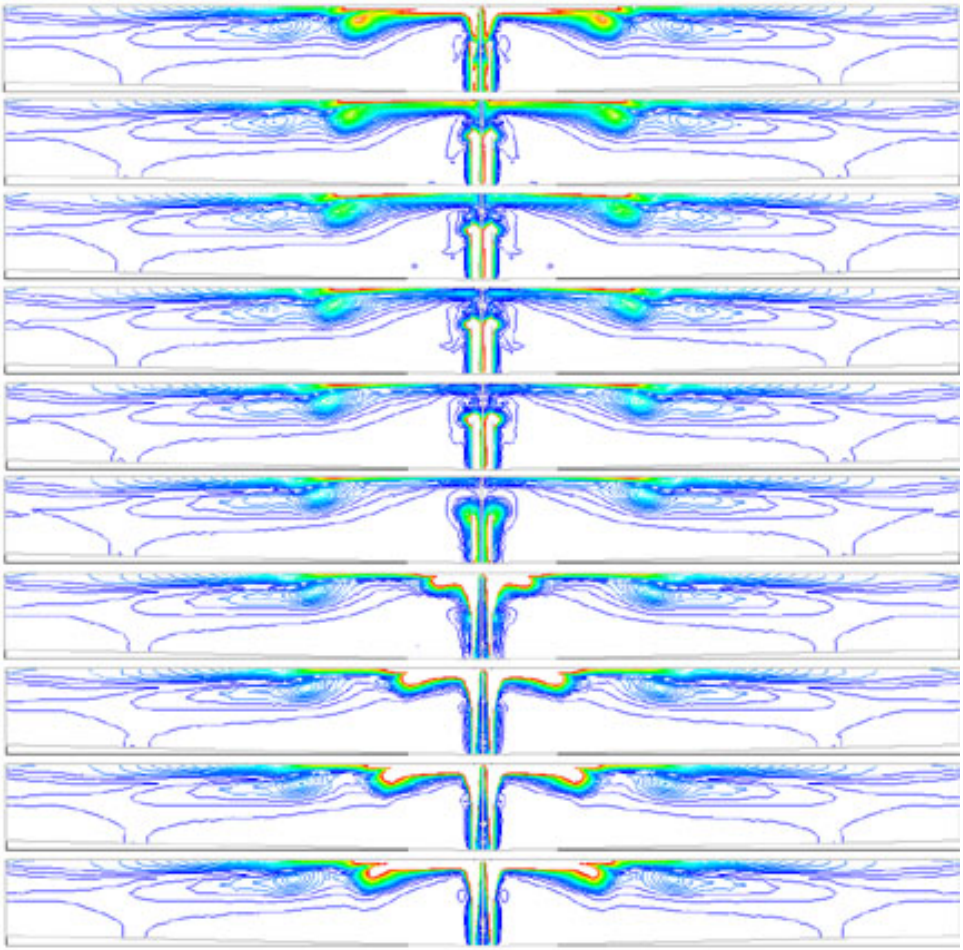

Figure 5.33: Vorticity contours of free synthetic jet impingement (H/d_j=2, d_j=1mm)

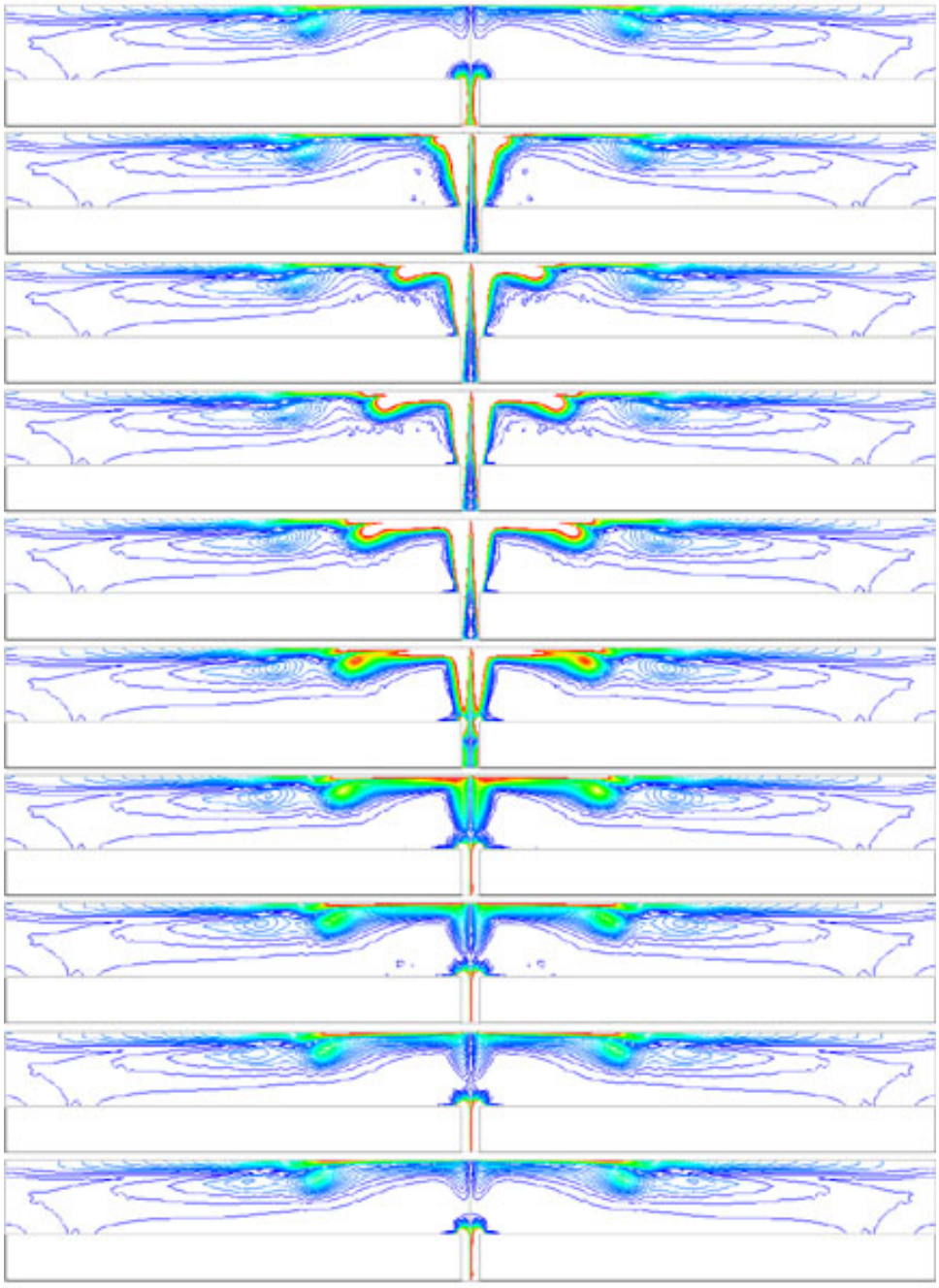

Figure 5.34: Vorticity contours of free synthetic jet impingement (H/d_j=4, d_j=1mm)

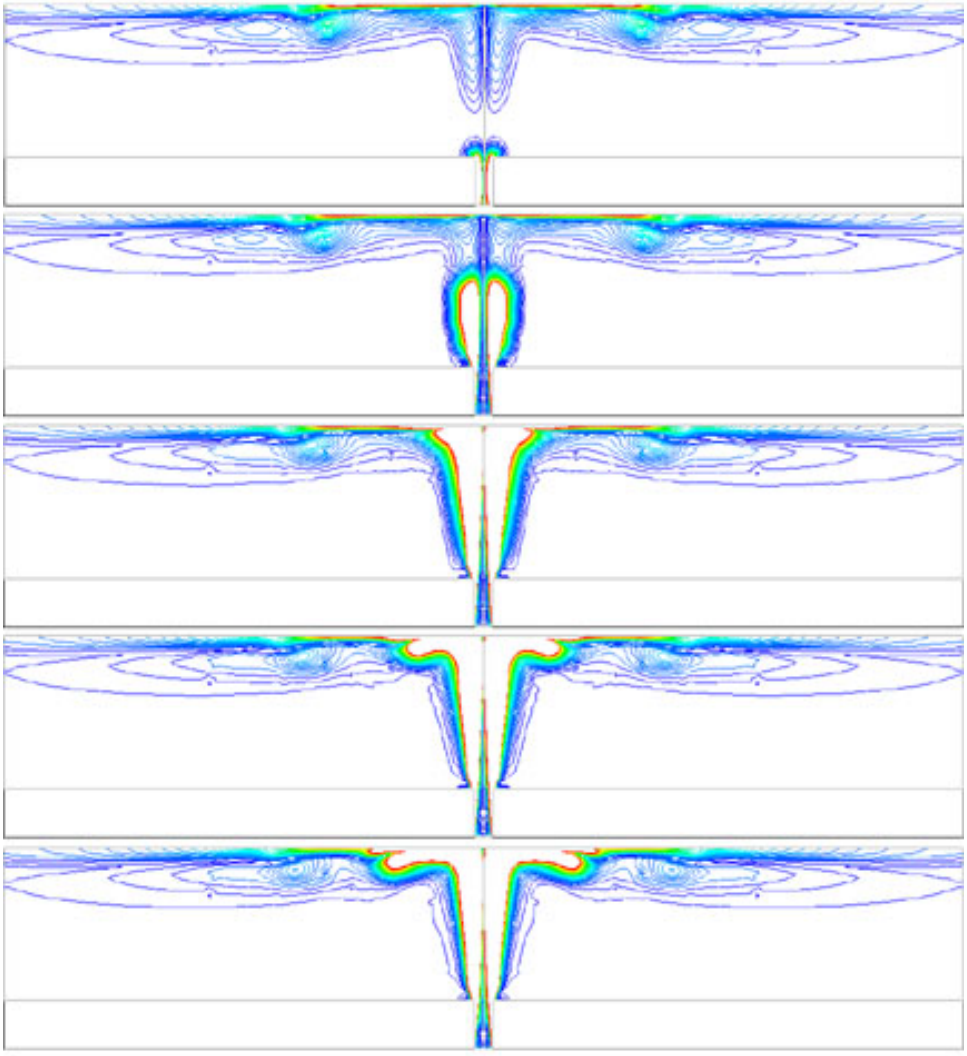

Figure 5.35: Vorticity contours of free synthetic jet impingement (H/d_j=8, d_j=1mm)

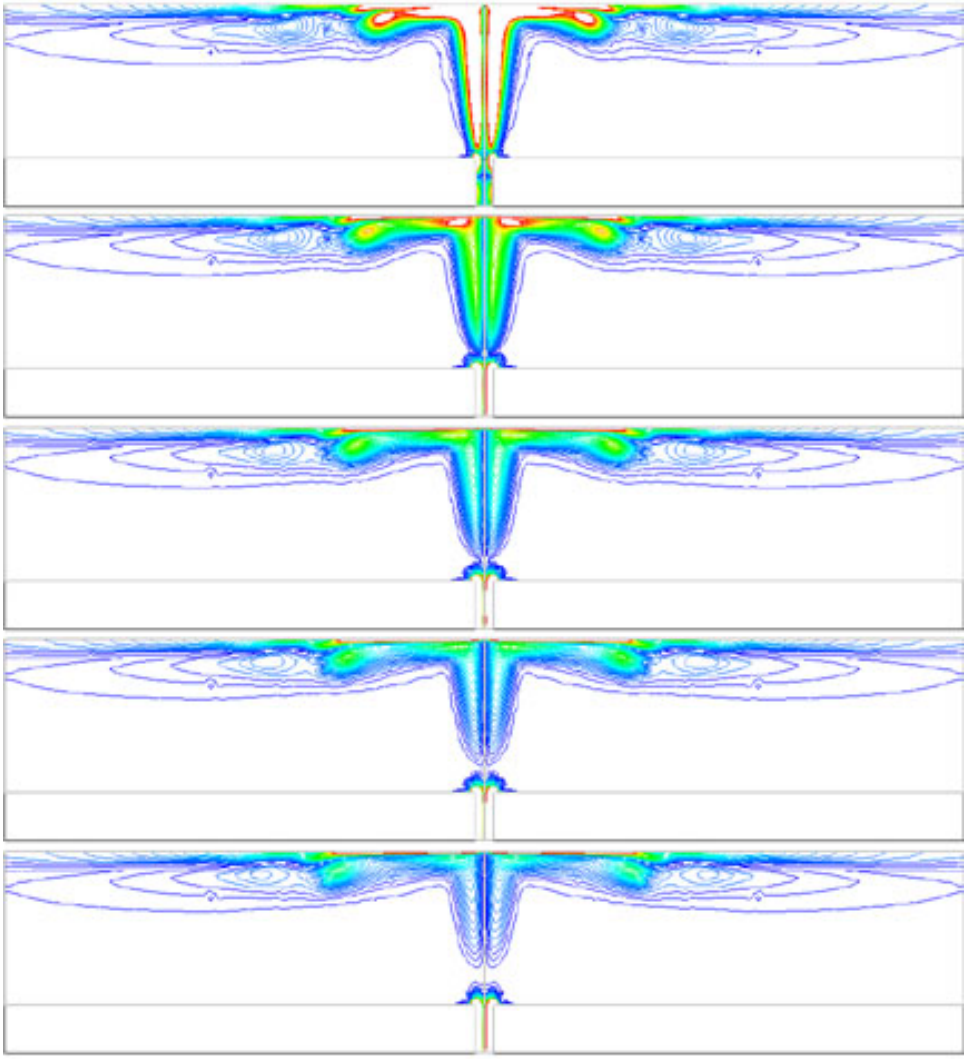

Figure 5.36: Vorticity contours of free synthetic jet impingement (H/d_j=8, d_j=1mm)

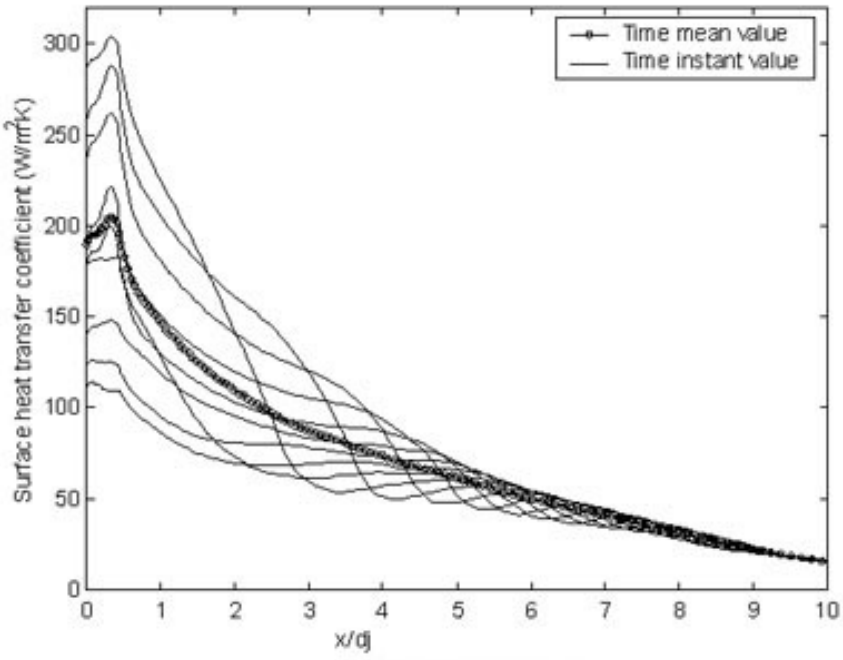

Figure 5.37: Surface heat transfer coefficient distribution on the impingement plate, d_j=6.35 mm, H/d_j=4

under different synthetic-jet configurations were compared. The investigated parameters included the nozzle-to-impingement-plate ratio H/d_j, nozzle diameter d_j, synthetic-jet working frequency and synthetic-jet nozzle velocity.

For confined synthetic jet impingement, a representative case had d_j=6.35 mm, H/d_j = 4, and a working frequency of 80 Hz. The total amount of heat removed from the top plate was 48.2 W. The average surface heat transfer coefficient and Nu are $38W/m^2K$ and 1304. The half-stroke time-mean velocity at the nozzle exit was 18 m/s. The non-dimensional stroke length L_{stroke}/d_j=17.7, Re_{I_0}= 1.61x10^5. The time-mean and time-average heat transfer coefficient distribution in radial direction are shown in Figure 5.37.

The maximum heat transfer coefficient was located at x/d_j = 0.6. The synthetic jet impingement differs from conventional jet impingement by the presence of vortex rings. The circular flow associated with the vortex rings induces additional impinging velocity to the main impinging jet flow. The vortex also modifies the development of the boundary layer. As illustrated in the Figure 5.39 and 5.40, the instantaneous surface heat transfer coefficient

distribution along the heater surface shows a strong relation to the vortex position. As the circular flow of the vortex is clockwise, additional impingement of this circular flow occurs on the left side of the vortex core and this flow blows on the developing boundary layer and makes it thinner. Thus, the corresponding maximum surface heat transfer coefficient is off the stagnation point and moves with the vortex. The location where the local minima occurred moved radially outward. Unlike conventional-jet impingement, there is no second local maxima for the average heat transfer coefficient. However, for the instantaneous heat transfer coefficient, there is a local maxima in the x/d_j range 4 ~6. Beyond x/d_j =9, the fluctuations of the heat transfer coefficient become small. All of these phenomena can be explained by the vortex dynamics. As observed in the previous section, the vortex pair hits the top plate and moves radially outward to merge into a residual vortex structure.

To compare to conventional-jet impingement heat transfer, the jet exit velocity was set to 18 m/s, the blow-stroke half-phase average velocity of the synthetic jet. Synthetic-jet impingement had a 48.3% improvement in total heat transfer, a 53.2% improvement in the average heat transfer coefficient and a 54.7% improvement in average Nu. The comparison between the heat transfer coefficients on the impingement plate for conventional-jet impingement and synthetic-jet impingement is shown in Figure 5.38. The top figure is for free jets (no bottom plate in the configuration) and the bottom figure is for confined jets (with bottom plate). The advantage of using synthetic-jet techniques in impingement heat transfer is obvious.

Compared to conventional-jet impingement, synthetic-jet impingement removes more heat from the target area. However, the local heat transfer coefficient distribution on the impingement plate shows the high heat transfer region for synthetic-jet impingement is narrower than that for conventional-jet impingement. The local heat transfer coefficient decreases rapidly as x/d_j increases, but then the rate of decrease becomes smaller when the heat transfer coefficient is approximately 50% of the maximum. The local heat transfer coefficient decreases to half of its maximal value at $x/d_j = 2.3$, and decreases to one quarter of its maximal value at $x/d_j = 6$. In the conventional-jet impingement cases, the local heat transfer coefficient decreases to half of its maximal value at $x/d_j = 3.6$, and drops

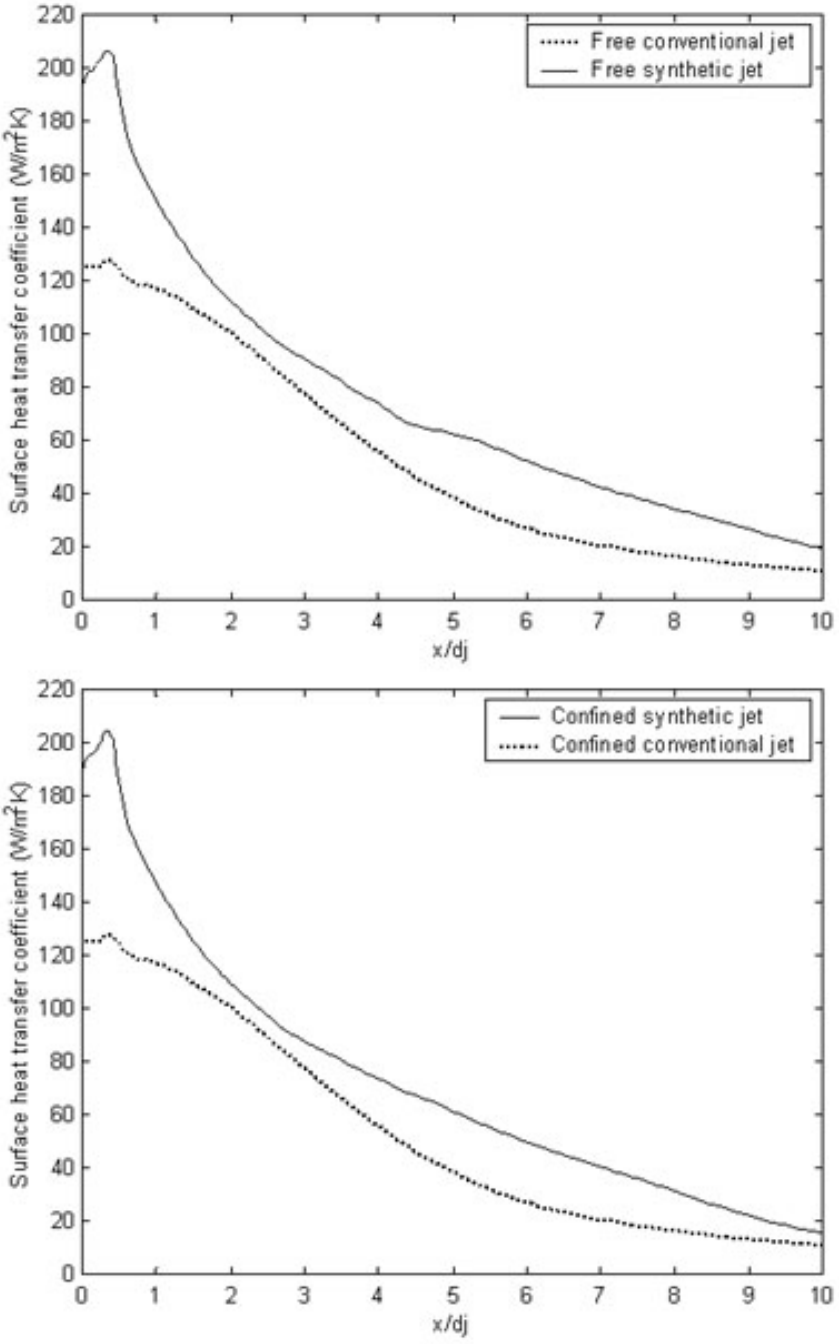

Figure 5.38: Distribution of time-mean local heat transfer coefficient on impingement plate

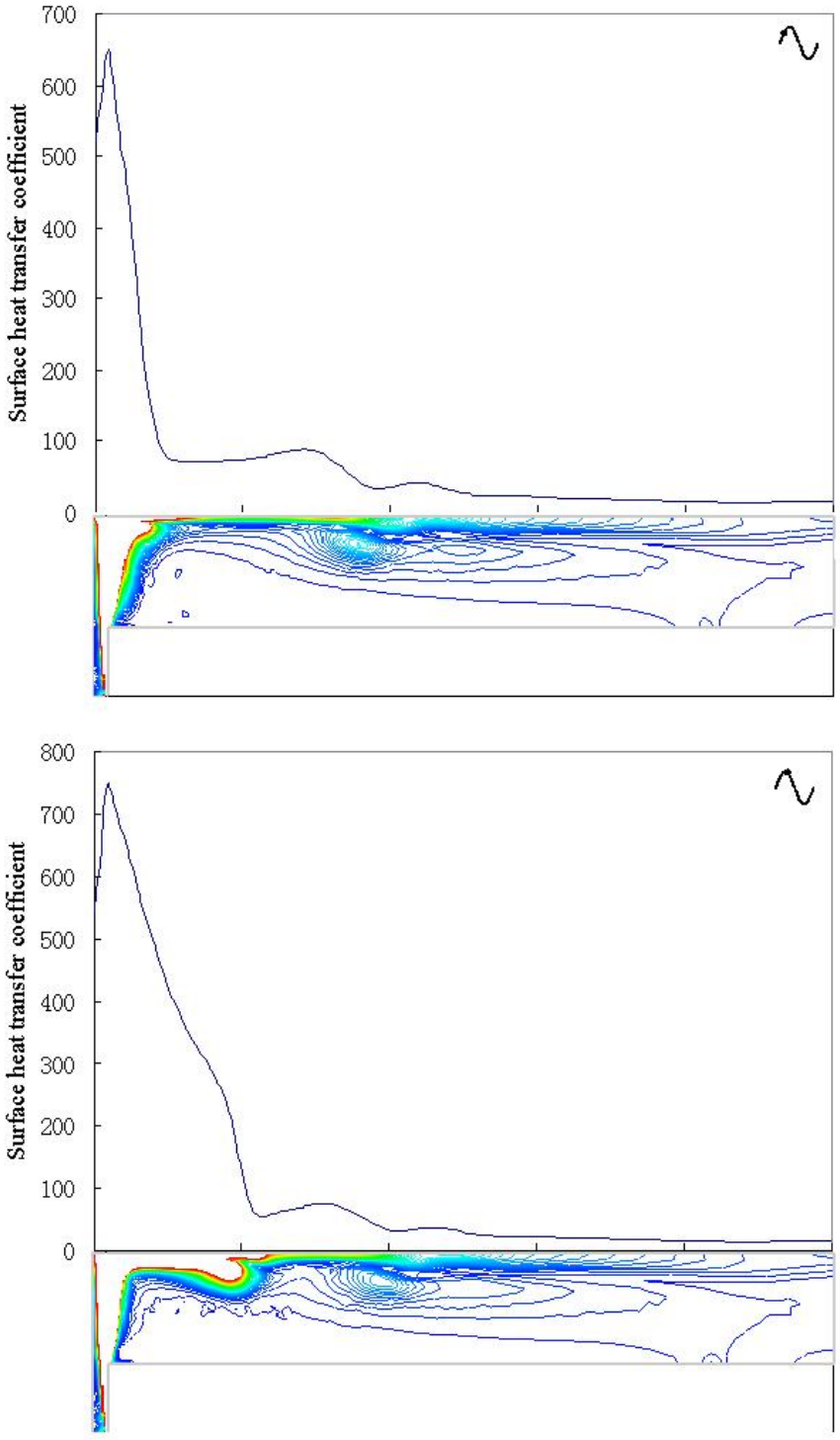

Figure 5.39: Surface heat transfer coefficient distribution vs. vortex motion, d_j=1 mm, H/d_j=4

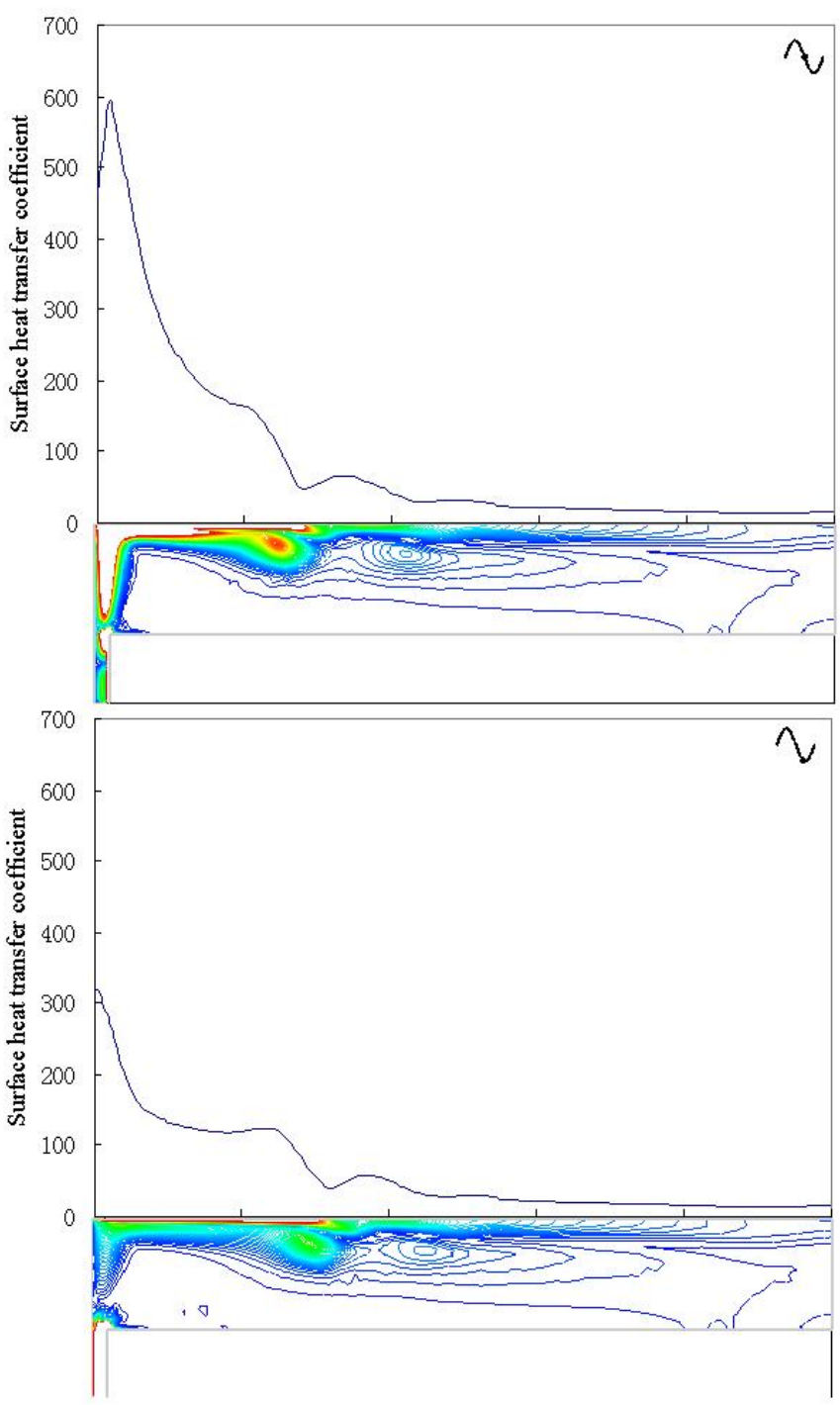

Figure 5.40: Surface heat transfer coefficient distribution vs. vortex motion (continued), d_j=1 mm, H/d_j=4

to one quarter of its maximal value at $x/d_j = 5.27$. In other words, high heat transfer coefficient region is more effectively limited to a specific target area with a synthetic jet. This characteristic makes synthetic-jet impingement very attractive in controlling hot spots.

For conventional-jet impingement, there was no noticeable difference in heat transfer between the confined-jet configuration and the free-jet configuration. For synthetic-jet impingement, a slight enhancement was observed for free-jet configurations. The details of the comparison between confined and free synthetic-jet impingement configurations will be presented later this chapter.

As an example, we examined free synthetic-jet impingement with a nozzle diameter of 1 mm, $H/d_j = 4$, and a frequency of 250 Hz. The half-stroke time-mean velocity was 29 m/s, the non-dimensional stroke length L_{troke}/d_j=58.1, Re_{I_0}=1.37x10^5, and the top wall diameter was 50 mm. For this case, the total heat transfer rate was 4.81 W and the time-mean surface heat transfer coefficient and Nu were 34.1 W/m^2K and 1157 respectively. The distribution of the heat transfer coefficient is quite similar to the confined-jet impingement case. The fluctuation becomes very weak after $x/d_j > 7$. During one period, the local maxima and minima shift back and forth between $x/d_j = 4$ and 6.

These two cases were selected to show the general heat transfer characteristics of synthetic-jet impingement. In the next section, a more detailed parametric study is presented.

5.7 Parametric Study

5.7.1 Nozzle/orifice diameter

The nozzle/orifice diameter directly determines the size of the synthetic jet flow and so the impingement area on the upper plate. To effectively control the hot spots in a thermal management application, the relation between the nozzle/orifice diameter and the heat transfer performance is needed. We investigated this relationship by examining how the nozzle/orifice diameter affected the total heat transfer rate and the local heat transfer coefficient.

Heat transfer of synthetic jets with equal nozzle average velocity impinging on an isothermal plate located $6d_j$ away from the nozzle exit was studied. The nozzle diameters were 0.5

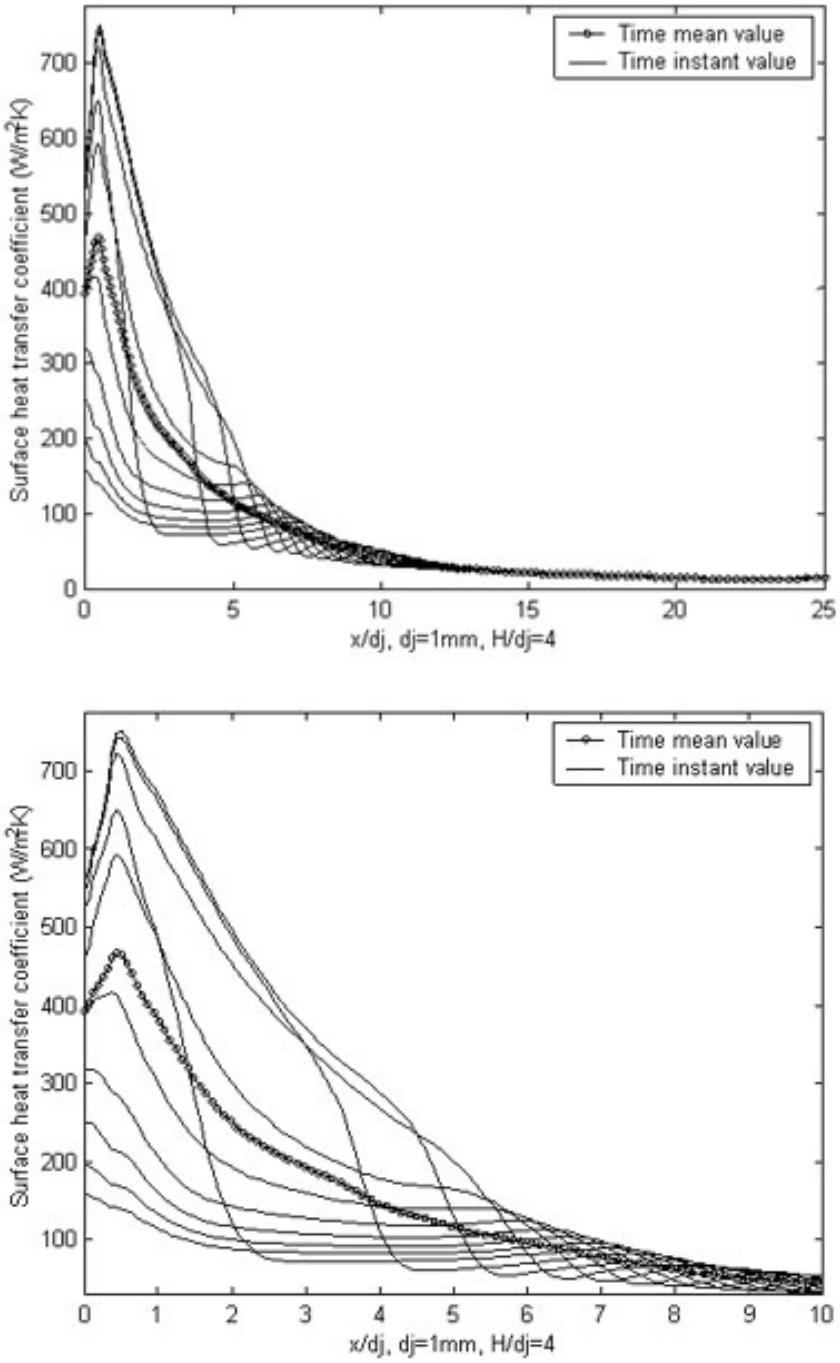

Figure 5.41: Local surface heat transfer coefficient distribution on the top plate

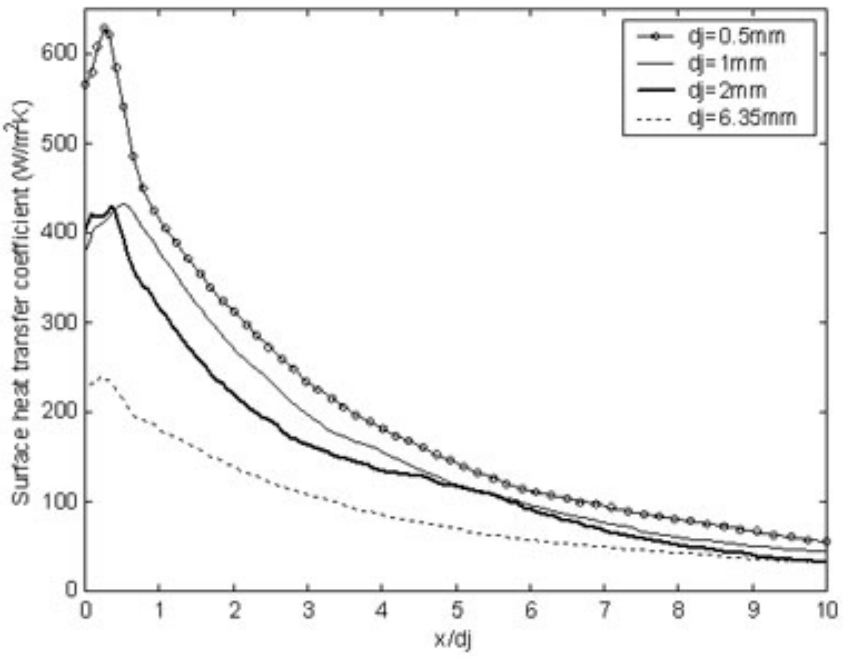

Figure 5.42: Time mean local heat transfer coefficient on impingement plate (d_j study)

mm, 1 mm, 2 mm, and 6.35 mm. The plate had a diameter of 50 mm and its temperature was kept at 360K. The fluid from the synthetic-jet nozzle was isothermal and kept at 300K. The working frequencies of all synthetic jets were 250Hz. The blowing-stroke half-cycle average velocity through each nozzle was 28.8 m/s.

The time mean local heat transfer coefficient distributions (shown in Figure 5.42) for all configurations reveal similar relation between the local heat transfer coefficient and dimensionless distance. Because the nozzle average velocities for all configurations were equal, when the nozzle diameter increases, the flow rate increases in corresponding square relation. Correspondingly, the heat transfer rates increased significantly. The difference in heat transfer coefficients is believed due to the absolute distance from the nozzle. As expected, if the distance between the nozzle and the plate is small, the heat transfer is stronger.

However, it was observed that for the $d_j = 1$ and $d_j = 2$ cases, the heat transfer coefficients are almost equal while the distances between the nozzle and the impingement plate are

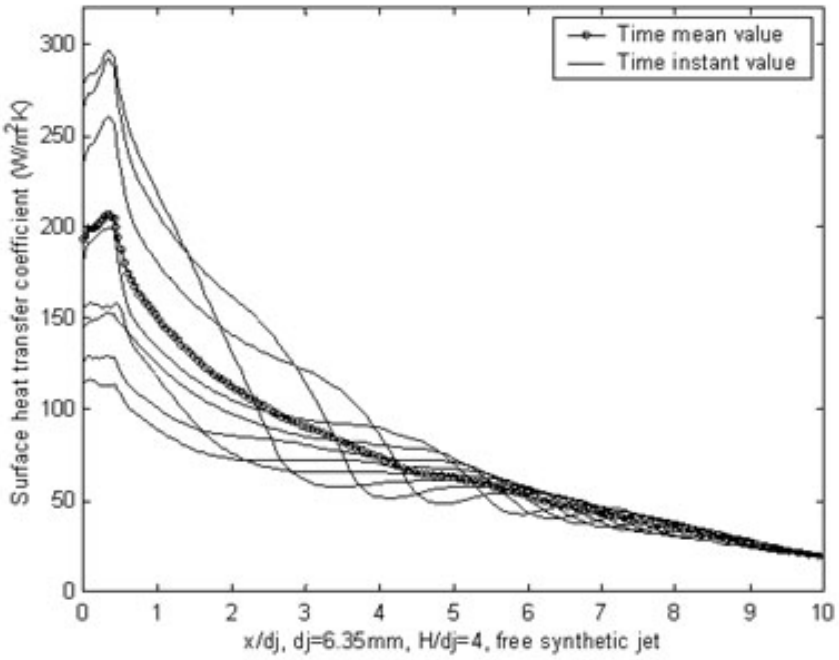

Figure 5.43: Impingement plate local heat transfer coefficient

two times different. The reason could be the velocity decay along the streamwise direction is relatively constant in this range. But we didn't intensively study this characteristic.

5.7.2 Effect of nozzle-to-impingement surface spacing ratio H/d_j

Because there is no potential core in synthetic-jet flows, the impingement heat transfer characteristics of synthetic jets are different from conventional jets. It has been shown in previous chapters that the time-mean velocity of synthetic-jet flow reaches its maximum value at around $2 \sim 3$ nozzle diameters from the jet exit. Beyond this point the centerline velocity decreases monotonously. The heat transfer is expected to decrease when the velocity decreases.

In this study, the nozzle-to-impingement surface spacing ratio H/d_j was varied from 2 to 10 for a synthetic-jet system with d_j=1mm and from 2 to 8 for a synthetic-jet system with d_j =6.35mm respectively. Both of them show similar characteristics. H/d_j=4 configuration yields highest overall heat transfer performance.

The local heat transfer coefficient for free-synthetic-jet impingement is only slightly

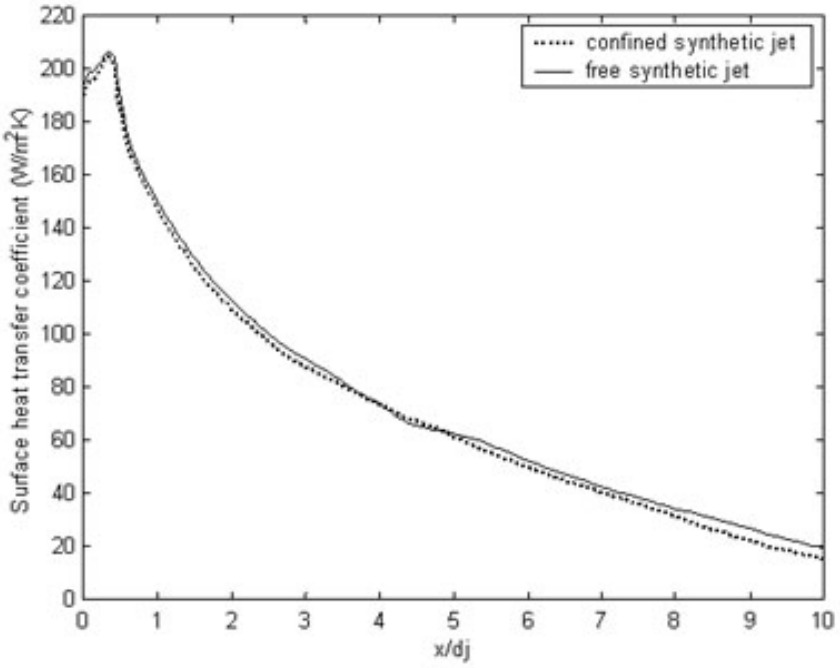

Figure 5.44: Impingement plate local heat transfer coefficient comparison

better than for confined-jet impingement. As shown in Figure 5.43 through 5.47, the time-mean local heat transfer coefficient curves of confined and free jet configurations (H/d_j=4 and H/d_j=8) are almost identical.

For free synthetic jet impingement (d_j =1mm), the optimal nozzle-to-impingement-plate distance to achieve the highest heat transfer performance is four as shown in Figure 5.48. We found that this result is also independent of nozzle diameter and jet velocity. Compared to conventional-jet impingement, this distance is shorter. So in microsystem applications, where space is limited, this is another advantage of using synthetic-jet technique.

5.7.3 Effect of frequency

The working frequency affects the heat transfer by two means. One is that the synthetic-jet velocity, with an equivalent cavity-volume change, increases with increasing frequency. The other way is that the frequency alters the time characteristic of the flow and turbulence.

For a cavity with the geometry: d_j=1 mm, l_j/d_j=10, d_c/d_j = 5, h_c/d_c=1, the frequency

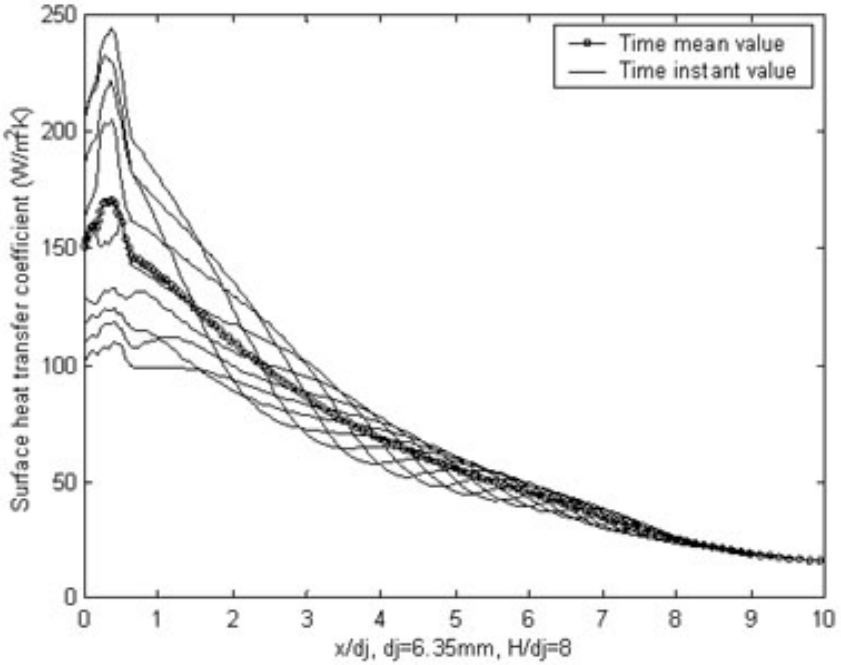

Figure 5.45: Impingement plate local heat transfer coefficient

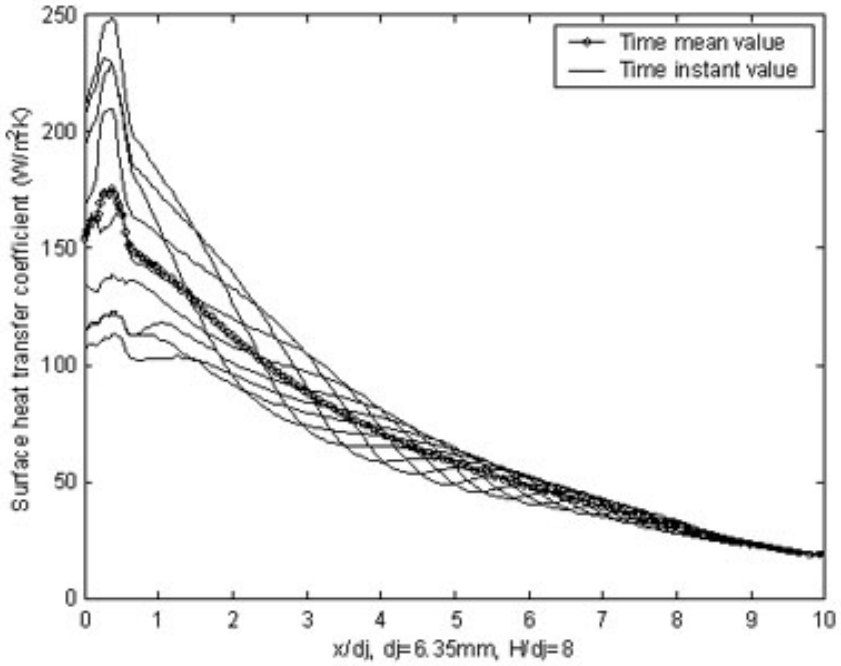

Figure 5.46: Impingement plate local heat transfer coefficient (free jet)

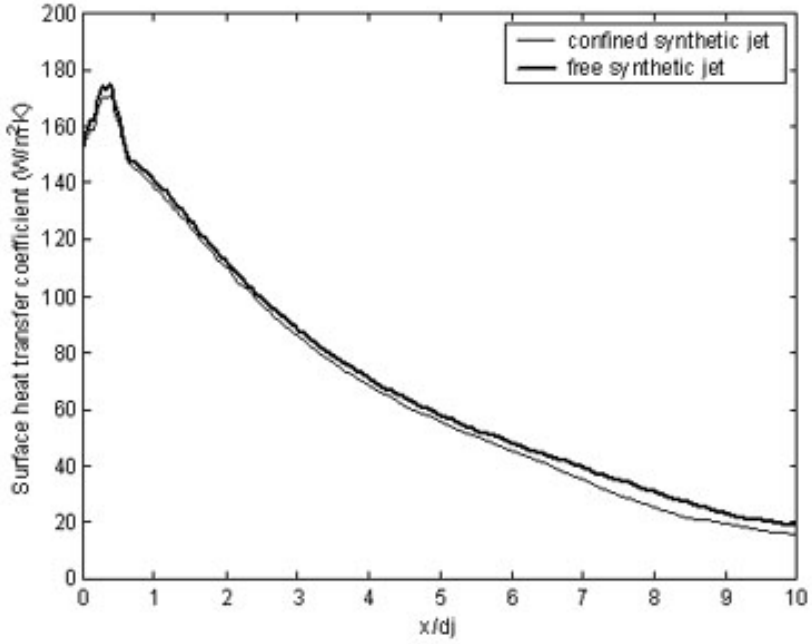

Figure 5.47: Impingement plate local heat transfer coefficient comparison

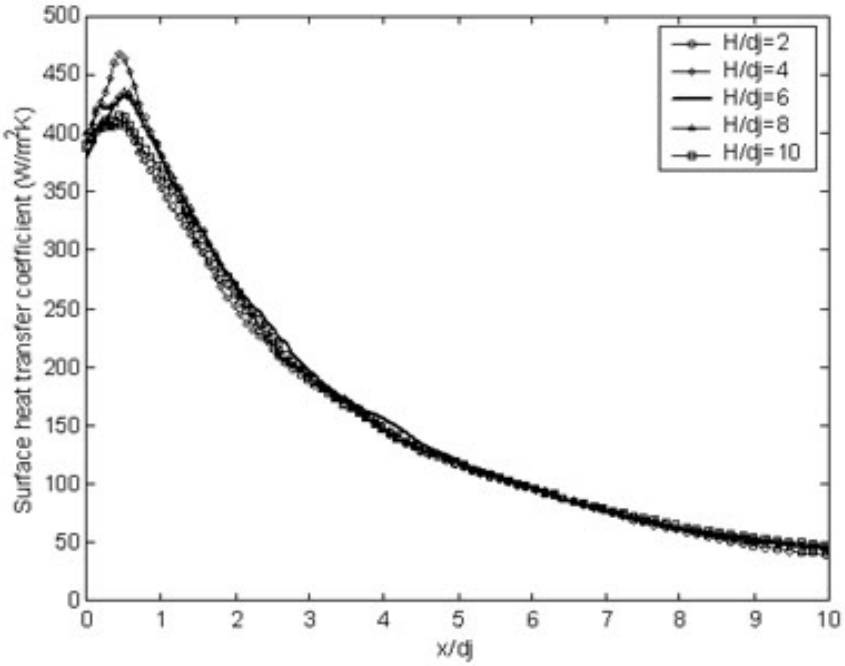

Figure 5.48: Time mean local heat transfer coefficient on the impingement plate (H/d_j study, d_j=1mm)

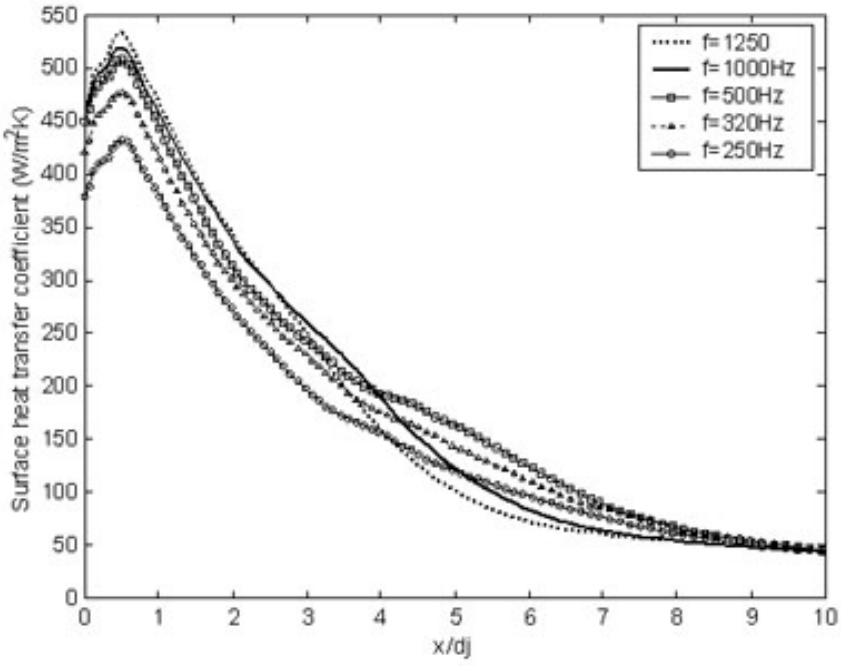

Figure 5.49: Time mean local heat transfer coefficient on the impingement plate (frequency study, d_j=1mm)

was varied from 250 Hz to 1250Hz. The local heat transfer coefficient plots on the impingement surface for these cases are similar (see Figure 5.49). All curves collapse into one beyond $x/d_j = 9$, like other examples in previous sections. The corresponding time mean average jet exit velocities of these cases are 28m/s (250Hz), 32m/s (320Hz), 36m/s (500Hz), 33m/s (1000Hz) and 30.3m/s (1250Hz). It is usually expected that better heat transfer will be achieved when the average jet exit velocity increases. However, we could see from the Figure 5.49 that the local heat transfer coefficient for the 500 Hz case is smaller than 1000Hz and 1250Hz cases in the small x/d_j region. Another interesting difference between high frequency cases and low frequency cases is that the local heat transfer coefficient drops more rapidly for low frequency cases beyond $x/d_j \approx 4$. Since the average jet exit velocity for 1250Hz and 1000Hz is smaller than in the 500Hz case, the difference may be due to the high working frequency changes the time characteristics of the jet flow and/or turbulence. The trend is that with the increase of working frequency, the heat transfer is getting better and the high heat transfer rate region is limited to a smaller area. The high frequency

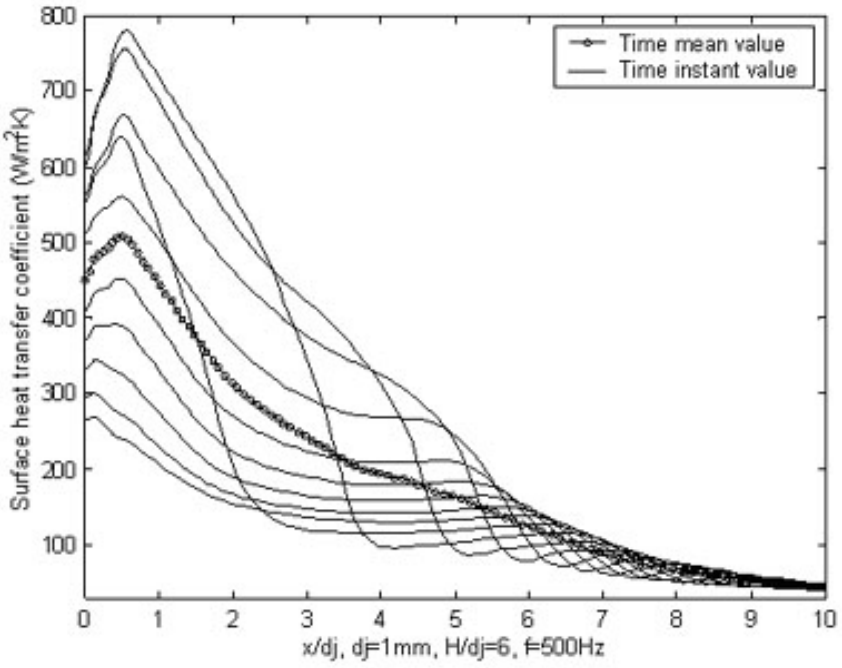

Figure 5.50: Local surface heat transfer coefficient on impingement plate (500Hz)

changes to the time characteristics of turbulence might be the reason of this enhancement. However, further investigation is needed to verify the physics underneath.

Plots for the local surface heat transfer coefficient verse time for the f=500, 1000 and 1250Hz cases are shown in Figure 5.50 through 5.52. Although the maximal time instant local heat transfer coefficient of 1000Hz and 1250Hz cases are smaller than the 500Hz jet, the average local heat transfer coefficients are close. It is observed that when the working frequency increases the time instant values of local heat transfer coefficient tend to be in a smaller range. For example, at 500Hz, the time instant value is between 270 and 780, but at 1000Hz and 1250Hz this range shrinks to $350 \sim 720$ and $390 \sim 712$. This is because when the working frequency becomes higher, the velocity fluctuation of the synthetic jet flow becomes smaller. If the frequency is infinite, only one value exists.

Another trend observed is that the local surface heat transfer coefficient becomes relatively stable earlier in the radial direction when the working frequency increases. At 500Hz, the local surface heat transfer coefficient in the radial direction becomes almost invariant

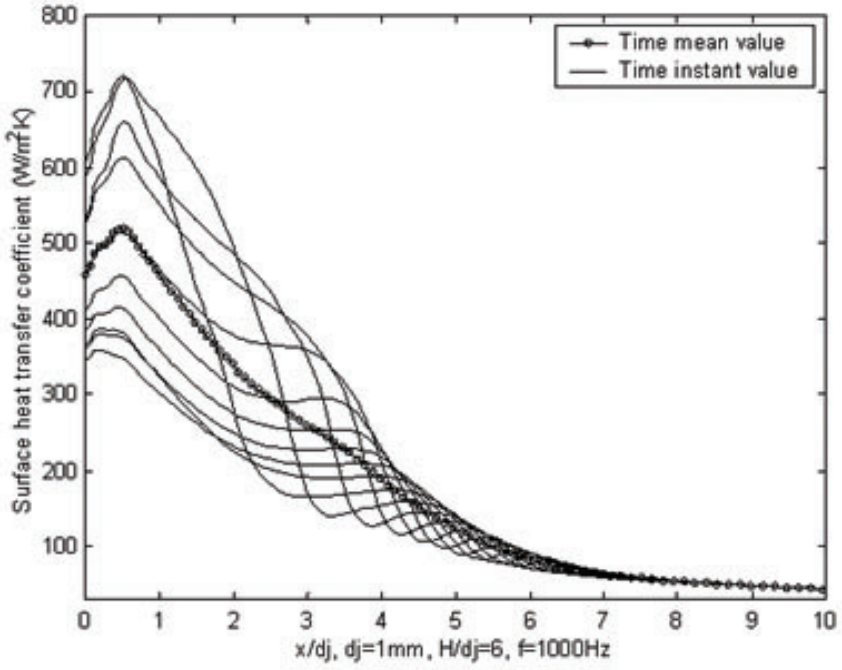

Figure 5.51: Local surface heat transfer coefficient on impingement plate (1000Hz)

in time beyond x/d_j =9, but at 1000Hz and 1250Hz this location moves back to approximately 7 and 6 respectively. This explains the phenomenon mentioned before that the high average local surface heat transfer coefficient region at high working frequency trends to be "narrower" in the radial direction.

Both of these observations show the advantages of using high frequency synthetic jets in impingement heat transfer. For a high frequency synthetic jet, the heat transfer coefficient on the impingement plate has less fluctuation in magnitude both in time and in space(radial direction), which helps the device to work at a more stable thermal environment. Also, the high heat transfer rate region could be more focused on the target device to improve the efficiency of the local thermal management.

5.7.4 Effect cavity volume change (diaphragm motion)

It was found that the effect of changes in the cavity volume due to diaphragm motion is reflected by the average velocity through the nozzle/orifice. Due to resonance, there is no one to one mapping of this relation. The jet exit velocity determines the impingement

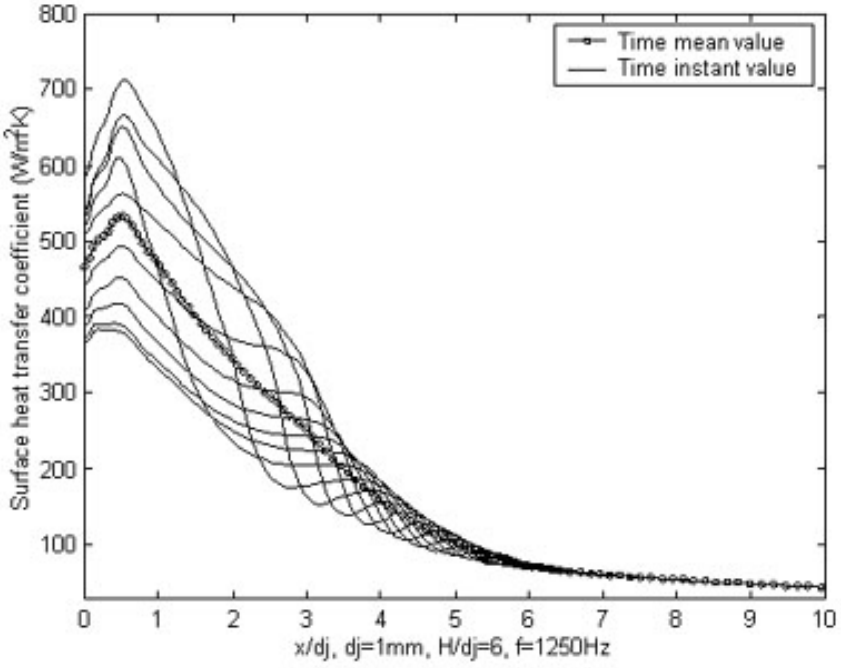

Figure 5.52: Local surface heat transfer coefficient on impingement plate (1250Hz)

afterwards. In this section, the effect of cavity volume change was studied through the study of the effect of the average jet exit velocity through the nozzle.

The nozzle diameter d_j is 6.35mm, the impingement plate was placed $4d_j$ from the nozzle. The synthetic jet was operated at 80Hz. The average jet exit velocity was varied from 14.9 m/s to 35.9 m/s, corresponding to the amplitude of the diaphragm motion of 0.19mm to 0.45mm.

In Figure 5.53, the distributions of local heat transfer coefficient on the impingement plate were plot. As expected, the heat transfer was enhanced when the jet exit velocity increased. The overall shapes of the distribution curves are similar, but the heat transfer coefficient increases in the whole domain as the jet-exit velocity increases.

5.8 Summary

In this chapter, a numerical study on synthetic-jet impingement heat transfer was presented. The study was completed using the commercial CFD packages FLUENT and CFDACE+.

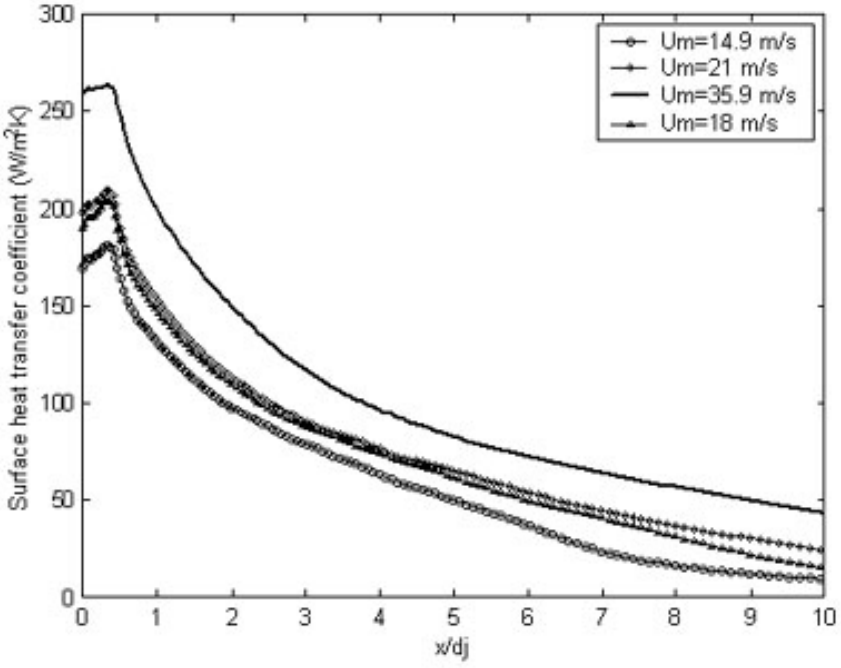

Figure 5.53: Time mean local heat transfer coefficient on the impingement plate

Both full-cavity simulations and modeled-cavity simulations were done and compared with experimental measurements. It was found that the modeled-cavity simulation did a good job in determining the flow structure.

This study covered synthetic jets working at 80 Hz to 1250 Hz, with nozzle/orifice diameters from 0.5 mm to 6.35 mm, nozzle-to-impingement-plate distance ratios H/d_j from 2 to 10; average jet exit velocity from 13.5m/s to 36.1 m/s, and the cavity-volume change from 3% to 10%. The non-dimensional stroke length L_{stroke}/d_j varied from 13 to 63. The effects on the local heat transfer on the impingement plate of all of these parameters were investigated.

The vortex dynamics of synthetic-jet impingement under different geometry configurations shows similar characteristics. The vortex pair generated at the nozzle/orifice travels towards the target plate, after impingement it moves in the radial direction towards a residual vortex pair, and then merges with the residual vortex. When the impingement plate moves further from the nozzle, the residual vortex pair moves further from the centerline

and so the vortex pair moves further along the impingement wall. For configurations without a bottom plate (free synthetic-jet impingement), the residual vortex pair also moves a small distance away from the impingement plate.

It was found that using synthetic-jet impingement significantly improves the heat transfer compared to conventional jet impingement with equal average jet exit velocities. A roughly 50% improvement in the total heat transfer rate and Nu were achieved in this study. The high local heat transfer rate region for synthetic-jet impingement is more concentrated near the stagnation area compared to conventional-jet impingement which makes synthetic-jet impingement more attractive in applications requiring local thermal management limited to a small area. It was observed that the heat transfer performance of free synthetic-jet impingement (no bottom plate) was only slightly better than confined synthetic-jet impingement.

The optimal nozzle-to-impingement-plate distance ratio H/d_j, for synthetic-jet impingement is four, which is smaller than conventional-jet impingement. With the same average jet velocity, H/d_j, and working frequency, the local heat transfer coefficient on the impingement plates increases when the nozzle diameter decreases. As the jet velocity decays along the axis of the jet, it is believed that the absolute distance plays important role in heat transfer performance too. The working frequency of the synthetic-jet affects the impingement heat transfer significantly. With a high working frequency, the synthetic-jet impingement heat transfer is larger and the high heat transfer rate region is more concentrated.

CHAPTER VI

PARAMETRIC STUDY OF AN ACTIVE HEAT SINK

6.1 Introduction

Our economy and everyday life rely on electrical systems more than anytime in human history. The electron power used in these systems has to be efficiently removed in the form of heat from the system to keep the system working reliably. In addition to optimizing the thermal design of microelectronic systems, advanced technologies for thermal management have to be developed to fulfill the increasing cooling requirements of future systems. The junction-ambient thermal resistance requirement will reach $0.18°C/W$ for high performance computers according the international technology roadmap for semiconductors 2001 [60].

Air cooling techniques are still being intensively studied for system simplicity and relatively easy implementation. Forced convection air cooling systems typically employ fans or blowers to drive air through high conductive metal (cooper, aluminum, or combined) heat sinks. Although fans can produce large volume flow rates, their low thermal effectiveness and noise prevent further application in system requiring high heat dissipation.

A synthetic jet is able to direct airflow along heated surfaces in confined environments and induce small-scale mixing. These jets are ideally suited for cooling applications at the package and heat-sink levels. Thompson et al. (1997) [58] used synthetic jet technology in a direct, normal impingement cooling application and gained a 250% increase in power dissipation over natural convection.

The prototype active heat sink studied in this chapter was designed and experimentally studied by Mahalingam et al. [28] (2001). It is a heat sink with cooling air flow driven by synthetic jets. A typical cell of this active heat sink is shown in Figure 6.1.

To achieve the best performance of this active heat sink, a deep understanding of the flow structure, heat-transfer characteristics, and their sensitivity on the geometry and other design and operational parameters is required. However, because of the small geometry size of the cell, detailed experimental measurement is difficult. CFD analysis offers an alternative approach to investigate the flow details in the cell. In this study, the flow details and heat transfer characteristics of this active heat sink with different configurations were analyzed based on CFD simulations. The heat-transfer performance of the active heat sink at different wall temperatures was also studied.

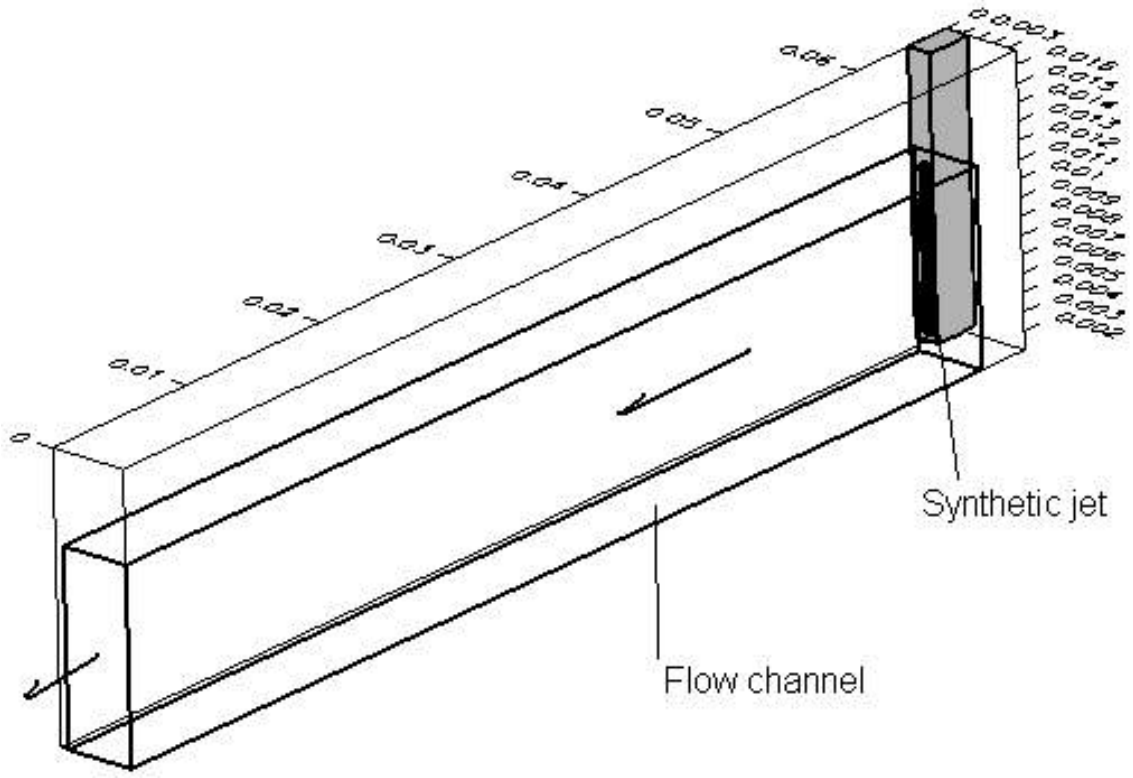

Figure 6.1: Typical geometry of an active heat sink cell

6.2 Numerical Approach

The commercial CFD package Fluent, developed by Fluent, Inc. was selected to perform the numerical simulations. Fluent is a general purpose CFD package for modeling single or multi-phase fluid flow with or without various modes of heat transfer and chemical reactions. Details about this software can be found in Chapter 1 or [2]. As one of the most widely used commercial CFD package in the world, Fluent has demonstrated its capability to solve complex engineering problems. In addition, it is reliable and numerically efficient.

6.2.1 Geometry model and computational domain

The geometry model used in this study is based on the original design of the active heat sink by Mahalingam et al. [28]. The whole system consisted of a large synthetic jet actuator cavity driven by a piezo-ceramic disk , metal heat sink fins and connecting tubes from the cavity to the heat-sink cells. A synthetic air jet is formed in each active heat sink cell from

a slit in the tube connected to the cavity. The jet is synthesized by the time-dependent periodic flow from the slit/nozzle.

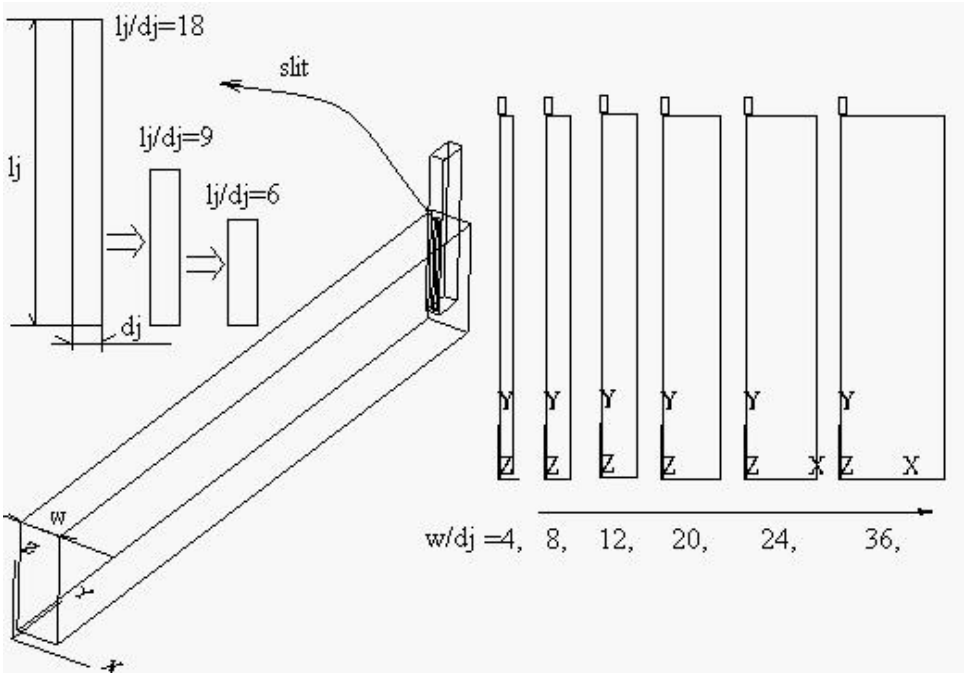

Figure 6.2: Geometrical parameters varied in this study

We varied the channel width d (non-dimensional channel width d/d_j =4 to 36), slit height l_j (non-dimensional slot height l_j/d_j =6, 9 and 18), and slit position in the z-direction for the $l_j/d_j = 6$ case. Figure 6.2 shows a diagram of these geometry variations. The length of the channel was also varied. The baseline design (original design) for these geometrical parameters are shown in Table 6.1.

Table 6.1: Dimension of Computational Domain (original design)

Domain	Length (mm)	Width (mm)	Height (mm)
Tube	Irregular	Irregular	15.24
Slit	3.3	0.5	8.89
Channel	63.5	4.06	10.7

The computational domain includes the last part of tube, slit, and channel. Body adapted structured grids were used with a typical mesh size of $200,000 \sim 400,000$ nodes. For the grid convergence study, fine meshes with about 1 million nodes and coarse meshes with around 60,000 nodes were also used. All results reported here were conducted on

the medium-density grids, if no exception is noted. Since the cross section of the cavity has been shown to have little effect on the synthetic jet flow, the shape of the cavity in the computational model was modified to a relatively simple shape with the cross-sectional area kept unchanged (Figure 6.3).

6.2.2 Fluid properties

Compressibility is important when the local Mach number of the flow is larger than 0.3. In terms of computational cost, compressible models are much more expensive than using incompressible models. In this study, the airflow is assumed incompressible because of small Mach number through the slot (the largest velocity in the entire computational domain occurs in the slot).

If the temperature change is large, air properties change significantly. Therefore, a linear-piecewise property table was used for density, viscosity, specific heat and thermal conductivity in the range of T=$293K \sim 373K$ ($20°C \sim 100°C$).

To verify the above assumptions, simulations of one selected case (ld608top) with the largest nozzle velocity were completed using both incompressible and compressible models. The results showed that the incompressible model and linear-piecewise air properties are sufficiently accurate. As shown in Table 6.2, the difference in the total heat transfer, and the overall heat transfer coefficients are all less than 1.5%. The non-dimensional velocity profile and temperature profile at a line (y=0.06m, z=0.055) were shown in Figure 6.4. The difference between incompressible simulation and compressible model is small (less than 1.5%).

Table 6.2: Comparison between compressible and incompressible simulations

	Total heat transfer rate (W)	Overall surface heat transfer coefficient (W/m^2K)	Nu
Incompressible	2.21	16.5	548.3
Compressible	2.18	16.26	540.9
Difference (%)	1.4	1.4	1.34

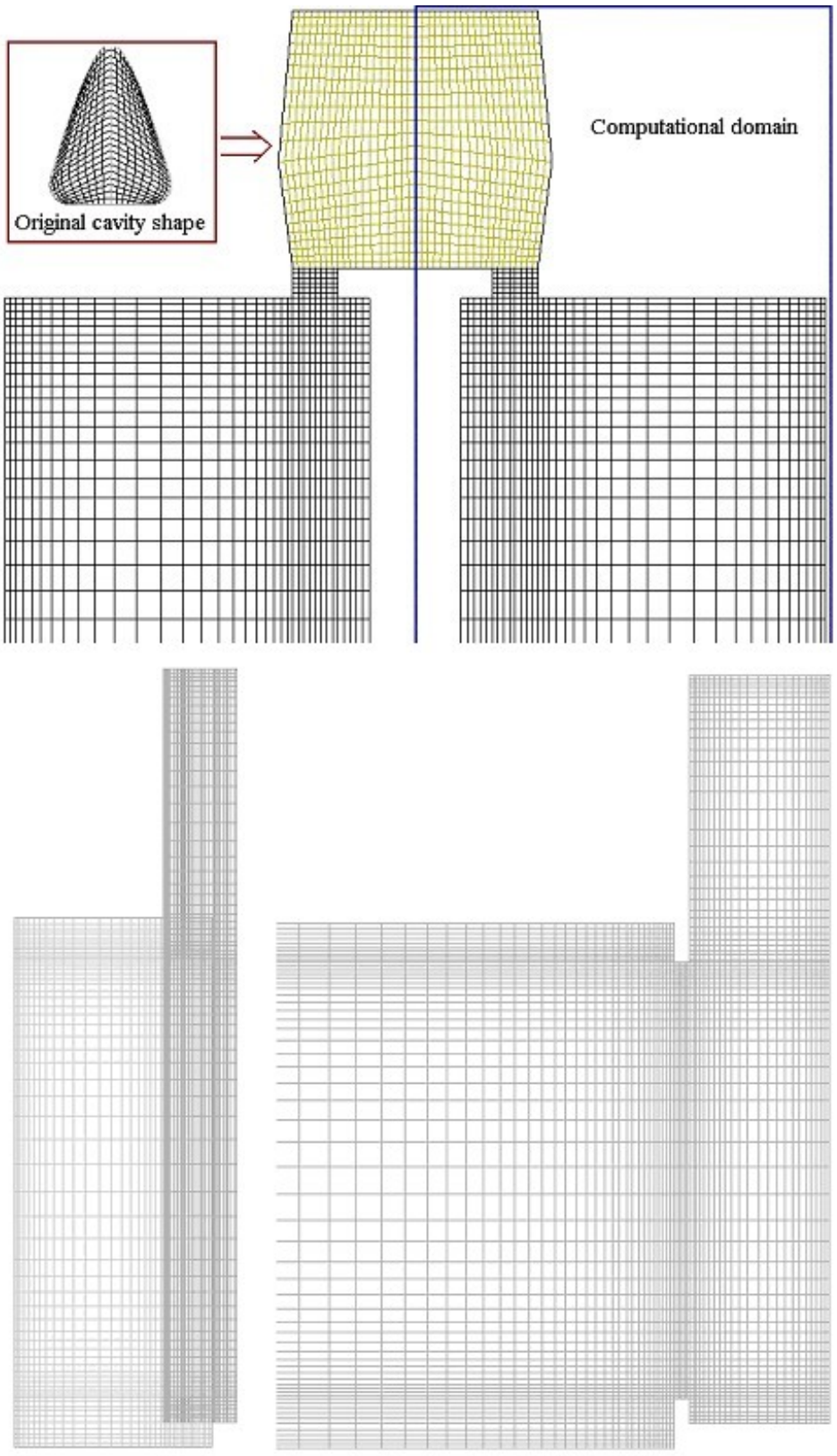

Figure 6.3: Illustration of typical mesh in x-, y- and z-cutting planes

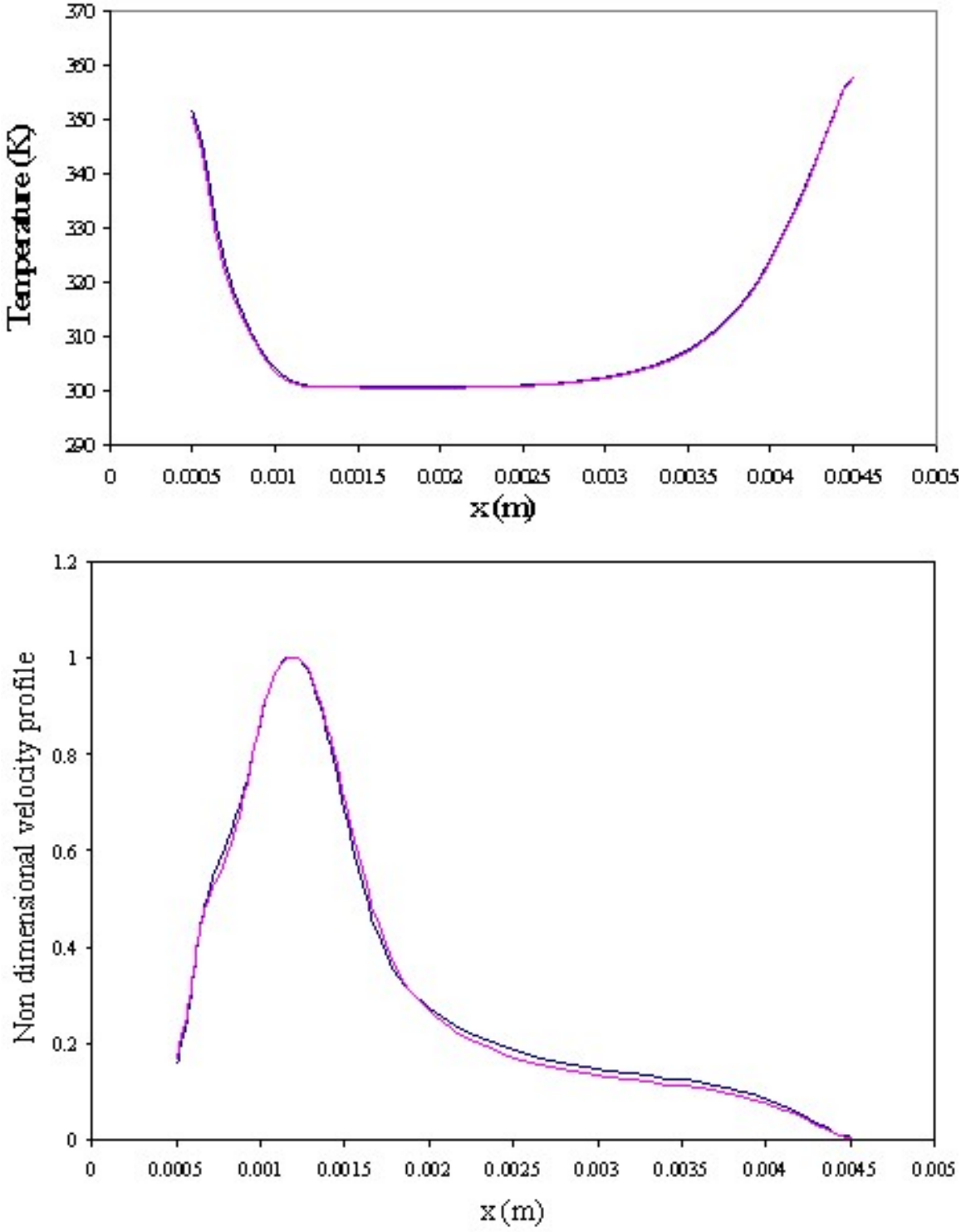

Figure 6.4: Temperature and velocity profile at an arbitary line

6.2.3 Boundary conditions

As mentioned in the previous section, the synthetic jet cavity was not included in this computational model. Instead, a uniform velocity boundary condition was assigned at the cavity tube top surface. For a frequency of 200Hz, the velocity profile of pulsatile flow is quite similar to the top hat profile.

The inlet velocity magnitude was determined by matching the flow rate in the channel with the measured value by Mahalingam et al. (2001) [28]. The velocity magnitude was set to be 9m/s at the inlet, and so the average velocity from the nozzle (slit) was around 12 m/s. The pressure outlet boundary conditions at all openings were set to gauge pressure 0. Numerical experiments showed that these settings were sufficient to resolve the flow details without including out of channel geometry, which requires much more computational resources.

For the heat transfer simulations, isothermal wall temperature boundary conditions were assigned to four channel walls. There are several reasons to inside the channel use these thermal boundary conditions. First, the heat sink generally is made of good conductive metal materials like aluminum and copper, and the temperature difference throughout the heat sink is not large. Second, the conjugate computation, which includes conduction in the channel walls, requires a prohibitive number of iterations to achieve a converged solution. This is partially attributed to the generally large differences between the thermo physical properties of the fluid and solid which, leads to a very slow convergence rate for the numerical solution. In addition, for a typical heat conduction simulation, the time constant determines how much real time has to be simulated, which is typically several minutes for forced air cooling. For an unsteady simulation of a synthetic jet, this means hundreds of thousands of time steps, which would take approximate several weeks to complete on a 3 GHz workstation. The system reaches a periodic state much faster when using the isothermal wall temperature boundary conditions. Therefore, the computational cost is much lower. The wall temperature was set at 360K (87°C) for all simulations except those cases designed particularly for the wall temperature boundary condition sensitivity study.

6.2.4 Viscous model

As mentioned in Chapter 2, one important issue met in this study was to choose a good turbulence model to simulate the synthetic jet flows. Turbulence models available in FLUENT include:

- Prandtl mixing length model, which solves the N-S Equations with a modified turbulent viscosity derived from a Prandtl mixing length model,
- Eddy viscosity models; a 2-equation $k-\epsilon$ model and the renormalization group RNG $k-\epsilon$ model
- Second moment closure models which use differential transport equations to solve the stresses at each point in the system, e.g., the Reynolds stress Model (RSM).
- Large Eddy Simulation (LES), which is the current state of the art research level turbulence model. Transient calculations on a fine mesh solve for the large eddy motion with a sub-grid scale model representing those eddies smaller than the mesh and faster than the time step.

The flow in the active heat sink channel was a time dependent turbulent flow with regions of relaminarization. To choose the most suitable turbulence model, a comparison of different models available in FLUENT was conducted, including laminar, $k-\epsilon$, $k-\omega$, and LES. The testing problem was a simple rectangular flow through a 0.2m x0.02m x0.03m tube. Three different Reynolds numbers were designed to cover laminar flow (Re=500), transition (Re=1500) and turbulent flow (Re=16666.7).

Table 6.3: Summary of Models Comparison at Re=500 (%)

		Difference between Laminar/LES	Difference between Laminar/ $k-\omega$	Difference between Laminar/ $k-\epsilon$
Outlet	Wall Shear Stress	4.4	10.8	99.4
Wall 5	Wall Shear Stress	1	27.9	121.6
Outlet	Skin Friction	4.4	10.8	99.4
Wall 5	Skin Friction	1	27.9	121.6
Wall 5	Static Pressure	0.07	34.4	119.5

The wall shear stress, skin friction, and static pressure at the outlet and a randomly selected wall were compared. The conclusion is clear: the large eddy simulation (LES) provides acceptable results at low Reynolds number. The difference of wall shear stress and skin friction between LES and pure laminar flow were less than 5% and the difference in the statics pressure was less than 0.1%. All of these are much less than the corresponding values from $k-\epsilon$ and $k-\omega$ turbulence model. At the higher Re=1,500, LES performed better than the RANS-based models, with difference to laminar flow less than 3.5%. Therefore, LES is a better choice when simulating transition problem or problems in which both laminar flow and turbulent flow exist.

The results also showed that the performance of the $k-\omega$ model was better than the $k-\epsilon$ model for both of the relatively low Reynolds's number cases. This supports our selection of the $k-\omega$ in the 2D synthetic jet simulations reported in chapter 3.

Although, LES may be our best choice, it has its own weaknesses. The most basic of the subgrid-scale models was proposed by Smagorinsky and further developed by Lilly. For laminar flow, the Reynolds equations revert to the Navier-Stokes equations, and the Reynolds stresses are zero. In contrast, the residual-stress tensor generally is non-zero in laminar flow. This general result notwithstanding, for several important flows the residual stresses are essentially zero. For laminar shear flows, in which the residual shear stresses are zero, the appropriate value of the Smagorinsky coefficient is $C_s = 0$. A non-zero value of C_s would incorrectly lead to residual shear stresses on the order of Δ^2. So the Smagorinsky model with a constant non-zero value for C_s is incorrect for laminar flow.

Table 6.4: Summary of Models Comparison at Re=1500 (%)

		Difference between Laminar/LES	Difference between Laminar/ $k-\omega$	Difference between Laminar/ $k-\epsilon$
Outlet	Wall Shear Stress	2.35	34.6	170.2
Wall 5	Wall Shear Stress	3.32	34.3	138.1
Outlet	Skin Friction	2.35	34.6	170.3
Wall 5	Skin Friction	3.33	34.2	138.2
Wall 5	Static Pressure	1.8	17.74	79.7

Fluent provides another LES subgrid model the RNG-based subgrid model in order to correct this problem. In highly turbulent regions of the flow, the RNG-based subgrid scale model reduces to the Smagorinsky-Lilly model with a different model constant. In low-Reynolds-number regions of the flow, the argument of the ramp function becomes negative and the effective viscosity becomes equal to the molecular viscosity. This enables the RNG-based subgrid-scale eddy viscosity to model the low-Reynolds-number effects encountered in transitional flows and near-wall regions.

We used the viscous model Large Eddy Simulation (LES) in Fluent to simulate the three dimensional active heat sink. To yield numerically accurate solutions, a sufficiently fine mesh is needed. However, better numerical accuracy comes with a higher price. With the numerical methods usually employed in LES, halving the grid spacing increases the computational cost by about a factor of $2^4 = 16$. Although it is necessary to demonstrate that the LES solutions are grid-independent, due to the overwhelming computational cost, as indicated by Pope et al. [43], this is seldom done. Meyers et al. [33] deposed the LES error by comparing LES results with reference DNS results. Modeling and numerical errors were identified as the two basic sources of error. In engineering applications the grid-independent mesh often reaches the resolution requirement of DNS. This is not only losing the advantage of using the LES technique, but it also introduces larger modeling errors, which often trades off the advantage of the lower numerical error by using a finer mesh. In practice, researchers usually only follow some generally recognized rules, like the first row of cells locates within the region of $y^+ \sim 1$.

In summary, this study used LES with the RNG-based subgrid model to complete all simulations. The constants were set as: $C_{RNG} = 0.157$, wall Pr=0.85. Viscous heating was neglected.

6.2.5 Validation

Due to technical difficulties, experimental measurements of the flow field inside the active heat sink are not available. The validation of the numerical approach was done through a series of carefully designed numerical experiments, in which a grid-dependence study and a

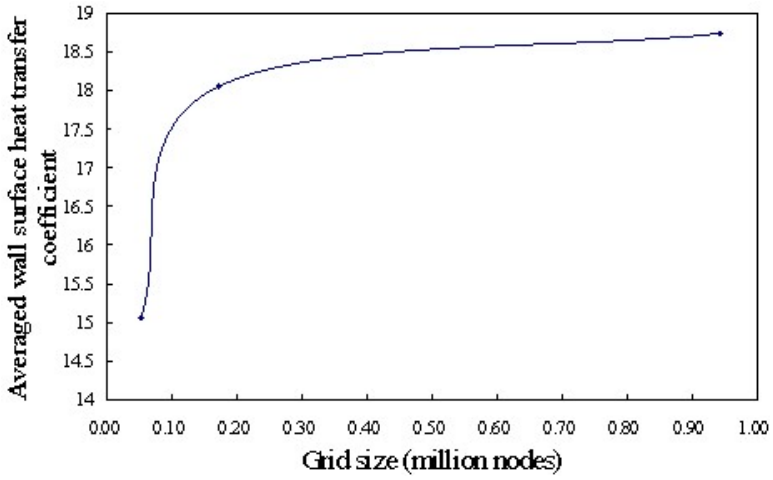

Figure 6.5: Averaged wall surface heat transfer coefficient convergence on mesh size

time-step study were conducted. Typical mesh sizes used in these studies are listed in table 6.5.

Table 6.5: Typical mesh information of grids used in mesh dependency study

	Cells	Faces	Nodes
Coarse	46,956	145,896	52,140
Medium	160,400	492,528	171,960
Fine	1,283,200	3,801,792	1,328,975

The difference in the averaged wall shear stress between the medium and fine meshes was 5.55% and the difference in the averaged surface heat transfer coefficient was 4.77%. Figure 6.5 shows the convergence of wall surface heat transfer coefficient. These results showed that the medium-sized mesh was sufficient to yield acceptable accuracy. To avoid the high computational costs with the fine mesh, medium-sized meshes were used in most cases of this study.

The time steps per cycle was set to 36. Through a time-step-size study (with 72 and 144 time steps per cycle), this value was found sufficient to capture the transient characteristics of synthetic-jet flow. In comparison with simulations to 144 time steps per cycle, the wall shear stress difference was 1.21% and the difference in the surface heat transfer coefficient was 2.62%.

6.2.6 Solution strategies

For all simulated configurations, the flow field was solved first and then the heat transfer model was turned on. After $5 \sim 6$ cycles, the flow field generally reached a periodic state. Typically, 10 cycles were simulated to guarantee that this periodic state was reached. In heat transfer simulations, the computations were continued until several specially selected parameters met the following criterion:

1. the RMS error between the total heat transfer rates during the last two cycles was less than 0.5%; and

2. the RMS error between the channel-outlet averaged flow temperature during the last two cycles was less than 0.5%.

Although for isothermal boundary conditions the real time simulated was much less than in simulation where heat conduction in the channel walls was modeled, the heat transfer simulation was still computationally expensive. Typically, to complete 40 cycles (0.2 sec real time) on a 200,000 node mesh, nearly 70 hours were needed on a 2GHz Intel Xenon-level workstation with 1G of memory.

The characteristics of three synthetic jets are summarized in Table 6.6. Table 6.7 lists all numerical parameters used in simulations (no numerical study cases are included).

Table 6.6: Synthetic jet characteristics

l_j/d_j	$d_j(mm)$	$d_{Hydraulic}(mm)$	stroke Length	stroke length 2	$V_{avg}(m/s)$	Re_{I_o}
18	0.5	0.947	33.5	17.7	6.71	8812
9	0.5	0.9	55	30.6	11	24955
6	0.5	0.857	86.1	50.22	17.22	61573

Notes: $d_{Hydraulic} = 4A_{cross-section}/P_{cross-section}$

6.3 Superior Performance over conventional heat sink

In order to evaluate the performance of the active heat sink, three baseline cases without using synthetic-jet technology were designed.

The first baseline case was designed to compare the performance of the active heat sink with a heat sink driven by a conventional jet through the same nozzle such that the net

Table 6.7: Summary of simulated cases (normalized by jet nozzle width d_j)

Case ID	l	d	l_j	Jet position	Remarks
Ld1808base1	127	8	18	Bottom	Steady state case, flow rate in the channel matched with cases with synthetic jet on,
Ld1808base2	127	8	18	Bottom	Steady state case, pure channel flow, inlet flow from one end of channel
Ld1808base3	127	8	18	Bottom	Steady state case, average inlet velocity matched with synthetic jet on,
Ld1808ht	127	8	18	Bottom	With synthetic jet on.
Ld1812ht	127	12	18	Bottom	
Ld1820ht	127	20	18	Bottom	
Ld1824ht	127	24	18	Bottom	
Ld1836ht	127	36	18	Bottom	
Ld1808topoff	127	8	18	Bottom	Open channel case, without top wall.
Ld1808short	30	8	18	Bottom	
Ld908	127	8	9	Bottom	
Ld912	127	12	9	Bottom	
Ld920	127	20	9	Bottom	
Ld924	127	24	9	Bottom	
Ld936	127	36	9	Bottom	
Ld608b	127	8	6	Bottom	
Ld612b	127	12	6	Bottom	
Ld620b	127	20	6	Bottom	
Ld624b	127	24	6	Bottom	
Ld636b	127	36	6	Bottom	
Ld608m	127	8	6	Middle	
Ld612m	127	12	6	Middle	
Ld620m	127	20	6	Middle	
Ld624m	127	24	6	Middle	
Ld636m	127	36	6	Middle	
Ld608t	127	8	6	Top	
Ld612t	127	12	6	Top	
Ld620t	127	20	6	Top	
Ld624t	127	24	6	Top	
Ld636t	127	36	6	Top	
Ld620mpos1	127	20	6	Middle	Jet positioned $4.8d_j$ from side wall
Ld620mpos2	127	20	6	Middle	Jet positioned $9.8d_j$ from side wall

flow rate through the heat sink channel was the same. This case shared the same geometry design of the active heat sink (ld1808). All the boundary conditions were the same except the inlet velocity boundary condition which was set to a constant velocity. The velocity magnitude was determined by matching the average flow rate through the channel with the original design (ld1808). The averaged flow rate through the channel was 0.1 CFM or $4.66\text{x}10^{-5}$ kg/s. The inlet velocity was found to be 6.15 m/s by a series of trial and error simulations.

The second baseline case was designed to compare the performance of the active heat sink with a heat sink driven by a conventional jet with an inlet velocity equal to the averaged inlet velocity in the blowing stroke half cycle of the synthetic jet. The averaged inlet velocity of the synthetic jet driven heat sink was 2.8648 m/s. Again, this case shared the same geometry design and all other boundary condition settings except for the inlet velocity boundary condition.

The third baseline case was designed to compare the performance of the active heat sink to a heat sink without any jet. This case shared the same geometry, but there was no jet flow from the nozzle (slit). A velocity inlet boundary condition was assigned at one end of the channel. The velocity determined by matching the average flow rate through the channel was found to be 0.82 m/s.

The results from these three baseline cases and the ld1808 case are listed in Table 6.8.

From these results, we found that the active heat sink showed significant advantages over a conventional heat sink and a heat sink driven by a conventional jet. Compared to a conventional channel flow (case 3) with the same flow rate through the channel, a 16.5% increase in the total heat transfer rate was observed. The overall heat transfer coefficient was improved by 21%. The improvement is more significant, when comparing the ld1808 case with case 2, which has the same averaged inlet velocity. The total heat transfer was increased by 108%, and the overall heat transfer coefficient was increased by 109%. The total heat transfer for case 1 was 14% more than that of the active heat sink, but this was achieved by a 115% larger inlet velocity. There is no doubt that if the averaged inlet velocity of the active heat sink increased by 115%, its heat transfer performance would be

Table 6.8: Comparison of active heat sink and non-synthetic jet heat sinks

	Active heat sink	Case 1	Case 2	Case 3
Mass flow rate through channel (x$10^{-5} kg/s$)	4.66	4.66	1.53	4.66
Flow rate (CFM)	0.1	0.1	0.035	0.1
Outlet velocity (m/s)	1.01	1.07	0.36	0.91
Inlet velocity (m/s)	$9 \sin(\omega t)$	6.15	2.86	0.85 (channel)
Outlet temperature (K)	348	352	358	344
$Surfaceheatflux_{leftwall}$ (W)	0.874	0.814	0.349	0.693
$Surfaceheatflux_{rightwall}$ (W)	0.809	0.949	0.389	0.693
$Surfaceheatflux_{topwall}$ (W)	0.097	0.147	0.029	0.206
$Surfaceheatflux_{bottomwall}$ (W)	0.323	0.482	0.241	0.206
$Surfaceheatflux_{total}$ (W)	2.095	2.392	1.008	1.798
$h_{leftwall}(W/m^2K)$	17.915	16.679	7.157	14.202
$h_{rightwall}(W/m^2K)$	16.581	19.444	7.97	14.202
$h_{topwall}(W/m^2K)$	5.314	8.046	1.57	10.017
$h_{bottomwall}(W/m^2K)$	17.75	26.422	13.196	10.017
$h_{total}(W/m^2K)$	15.693	17.836	7.514	12.964
$Nu_{leftwall}$	594.5	553.2	236.9	473.1
$Nu_{rightwall}$	550.5	645.4	263.8	473.1
$Nu_{topwall}$	177.8	266.6	51.7	334.6
$Nu_{bottomwall}$	591.4	893.3	441.2	334.6
$Nu_{totalwall}$	521.4	594.1	249.3	432.1

much better than baseline case1.

It is believed that the periodic boundary layer development on the heat sink channel walls is the key mechanism for the heat transfer enhancement seen in the active heat sink. From the temperature contours for the baseline cases (shown in Figure 6.6), one can see a significant difference in boundary-layer development. The temperature contours for the ld1808 case shown in the figure is not the averaged temperature contour but a time instant contour. The boundary layer in this case was significantly thinner than the others. Although the boundary layer of case 1 is thicker than the pure channel flow case, the better mixing in the channel enhances the heat transfer weakened by the boundary layer development. In addition, the boundary layers of baseline case 1 and 2 are not evenly developed: the boundary layer along the left wall is thicker than right wall. The reason is that the jet flow moves down along the channel direction and somewhat towards the right due to the geometry of the nozzle/slit. This also answers the question of why the heat transfer rate on the right wall is higher than the left wall. In the ld1808 case, the heat transfer from the left wall was slightly stronger than the right wall. Further flow details will be discussed in the following section.

In summary, the active heat sink employing synthetic jet technology showed better performance than a heat sink using conventional techniques, including conventional jets.

The mechanisms for heat transfer improvement in the active heat sink include:

1. the unsteady jet flow causes a periodic development of the thermal boundary layer. The thickness of the thermal boundary flow is significantly reduced when the synthetic jet operates.

2. low temperature ambient air was entrained by the synthetic jet;

3. jet impingement occurs in some regions.

In practice, engineers quantify the total heat dissipation capability of a heat sink in two ways. The first is the heat transfer flux based on the bottom wall area q_{area}. If we consider an active heat sink cell with length L, height H, channel width d, and channel wall

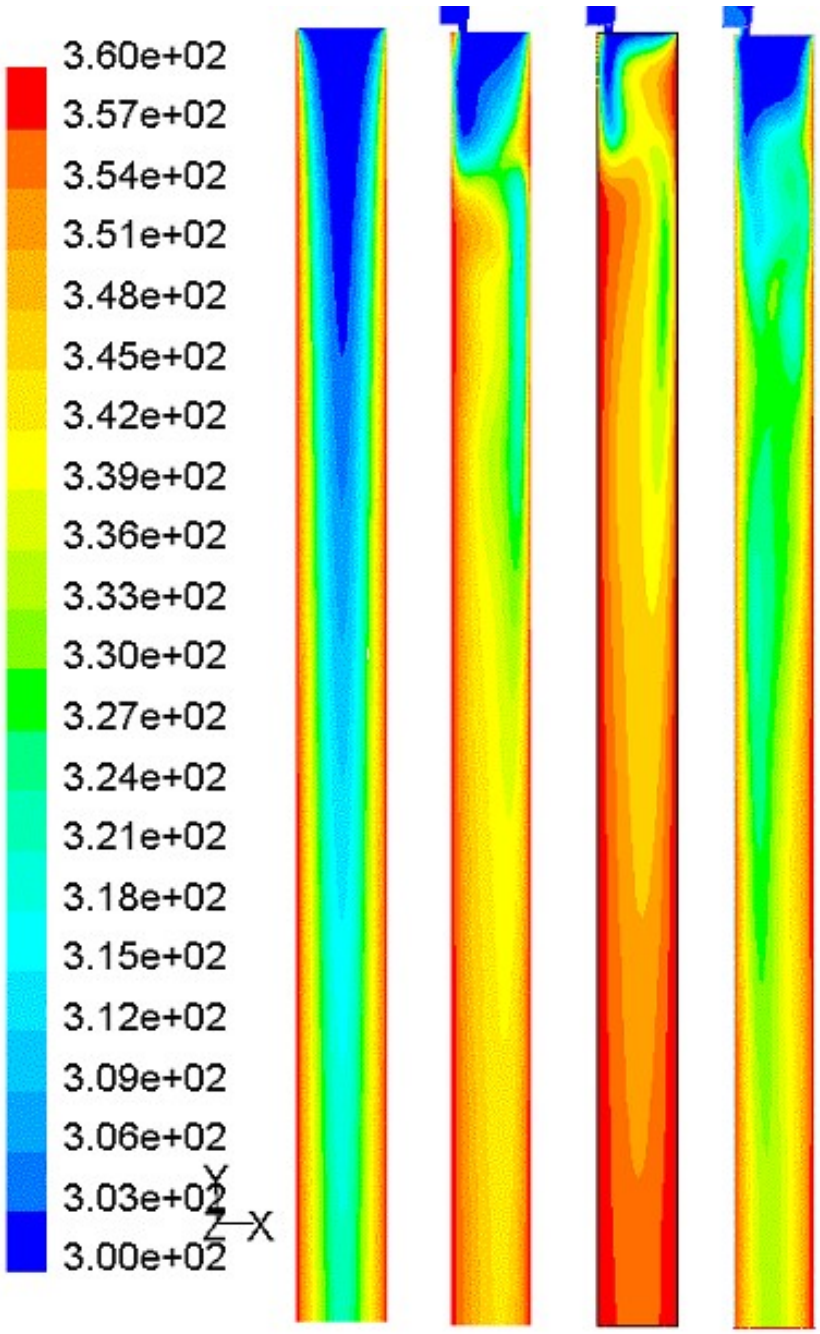

Figure 6.6: Temperature contours on the z-cutting plane at the half-height of the channel, from left to right: baseline 3, baseline 1, baseline 2 and ld1808

thickness δ, then this flux is defined as:

$$q_{area} = \frac{Q_{cell}}{L \cdot (d + \delta)}. \tag{6.1}$$

The second way, used for heat transfer devices, is called the volume heat dissipation

rate. It is defined as:

$$q_{vol} = \frac{Q_{cell}}{V_{cell}} = \frac{Q_{cell}}{L \cdot (d + \delta) \cdot H}. \tag{6.2}$$

For the four baseline heat sinks discussed above, the calculated q_{area} and q_{vol} are list in table 6.9. The active heat sink cell length L is 63.5 mm, height H is 10.7 mm, channel width d is 4.0 mm, and fin thickness δ is 1mm.

Table 6.9: Comparison of q_{area} and q_{vol}

	Active heat sink	Case 1	Case 2	Case 3
$q_{area}(W/cm^2)$	0.66	0.75	0.32	0.57
$q_{vol}(W/cm^3)$	0.62	0.7	0.3	0.53

6.4 Flow structure and characteristics

6.4.1 General flow structure

The flow in the active heat sink cell is complex. This is illustrated in Figure 6.7, which shows the tracks of particles released at the channel inlet in case 2 simulations (see previous section). The strong secondary flow in the channel near the nozzle/slit is illustrated by particles moving towards the outlet by circling in the channel. After a certain distance downstream, the flow begins to show the ordinary characteristics of channel flow.

The flow field for an active heat sink is even more complex, partially because of its time dependent nature. Vorticity contours with the velocity vector field overlaid at different phases in one cycle are shown in Figure 6.8. The z-cutting plane was 2 mm above the bottom wall.

During the blowing stroke, a vortex pair generated from the slit travels towards the right wall. The high vorticity region grows until the vortex pair separates from each other. When the synthetic jet is in the suction stroke, the residual vortex pair dissipates and at the same time a new vortex pair forms in the nozzle cavity from the nozzle/slit inner edge. As we can see from the plots, the highly disturbed flow exists in the region about 3 channel widths from the entrance or about $25d_j$. It is expected that in this region, better heat transfer performance occurs.

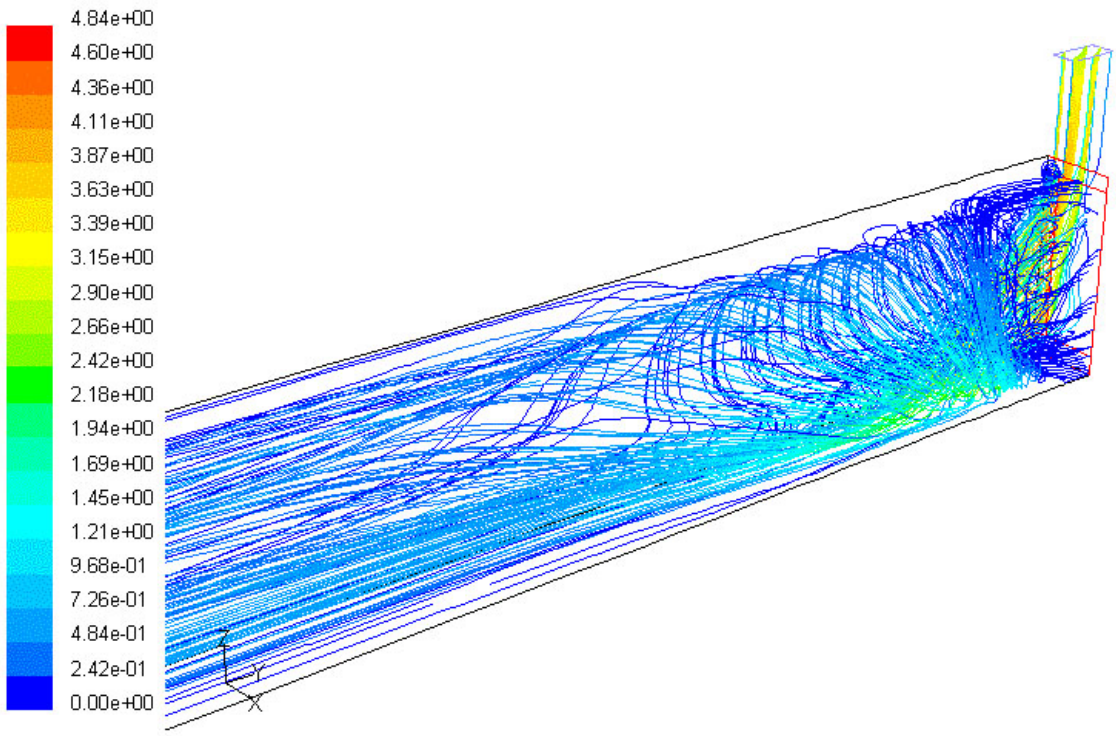

Figure 6.7: Particle tracks in the flow of case 2, legend shows the residual time of the particle

To describe the 3d flow field, plots of the velocity vectors overlaid with temperature contours on several cutting plane during one cycle are shown in Figures 6.9 through 6.14.

A large vortex can be identified near the entrance to the channel. The vortex moves downstream for a certain distance and then dissipates into the channel flow. The development of the hydraulic boundary layer and the thermal boundary layer are strongly disturbed in the region near the entrance. At some distance downstream from the slit, the flow becomes relatively smooth compared to the entrance region. Velocity fluctuations become smaller and no obvious reverse flow is observed after around six times the width of the channel (d) or 50 times the jet nozzle width (d_j).

6.4.2 Effect of active heat sink geometry on flow characteristics

The flow characteristics change when the geometry configuration of the heat sink is changed. In the previous section, general flow patterns were described. In this section, the effect of active heat sink geometry on the flow characteristics will be discussed.

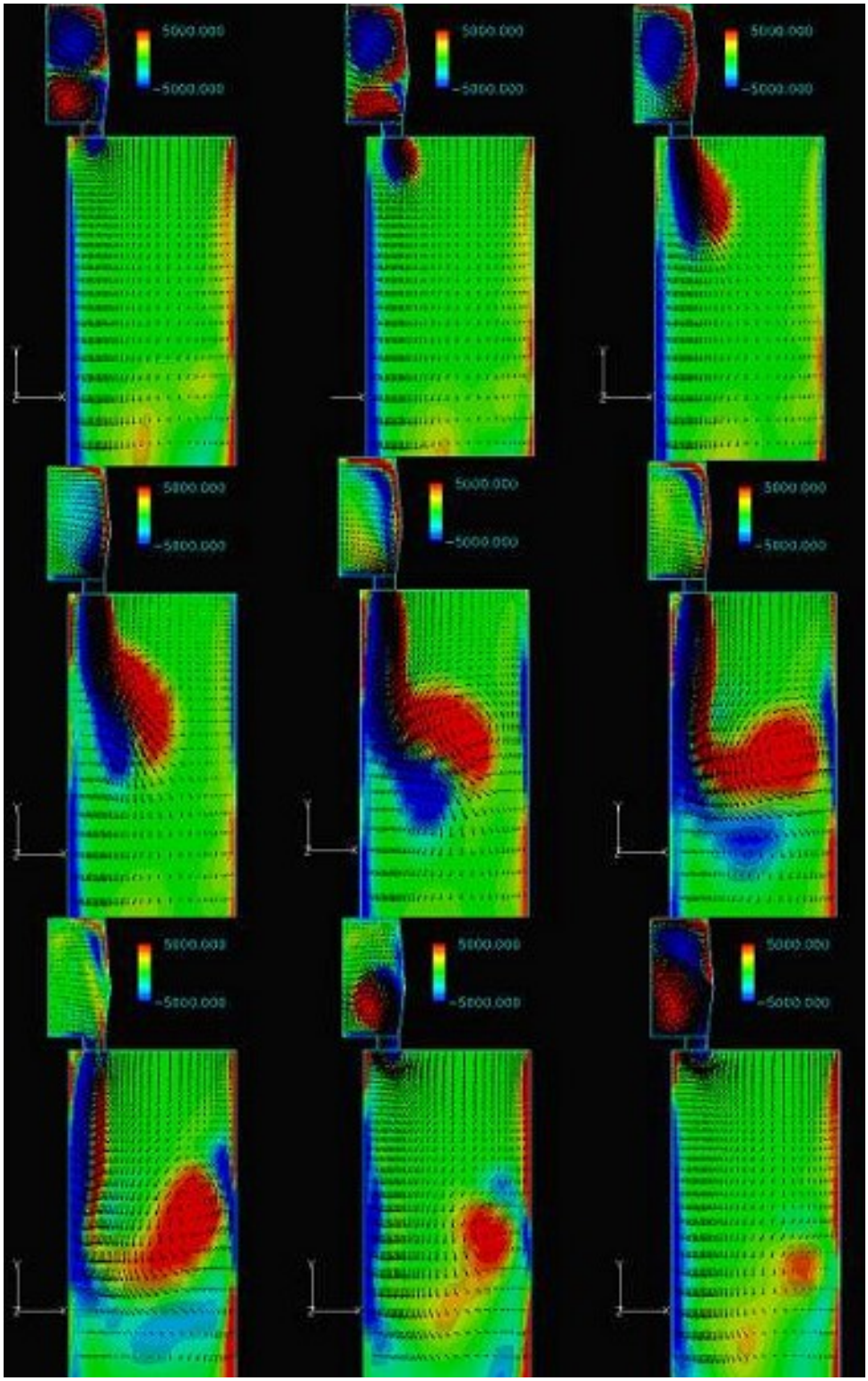

Figure 6.8: Velocity vector on vorticity contour in one cycle

It is difficult to show all of the visualization results in this dissertation because of the limited space, so only typical results were chosen. In addition, to avoid the possible distraction and confusion caused by certain visualization techniques, only results obtained from the most commonly used techniques are shown. In Figure 6.15, velocity vector fields colored by vorticity magnitude for $l_j/d_j = 18$, and $d/d_j = 8 \sim 36$ are shown.

Although there is only one jet nozzle, the velocity profile in the channel looks like a saddle shape with a peak near each side wall. The time-mean flow fields show a similar flow pattern. The time-mean velocity fields at different cutting planes for the ld1808 case are shown in Figures 6.16 through 6.20. The positions of these cutting planes are shown in Figure 6.16 and the z-cutting plane vector plots and x-cutting plane vector plots are shown in Figure 6.17 through 6.20.

6.4.3 Flow characteristics

Both the entrained flow rate and the average velocity through the channel affect the heat transfer performance. A higher entrained flow rate means that more low temperature ambient air is present in the flow, and a larger average velocity implies a higher heat

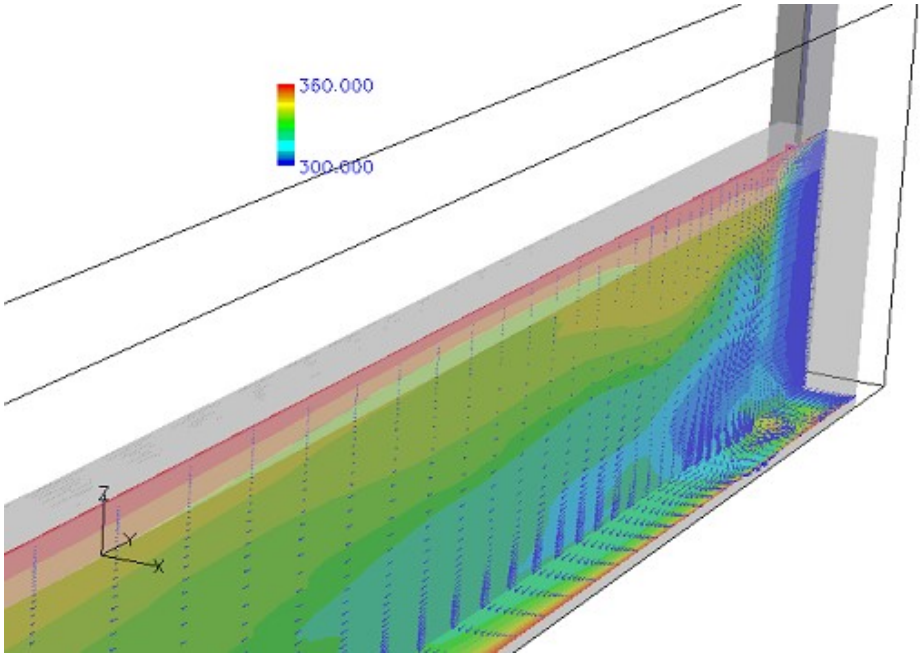

Figure 6.9: 3D flow field of an active heat sink (a)

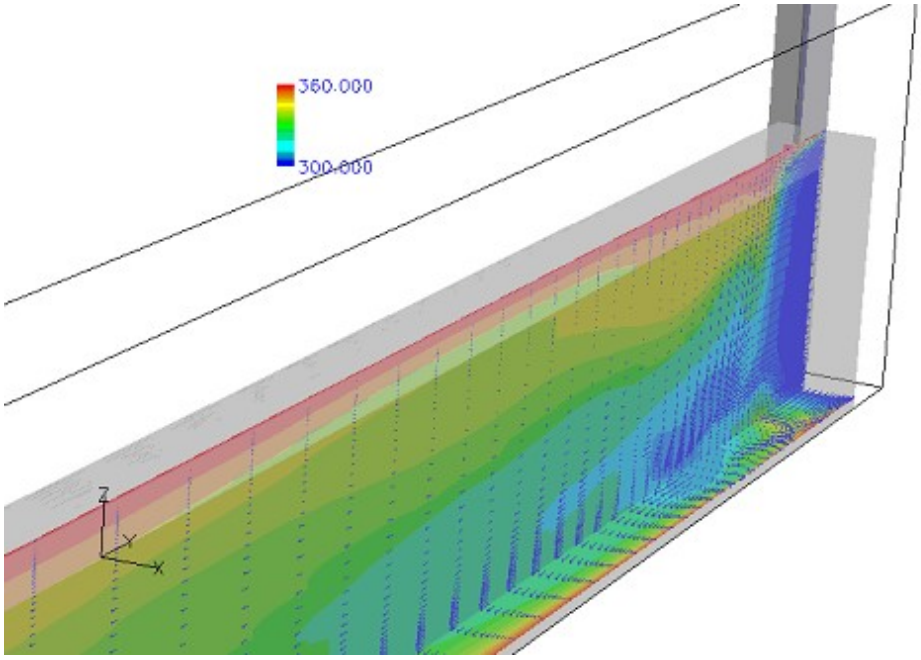

Figure 6.10: 3D flow field of an active heat sink (b)

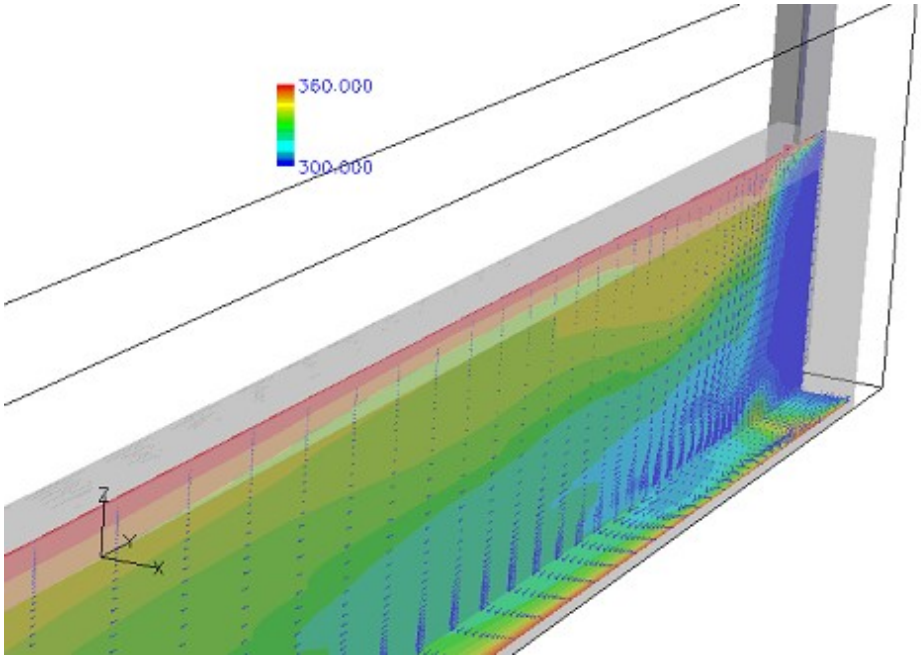

Figure 6.11: 3D flow field of an active heat sink (c)

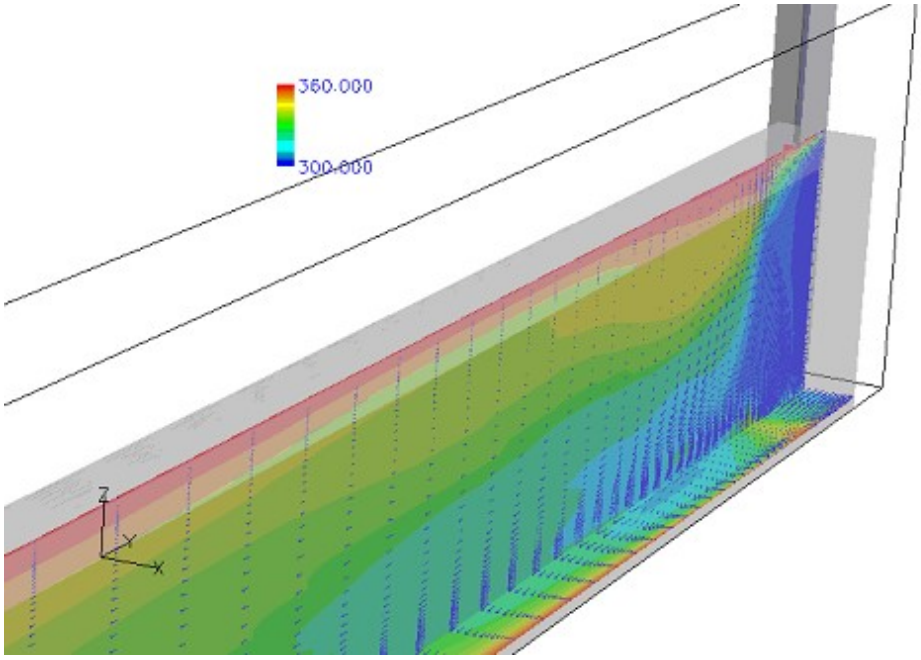

Figure 6.12: 3D flow field of an active heat sink (d)

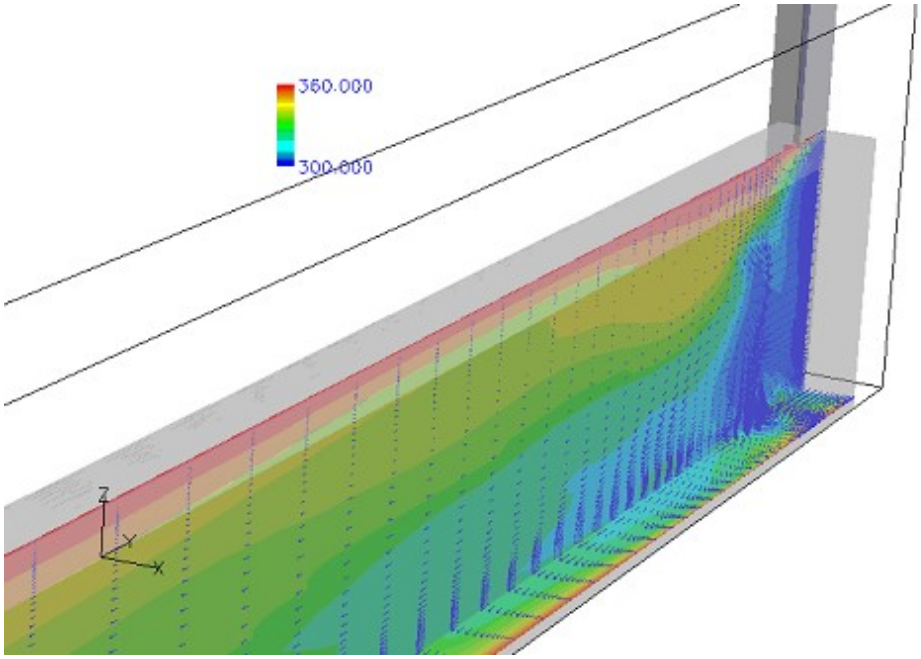

Figure 6.13: 3D flow field of an active heat sink (e)

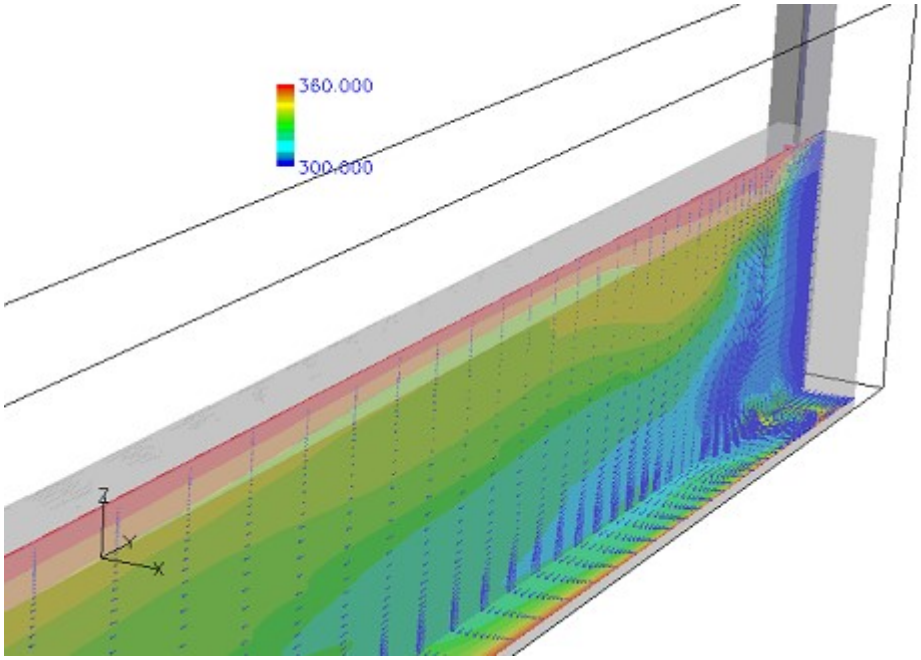

Figure 6.14: 3D flow field of an active heat sink (f)

transfer coefficient.

The entrained flow rate and average outlet velocity corresponding to different channel widths d were investigated using three different slit geometries $l_j/d_j = 18, 9$,and 6. The inlet velocity boundary condition was kept constant, so the jet exit velocities corresponding to different l_j/d_j were 6.71 m/s, 11m/s and 17.7m/s, respectively.

Figure 6.21 shows that for a given jet exit velocity (slit geometry) there exists a maximum entrained flow rate with d/d_j. As expected, the entrained flow rate increases when the jet exit velocity increases (l_j/d_j decreases).

For the geometry configurations with l_j/d_j =6 and 9, the maximum flow rate is between $d/d_j = 10 \sim 20$. The flow rate then drops until $d/d_j = 24$. A monotonically increasing flow rate to an asymptotic level was observed for $l_j/d_j = 18$, which was also observed in the experiments conducted by Mahalingam et al.(2002) [29]. For d/d_j greater than 36, the entrained flow rate becomes almost constant.

Changing the channel length also affects the flow rate through the channel. A shorter length reduces the pressure drop, which in turn increases the flow rate. Over the l_j/d_j=18,

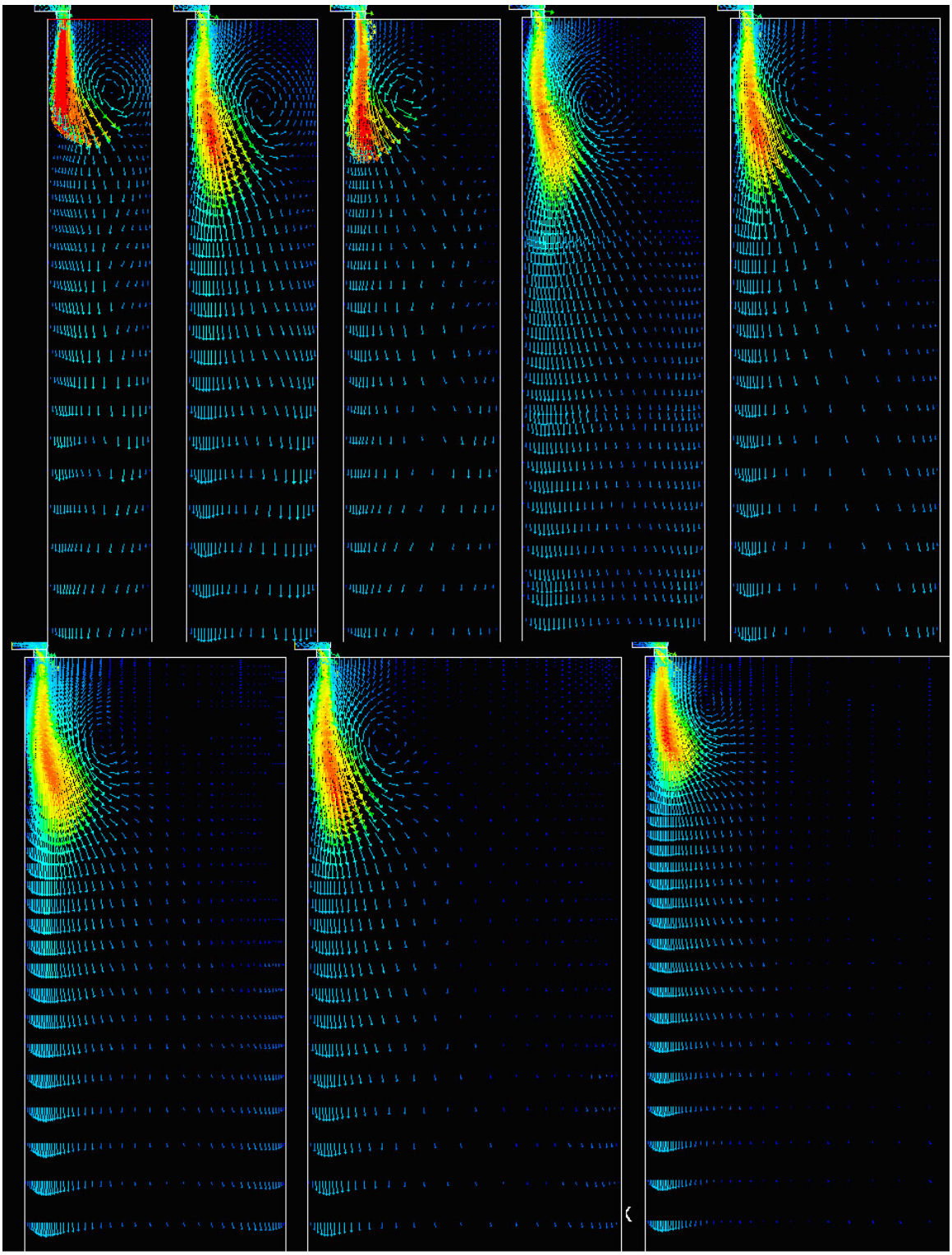

Figure 6.15: Typical stroke phase velocity fields of l_j/d_j=18, d/d_j=8, 10, 12, 14, 16, 20, 24, 36

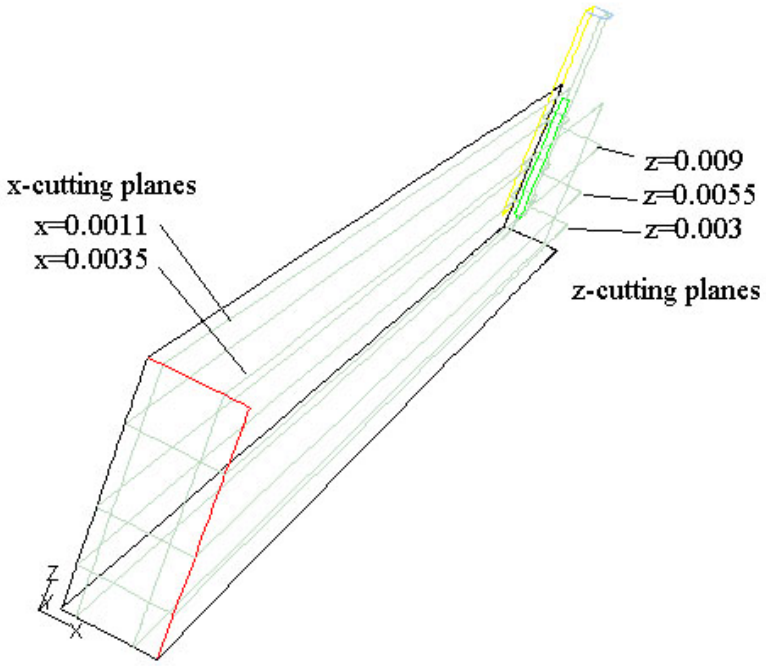

Figure 6.16: Positions of cutting planes

$d/d_j = 8$ configuration,the flow rate increased to 0.08793 CFM, a 30% increase when the channel length was shortened to 23.6% of the original length ($L_{ch} = 30d_j$).

Numerical studies on the effect of the position of a slit with l_j/d_j=6 were conducted. The slit was placed near the bottom wall, near the top wall, and in the middle of the channel in the z-direction. Because of the cavity and nozzle geometry, the synthetic jet flow is directed to the bottom and right walls at a certain angle. Therefore, the position of the slit could affect the flow fields significantly. The Figure 6.22 shows the flow rate comparison for different slit positions. When the slit was placed in the middle of the channel, the resulting flow rate is largest. When the slit was placed at the bottom, the cell entrained the least flow.

A study on the slit position in the x-direction was also conducted based on a l_j/d_j=6 nozzle placed in the middle of the channel, because it has the largest entrained flow rate among the three l_j/d_j configurations. The nozzle was placed 4.8 d_j and 9.8d_j from the left side wall respectively. Figure 6.23 shows that the entrained flow rates for these two cases are almost the same, but with the flow rate of the nozzle closer to the center slightly larger

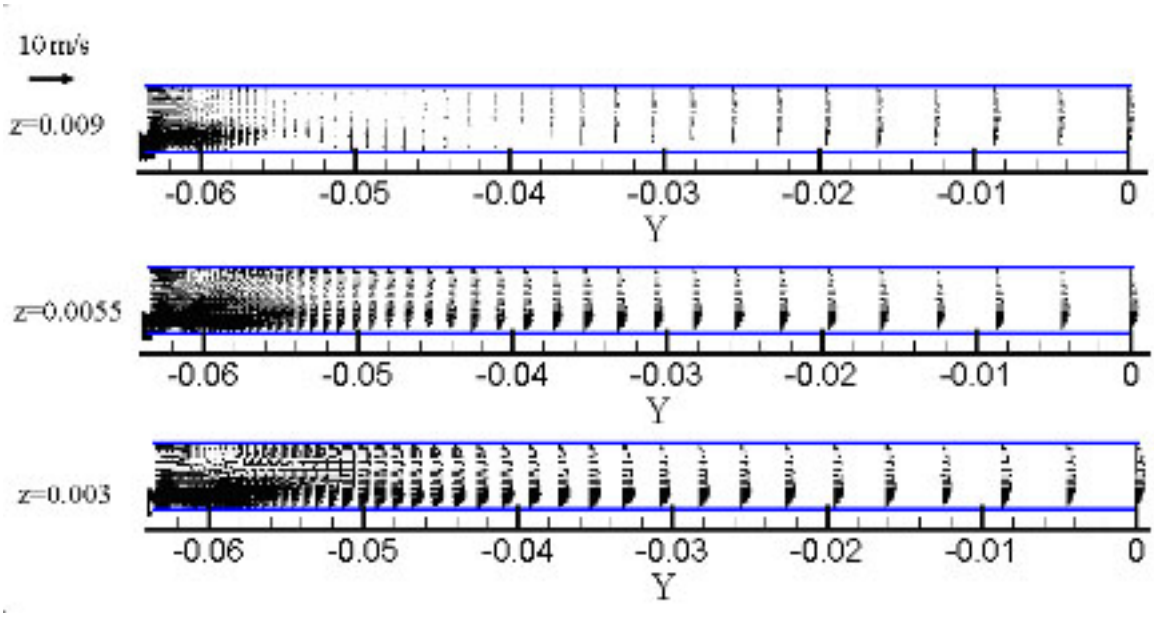

Figure 6.17: z-view of velocity profiles in the channel

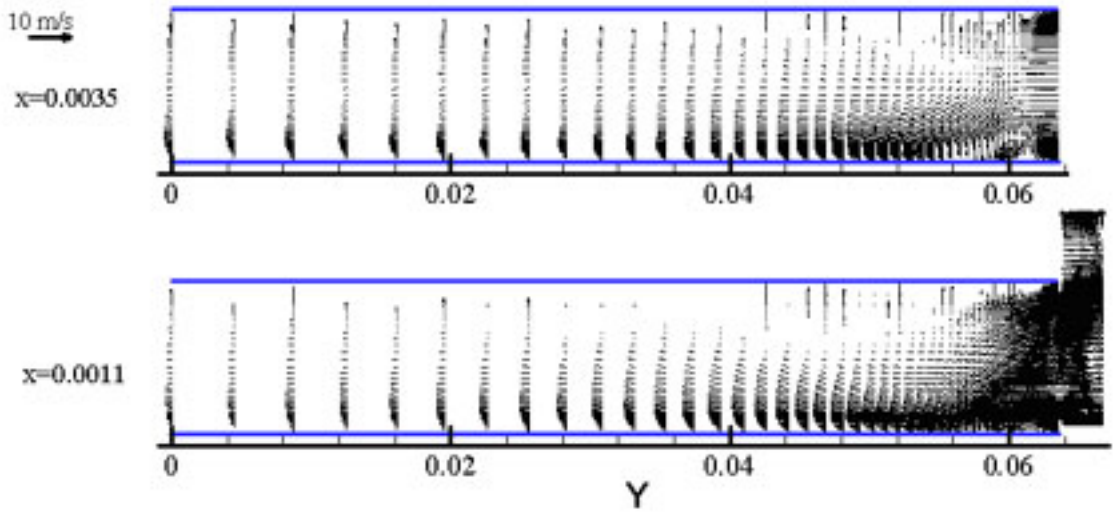

Figure 6.18: x-view of velocity profiles in the channel

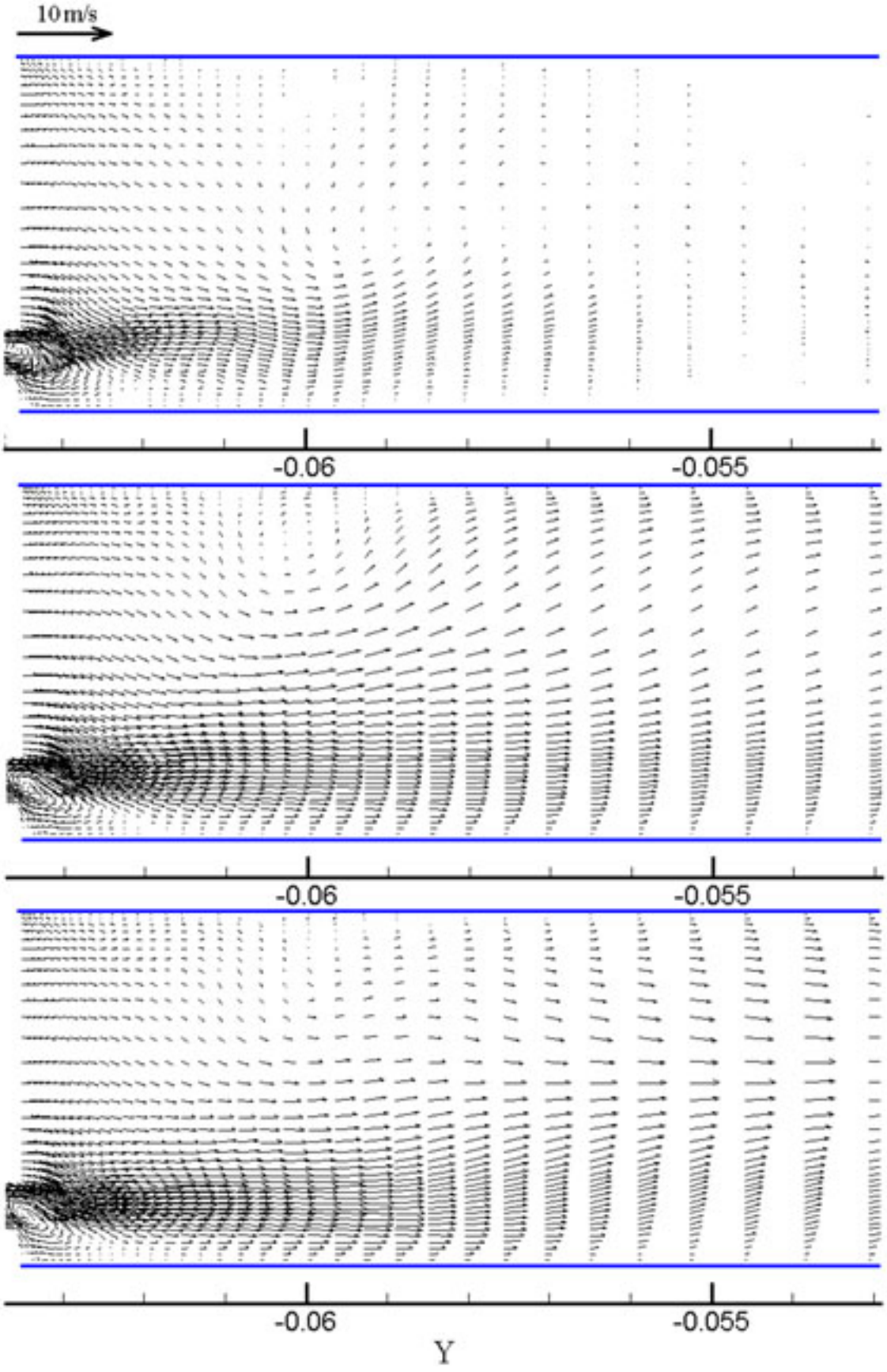

Figure 6.19: z-view of velocity profiles in the channel enlarged

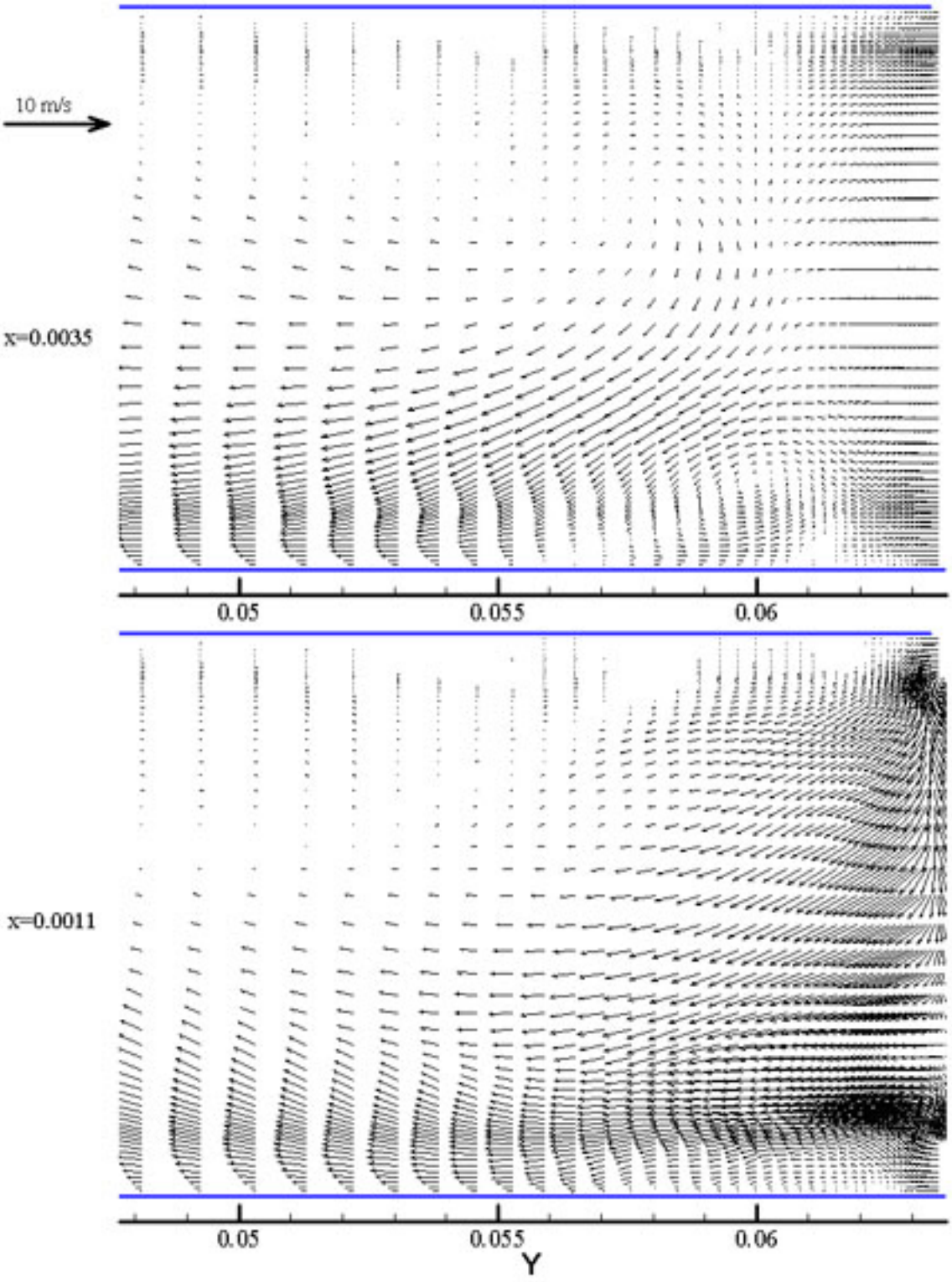

Figure 6.20: x-view of velocity profiles in the channel enlarged

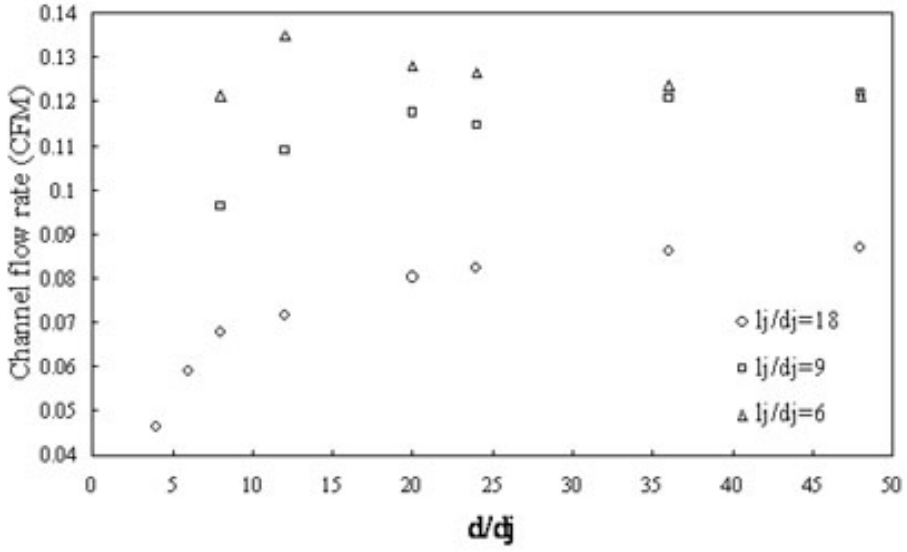

Figure 6.21: Channel flow rate verses channel width for various l_j/d_j

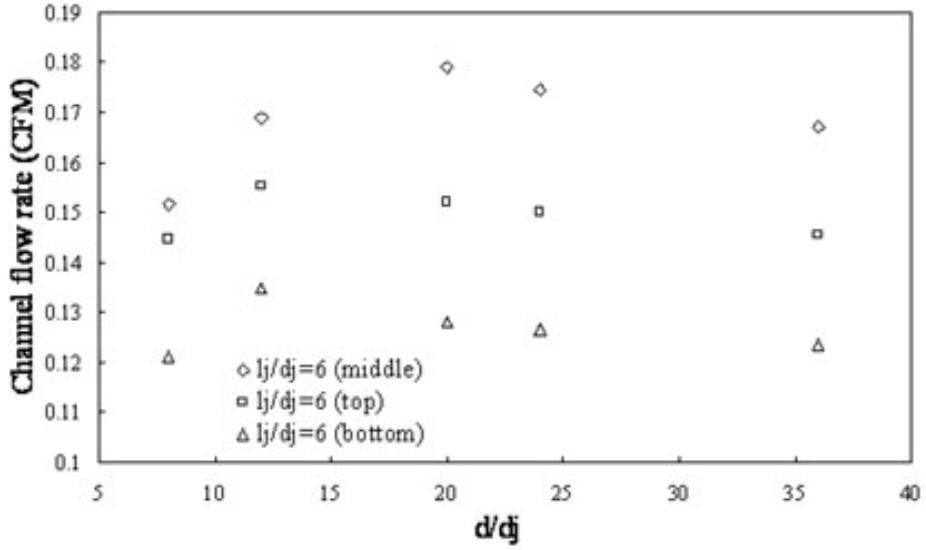

Figure 6.22: Channel flow rate verses channel width for various nozzle positions

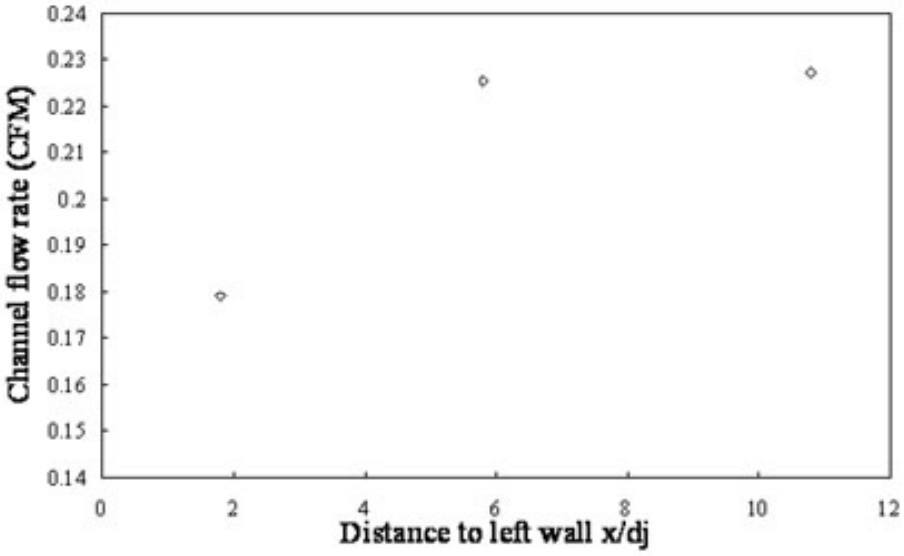

Figure 6.23: Channel flow rate verses the nozzle position in x-direction

than the other one. The entranced flow rates for these two cases are almost 26% higher than the original case in which the nozzle was placed only $0.8d_j$ or 400 μm to the left wall. The velocity fields for these three cases are shown in Figure 6.24 through 6.26.

The flow in the channel becomes quite uniform after a certain distance from the slit as discussed in the previous section. Therefore, the average outlet velocity could represent the overall velocity characteristics in the channel. As expected, with an increase in the channel width, the average velocity decreases rapidly. The heat transfer enhancement gained by the increased entrained flow rate might be canceled out. The heat transfer analysis in the next section will discuss these results. Figure 6.25 shows that the average outlet velocity for the cases with the nozzle position at the top and middle decrease more rapidly than the case with the nozzle positioned at the bottom of the channel.

6.5 Heat transfer characteristics

Flow characteristics determine heat transfer characteristics. However, because of the complex flow in this system, detailed heat transfer characteristics have to be analyzed separately

Figure 6.29 and 6.30 show the surface heat transfer coefficient contours on the channel walls (side walls and bottom wall). This is the configuration with l_j/d_j=18, $d/d_j = 8$.

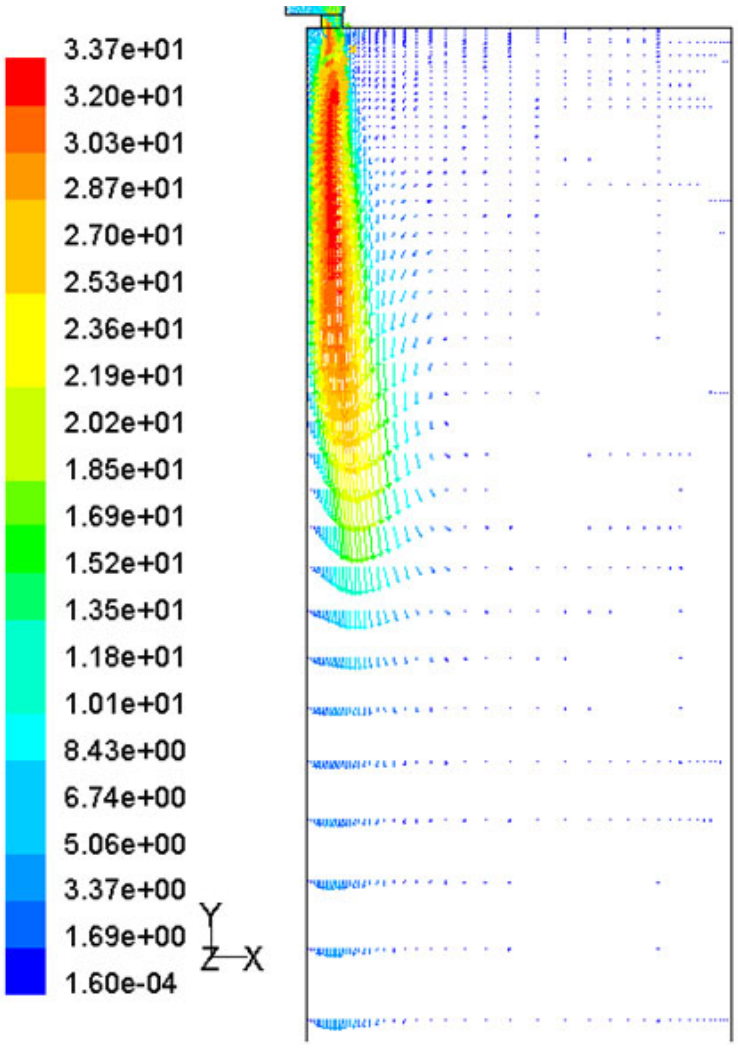

Figure 6.24: Velocity field of nozzle x-position study $x/d_j = 1.8$

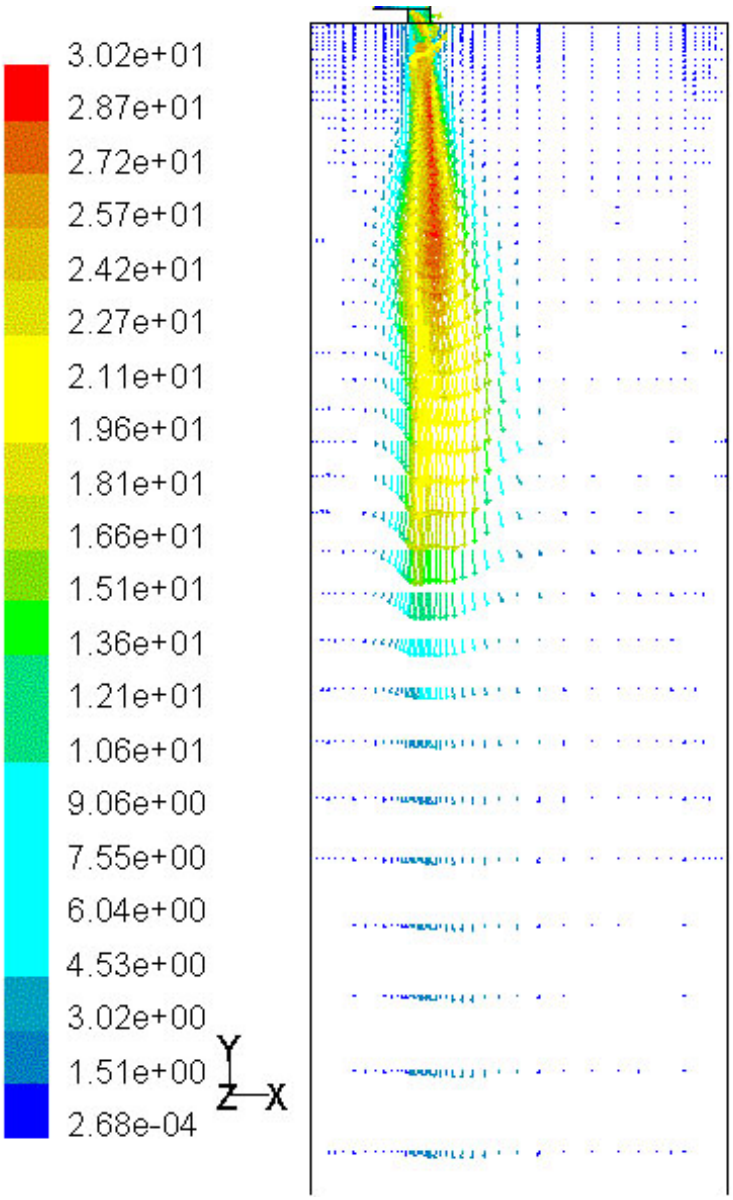

Figure 6.25: Velocity field of nozzle x-position study $x/d_j = 5.8$

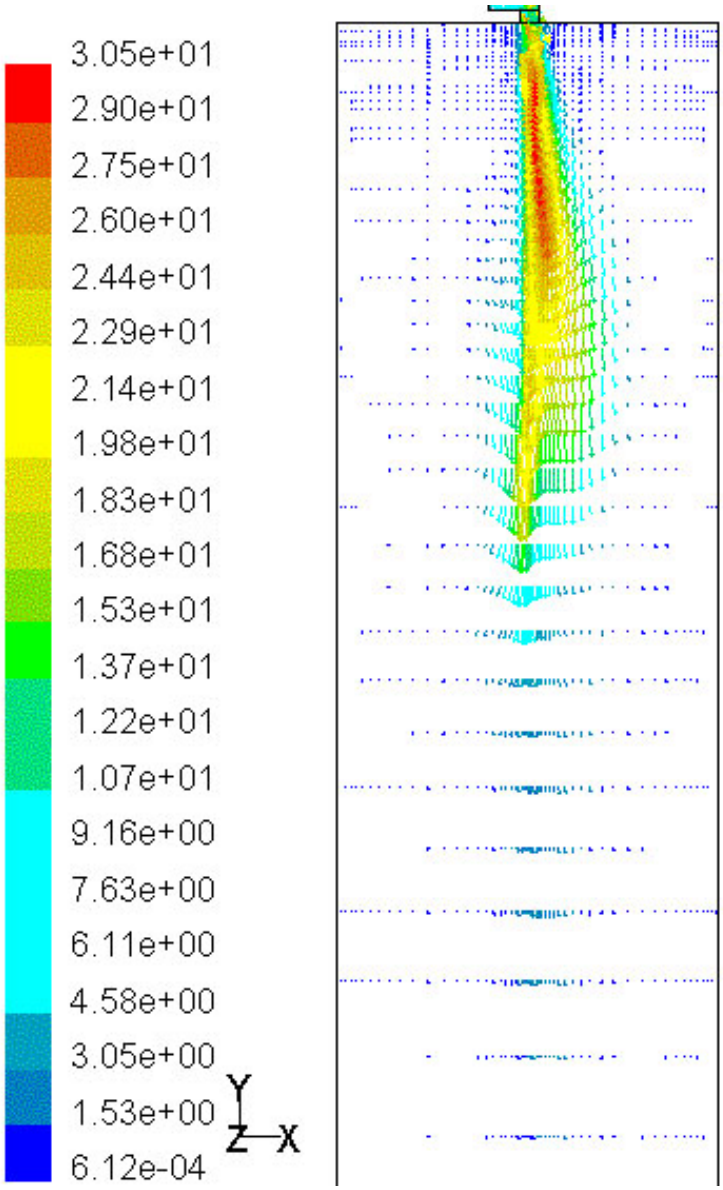

Figure 6.26: Velocity field of nozzle x-position study $x/d_j = 10.8$

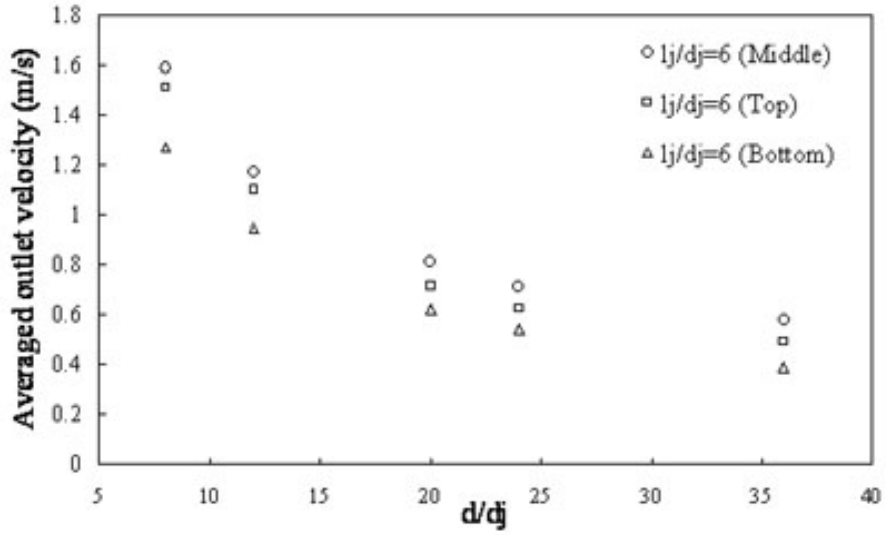

Figure 6.27: Channel outlet average velocity of different geometrical configuration

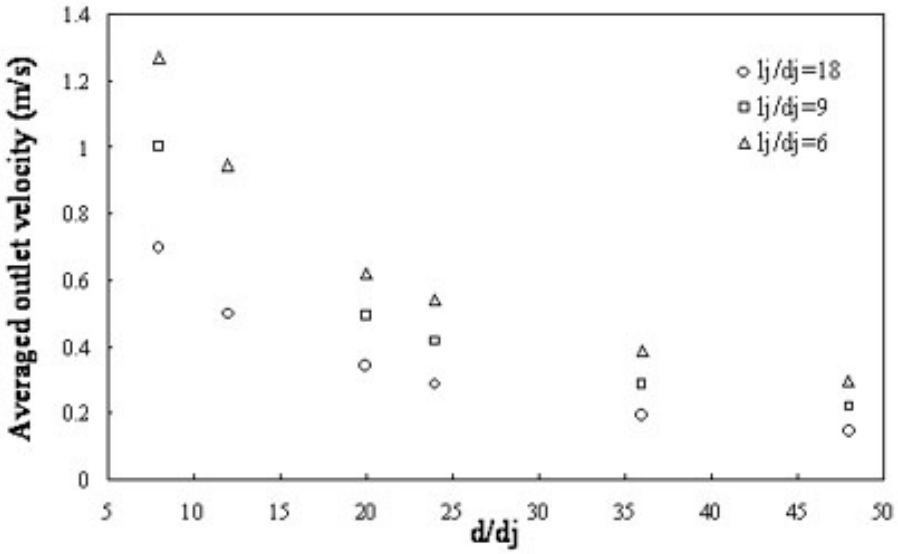

Figure 6.28: Channel outlet average velocity of different nozzle positions

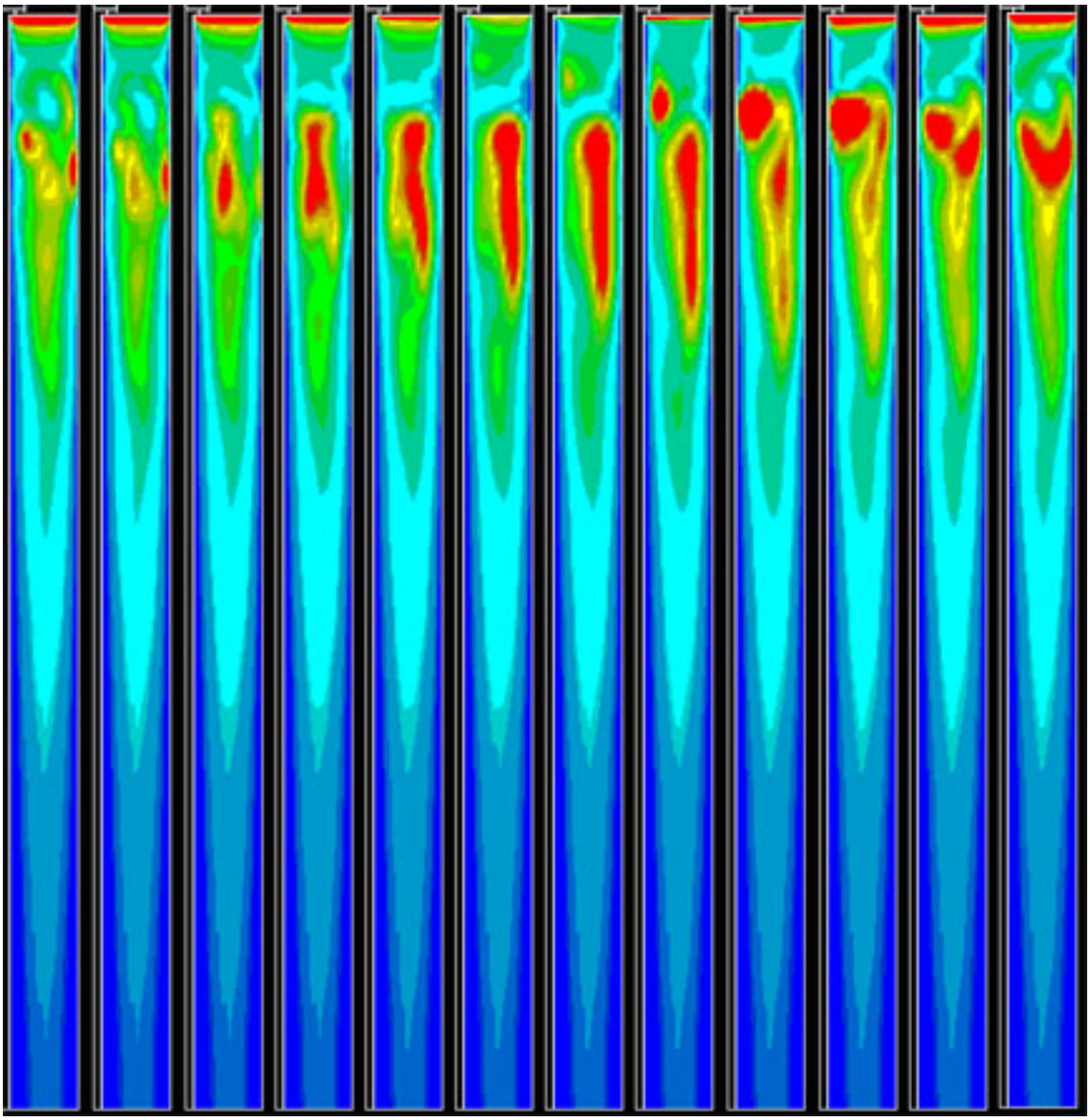

Figure 6.29: Heat transfer coefficient on the bottom wall in one cycle (in 30° interval)

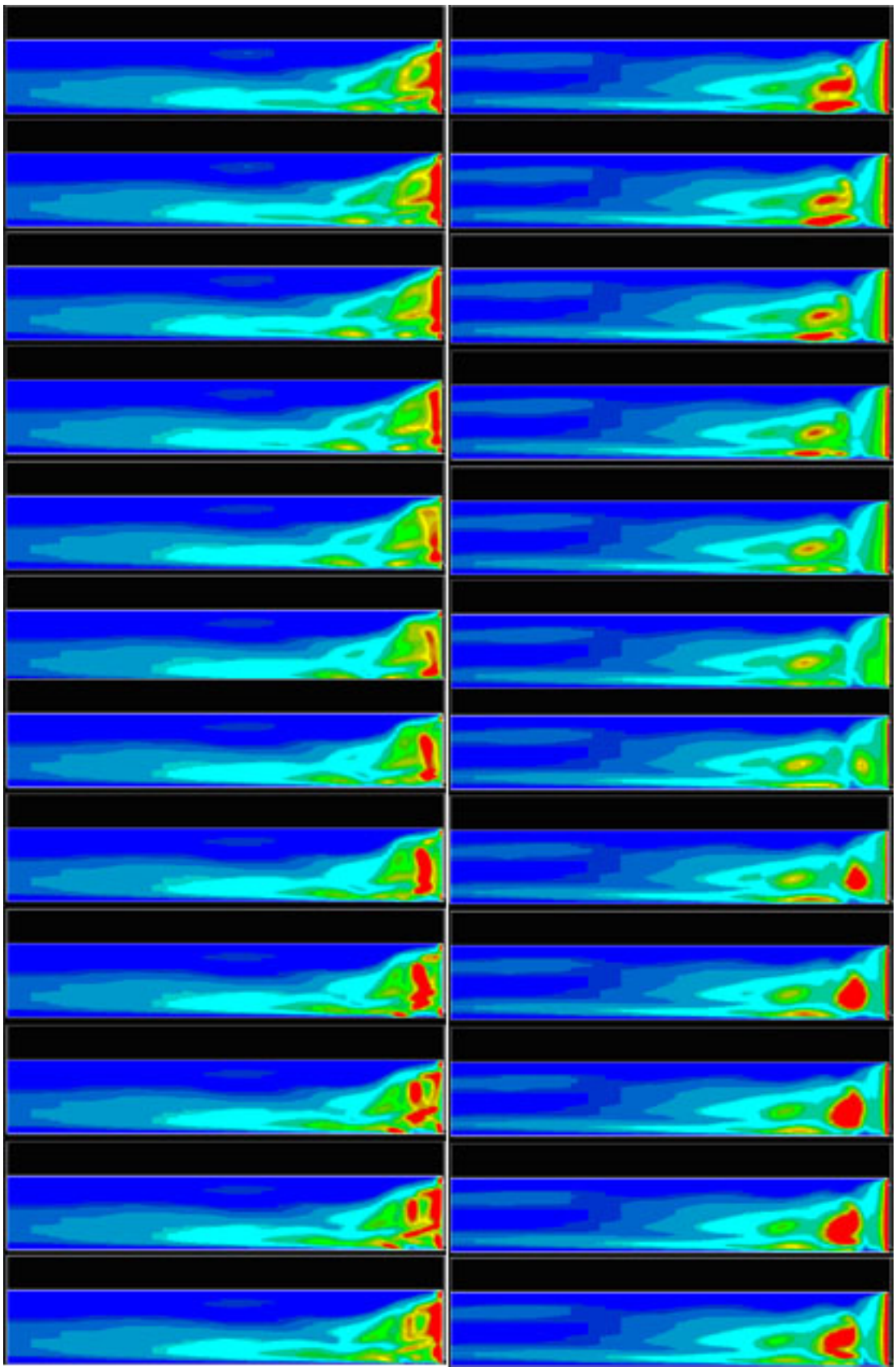

Figure 6.30: Heat transfer coefficient on left and right wall during one cycle

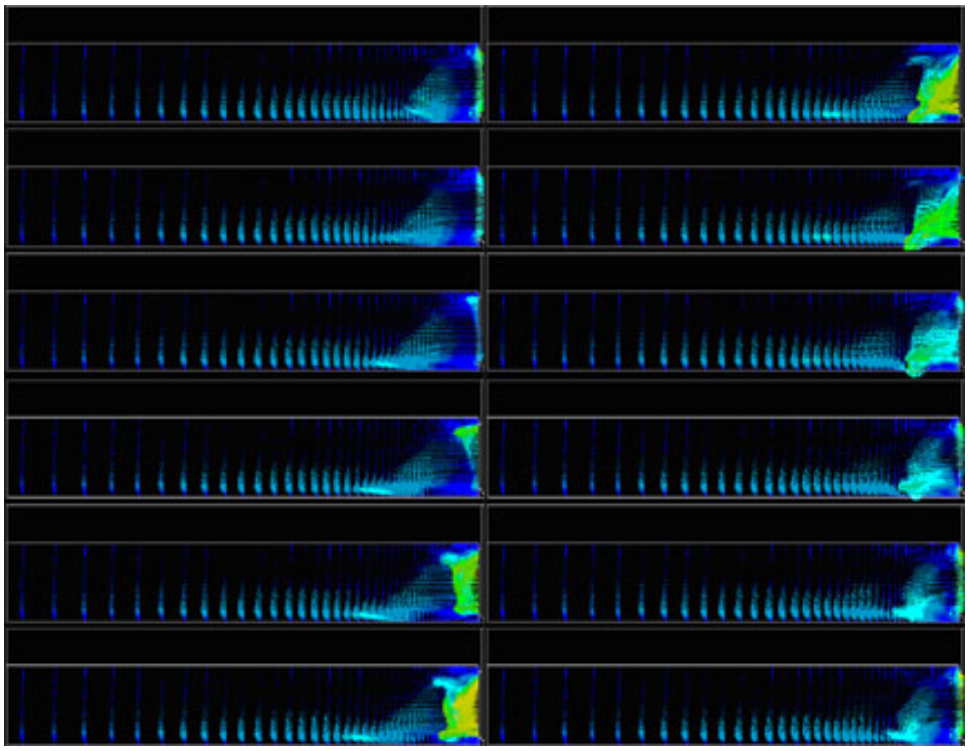

Figure 6.31: Velocity vector on the centerline plane of the jet nozzle

Regions of high surface heat transfer coefficient were located between the entrance and a distance from the jet exit of $x = 5d = 40d_j$ on all walls. However, the largest heat transfer coefficient occurred at different phases for different walls. This is because the three dimensional jet flow from the nozzle is not directed parallel to the channel but at an angle to the bottom and side walls.

In convective heat transfer, a larger flow disturbance usually means better heat transfer. When vorticity is large, generally the heat transfer coefficient is also large. The high vorticity region of the synthetic jet flow moves through the channel, and as a result, the high heat transfer region moves in almost same manner.

In the experiments conducted by Mahalingam et al.(2002) [29], there is no top wall for this channel. The centerline plane velocity vector plots shown in Figure 6.31 are similar to Figure 6.32, which is the ld1808 case. By comparing Figure 6.29 and Figure 6.33, we find that the heat transfer coefficient for the configuration without a top wall is smaller than the configuration with a top wall, which is the major configuration in this study.

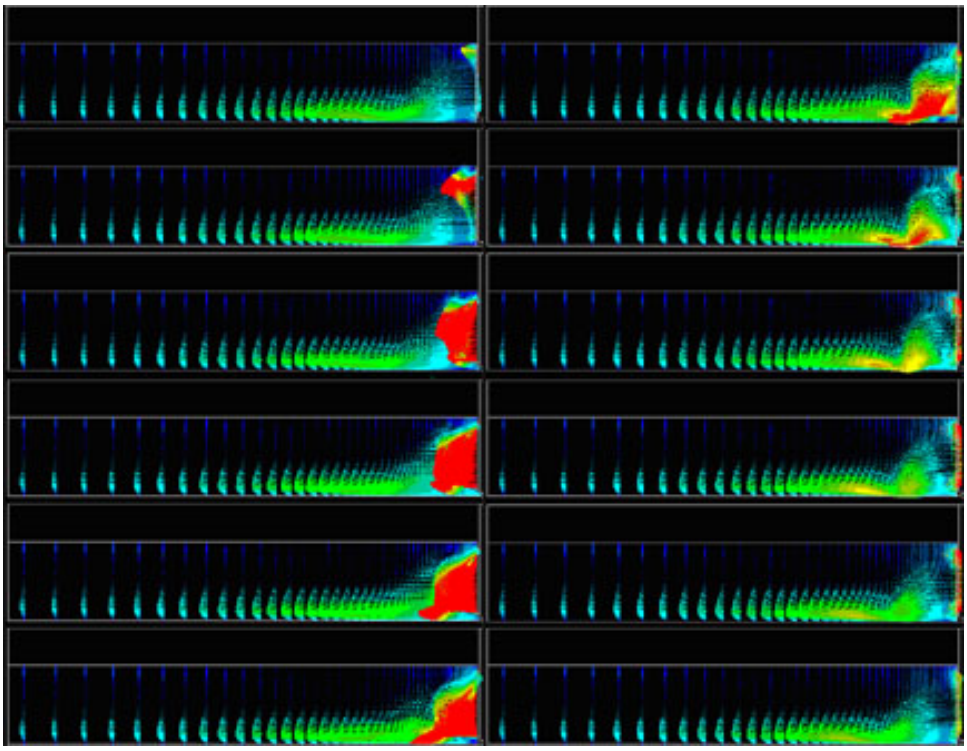

Figure 6.32: Velocity vector on the centerline plane of the jet nozzle (without top wall)

Figures 6.34 $\sim$ 6.36 show the total heat transfer rate for one cell corresponding to different geometrical configurations ($d/d_j, l_j/d_j$, nozzle position in x, and nozzle position in z). The total heat transfer rate increases as the channel width d increases. However, a drop in the heat transfer rate was observed from d=20 to d=24 for l_j/d_j=6 cases. As the area of the bottom and top walls increase, with increasing d/d_j the entrained fresh air increases, but the velocity in the channel decreases. All of these factor function together to determine the final heat transfer performance. Therefore, it's helpful to examine the heat transfer on individual walls. Figures 6.37 to 6.41 show the averaged surface Nu for four channel walls with different geometrical configurations. Data from all cases are plotted in one figure for easier comparison.

Because the left wall is placed less than $1d_j$ away from the nozzle/slit, heat transfer from this wall is stronger than that from the right wall. For small channel widths, the difference is small. As the d/d_j increases the difference becomes larger. The Nu on the right wall monotonically drops, however the Nu on the left wall increase for some configurations with

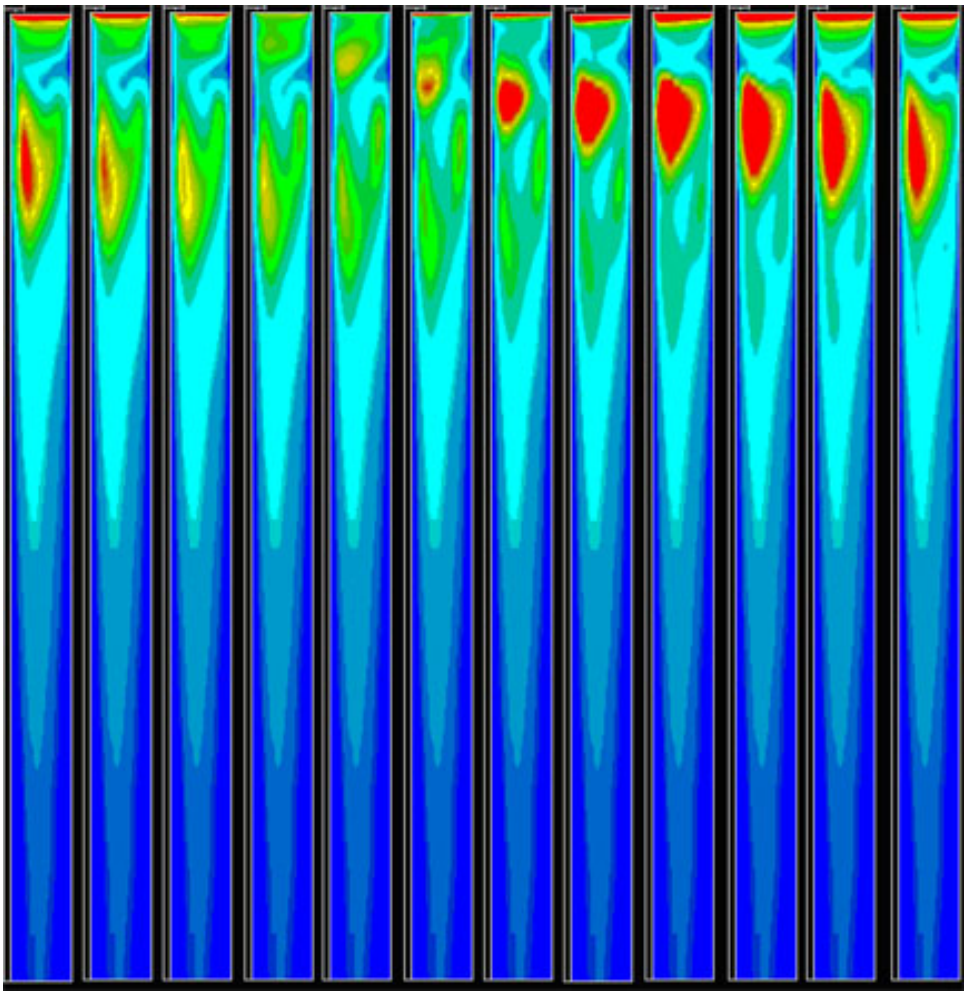

Figure 6.33: Heat transfer coefficient on the bottom wall in one cycle (without top wall) ($0° \sim 360°$ in $30°$ interval)

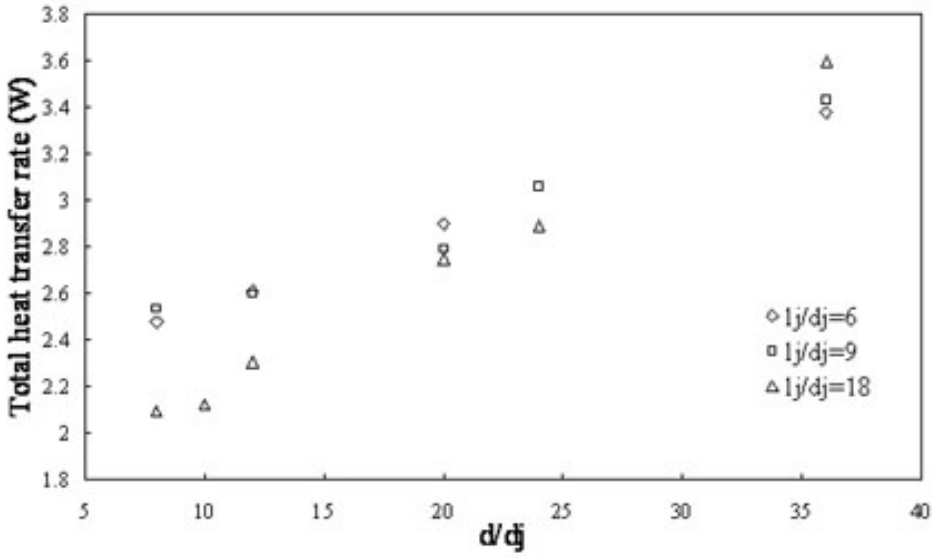

Figure 6.34: Total heat transfer rate for different l_j/d_j

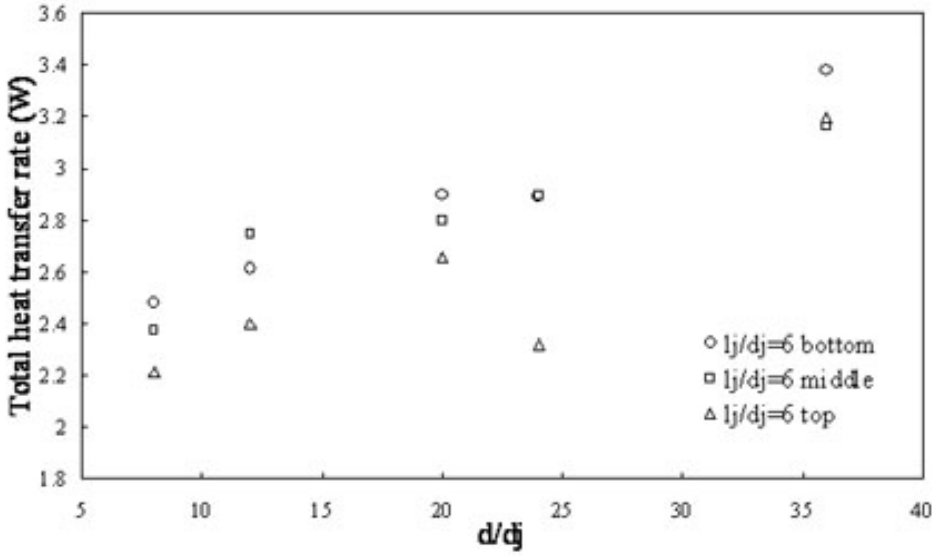

Figure 6.35: Total heat transfer rate for nozzle at different y-positions

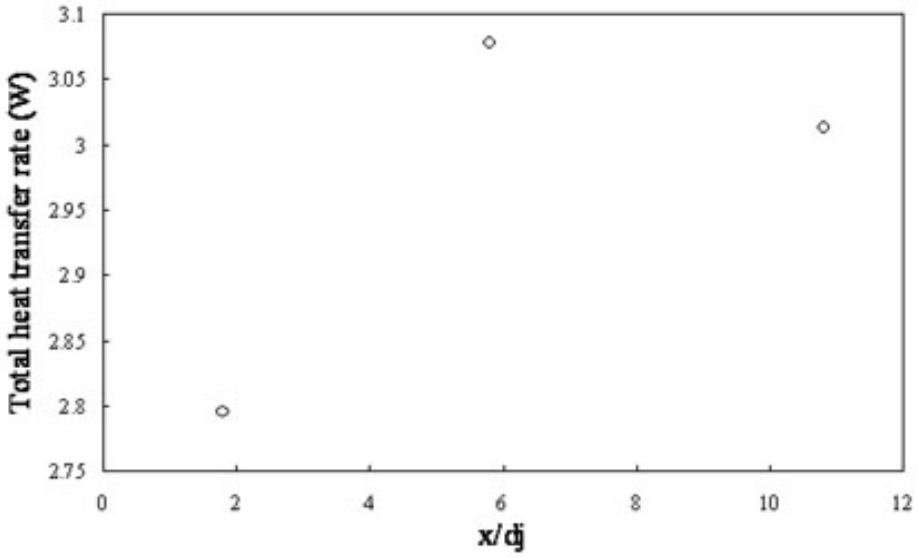

Figure 6.36: Total heat transfer rate for nozzle at different x-positions

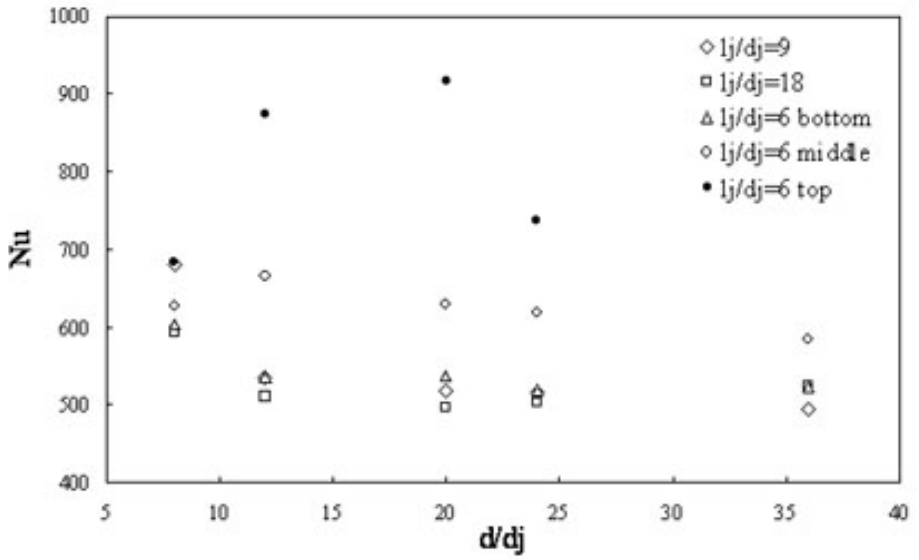

Figure 6.37: Left wall averaged Nu for different l_j/d_j and z-position of the nozzle

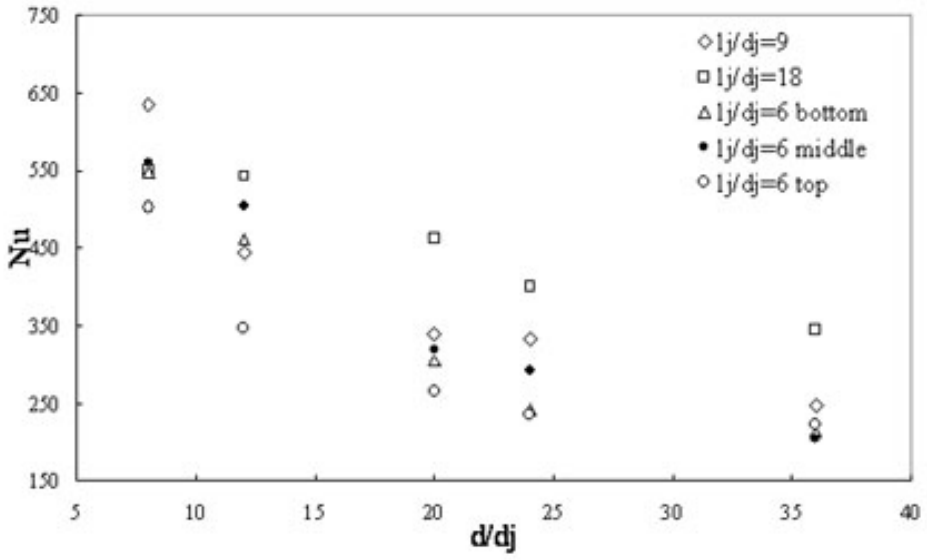

Figure 6.38: Right wall averaged Nu for different l_j/d_j and z-position of the nozzle

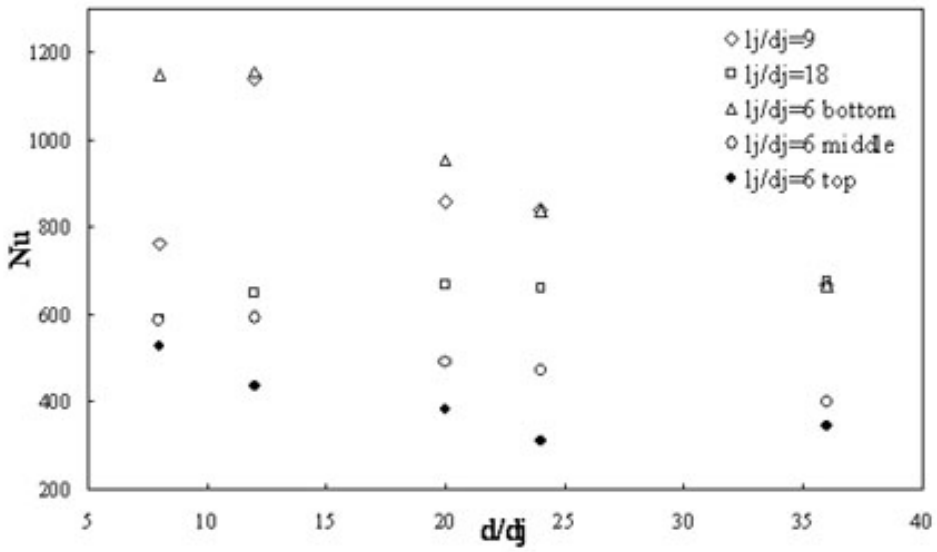

Figure 6.39: Bottom wall averaged Nu for different l_j/d_j and z-position of the nozzle

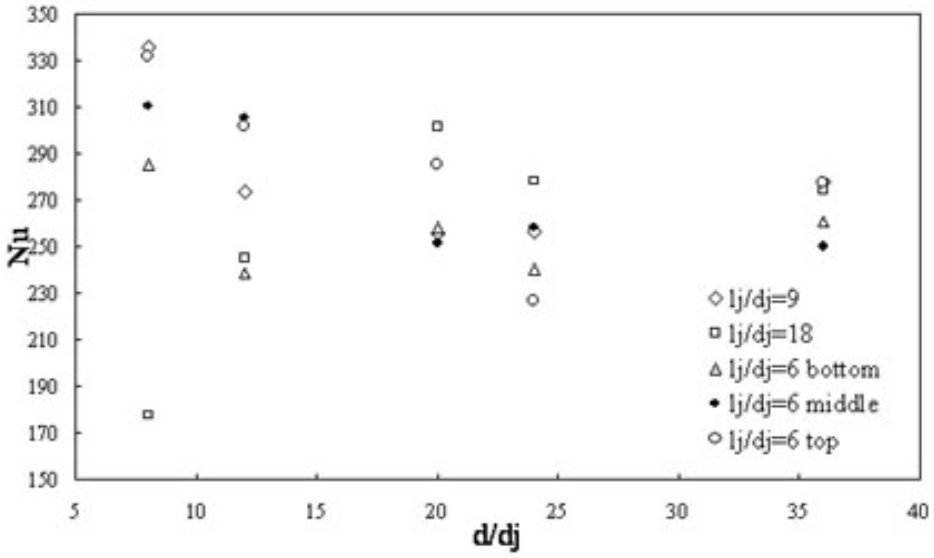

Figure 6.40: Top wall averaged Nu for different l_j/d_j and z-position of the nozzle

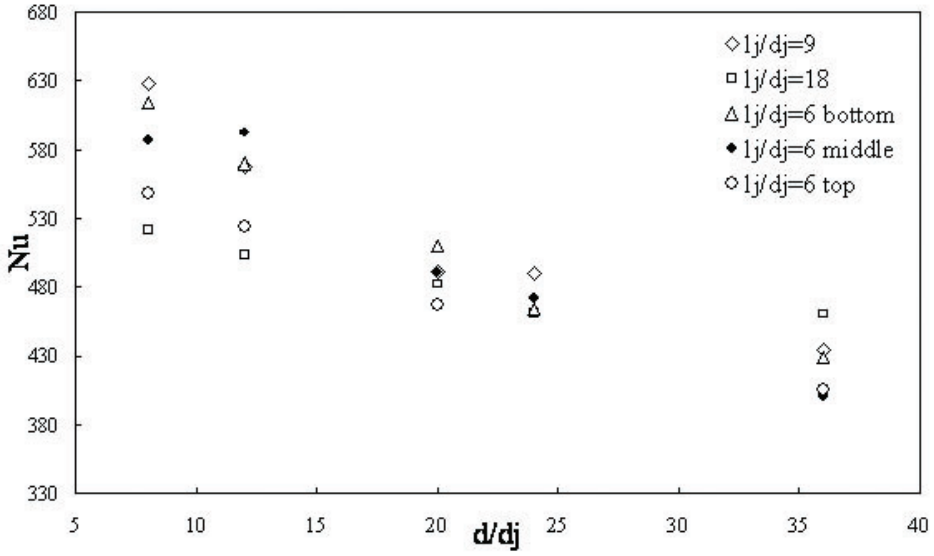

Figure 6.41: Overall surface averaged Nu

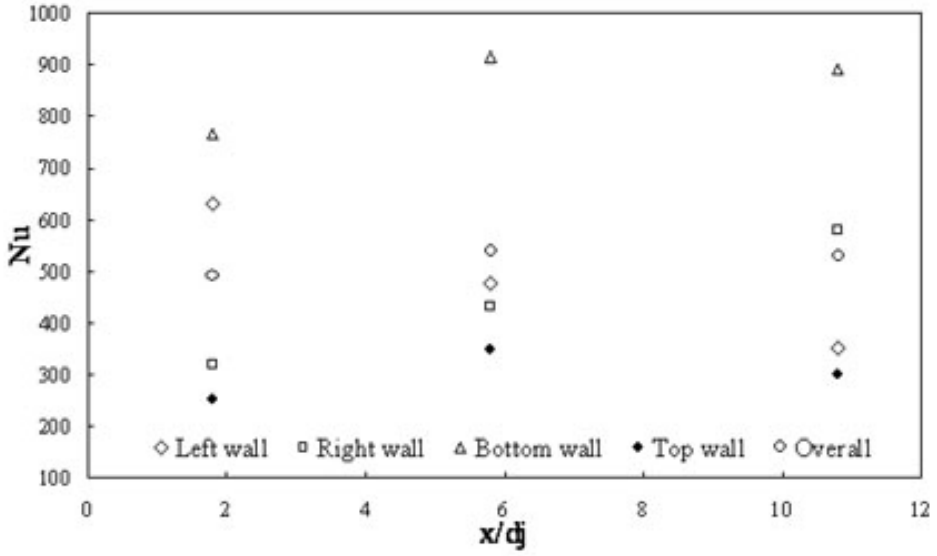

Figure 6.42: Averaged surface Nu of ld620m cases with nozzles at different x-positions

d/d_j ranging from 12 to 24. For all the cases where the slit was placed at the bottom of the channel (normal slit configuration), the heat transfer on the left wall also drops monotonically, but for l_j/d_j=6 (middle and top configuration), the heat transfer is enhanced when the channel is wider than the original d/d_j=8 case.

The heat transfer enhancement for the slit placed near the top wall is more than that for the slit placed in the middle of the channel, which actually entrained the most flow in all configurations. The reason for this is that the jet flow in the top configurations covers more area than in the middle and bottom configurations because the jet is directed towards the bottom wall and slightly to the right wall. Therefore, the configuration with the slit placed at the top yields the highest heat transfer coefficient on the left wall. When the channel width increases, the increased entrained flow rate improves the heat transfer even more. Because the jet is also directed slightly towards the right wall, when the channel width increases, the jet flow in the "top" and "middle" configurations may developed with less constrain than the original cases. So some heat transfer improvements were observed. When the channel width increases even more, the significant drop of flow velocity causes the average Nu decreases.

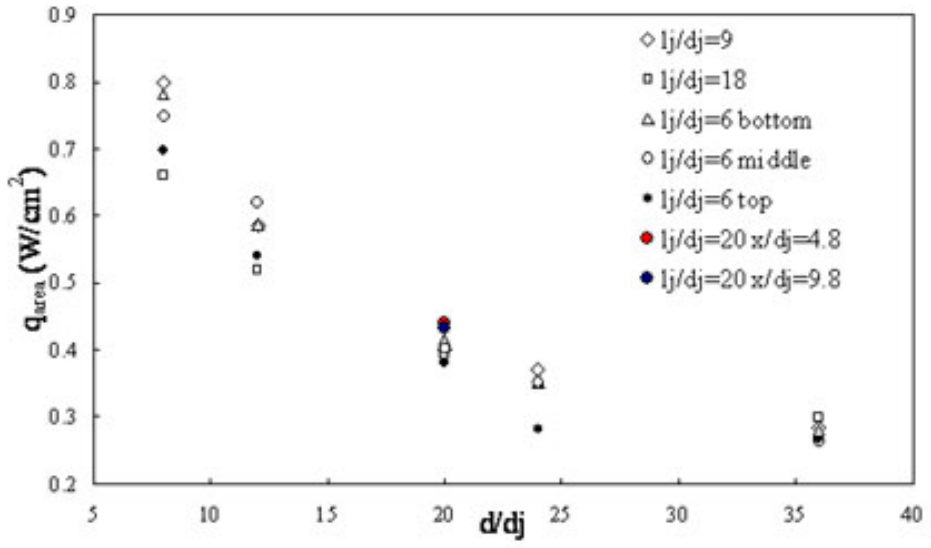

Figure 6.43: Comparison of q_{area}

The heat transfer on the bottom wall was expected to be the highest among all the walls for all cases because of the jet impingement. Even for the possible weakest case (l_j/d_j=6, top), the heat transfer on the bottom wall is larger than the heat transfer on the top wall. From Figure 6.39, there is a peak at d/d_j=12 observed for the l_j/d_j=9 and 6 bottom configurations. The highest Nu for the l_j/d_j=18 configuration occurs when d/d_j=20. The reason for this is that the jet flow develops better when the channel is reasonably wide. For the l_j/d_j=6 top and middle configurations, the heat transfer on the bottom wall decreases as the channel width increases.

The heat transfer on the top wall generally drops when the channel becomes wider except for the l_j/d_j=18 configurations. Like the heat transfer on the bottom wall, these configurations have a peak near $d/d_j = 20$. For the l_j/d_j=18 configurations, the distances from the slit to the top and bottom walls are nearly equal, so the heat transfer on these two walls would show similar characteristics. The heat transfer on the top wall is relatively weak, but the change of Nu for different channel widths is relatively small for $d/d_j > 20$.

In most applications, the bottom wall is attached to the heat source, so better heat transfer on this wall is desired. If we examine the results, the l_j/d_j=6 bottom configuration

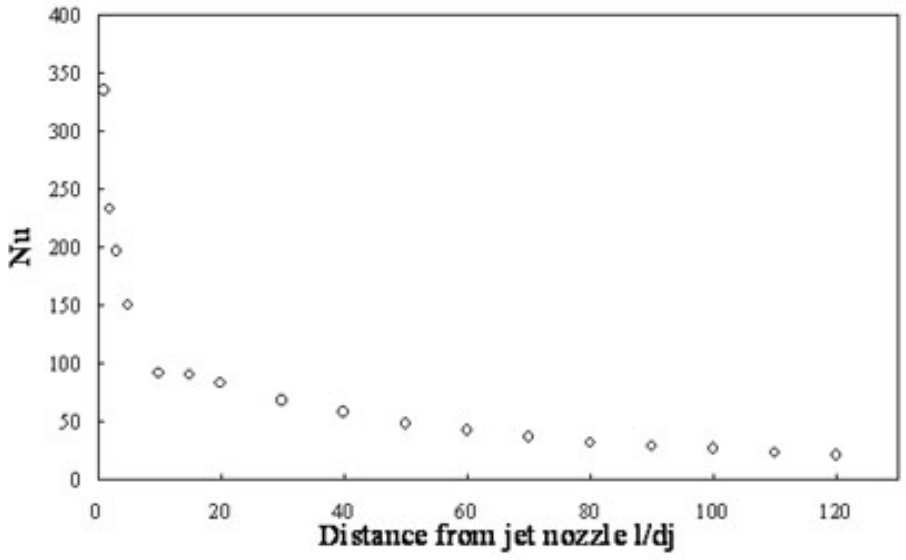

Figure 6.44: Average Nu along the channel length

shows significant advantages over others: the Nu is 100% higher than the original design configuration of l_j/d_j=18, and it is 50% higher than the l_j/d_j=9 configurations at d/d_j channel width. Another interesting observation is that when the channel is wide enough (e.g. $d/d_j > 35$) the heat transfer for all bottom cases becomes the same.

The overall Nu decreases when d/d_j increases. The configuration with l_j/d_j=9 outperforms all others when d/d_j is small. The configuration with l_j/d_j=6 middle has the best heat transfer performance at d/d_j=12. The heat transfer performance of the l_j/d_j=18 configuration is somewhat stable, mainly because its slit covers over 90% of the channel height and the heat transfer on all walls and the in-channel air mixing are more even than others. The heat transfer performance of all configurations are quite similar when d/d_j is around 20, which implies that the configuration is not as important as it is for narrower channels. Note that when d/d_j =20 the channel cross section is square ($H/d = 1$).

Although the entrained flow rates of the x/d_j =4.8 and 9.8 configurations are significantly higher than the original x/d_j =0.8 configuration, the heat transfer improvement is not so significant. The overall Nu are almost the same, although the Nu of the x/d_j =4.8 configuration is slightly higher.

Table 6.10: Comparison of short channel configuration with original configuration

Channel length	$Nu_{Leftwall}$	$Nu_{rightwall}$	$Nu_{topwall}$	$Nu_{bottomwall}$	$Nu_{overall}$	$q_{area}(W/m^2)$	$T_{outlet}(K)$
$127d_j$	594.5	550.5	177.8	591.4	521.4	0.66	348.5
$30d_j$	1363.3	1014.3	500.5	1483.8	1135.3	1.779	307.4
Difference (%)	129	81	181.5	151	117.8	169.5	N/A

Considering the performance of the entire heat sink cell, configurations with a slit of l_j/d_j=9 aspect ratio in a narrow channel is the best. For requirements of best performance on particular walls or for specific channel width, other configurations could be recommended according to the results shown.

To evaluate the overall heat transfer performance of the active heat sink, we should compare q_{area}. As expected, in Figure 6.43 q_{area} decreases rapidly. For similar slit positions, the q_{area} show similar trends: l_j/d_j=6 bottom, l_j/d_j=9 and l_j/d_j=18 configurations are closer on this figure than the l_j/d_j=6 top and middle configurations.

The flow characteristics of the active heat sink show that the region with the highest heat transfer coefficient is near the slit exit. In this region, strong flow disturbances, a relatively high flow velocity, jet impingement and the low temperature of the entrained flow are the four main factors contributing to better heat transfer than in the rest of channel. This is also illustrated in Figure 6.44, which is the average Nu along the channel length of the ld1808 case. From the figure, we observe that the Nu drops rapidly in the region of l/d_j less than 10 and the rate of dropping becomes smaller beyond $l/d_j = 10$. In this region ($y < 10d_j$), the boundary layer could not develop due to the strong disturbance of the synthetic jet flow. It is obvious that the heat transfer efficiency suffers if a long channel configuration is used.

A heat sink based on the ld1808 configuration, but with a much shorter channel length was simulated. The channel length for this configuration was $30d_j$. The results show significant improvement on heat transfer on all walls. The comparison is shown in Table 6.10. It is clear that shortening the channel is a good way to improve the design of this active heat sink.

Finally one ld1808 configuration with a higher inlet velocity boundary condition was simulated to compare the heat transfer improvement due to increasing the jet velocity. The inlet velocity magnitude was determined by matching the averaged jet velocity equal to the maximum velocity in the $l_j/d_j = 18$ configuration jets. The velocity magnitude was found to be approximately 28m/s. So the inlet velocity boundary condition was set as: $28\sin(2\pi ft)$, where f=200. The results were summarized in Table 6.11. From the results we found that when the jet velocity was increased, the largest enhancement occurred on the top wall: the Nu improved by nearly a factor of five. The difference in the heat transfer on different walls was smaller than in the original configuration.

Table 6.11: Comparison of the heat transfer performance between high inlet velocity and original parameters

	Original case	High inlet velocity case	Changes (in %)
Mass flow rate through channel (x$10^{-5}kg/s$)	4.66	18	276
Flow rate (CFM)	0.1	0.37	262
Inlet velocity (m/s)	9sin(ωt)	18sin(ωt)	310
Outlet temperature (K)	348	337	N/A
Surface heat flux on left wall (W)	0.874	2.05	134.4
Surface heat flux on right wall (W)	0.809	2.00	148.0
Surface heat flux on top wall (W)	0.097	0.537	453.9
Surface heat flux on bottom wall (W)	0.323	0.975	201.0
Surface heat flux overall (W)	2.095	5.57	165.8
q_{area} (W/m^2)	0.66	1.754	165.8
$h_{leftwall}$ (W/m^2K)	17.915	42	134.4
$h_{rightwall}$ (W/m^2K)	16.581	41.1	148.0
$h_{topwall}$ (W/m^2K)	5.314	29.4	453.9
$h_{bottomwall}$ (W/m^2K)	17.75	53.4	201.0
h_{total} (W/m^2K)	15.693	41.5	165.0
$Nu_{leftwall}$	594.5	1405.7	136.4
$Nu_{rightwall}$	550.5	1373.6	149.5
$Nu_{topwall}$	177.8	989.8	456.7
$Nu_{bottomwall}$	591.4	1813.1	206.6
Nu_{total}	521.4	1392.8	167.2

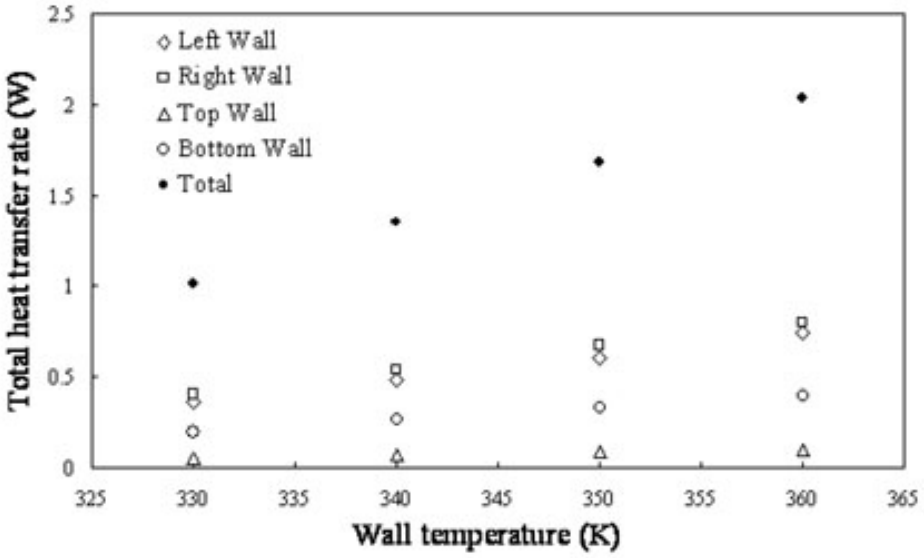

Figure 6.45: Heat transfer removal capability changes with wall temperature

6.6 Total heat transfer rate prediction for different wall temperature

According to the equation of convection heat transfer, temperature difference is one of the parameters that affect the total heat transfer rate. By varying the wall temperature from 330K to 360K, we examined the dependence of the heat transfer characteristics on the wall temperature. The total heat transfer rate from one heat sink cell changes almost linearly with the wall temperature (Figure 6.45), although the area weighted averaged heat transfer coefficient and Nu show a trend of increasing while the wall temperature increased.

Almost all of the heat transfer characteristics show a linear trend with the wall temperature. This is quite interesting and makes the task to predict the performance of the heat sink at different wall temperatures easier. (The radiation heat transfer change due to wall temperature change could be calculated using radiation heat transfer formula, this correlation only considers convection heat transfer). By using the linear regression relation obtained from the above results, the total heat removal capability of the heat sink cell at wall temperatures of 370 K and 380 K are: 2.364 W and 2.704 W. The CFD results of total heat transfer at 370 K and 380K wall temperature are 2.399 W and 2.705 W respectively.

The difference is less than 1.5% for the 370K wall temperature case and less than 0.05% for the 380 K wall temperature case. This suggests a simple way to estimate the performance of the active heat sink under different operating conditions.

6.7 Summary

In this chapter, a parameter study of an active heat sink developed at the Georgia Institute of Technology was documented. One cell of this active heat sink was studied numerically using the commercial CFD package Fluent. The parameters investigated including: jet nozzle(slit) geometry (l_j/d_j), placement of nozzle(slit) in the x- and z- directions, the cell channel width (d), the cell channel length (L), inlet velocity, and wall temperature.

The flow was modeled as an incompressible turbulent flow, Large Eddy Simulation (LES) with the RNG-based subgrid-scale model was employed to simulate the turbulence. An isothermal wall boundary condition was used in the heat-transfer simulations. Temperature-dependent material properties were used.

Three synthetic jets were intensively studied corresponding to different nozzle/slit geometries with the same inlet-velocity boundary condition. The non-dimensional stokes lengths for these three synthetic jets were 33.5, 55 and 86 respectively.

From the fluid dynamics point of view, the flow of an active heat sink cell is a confined jet flow. However, it is a complex, three dimensional, confined jet flow in which the jet flow direction is not parallel to the confining walls. To improve the heat transfer performance of the active cooling cell, from the flow analysis view point, higher flow velocities and more fresh low temperature airflow from surroundings are desired. In this study, the effect of geometrical parameters on the flow characteristics of the active heat sink cell were investigated. The flow pattern in the channel was analyzed. The entrained flow rate and the averaged channel velocity were compared. It was found that the strong flow disturbance in the channel was limited to the region near the synthetic jet nozzle/slit exit. Both the hydraulic and thermal boundary layer are destroyed and reconstructed in this region. A strong vortex, formed from the nozzle/slit edge, developed and dissipated mainly in this region. After around 50 times the nozzle/slit width from the nozzle/slit exit, the flow tends

to be a uniform channel flow only with slight fluctuations.

Driven by the same synthetic jet, the entrained flow rate increased when the channel width increased but for the l_j/d_j=6 nozzle/slit, there was a peak between d/d_j =12 to 20 for all nozzle/slit positions in the z-direction. As the nozzle/slit was placed further from the left wall, the entrained flow rate increased.

In the active heat sink cell forced convection heat transfer plays a more important role than conduction and radiation heat transfer (the conduction in the fin was not studied). The heat transfer performance of the active heat sink with different geometrical configurations were analyzed and compared. The heat transfer in the near nozzle/slit exit region was stronger than in the rest of the channel, which was expected by observing the flow characteristics. The heat transfer performance of configurations with the slit placed at the bottom of the channel was better than that of other configurations although the entrained flow rates were smaller. Driven by the same synthetic jet, the overall heat transfer coefficient generally decreases as the channel widened, but the heat transfer coefficients on the different channel walls changed in difference ways. It was also found that given a specific configuration, the total heat transfer rate changed with the wall temperature almost linearly.

CHAPTER VII

CONCLUSION

Devices related to micro synthetic jet have been intensively studied in recent years. Synthetic jets have been used in active flow control. Its unique no-flux characteristic also makes it attractive in thermal management applications. Numerical studies of synthetic jet flow, cavity modeling, synthetic-jet impingement, and its applications in thermal management were conducted in this research.

First, a free synthetic jet flow was studied. The synthetic jet cavity was modeled as a rigid chamber with a piston-like moving diaphragm located at its bottom. For turbulent synthetic jets, the shear stress transportation (SST) $k-\omega$ model was used to simulate the turbulence. Typical vortex dynamics and flow structures were identified. Time mean jet flow characteristics were studied. The working frequency, cavity geometry (mainly aspect ratio), and nozzle geometry (nozzle diameter) were varied to investigate the synthetic jet flow formation and evolution.

A synthetic jet flow can be divided into three regions analogous to conventional jets based on the time-mean velocity field analysis. The developing region was found much shorter than conventional jets if the non dimensional stroke length L_{stroke}/d_j is sufficiently large. In the fully developed region, the normalized velocity profiles reveal self-similarity too. A general velocity profile was found and it is close to the analytical solution for conventional axisymmetric turbulent jets. The linear relation between half jet width and distance from jet nozzle exit was found to be general, provided that the non dimensional stroke length is large enough. However, for small non dimensional stroke length cases, the synthetic jet flow was found to be wider than large L_{Stroke}/d_j cases.

A synthetic jet cavity model was derived based on the numerical study of free synthetic jet flows. As the pressure change occurs mainly in the nozzle/orifice region, the pressure distribution in the cavity could be reasonably assumed to be uniform. Then the synthetic jet cavity was assumed to be a lumped element device. The continuity conservation was applied to the control volume including the cavity with an opening in the top wall. By assuming the air in this system behave to be an ideal gas and obeys the polynomial law of states, a first-order ODE for the cavity pressure with time coupled with an average velocity through the nozzle/orifice was derived.

Another system, which included the nozzle and the space extending a few diameters out of the nozzle, was analyzed. An unsteady, compressible Bernoulli's equation with loss terms was applied to this system. By assuming that the average velocity and the time rate of change of the average velocity were constant in the nozzle, a first-order ODE for the average velocity through the nozzle with time coupled with cavity pressure was derived. The loss terms were calculated using correlations for pipe flows.

The inputs for this model are the cavity volume change in time, the working frequency, and the geometries of the cavity and nozzle. The ODE system was solved numerically to determine the cavity pressure and the average velocity through the nozzle/orifice. The solution could then be used to determine the two key parameters that characterize synthetic jet flow: non dimensional Stroke length L_{Stroke}/d_j and Re_{I_0}. In other words, once the design and operating parameters are known, the synthetic jet flow is fully characterized by this model.

The model predicted the cavity pressure and average velocity well when the model parameters were determined by simple physical analysis or numerical matching. Overall RMS errors for the cavity pressure and average velocity are within 10% and 6% respectively in test cases when compared to the full simulations.

This model is proposed as a replacement for a fully simulated cavity. By assigning the average .velocity as the inlet boundary condition at an appropriate cross section of the nozzle, the synthetic jet flow could be resolved without completely simulating the cavity. A sample case was documented and demonstrated the performance of this methodology. The modeled simulation well resolved the vortex dynamics of the synthetic jet flow compared to the full simulation. The flow field was well resolved also

A numerical study on synthetic jet impingement heat transfer was conducted. Both a full system simulation and a simulation using the proposed cavity model were used and compared with experimental measurements. It was found that both techniques resolved the typical flow structures, like vortex dynamics, reasonably well.

The vortex dynamics of synthetic jet impingement under different geometry configurations showed general characteristics. The vortex ring generated at the nozzle/orifice traveled

towards the target plate, and after impingement it expanded in the radial direction towards a residual vortex ring dissipated. When the impingement plate was further from the nozzle, the residual vortex ring moved further away from the centerline.

It was found that using synthetic jet impingement significantly improved the heat transfer compared to conventional jet impingement with velocity equal to the average jet exit velocity during the blow stroke of the synthetic jet. A roughly 50% improvement in total heat transfer rate and Nu was achieved in a sample study. The high local heat transfer rate region of synthetic jet impingement is limited in a smaller region near the stagnation area than the conventional jet impingement, which makes synthetic jet impingement more attractive in applications requiring a highly concentrated local thermal management solution.

There exists an optimal nozzle-to-impingement-plate distance ratio H/d_j. For a synthetic jet, the optimal H/d_j is 4, shorter than that of a conventional jet, H/d_j=6. With the same average jet velocity on the blow stroke, H/d_j, and working at the same frequency, the local heat transfer coefficient on the impingement plates increased when the nozzle diameter decreased. The working frequency of the synthetic jet affects the impingement heat transfer significantly. With a high working frequency, synthetic-jet-impingement heat transfer is stronger and the high heat transfer rate region is concentrated to a smaller region.

Finally, a parameter study of an active heat sink was conducted. One cell of this active heat sink was studied numerically using a commercial CFD package. The flow was modeled as an incompressible turbulent flow. The large eddy simulation (LES) with RNG-based subgrid-scale model was employed to simulate the turbulence. Isothermal wall boundary conditions were used in the heat transfer simulations. Temperature dependent material properties were used.

The parameters studied included the nozzle/slit geometry, channel geometry, inlet velocity boundary condition, and wall temperature boundary condition. The flow of an active heat sink cell is a three dimensional confined jet flow in which the jet flow direction is not parallel to the channel walls. The flow structure in the channel was analyzed. The entrained flow rate and averaged channel velocity were compared.

Due to the focus of this research, only axisymmetric micro synthetic jet flows with nozzle diameters between 100 $\mu m \sim 1\ mm$ were intensively studied. Limited by the author's knowledge, it is possible that the importance of certain parameters were underestimated. The accuracy of the available turbulence models may also have affected the accuracy of some finding in this study.

Although this research is not as perfect as author wishes, through this research, deeper understanding of synthetic jet flow was obtained. A cavity model was proposed and demonstrated efficient, effective and accurate. The superior thermal management performance using synthetic jet technique was investigated, including parametric study of some specific devices.

REFERENCES

[1] *Theory Manual of CFDACE+*, 1998.

[2] *User Guide Manual of Fluent 4.5*, 1999.

[3] Allen, M. G. and Glezer, A., "Jet vectoring using zero mass flux control jets," in *AFOSR contractor and grantee meeting on turbulence and internal flows*, (Wright Patterson AFB), May 1995.

[4] Baughn, J. and Shimizu, S., "Heat transfer measurements from a surface with uniform heat flux impinging jet," *Trans. ASME J. Heat Transfer*, vol. 111, pp. 1096–1098, 1989.

[5] Cain, A. B., Kral, L. D., Donovan, J. F., and Smith, T. D., "Numerical simulation of compressible synthetic jet flows," *AIAA Paper 1998-0084*, 1998.

[6] Camci, A. and Herr, F., "Forced convection heat transfer enhancement using a self-oscillating impinging planar jet," *ASME Journal of Heat Transfer*, 2002.

[7] Chen, Y., Scarborough, D., Liang, S., Aung, K., Glezer, A., and Jagoda, J., "Enhanced mixing in a simulated combustor using synthetic jet actuators," in *AIAA paper 99-0449*, (Reno, NV), Jan 1999.

[8] Chen, Y., Scarborough, D., Liang, S., Aung, K., and Jagoda, J., "Manipulating pattern factor using synthetic jet actuators," in *AIAA paper 2000-1023*, (Reno, NV), Jan 2000.

[9] Coe, D. J., Allen, M. G., Trautman, M. A., and Glezer, A., "Micromachined jets for manipulation of macro flows," in *Solid-State Sensor and Actuator Workshop*, (Hilton head, SC,), pp. 243–247, 1994.

[10] Dequand, S., Hulshoff, S., Kuijk, H. v., Willems, J., and Hirschberg, A., "Helmholtz-like resonator self-sustained oscillations, part 2: Detailed flow measurements and numerical simulations," *AIAA Journal*, vol. 41, pp. 416–423, March 2003.

[11] Dhaubhadel, M. N., "Review: Cfd application in automobile industry," *ASME. J of Fluid Engineering*, vol. 118, no. 4, pp. 647–653, 1996.

[12] Freitas, C. J., "Perspective: Selected benchmarks form commercial cfd codes," *ASME. J of Fluid Engineering*, vol. 117, no. 2, pp. 208–218, 1995.

[13] Gallas, Q., Holman, R., Nishida, T., Carroll, B., Sheplak, M., and Cattafesta, L., "Lumped element modeling of piezoelectric-driven synthetic jet actuators," *AIAA Journal*, vol. 41, no. 2, pp. 240–247, 2003.

[14] Gardon, R. and Akfrat, J., "The role of turbulence in determining the heat transfer characteristics of impinging jets," *Int. J. Heat Mass Transfer*, vol. 8, pp. 1261–1272, 1965.

[15] Gardon, R. and Cobonpue, J., "Impingement cooling from a circular jet in a cross flow," *Proceedings of 2nd International Heat Transfer Conference*, pp. 719–730, 1962.

[16] Gauntner, J. W., Livingood, J. N. B., and Hrycak, P., "Survey of literature on flow characteristics of a single turbulent jet impinging on a flat plate," *NASA TN D-5652 NTIS N70-18963*, 1970.

[17] Gilarranz, J. L., Yue, X., and Rediniotis, O. K., "Piv measurements and modeling of synthetic jet actuators for flow control," in *Proceedings of FEDSM'98*, (Washington, DC), June 1998.

[18] Giralt, F., Chia, C. J., and Trass, O., "Characterization of the impingement region in an axisymmetric turbulent jet," *Ind. Eng. Chem. Fundam.*, vol. 16, pp. 21–28, 1977.

[19] Glezer, A. and Amitay, M., "Synthetic jets," *Annu. Rev. Fluid Mech.*, vol. 34, pp. 03–29, 2002.

[20] Ingard, U. and Labate, S., "Acoustic circulation effects and the nonlinear impedance of orifices," *J. Acoust. Soc. Am.*, vol. 22, pp. 211–219, 1950.

[21] Jambunathan, K., Lai, E., Moss, M. A., and Button, B. L., "A review of heat transfer data for circular jet impingement," *Int. J. Heat and Fluid Flow*, vol. 13, no. 2, pp. 106–115, 1992.

[22] James, R. D., Jacobs, J. W., and Glezer, A., "A round turbulent jet produced by an oscillating diaphragm," *Physics of Fluids*, vol. 8, no. 9, pp. 2484–2495, 1996.

[23] Kral, L. D., Donovan, J. F., Cain, A. B., and Cary, A. W., "Numerical simulation of synthetic jet actuators," *AIAA Paper 1997-1824*, 1997.

[24] Lee, C. Y. and Goldstein, D. B., "Two-dimensional synthetic jet simulation," in *AIAA paper 2000-0406*, (Reno, NV), Jan 2000.

[25] Lee, C. Y. and Goldstein, D. B., "Dns of micro jets for turbulent boundary layer control," in *AIAA Paper 2001-1013*, 2001.

[26] Lee, C. Y. and Goldstein, D. B., "Two-dimensional synthetic jet simulation," *AIAA journal*, vol. 40, no. 3, pp. 510–516, 2002.

[27] Li, Z. X., Yi, M., and Luo, X. B., "Experimental investigation on synthetic jet," in *Kyoto-Seoul National-Tsinghua University Thermal Engineering Conference*, (Kyoto, Japan), pp. 119–124, 2001.

[28] Mahalingam, R. and Glezer, A., "An actively cooled heat sink integrated with synthetic jets," *NHTC paper 2001-20025*, 2001.

[29] Mahalingam, R., Rumigny, N., and Glezer, A., "Thermal management using synthetic jet ejectors," in *8th THERMINIC Workshop*, (Madrid), October 2002.

[30] Mallinson, S. G., Hong, G., and Reizes, J. A., "Some characteristics of synthetic jets," in *AIAA Paper 1999-3651*, 1999.

[31] Mednikov, E. and Novitskii, B., "Experimental study of intense acoustic streaming," *Sov. Phys. Acoust.*, vol. 21, no. 152–154, 1975.

[32] Menter, F., "Two-equation eddy-viscosity turbulence models for engineering applications," *AIAA-Journal*, vol. 32, no. 8, pp. 269–289, 1994.

[33] Meyers, J., Geurts, B. J., and Baelmans, M., "Database analysis of errors in large-eddy simulation," *Physics of Fluids*, vol. 15, no. 9, pp. 2740–2755, 2003.

[34] Mittal, R., Rampunggoon, P., and Udaykumar, H. S., "Interaction of a synthetic jet with a flat plate boundary layer," *AIAA Paper 2001-2773*, 2001.

[35] Mittal, R., Rampunggoon, P., and Udaykumar, H. S., "On the virtual aeroshaping effect of synthetic jets," *Physics of Fluids*, vol. 14, no. 4, pp. 1533–1536, 2001.

[36] Moran, R. P., Peter, W. D., Muller, M. O., Bernal, L. P., Parviz, B. A., and Najafi, K., "Numerical simulation of micromachined acoustic resonators," in *AIAA paper, 2000-0546*, 2000.

[37] Nae, C., "Unsteady flow control using synthetic jet actuators," in *AIAA Paper 2000-2403*, 2000.

[38] Nae, C., "Numerical simulation of a synthetic jet actuator," in *ICAS2000-ICA0266.1*, 2000.

[39] Ohmi, M., Iguchi, M., Kakenhashi, K., and Tetsuya, M., "Transition to turbulence and velocity distribution in a oscillating pipe flow," *Bull. JSME*, vol. 25, pp. 365–371, 1982.

[40] Ollsson, M. and Fudus, L., "Large eddy simulations of a forced semiconfined circular impinging jet," *Physics of Fluids*, vol. 10, no. 2, pp. 998–1011, 1998.

[41] Pes, M., Lukovic, B., Orkwis, P., and M., T., "Modeling of two dimensional synthetic jet unsteadiness using neural network-based deterministic source terms," in *AIAA Paper 2002-2860*, (Louis, Missouri), June 2002.

[42] Peyret, R., *Handbook of Computational Fluid Mechanics*. Academic Press, 1996.

[43] Pope, S. B., "Ten questions concerning the large-eddy simulation of turbulent flows," *New Journal of Physics*, vol. 6, no. 35, p. 1, 2004.

[44] Rao, P., Gilarranz, J. L., Ko, J., Stranac, T., and K., R. O., "Flow seperation control via synthetic jet actuation," in *AIAA Paper 2000-0407*, 2000.

[45] Rathnasingham, R. and Breuer, K. S., "coupled fluid-structual characteristics of actuators for flow control," *AIAA Journal*, vol. 35, no. 5, pp. 832–837, 1997.

[46] Ravi, B., Mittal, R., and Najjar, F., "Study of three dimensional synthetic jet flowfields using direct numerical simulation," in *AIAA Aerospace Sciences Meeting and Exhibit*, (Reno, NV), Jan 2004.

[47] Rediniotis, O. K., Ko, J., Yue, X., and Kurdila, A. J., "Synthetic jets, their reduced order modeling and applications to flow control," in *AIAA paper 99-1000*, (Reno, NV), Jan. 12–15 1999.

[48] Ritchie, B. D., Mujumdar, D. R., and Seitzmann, J. M., "Mixing in coaxial jets using synthetic jet actuators," in *AIAA Paper 2000-0404*, (Reno, NV), Jan. 2000.

[49] Rizzetta, D. P., Visbal, M. R., and Stanek, M. J., "Numerical investigation of synthetic-jet flowfields," *AIAA Journal,*, vol. 37, no. 8, 1999.

[50] Rumsey, C. L., Gatski, T. B., Sellers, W. L., Vatsa, V. N., and Viken, S. A., "Summary of the 2004 cfd validation workshop on synthetic jets and turbulent sepeartion control," *AIAA Paper AIAA-2004-2217*, July 2004.

[51] Russel, G. B., "Local and system-level thermal management of a single level integrated module (slim) using synthetic jets," Master's thesis, Georgia Institute of Technology, 1999.

[52] Schilichting, H., *Boundary layer Theory*. New York: McGraw-Hill, 7 ed., 1987.

[53] Smith, B. L. and Glezer, A., "Vectoring and small-scale motions effected in free shear flows using synthetic jet actuators," in *35th AIAA Aerospace sciences meeting and Exhibit*, (Reno, NV), AIAA paper, Jan 1997.

[54] Smith, B. L. and Glezer, A., "The formation and evolution of synthetic jets," *Physics of Fluids*, vol. 10, no. 9, pp. 2281–2297, 1998.

[55] Smith, B. L. and Swift, G. W., "A comparison between synthetic jets and continuous jets," *Experiments in Fluids*, vol. 34, pp. 467–472, 2003.

[56] Smith, B. L., Trautman, M. A., and Glezer, A., "Controlled interactions of adjacent synthetic jets," in *AIAA paper, 99-0669*, (Reno, NV), Jan 1999.

[57] Tamburello, D. A., "Parametric analysis of the synthetic air jet using numerical simulations," Master's thesis, Georgia Institute of Technology, 2003.

[58] Thompson, M. R., Denny, D. L., Black, W. Z., Hartley, J. G., and Glezer, A., "Cooling of microelectronic devices using synthetic jet technology," in *11th European Microelectronics Conferences*, (Venice, Italy), pp. 362–366, 1997.

[59] Travnicek, Z. and Tesar, V., "Annular synthetic jet used for impinging flow mass-transfer," *Int. J. of Heat and Mass Transfer*, vol. 46, pp. 3291–3297, 2003.

[60] Tummala, R., Rymaszewski, E., and Klopfenstein, A., *Microelectronics Packaging Handbook*. New York, NY: Chapman and Hall, 1997.

[61] Utturkar, Y., Holman, R., Mittal, R., Carroll, B., Sheplak, M., and Cattafesta, L., "A jet formation criterion for synthetic jet actuaors," in *AIAA Paper 2003-0636*, 2003.

[62] Utturkar, Y., Mittal, R., Rampunggoon, P., and Cattafesta, L., "Sensitivity of synthetic jets to the design of the jet cavity," in *AIAA paper 2002-0124*, 2002.

[63] Viskanta, R., "Heat transfer to impinging isothermal gas and flame jets," *Experimental Thermal and Fluid Science*, vol. 6, pp. 111–134, 1993.

[64] Vukasinovic, J. and Glezer, A., "An active radial countercurrent heat sink driven by a synthetic jet actuator," (New York), November 2001.

[65] Vukasinovic, J. and Glezer, A., "Spot-cooling by confined, impinging synthetic jet," *Proceeding of HT2003: 2003 ASME Summer Heat Transfer Conference*, July 2003.

[66] Watson, M., Jaworski, A. J., and Wood, N. J., "Contribution to the understanding of flow interactions between multiple synthetic jets," *AIAA Journal*, vol. 41, no. 4, pp. 747–749, 2002.

[67] Wolfgang, V., Thomas, E., and Florian, M., "Heat transfer predictions using advanced two-equation turbulence models," tech. rep., CFX.

[68] Wu, E. K. and Breuer, S. K., "Dynamics of synthetic jets actuator arrays for flow control," *AIAA paper 2003-4257*, 2003.

[69] Zumbrunnen, D. A. and Aziz, M., "Convective heat transfer enhancement due to intermittency in an impinging jet," *Journal of Heat Transfer*, vol. 115, pp. 91–98, 1989.